Inner structure and atmospheric dynamics of gaseous giant planets

Florian Debras

To cite this version:

Florian Debras. Inner structure and atmospheric dynamics of gaseous giant planets. Atmospheric and Oceanic Physics [physics.ao-ph]. Université de Lyon, 2018. English. NNT : 2018LYSEN085 . tel-01998245

HAL Id: tel-01998245
https://theses.hal.science/tel-01998245v1

Submitted on 29 Jan 2019

Numéro national de thèse: 2018LYSEN085

THÈSE DE DOCTORAT DE L'UNIVERSITÉ DE LYON

opérée au sein de

l'Ecole Normale Supérieure de Lyon

École Doctorale No 52

Physique & Astrophysique de Lyon

Spécialité de doctorat: Physique - Astrophysique

Soutenue publiquement le 21/12/2018, par:

Florian DEBRAS

Inner structure and atmospheric dynamics of gaseous giant planets

-

Structure interne et dynamique atmosphérique des planètes géantes gazeuses

---

Devant le jury composé de:

FROMANG Sébastien, Ingénieur chercheur, IRFU	Rapporteur
GUILLOT Tristan, Directeur de recherche, OCA	Rapporteur
MORBIDELLI Alessandro, Directeur de recherche, OCA	Examinateur
SAINT-RAYMOND Laure, Professeure, UMPA	Examinatrice
CHABRIER Gilles, Directeur de recherche, CRAL	Directeur de thèse

Résumé

Lors de cette thèse, je me suis attaché à améliorer notre connaissance des planètes géantes, depuis notre voisine Jupiter jusqu'aux exoplanètes lointaines : les Jupiter chauds.

Grâce aux nouvelles observations gravitationnelles extrêmement fines du satellite Juno, entré en orbite autour de Jupiter en juillet 2016, il est possible d'améliorer significativement les modèles de structure interne de la planète. Cependant, cela ne peut se faire qu'à condition d'avoir une méthode suffisamment précise pour exploiter au maximum les données. J'ai donc étudié la méthode des sphéroides de Maclaurin concentriques et ses limitations.

A l'aide des connaissances contemporaines sur les équations d'état, les propriétés diffusives et les transition ou séparation de phase entre l'Hydrogène et l'Hélium, il m'a alors été possible de produire de nouveaux modèles de Jupiter. Arriver à combiner les observations gravitationnelles de Juno et les abondances d'éléments observées par Galiléo n'a pu se faire qu'en décomposant Jupiter en au moins 4 zones, de l'envelope externe jusqu'au coeur compact. J'ai montré que la taille de ce coeur compact était dégénérée avec la variation d'entropie à l'intérieur de la planète.

La structure interne des Jupiter chauds quant à elle est très dépendante de leur dynamique atmosphérique, qui entraîne une inflation de leur rayon. J'ai étudié les atmosphères de ces planètes à l'aide du modèle de circulation globale de l'Université d'Exeter et d'un code linéaire que j'ai développé, appelé ECLIPS3D. La caractéristique la plus importante de la circulation atmosphérique est la présence d'un jet superrotatif, étendu en latitude.

J'ai donc étudié la création de ce jet à l'aide d'arguments théoriques pour s'assurer de sa pertinence physique. L'étude de la solution linéaire dépendante du temps, associée à des arguments numériques sur la convergence de quantité de mouvement par les vents verticaux m'ont permis d'établir une compréhension globale, cohérente de l'accélération de la superrotation dans l'atmosphère de ces planètes.

Avec ce travail, j'ai amélioré ma compréhension théorique des planètes géantes et dévelopé des codes qui peuvent être utilisés pour améliorer nos connaissances sur la structure interne et la dynamique atmosphérique des planètes géantes, que ce soit Jupiter, Saturne ou les Jupiter chauds.

Abstract

Through this thesis, I have been motivated by the will to improve our knowledge of giant planets, from our neighbouring Jupiter to the far away worlds across the galaxy: hot Jupiters.

With the latest, extremely precise observations of the satellite Juno, new models of the interior of Jupiter can be derived. A precise enough method is required to take full advantage of these outstanding data, and I therefore studied the concentric Maclaurin spheroid method and its limitations.

With contemporary understanding on the equations of state, diffusive properties and phase transition/separation of hydrogen and helium, I could then focus on producing new interior models of Jupiter. Combining the gravitational observations of Juno with the elemental observations of Galileo has proven to be a complicated task, which required to decompose the planet into at least four regions from the outer envelope to the inner, compact core. I have shown that the size of the compact core is degenerated with the entropy variation within the planet.

Concerning hot Jupiters, I have reminded of the need to understand their atmospheric dynamics to constrain their interior structure, as the wind circulation can lead to an inflation of their radius. Studying numerically their atmospheric dynamics was performed with the University of Exeter's global circulation model as well as with the development of a linear solver that I called ECLIPS3D. An important, robust feature is the presence of a broad equatorial superrotation in the atmosphere of these planets.

Finally, I have explored the spin up of this superrotation on theoretical grounds, to assess its physical relevance. I have calculated the linear time dependent solution to show the importance of differential drag and radiative damping, and have used numerical simulations to highlight the importance of vertical momentum acceleration. Globally, a coherent picture of the initial spin up of superrotation was obtained.

Through this work, I have improved my theoretical understanding of giant planets and developed various codes that can be used to study and improve our knowledge of the interior structure and atmospheric dynamics of giant planets, from Jupiter and Saturn to hot Jupiters.

Acknowledgements

During these three years, travelling between England and France, I have met and worked with numerous people that accompanied me through this journey, whom I wish to acknowledge. Chronologically speaking, I'll begin with my time in Exeter, before turning to Lyon.

First things first, I want to thank Nathan deeply. As his first PhD student (forgetting more or less about Ben), I was thrilled to dive into planetary atmospheres under his supervision and never failing enthousiasm. He has reminded me lately that I told him in my first days "I agree to begin with HD209, but most of all I want to work on terrestrial planets". Funny to remember that three years later, with no plan whatsoever to work on the atmosphere of terrestrial planets ! Although he needs to improve his sense of humour when France loses a rugby game, it has been a real pleasure to be involved in his group for the past three years. Still waiting for a dinner at yours !

This time in Exeter would not have been the same either without Isabelle. She has always included me with the rest of her group, although I was the youngest and not working on stars (my Frenchiness might have helped). Professionally speaking, she has been a guide throughout my work and our many discussion have directed my thoughts to the level of understanding I now have about atmospheric processes. I did learn a lot with her, both with a blackboard or a beer in hand, and I notably remember the conference in Cambridge defending our work !

Tom obviously deserves a particular place in this thesis. Not only has he taught me everything I know about parallel computing, Fortran libraries and actually computer science, he has been an important friend for the past three years. My wallet and my liver might have suffered from our pub nights, but I don't regret anything ! Most of my fun times in Exeter have been in his and Olivia's company.

Thank you also Ben - and Lucy - and Tom II, I do wish you all the best for your personal and professional future and hope to see you again soon. I also want to thank Pascal Tremblin: he has taught me a lot, and I will soon be in his position, a post doctoral fellow supervising an intern from polytechnique 7 years later ... Good luck on being a dad !

To name a few, I want to acknowledge the support of other PhD students (407 rules) - Ahmad, Liz, Jess, Tom, Mark, Sally, Lewis ... -, post docs - Stef, Tom, Tom and Tom - and staff members - Eric, David, Dave, Ian, James, Sean and Matt. Emma and Martyn have always been available for everything I needed, and one can only acknowledge their work ethics and kindness. Professionally speaking, Geoff Vallis, Beth Wingate and John Thuburn have influenced me a lot and I do wish to thank them.

Finally, I need to thank the PhD basketball team - Ricardio, Jean-Toma and Jean-Pat. From sport science to biology and science philosophy, we covered a wide range of subjects and almost all positions of a starting five for a basketball team. We would have beaten any team that the University could have come up with, without a doubt. We now are the "internationnally spread post-doc team", but the conclusion on us smashing everyone else clearly remains unchanged.

A Lyon, je me dois de commencer par remercier Gilles. Sa compréhension de la physique et son approche de la recherche m'ont fait me sentir (très) petit pendant la plupart de nos discussions, mais m'ont aussi permis de grandir plus que je ne pensais le pouvoir ! Plus que cela, il a été d'un support sans faille pendant ma thèse, aussi bien professionnellement que personnellement. Ses maintes blagues et anecdotes, son franc parler et ses (courtes) tenues de sport alimentent le labo d'une flamme pétillante qui ne faiblit pas. Il a été plus qu'un simple directeur de thèse pour moi, et je ne peux pas assez le remercier pour ça.

Je veux aussi réserver un paragraphe à Guillaume, pour toute l'aide qu'il m'a apportée sans broncher pendant ces années. Bien qu'il soit maître de conf, encadrant de thèse et de moultes stagiaires et père de deux enfants, il a toujours réussi à trouver du temps pour mes questions, qu'elles soient sur la physique ou pas. Entre autres, ma candidature de post-doc n'aurait pas la même tête sans lui (on a des preuves) et mon approche de l'enseignement serait moins poussée. Merci pour ton aide, et cette joie de vivre qui émane de toi en permanence ! Quatre mots pour conclure : ça wraps au top !

Merci aussi à Benoît, qui m'a trouvé une équipe de basket, un kiné, une invitation (avec Guillaume) dans une conf .. en plus de beaucoup de réponse de questions sur la MHD et la physique des coeurs stellaires, et aussi d'une sympathie sans faille (malgré un goût prononcé pour le clash de thésard). Si je suis guéri en mars on la fait cette nuit du basket ! Merci aussi Christophe, pas tellement parce que tu m'as guidé pour encadrer des TP, écrire un sujet ou comprendre un peu plus la physique, mais pour m'avoir fait découvrir les gâteaux à la poële ! Evidemment, un immense merci à Stéphanie s'impose ! On a une incroyable chance de l'avoir autour de nous, et je dis pas ça parce qu'elle nous a prêté l'appart au ski ! Merci pour ta disponibilité, ton adaptabilité et ton sourire permanent !

Vient le tour des autres thésards. On peut le dire, on se sera bien amusé ! D'abord avec Pierre Marchand et Pierre Mourier, dans le M6. On avait notre petit équilibre, à base de système solaire sur le tableau et de quantité mesurée de biscuits. En échange d'accepter de manger à 12h45, Pierre Mourier m'a aidé à remplir des tableaux d'équations, à propos d'instabilité autant que de moteurs à effets Casimir ! Mais le départ de l'autre Pierre et le déménagement ont tout chamboulé ... A la place, on s'est retrouvé avec les poussiéreux : Ugo et Maxime, fans de dinosaure ou de jazz. Le premier, toujours un café en main, et le deuxième, toujours une chanson en bouche, nous ont demandé de grandes facultés d'adaptation ! Heureusement, quelques constantes restent, et j'attends toujours de voir Pierre manger une salade ou boire du vin. Mais tout s'est vraiment cassé la tête quand les stagiaires sont arrivés. Arthur, Couenne-Tine Winemaker, cycliste invétéré aux sandales et longs cheveux, et le gros Jaupart, ils étaient pas là pour être ici. Tellement pas d'ailleurs qu'ils ont voulu rester ici pour trois ans de thèse, là ! Avec un peu de temps, dans toutes ces personnes susnommées, j'ai trouvé des amis plein d'énergie. Un big up quand même pour Etienne, mélange subtil de Boris Diaw et Teddy Rinner, mon jumeau bonobo, avec qui nous passons en une journée du basket au gaz parfait. Very nice !

Au labo et à l'ENS, je veux enfin remercier les nombreuses personnes avec qui j'ai eu des interactions plus sporadiques, mais enrichissantes (ou drôles). Merci Martin, GéGé, Evghény, Jeff, François, Benjamin, Barbara, Aude Caussarieu, Stéphane Labrosse, Je veux adresser une pensée particulière pour Antoine Venaille, qui a été très disponible tout au long de ma thèse.

Enfin, et je sais qu'ils n'attendent que ça, il me faut remercier ma famille qui me soutient depuis toujours et a une importante part dans mon parcours professionnel. Tout d'abord, je veux évoquer le souvenir des mes grands parents, papy Christian, papy Valentin - dont j'ai hérité le nom - et mamy Marinette. On dit que les paroles s'envolent mais que les écrits restent, en couchant leur nom sur le papier j'espère leur donner une petite place, aussi relative soit-elle dans une thèse, à la postérité.

Je commence donc par remercier mamy Colette qui nous accueille toujours avec son énergie débordante, mais que je n'aurai pas réussi à convaincre de venir à ma soutenance ! Heureusement, comme j'arrive à Toulouse, je pourrai encore plus souvent profiter de sa cuisine fameuse ! Je pense aussi à tous mes oncles, tantes et cousins, avec qui, en plus de tous les bons moments ensemble, j'ai eu maintes discussions intéressantes d'astrophysique, me poussant à ne jamais rien laisser au hasard.

Pour ma famille directe, ma soeur ayant mis le paquet dans sa thèse de médecine je sais que je ne l'emporterai pas sur le terrain de l'émotion, tentons un peu d'humour ! Et parce qu'ils seraient capables de faire des conclusions sur qui dirige la famille selon l'ordre de mes remerciements, j'ai donc choisi de les tirer au sort ... Et on commence par ... Elodie, puis Bastien, Papa, Maman et Simon ! Presque l'ordre que j'aurais choisi ...

Merci donc à ma grande soeur, pour toutes ces années à soutenir et défendre ses petits frères sans relâche. A peu près au même moment où je deviens docteur, elle commence une thèse pour devenir docteure docteure, histoire d'être sûre qu'elle puisse continuer à jouer le rôle de soeur protectrice ! Quel dévouement ... Et dans cette tâche, elle est bien accompagnée par son aveyronnais - mauvais perdant au risk - et la sublime Nanouille ..

C'est dur de remercier son jumeau, tellement il parait évident qu'il sait ce que je pense, et qu'on ne sait même pas comment se dire bonjour quand on se voit ! J'essaye quand même : merci à Bastien pour avoir fui en Nouvelle Calédonie pour toute la durée de ma thèse et m'avoir donc permis de rester concentré pendant trois ans. Après ces années à me soutenir à distance, ton emménagement sur Toulouse va nous permettre de rattraper le temps perdu !

Merci aussi papa, pour nous avoir tellement botté les fesses pendant toutes ces années en nous obligeant à travailler ! Encore aujourd'hui, tu ne supportes pas de nous voir inactif, nous poussant à toujours nous dépasser ! Bon, on n'est plus des enfants, mais au fond je crois qu'on aime tous bien ça ... Maintenant, à toi de travailler et nous de te botter les fesses, ce vin va pas se faire tout seul et il a intérêt à être bon !

Comment ne pas remercier ma petite maman, et son soutien inconditionnel quoi que j'entreprenne. Ton bonheur à parler de tes enfants est peut être un peu fort (elle m'a demandé une dizaine de fois mon titre de thèse pour qu'elle soit sûre de pouvoir en parler sans faire de fautes à tout son bureau !), mais ton amour de tous les instants nous remplit d'une détermination extrême pour la vie, j'en suis sûr !

Simon, enfin, mérite un remerciement particulier parce qu'il a été jusqu'à envoyer sa fiancée à Lyon pour me soutenir ! Merci donc de nous aimer à ta manière (principalement sous formes de baffes) et de toujours vouloir le meilleur pour tes petits frères et essayer de nous guider dans la vie (N.B. : je n'ai pas dit que ses conseils étaient bons). Et merci à Claire, madame Crousier (plus pour longtemps) pour ces moments en salles de TP !

Enfin, je veux évidemment remercier Andréa - mon chaton doux ou baby love, mais je ne sais pas si on peut dire ça dans une thèse - dont l'importance ne saurait être résumée par quelques lignes sur du papier. En trois ans, nous avons cumulé 9 appartements dans 5 villes et 2 pays (ce qui fait des dizaines de plantes, une peluche et un enfant imaginaire), et pendant tout ce temps elle n'a pourtant jamais arrêté de m'encourager à continuer dans cette voie. Nous avons tellement rêvé du 10ème appartement, où nous vivrions enfin ensemble, que c'est dur de penser qu'on y est arrivés ! Entre autres, elle a résisté à l'envie de me quitter toutes les fois où je n'arrivais pas à déconnecter (surtout en week-end ..) et elle a toujours été disponible pour m'écouter parler de mon travail, une partie non négligeable de mes idées lui est clairement dûe ! (Elle prétend que toutes mes idées viennent d'elle, cette page n'est pas le lieu pour en débattre. Appeler HD209458b "Ed", je veux bien reconnaître que ça vient de toi.) Je suis impatient que nous commencions pour de bon notre aventure toulousaine, et j'espère te rendre tout le soutien, l'amour et les rires (et les engueulades, il paraît que c'est sain de s'engueuler) que tu m'a apportés pour le reste de notre vie ensemble. Comme tu le sais, à tes côtés, la vie semble prendre du sens.

Summary

Chapter 1

Introduction

> *The story so far: in the beginning the Universe was created. This has made a lot of people very angry and been widely regarded as a bad move.*
>
> *Douglas Adams* - The Restaurant at the End of the Universe

In the 4th century before our time, Aristotle proposed that the Earth was made of 4 concentric spheres, composed solely of earth, water, air then fire, respectively. According to Descartes in 1644, Earth's interior was simply empty, whereas in 1695, Woodward [1695] pictured it as a crust covering a ball of water in order to explain the Genesis deluge. By studying meteorites, Édouard Albert Roche proposed the first two layer model of the composition of the Earth in 1883 [Roche, 1883]. This was permitted by the knowledge of the mass of the Earth from gravitational observations, and the knowledge of the behaviour of rocks under high temperature and pressure. Our contemporary understanding of the Earth's composition dates only back to the beginning of the 20th century, with the first seismological studies of Oldham [1906]. A hundred years of studying the propagating, diffracted and refracted waves have brought us to the current picture of the Earth, with a crust, a mantle, a liquid core and a solid inner core. The success of seismic studies is about to be brought to Mars, where Nasa's Insight rover will soon perform the first extraterrestrial seismological studies. Comparing the structure and composition of the Earth and Mars is expected to shed light on many unknowns of terrestrial planetary formation.

Gaseous planets, on the other hand, are a bit more challenging. First the formation process is less clear as the mass coming from accretion of planetesimals is unknown, contrary to terrestrial planets mainly formed by colliding rocks. But most importantly classical seismology is impossible to perform on these planets. On stars, asterosismology is a growing field. The pulsations of the Sun were discovered in 1960 by Robert Leighton [Leighton et al., 1962] and allowed the inference of the Sun's structure in the last 50 years. Mainly, we can observe acoustic waves with sufficient magnitude to decompose them onto spherical harmonics up to orders superior to 1000. On Jupiter, the convection zone breaks the propagation of gravity waves, as in the sun, but the acoustic waves on this cooler and smaller object have a lower amplitude and lower frequency, which make them harder to separate from the atmospheric motions. Still, Gaulme et al. [2011] were able to provide the first observations of Jupiter's pulsation. This work hasn't been used yet to derive internal models of Jupiter because signal to noise ratios are still too low, and these observations are quite scarce and preliminary.

One of the remaining options to understand giant planets' structure and formation is to study their gravitational field. If Jupiter was a homogeneous sphere, we could only learn its mass from the knowledge of its gravity. Fortunately, Jupiter is stratified in density and rotating hence the deviation of the gravity field from that of a homogeneous sphere can teach us lots about the composition of the planet. The first satellite observations were made 40 years ago, when the trajectories of Pioneer and Voyager allowed the evaluation of the Jovian gravity field (see notably Campbell and Synnott [1985]). Subsequent satellites have since studied the attraction of Jupiter in depth. Galileo provided better constraints on the atmospheric composition of the planet, especially with its entry probe that dived into the outer layers (Seiff et al. [1998] and von Zahn et al. [1998]). More recently, Juno has measured with unprecedented accuracy the gravity field and magnetic field of the planet (Bolton et al. [2017], Iess et al. [2018], Connerney et al. [2018]). Juno also provided pictures of the planet of tremendous quality, as displayed on Figure 1.1.

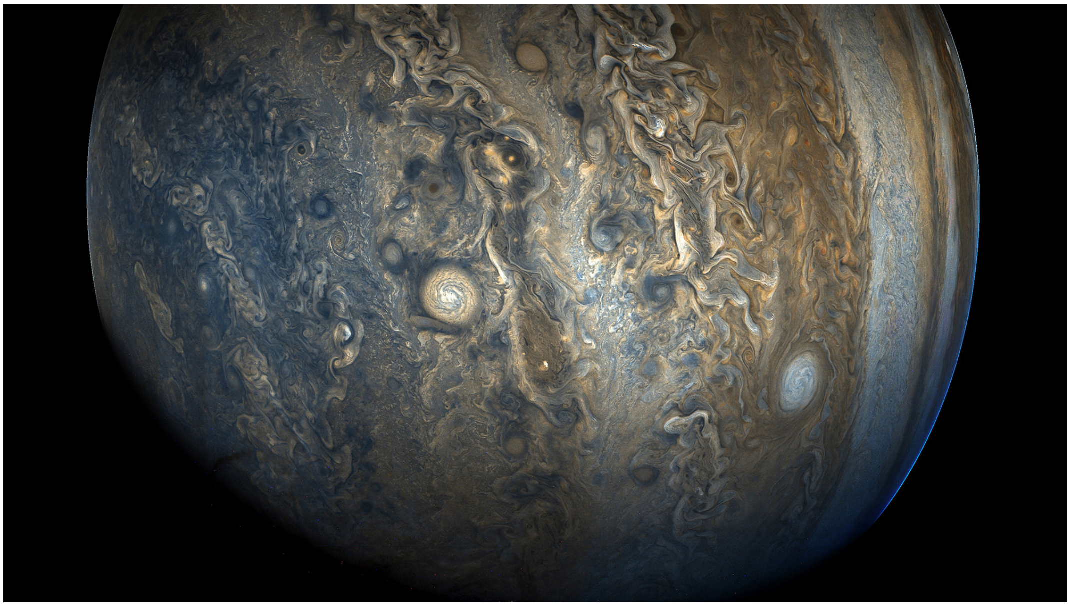

Figure 1.1: Jupiter Southern hemisphere as seen by Juno. Credits: NASA/JPL-Caltech/SwRI/MSSS/Gerald Eichstädt/ Seán Doran

Such a precision on the gravity field of Jupiter is a tremendous opportunity for the astrophysical community. It allows us to refine appropriate models or refute previous underconstrained propositions. But it also reminds us of the huge degree of degeneracy in the models. No matter the precision, inferring Jupiter's composition by solely observing its external gravity field yields a huge span of fitting models. Additionally, older models predicted a metallization transition with an entropy jump (see Guillot and Gautier [2014] for a review), but recent calculations with double diffusive convection in Leconte and Chabrier [2012] propose a gradient of entropy and heavy elements throughout the whole planet, eventually suppressing the need for a compact core in Jupiter. The different proposed physical processes increase yet further the degeneracy.

In this context, we have been interested in understanding Jupiter with the most up to date physical and mathematical developments. Mathematically speaking, William Hubbard in Hubbard [2012] and Hubbard [2013] has developed a powerful method to calculate the gravitational potential of a barotropic, hydrostatically balanced celestial body (said otherwise, a giant planet). Although its numerical cost is quite expensive, the level of adaptability of this method makes it an outstanding tool for understanding giant planets. Our first contribution was to study the limitations of this method in the context of Jupiter, to assess that its level of accuracy is sufficient with the extremely precise data of Juno. As reported in Debras and Chabrier [2018], we have highlighted the conditions under which the method can be safely used, and our knowledge of Jupiter improved.

Physically speaking, the advances in numerical quantum molecular dynamics (e.g., Soubiran and Militzer [2016], Mazzola et al. [2018] and other references throughout the thesis), plasma experiments (e.g., Loubeyre et al. [1985], Pépin et al. [2017], Celliers et al. [2018], etc.) and transport processes from numerical simulations and analytical expectations (e.g., Rosenblum et al. [2011], Moll et al. [2017], Leconte and Chabrier [2012], etc.) allow us to understand the conditions prevailing in the interior of Jupiter with much more subtlety. Based on these recent results, we have worked on deriving new interior structures of the planet, constrained by the knowledge of theoretical physics. Our work, submitted for revision in the Astrophysical Journal, shows that the structure of Jupiter is more complex than previously thought. However, lots of questions remain unanswered, and our knowledge of the interior of Jupiter will without a doubt improve in the fortchoming years.

Nonetheless, this broad picture of the structure of Jupiter and the understanding of the physical processes at stake in the planet have a fundamental, contemporary application: extrasolar planets. Since the first discovery of an exoplanet in 1995 [Mayor and Queloz, 1995], more than 3000 planets have been detected (`http://exoplanet.eu`) and there are still more than 8000 candidates yet to be confirmed. Among them, a few percent are gas giants, with sizes and masses ranging from sub-Neptune to super-Jovian, and orbits, eccentricities, radius and inclinations scattered across the parameter space. As we have seen, although 6 satellites have observed Jupiter from up close, our knowledge of the planet remains quite poor. In that regard, deeper understanding of extrasolar planets is a difficult, observationally limited task. Although comparison can be misleading when conditions are extremely different, it seems that using the solar system planets as templates for exoplanet structure is one of the only few ways of gaining further information. Of course, it is also needed to explore and exploit as much as possible the physics we can assess from the sole observations of these planets, reminding that to date, a direct image of a planet is actually one saturated pixel on a state of the art camera, with a 8 meters telescope.

Most exoplanets have been detected by two methods: radial velocities and transits. The imprecision from the transit, not able to distinguish a planet from a distant binary for example, requires a validation by radial velocities to confirm the existence of a planet. This seems constraining, but it has the advantage of providing complementary information on extrasolar planets. On the one hand, the radial velocity technique aims at observing the motion of the star around the centre of gravity of the star+planet system. It allows to estimate the mass of the planet (given the mass of the star and an unknown inclination) as well as its semi major axis and eccentricity. The more massive the planet, the easier the detection is.

On the other hand, in order to observe a transit, the planet has to cross our line of sight between its star and the

Earth. As the planet passes in front of its star, we can observe a dip in the luminosity of the star, which gives an estimate of the radius of the planet given the radius of the star. Therefore, the bigger the planet and the shorter its orbital period, hence the closer it is to its star, the easier the detection. At the dawn of exoplanetary science, the biggest, closest to their stars planets were therefore the first to be observed. At the time this thesis was written, we are approaching the limit were a planet strictly analogous to the Earth could be discovered (which happens to be the most difficult targets to observe). We show in Figure 1.2 the fraction of planet per star, as we picture it to date, as well as the diversity of observed planets by Kepler. Clearly, the solar system is not enough to fully understand extrasolar planets.

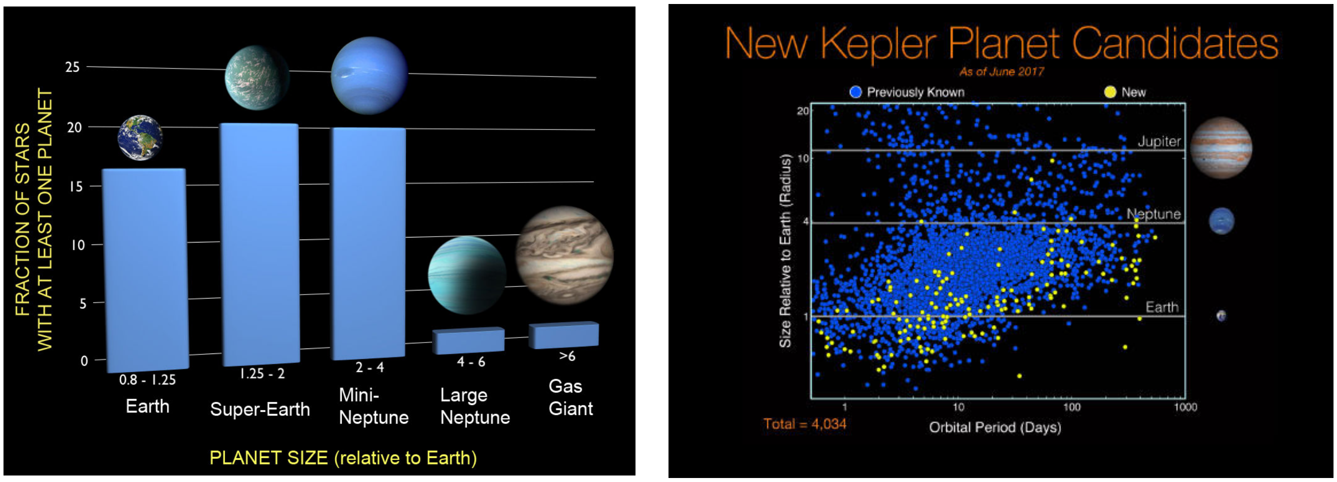

(a)

(b)

Figure 1.2: (a) Fraction of stars with planets as a function of the planet size as of our knowledge in 2017. Credit: F. Fressin (CfA) (b) Planets discovered by Kepler as of June 2017. Credits: NASA / Ames Research Center / Wendy Stenzel.

The first detection notably was amongst a class of planets that doesn't exist in the solar system: hot Jupiters. These are Jupiter-mass planets about 10 times closer to their star than Mercury is to the Sun. Because of this proximity, they are supposed to be tidally locked (see the review of Baraffe et al. [2010]) as the Moon is to Earth, thus always presenting the same side to the star. They also seem to have a much bigger radius than predicted by our understanding of planetary evolution. This issue of inflated radius is still a puzzle for the scientific community (see notably Guillot and Showman [2002], Batygin and Stevenson [2010] and Tremblin et al. [2017] and chapter 5).

What is really interesting with the transit detection method is that when the planet passes in front of the star the light of the star is affected by the composition of the planet. At the limbs, where the optical depth is low enough to let the incoming light from the star escape to our telescopes, molecules of the atmosphere of the planet can absorb a fraction of the energy. Therefore by comparing the spectroscopic signature of the star alone and the observed spectrum when the planet transits, one can obtain clues on the chemical composition of the atmosphere of the planet. It also becomes possible in some cases to observe the emission spectra of the planet during the secondary transit, just before the planet passes behind its stars. Instead of having a dip in the luminosity there is an increase in the received flux because of the reflection of the starlight by the planet. A comparative study of the composition of 10 hot Jupiters, as observed by transit techniques, has been performed in Sing et al. [2016]. Even with such a low statistical sample, it is quite obvious that there is a tremendous diversity of hot Jupiters.

The new data provided by exoplanetary observations demand new theories or numerical experiments in order to interpret them. Specifically, it is needed to predict what the atmosphere of hot Jupiters should be like. From meterological research, the numerical method used to study the evolution of an atmosphere is called a Global Circulation Models (GCM). First dedicated to weather prediction on Earth [Phillips, 1956], these models solve the equations of motion and of conservation (mass, energy, momentum) of an atmosphere to understand both the local scale for weather forecasting and the global scale for climate studies. These GCM are now adapted for astrophysics purposes, first on the solar system (on Venus typically [Kalnay de Rivas, 1975]) or to go back in time on Earth. In 2002, Showman and Guillot [2002] used for the first time a GCM on a hot Jupiter, leading the way to more than fifteen years of numerical predictions of exoplanet atmospheres. Many scientific teams across the world followed this pioneering work (Rauscher and Menou [2012], Perna et al. [2012], Dobbs-Dixon and Agol [2013], Heng et al. [2011] for example) and today there are multiples GCM used for exoplanetary science, not only dedicated to hot Jupiters. The university of Exeter works with the Unified Model (UM), their own adaptation of the Met Office GCM first presented in Mayne et al. [2014b] and used throughout this thesis.

These GCMs provide a framework for interpreting the observational data, but do not allow for a comprehensive grasp of the physical phenomena at stake. Additional understanding has to be provided by simpler, physically motivated studies. One of the main features obtained by GCM for hot Jupiter is the presence of an equatorial superrotation: at the equator the winds are going faster than the solid body rotation of the planet, up to a few kilometers per second. As we have shown in Mayne et al. [2017], this feature, first predicted by Showman and Guillot [2002], is largely insensitive to the equations and conditions used in the GCM as long as the planet is tidally locked and intensively irradiated.

The first comprehensive theory explaining this superrotation has been provided by Showman and Polvani [2011], later completed by Tsai et al. [2014] and Komacek and Showman [2016]. They rely on the propagation and interaction of stationary forced waves with the mean flow, setting up an initial circulation that eventually leads to superrotation. The complementarity of these three papers, from the simple 2D shallow water theory in Showman and Polvani [2011], to the 3D wave resonance study of Tsai et al. [2014] and the analytical orders of magnitude estimates of Komacek and Showman [2016], allows for a global coherent understanding of superrotation in hot Jupiters. However, there are still a few uncertainties, notably regarding the viability of the proposed mechanism with an accurate treatment of the radiative transfer and in the limits of low dissipation. In this context, we have also worked on enlightening the remaining areas of the physical explanation for superrotation on hot Jupiters. We have tackled this issue with the use of ECLIPS3D, a linear solver we have developed, and analytical arguments on both the dissipation of the waves excited by the stellar insolation and the momentum transfers they imply. This work, complemented by the numerical study performed in Mayne et al. [2017], is about to be submitted to Astronomy and Astrophysics.

Globally, in this thesis, I conduct a tour of many physical processes of prime importance in giant planets. Starting from the deep interior of Jupiter to the extreme conditions of the irradiated atmosphere of gaseous exoplanets, and notably HD209458b, I study the structure, equilibrium and disequilibrium properties of giant planets. In the context of Juno and the ever accelerating field of exoplanetary science, this manuscript is encapsulated in a thrilling context that brings new vision on the properties of gas giants. Jupiter, by its own, possesses more than 90% of the angular momentum of the solar system and is twice more massive than the other planets of the solar system altogether. Eventually, a better understanding of gas giants, starting 5 astronomical units from the Earth and going as far as a few hundreds of light years, will yield valuable knowledge on the formation and evolution of planetary systems across the galaxy.

Outline of the thesis

This manuscript is divided into 8 chapters, starting with this introduction. Chapter 2 details the theoretical background of the thesis, and notably the wave mechanisms relevant for atmosperic dynamics as well as the theory of convection in the deep interior of Jupiter. Then, chapter 3 provides a thorough study of the concentric Maclaurin spheroid method, which allowed me to derive new internal structures of Jupiter in chapter 4, based on the thermodynamical properties of hydrogen and helium. This work is the only one to date to match all the observational data, and we provide a thorough discussion on the physical assumptions of the models.

Chapter 5 is devoted to the transition from the core of Jupiter to the atmospheres of hot Jupiters, notably by explaining the issue of the inflated radius and by introducing global circulation models. In chapter 6 is detailed the linear code that I developed for the study of waves, instabilities and steady circulations in planetary atmospheres. As this chapter is mainly a benchmark of the code, it can be skipped at first reading. Combining theoretical calculations, global circulation models and ECLIPS3D, chapter 7 focuses on the understanding of the spin up of superrotation in hot Jupiters. This chapter extands prior works on the superrotation of hot Jupiters with the consideration of the time dependent linear solution and vertical momentum transfers. Finally, chapter 8 concludes the thesis, and details the perspectives for further studies.

Chapter 2

Definition of the basic concepts

Un bon discours ne doit être basé sur rien, tout en donnant l'impression d'être basé sur tout.

Pierre Dac

In this thesis, we are interested in the dynamics of fluids driven by a temperature gradient or in the structure of planets under hydrostatic equilibrium. In that regard, it is important to detail the Navier-Stokes equations and expose the physical conditions prevailing in the interior of giant planets. Additionally, we introduce the observed quantities to constrain the structure of a gas giant: the gravitational moments.

2.1 Equations of motion: Navier-Stokes equations

This section is largely inspired by Vallis [2006] where a full derivation of the equations can be found.

2.1.1 Eulerian and Lagrangian viewpoints

The notion of velocity in fluid dynamics is not obvious. When looking at a point object, its speed simply is the infinitesimal variation of its position with respect to time. For a solid, Newton laws are applied to its center of gravity and the inertia equation provides constraints on the equilibrium or global motion of an object. Its thermodynamical quantities can depend on the position in the solid, but the dynamical quantities are, on average, common to the whole object. The question is: how to define dynamical quantities for a fluid?

There are two ways of doing so. The first is to consider that an observer is in a fixed frame of reference and is looking at the properties of the fluid at a definite point of space. The quantities are then evolving with the fluid passing by and the observer sees the fluid as a field rather than an ensemble of particles. In that description, called the Eulerian description of a fluid, the evolution of the fluid (velocity, density, ...) ϕ would be defined as

$$\frac{\partial}{\partial t}\phi(x, y, z, t) = O(\phi, x, y, z, t),$$

where x, y and z are the cartesian coordinates, t the time and O is an operator determined by the laws of dynamics and thermodynamics.

The other approach is to consider that the fluid is an ensemble of parcels with their own properties that are moving together. In this Lagrangian description, we are following the evolution of a specific piece of the fluid within the surrounding flow. Therefore, the Lagrangian derivative, D/Dt represents the evolution with time of any quantity of the parcel, supposed constant within the parcel, as the parcel moves within the fluid. If an Eulerian observer was to follow the parcel, they would observe that a quantity q (temperature, density, ...) has an intrinsic change, $\partial q/\partial t$ plus an evolution due to the advection of the parcel within the fluid. The Lagrangian derivative can therefore be connected to the Eulerian derivative through:

$$\frac{Dq}{Dt} = \frac{\partial q}{\partial t} + \left(\vec{v} \cdot \vec{\nabla}\right) q,$$

where $\vec{v} = \vec{v}(x, y, z, t)$ is the velocity field of the fluid. Although most of this thesis is written from a Eulerian approach, this distinction is important to bear in mind when interpreting the results (convection within Jupiter, notably, is easier to understand phenomenologically from a Lagrangian point of view).

2.1.2 Equations of hydrodynamics

The description of motion for a fluid rely on three conservation laws, leading to a set of 5 equations. First in a closed system the mass must be conserved, which leads to the equation of continuity. This conservation implies that the change in the density of a parcel of fluid must be equal to the transport of density by the flow, so that there is no mass source or sink (we neglect any non conservation of mass due to nuclear effects). This gives:

$$\frac{\mathrm{D}\rho}{\mathrm{D}t} + \rho \vec{\nabla} \cdot \vec{v} = 0 \text{ , or equivalently } \frac{\partial \rho}{\partial t} + \vec{\nabla} \cdot (\rho \vec{v}) = 0, \tag{2.1}$$

where ρ is the density and $\vec{v}$ the velocity of the fluid.

The second conserved quantity is the momentum. As expressed in Newton's second law, the derivative of the momentum of a system with respect to time is equal to the forces applied on this system. With a fluid dynamics approach we obtain:

$$\frac{\partial \vec{v}}{\partial t} + \left(\vec{v} \cdot \vec{\nabla}\right) \vec{v} = -\frac{1}{\rho} \vec{\nabla} p + \nu \nabla^2 \vec{v} + \vec{F}, \tag{2.2}$$

where p is the pressure, ν the viscosity and $\vec{F}$ the external forces (per unit mass). This states that the change of the momentum of a parcel is determined by the forces applied to the parcel: the pressure gradient, the viscous effects and any other external force applied to the system (gravity mostly for a planet). This conservation law actually contains three equations as the velocity vector has three scalar components. At the first order, $|\nabla^2 \vec{v}|$ can be estimated as $|v|$ divided by the square of a characteristic length over which v changes. Calling L_v this length we have $|\nu \nabla^2 \vec{v}| \approx \nu v / L_v^2 = v/\tau_v$ where $\tau_v = L_v^2/\nu$ is a characteristic time of dissipation for the velocity. Diffusion by viscosity, which in the Navier Stokes equation acts as redistributing the momentum within the fluid, can also be seen as a friction which opposes the emergence of strong velocities on a timescale τ_v (which is not constant within the fluid). We will consider this approximation in the final chapters of this thesis.

Finally, the energy of a closed system is also conserved. In the general cases, we would write that the derivative of the energy with respect to time is equal to the sources and sinks of energy (for example the heating from the star). But as shown in Vallis [2006] this is equivalent to:

$$\frac{D\theta}{Dt} = \frac{\theta}{T}\frac{\dot{Q}}{c_p}, \tag{2.3}$$

where T is the temperature, θ is the potential temperature, $\dot{Q}$ is the heating rate and c_p is the specific heat capacity. θ is defined as the temperature a parcel of fluid would have if moved adiabatically to a reference pressure p_0 (usually 1 bar in the case of Earth atmosphere) and for an ideal gas we get:

$$\theta = T\left(\frac{p_0}{p}\right)^{R/c_p},$$

where R is the ideal gas constant divided by the mean molar mass of the system.

The sedulous reader will have noticed that we introduced six quantities (3 for the velocity and 3 thermodynamic variables) but only 5 equations, so our problem can't be resolved thus far. The last equation is describing how to link the thermodynamic quantities of the fluid, characterizing the type of fluid we have. This is the equation of state of the fluid, coming from physical processes intrinsic to the fluid. In this work, state of the art equations of state will be used to construct Jupiter's structure, but when considering atmospheric dynamics we will restrain ourselves to the ideal gas equation:

$$p = \rho R T\ . \tag{2.4}$$

2.1.3 The planetary case: rotating fluid under gravity

If the fluid we are studying is actually the atmosphere of a planet, we can go a bit further in the equations. We indeed know that the only force applied to our fluid is gravity. In our study, we will always neglect the tidal effects of the other celestial objects on the atmosphere. Although they play an important role in locking the planet in a synchronous orbit with the star (see Baraffe et al. [2010]) they are expected to only have a second order effect on the global dynamics.

Then the only remaining force is the attraction of the planet itself to its own atmosphere i.e., self-gravity. Usually, the self-gravity of the atmosphere itself can be neglected as its mass is negligible compared to the total mass of the planet. As for Earth, we can define a gravitational field $\vec{g}$ that expresses the gravitational attraction, always directed towards the centre of the planet for spherically symmetric planets. And if the atmosphere is at rest, we simply obtain:

$$\frac{1}{\rho}\frac{dp}{dr} = -g, \tag{2.5}$$

where r is the distance from the centre of the planet. In the general case, g is not constant and varies as $1/r^2$. Equation (2.5) is called hydrostatic balance or hydrostasy and is often a very good approximation even when the atmosphere is not in a rest state.

There is still another important physical effect: heating. In the case of Earth, the light we receive from the Sun dictates the whole thermal balance of the atmosphere and led to suitable conditions for developing life. It is also the cause of the large scale circulation of the atmosphere, from Hadley cells to Walker circulation. We don't expect to find life on hot Jupiters, but their closeness to their parent star leads to a huge level of irradiation. The whole treatment of radiative transfer is a very active field of research (see e.g., Amundsen et al. [2014]), out of the scope of this thesis, and it must be dealt with properly because its effect on the dynamics are huge, as we will see later in this section.

Finally, as obviously seen in the solar system, a planet is a rotating (almost) spherical body. It is then much more convenient to express the above equations in a rotating frame of spherical coordinates. As in the case of a point mass for classical mechanics, expressing the equations in the rotating frame of reference will lead to the emergence of pseudo forces: the centrifugal and Coriolis forces. They are easily expressed as a function of $\vec{\Omega}$, the vector of rotation of the planet and the position $\vec{r}$ on the planet:

$$\vec{f}_{\text{centrifugal}} = -\rho\vec{\Omega} \wedge (\vec{\Omega} \wedge \vec{r}), \tag{2.6}$$

$$\vec{f}_{\text{Coriolis}} = -2\rho\vec{\Omega} \wedge \vec{v}, \tag{2.7}$$

where $\vec{f}_{\text{centrifugal}}$ and $\vec{f}_{\text{Coriolis}}$ are the volumic centrifugal and Coriolis forces. Usually, centrifugal effects are incorporated in the gravity $\vec{g}$ as, at first order, they change the value of $\vec{g}$ but not its direction (this is less valid in the mid and high latitudes but the influence of the centrifugal force is smaller there).

Finally, in spherical coordinates, the unit vector depends on the position (it is easily seen that the longitudinal vector, which is always directed to the East in the rotating frame, is directed to the West for a fixed observer on the other side of the planet). Therefore, the derivative of vector quantities will induce the arising of new terms, the so called metric terms, that account for the infinitesimal changes of directional vectors with positions. Naming $\vec{e}_r$, $\vec{e}_\phi$ and $\vec{e}_\lambda$ the unit vector in the radial, meridional (directed to the North) and longitudinal (directed to the East) directions respectively, one can show that:

$$\frac{\mathrm{D}(u\vec{e}_\lambda)}{\mathrm{D}t} = \frac{\mathrm{D}u}{\mathrm{D}t}\vec{e}_\lambda + \frac{u^2}{r}(\tan\phi\,\vec{e}_\phi - \vec{e}_r), \tag{2.8}$$

$$\frac{\mathrm{D}(v\vec{e}_\phi)}{\mathrm{D}t} = \frac{\mathrm{D}v}{\mathrm{D}t}\vec{e}_\phi - \frac{uv}{r}\tan\phi\,\vec{e}_\lambda - \frac{v^2}{r}\vec{e}_r, \tag{2.9}$$

$$\frac{\mathrm{D}(w\vec{e}_r)}{\mathrm{D}t} = \frac{\mathrm{D}w}{\mathrm{D}t}\vec{e}_r + \frac{uw}{r}\vec{e}_\lambda + \frac{vw}{r}\vec{e}_\phi, \tag{2.10}$$

where u, v, w are the components of the velocity in the zonal, meridional (also called longitudinal, latitudinal) and radial directions respectively.

We can then summarize the equations of motions for a rotating atmosphere as follows:

$$\frac{\partial u}{\partial t} + \frac{u}{rcos(\phi)}\frac{\partial u}{\partial\lambda} + \frac{v}{r}\frac{\partial u}{\partial\phi} + w\frac{\partial u}{\partial r} - 2\Omega v\sin(\phi) + 2\Omega w\cos(\phi) + \frac{1}{\rho r\cos(\phi)}\frac{\partial p}{\partial\lambda} + \frac{uw}{r} - \frac{uv\tan(\phi)}{r} = 0, \tag{2.11a}$$

$$\frac{\partial v}{\partial t} + \frac{u}{rcos(\phi)}\frac{\partial v}{\partial \lambda} + \frac{v}{r}\frac{\partial v}{\partial \phi} + w\frac{\partial v}{\partial r} + 2\Omega u \sin(\phi) + \frac{1}{\rho r}\frac{\partial p}{\partial \phi} + \frac{vw}{r} + \frac{u^2 \tan(\phi)}{r} = 0, \tag{2.11b}$$

$$\frac{\partial w}{\partial t} + \frac{u}{rcos(\phi)}\frac{\partial w}{\partial \lambda} + \frac{v}{r}\frac{\partial w}{\partial \phi} + w\frac{\partial w}{\partial r} - 2\Omega u \cos(\phi) + \frac{1}{\rho}\frac{\partial p}{\partial r} + g - \frac{u^2 + v2}{r} = 0, \tag{2.11c}$$

$$\frac{\partial \rho}{\partial t} + \frac{u}{rcos(\phi)}\frac{\partial \rho}{\partial \lambda} + \frac{v}{r}\frac{\partial \rho}{\partial \phi} + w\frac{\partial \rho}{\partial r} + \rho\left(\frac{1}{r\cos(\phi)}\frac{\partial u}{\partial \lambda} + \frac{1}{r\cos(\phi)}\frac{\partial}{\partial \phi}\left(v\cos(\phi)\right) + \frac{1}{r^2}\frac{\partial}{\partial r}\left(r^2 w\right)\right) = 0, \tag{2.11d}$$

$$\frac{\partial \theta}{\partial t} + \frac{u}{rcos(\phi)}\frac{\partial \theta}{\partial \lambda} + \frac{v}{r}\frac{\partial \theta}{\partial \phi} + w\frac{\partial \theta}{\partial r} = \frac{\theta}{T}\frac{\dot{Q}}{c_p}, \tag{2.11e}$$

$$p = \rho R T, \tag{2.11f}$$

$$\theta = T\left(\frac{p_0}{p}\right)^{\frac{R}{c_p}}. \tag{2.11g}$$

The first three equations of (2.11) are the development in the rotating spherical frame of the Newton's second law eqn.(2.2). Then eqn.(2.11d) is the continuity equation (2.1) and eqn.(2.11e) the energy equation exactly as in eqn.(2.3). Finally, eqn.(2.11f) is just the ideal gas equation and eqn.(2.11g) links the thermodynamic variables we have used.

It is worth noting that in this set of equations we did not take into account viscous effects. Although this may well be a good approximation in the upper atmosphere, it is less obvious deeper. When the density becomes important we would expect to find some stress due to viscosity opposing any movement. Numerically, Mayne et al. [2014b] explains how it is dealt with in the UM, and we will go back to that point in the final chapters of this thesis.

The above set of equation is known for its difficulty to solve, and analytical solutions in 3 dimensions are very scarce. Obtaining insight into the nature of the solution of the Navier Stokes equations has actually been chosen as one of the Millenium problems by the Clay Mathematics Institute, with a reward of one million dollars. It is always possible to solve these equations numerically: with a properly coded solver, with appropriate initial and boundary conditions, numerical simulations can simulate flows evolving with time. This is basically what the UM does, by way of millions of lines of code being developed by approximately a hundred full time workers. The problem is that we lose the information of what is exactly going on in the physics and can only trust the numerical findings.

In that regard, it is essential to find some simplifications of the equations which can give an analytcial, physical insight in the fluid dynamics. Both for local and global scale studies, simplified set of equations have been derived that also conserve mass, energy and momentum, and allows for an easier approach of fluid dynamics. For planetary application, the shallow water equations as well as the beta-plane approximations are particularly insightful, and used extensively in chapter 7. We detail them in the next section.

2.1.4 Beta-plane approximation and shallow water equations

As said in Vallis [2006], the rotation of planets is of prime importance in the atmospheric dynamics but the sphericity not always so, especially for local scale applications. In that regard, the use of a local cartesian plane, called the tangent plane, often allows to simplify the equations while conserving the dominant physical mechanisms. If we also assume that we can neglect the components of $\vec{\Omega}$ not aligned with the local vertical, which is often a good approximation, then the momentum equations (2.11a)-(2.11c) greatly simplify to:

$$\frac{\mathrm{D}u}{\mathrm{D}t} - f_0 v = -\frac{1}{\rho}\frac{\partial p}{\partial x}, \tag{2.12a}$$

$$\frac{\mathrm{D}v}{\mathrm{D}t} + f_0 u = -\frac{1}{\rho}\frac{\partial p}{\partial y}, \tag{2.12b}$$

$$\frac{\mathrm{D}w}{\mathrm{D}t} = -\frac{1}{\rho}\frac{\partial p}{\partial y} - g, \tag{2.12c}$$

where $f_0 = 2\Omega \sin\phi_0$ with ϕ_0 the latitude where we considered the tangent plane. This set of equations forms the f-plane approximations.

For global scale application, the f-plane is not satisfactory: the change of the Coriolis force with latitude is a driver for many physical flows, and notably for the emergence of Rossby waves (see next section). This effect can be approximated by allowing the $f = 2\Omega\sin\phi$ term to change at the linear order. Namely, at the first order:

$$f \approx 2\Omega\sin\phi_0 + 2\Omega(\phi - \phi_0)\cos\phi_0 = f_0 + \beta y, \tag{2.13}$$

where we have defined $\beta = \partial f/\partial y = (2\Omega\cos\phi_0)/a$ where a is the radius of the planet. Naming $\vec{f} = (f_0 + \beta y)\vec{k}$ with $\vec{k}$ the vertical unit vector and $\vec{u} = (u, v, 0)$ the horizontal velocity vector, the last equation of (2.12) is unchanged but the first two can be written as:

$$\frac{\mathrm{D}\vec{u}}{\mathrm{D}t} + \vec{f} \wedge \vec{u} = -\frac{1}{\rho}\overrightarrow{\nabla_z} p, \tag{2.14}$$

where $\overrightarrow{\nabla_z}$ is the horizontal gradient. This equation, associated with the vertical momentum equation of the f-plane equations, form the beta-plane approximation. In chapter 7, we use an equatorial beta plane to detail analytically wave processes in hot Jupiters.

Additionally, some dynamical processes relevant for planetary atmospheres can be well described with a restriction to two dimensions: the vertical motions are often small compared to horizontal velocities. However, restraining to a plane with no vertical velocity or stratification can be too simplistic. In that regard, there has been extensive studies on the decomposition of a vertically stratified flow into consecutive layers of constant density. The simplest form is then to consider a single layer, with a depth varying with position, atop a rigid surface or at least a quiescent, denser layer (eventually allowing heat and mass transfers). When considering Earth's atmosphere, the bottom surface is set by the topography of the considered region of Earth which acts as a rigid surface, and the upper surface is allowed to move freely. This constitutes the shallow water system. In giant planets, there is no such rigid surface and we rather consider that the upper surface is the external radius of the planet, at constant r or z in cartesian coordinates, and the bottom surface moves freely with no drag with the lower layer. as was done for example in Showman and Polvani [2011]. This is equivalent to the shallow water approximation, as sketched on figure 2.1.

In this section we neglect the mass, heat and momentum exchanges between the upper and the lower layer but a more complete treatment can be found in Showman and Polvani [2011], with the addition of a term in the

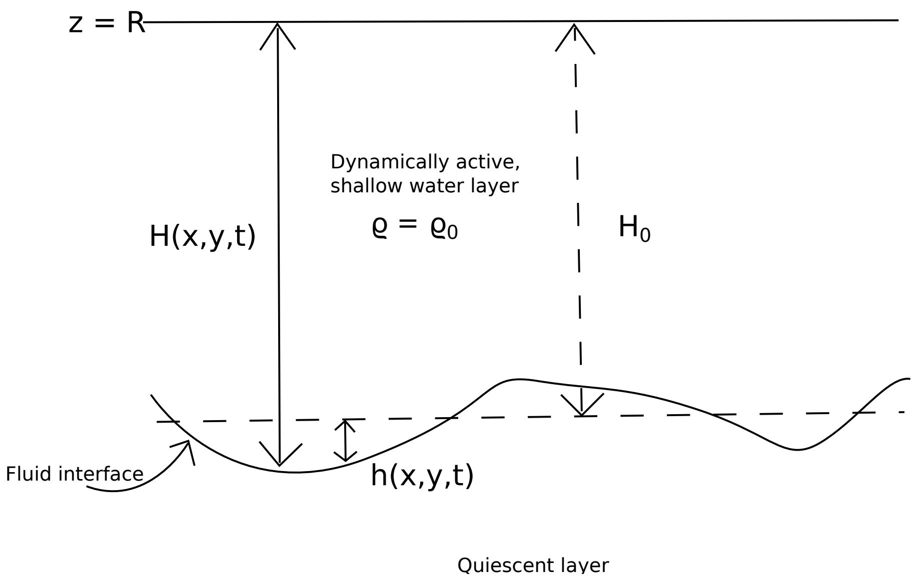

Figure 2.1: Schematic representation of a shallow water system. The dynamically active fluid has a constant density ρ_0, an initial mean height H_0 and a height that depends on position and time $H(x, y, t)$. We define $h(x, y, t) = H - H_0$ as shown.

momentum equation and a term in the energy equation. In that restriction, it can be shown (for example in Vallis [2006] pp.129-130) that the equations of motion write:

$$\frac{\mathrm{D}\vec{u}}{\mathrm{D}t} + \vec{f} \wedge \vec{u} = -g'\vec{\nabla}h, \tag{2.15a}$$

$$\frac{\mathrm{D}h}{\mathrm{D}t} + h\vec{\nabla} \cdot \vec{u} = 0, \tag{2.15b}$$

where the spatial derivative are only in the horizontal direction, $\vec{u}$ is the horizontal velocity, $\vec{f} = f\vec{k} = 2\Omega \sin\phi\vec{k}$ is the Coriolis parameter following the vertical unit vector and $g' = g(\rho_b - \rho_0)/\rho_0$ is the reduced gravity taking into account the density difference between the bottom layer ρ_b and the upper, active layer ρ_0. The first equation is simply the momentum equation in the shallow water system, and the second one is the mass conservation equation. These two equations form the shallow water approximation, which can be a very good approximation for atmospheric study as we will see in chapter 7. Notably, it allows for simpler derivation of certain wave processes, which we detail in the next section.

2.1.5 Importance of waves in the dynamics

Even with simplified equations as for the shallow water or beta plane approximations, the non linearity of the Navier Stokes equations prevents straightforward predictions. More generally, for physical flows, the existence of solutions is ensured by nature, but predicting the evolution of any flow from the sole knowledge of its initial conditions is today still out of reach. In that regard, the study of the linearised equations of motion allows for a better grasp of the physics involved in planetary fluid dynamics, through the study of propagating waves. We recall in the next section the most important wave mechanisms for planetary fluid dynamics, inspired by Holton [1992].

Acoustic waves

As for an oscillatory rope, a wave in a planetary atmosphere is essentially the propagation of a perturbation (a swing in the rope) with a restoring force transmitting the information (the stress of the rope). Setting aside electromagnetic waves, in an atmosphere only three forces can lead to such oscillatory phenomenon: pressure forces, gravity and the Coriolis force. The pressure forces simply lead to acoustic waves, as in other physical situations. They consist of small perturbations of the density, and are longitudinal waves: they propagate in the direction of the compression of the flow. Let's consider the cartesian coordinates in two dimensions and assume that the pressure gradient is dominating over rotation. If a small perturbation of pressure, δp, is triggered around an initial steady state at rest with constant pressure P_0, then the equation of motion in the first order, assuming the perturbation is small, can be written as:

$$\begin{aligned} \frac{\partial \delta u}{\partial t} &= -\frac{1}{\rho_0}\frac{\partial \delta p}{\partial x}, \\ \frac{\partial \delta v}{\partial t} &= -\frac{1}{\rho_0}\frac{\partial \delta p}{\partial y}, \\ \frac{\partial \delta \rho}{\partial t} + \rho_0\left(\frac{\partial \delta u}{\partial x}\right. &+ \left.\frac{\partial \delta v}{\partial y}\right) = 0, \end{aligned}$$

where δu, $\delta\rho$ and δv are the perturbation in the velocities and density in the two directions due to the perturbation in pressure, and ρ_0 the density of the initial state. There has been a long debate in the nineteenth century on the nature of the acoustic waves, whether they induced adiabatic or isothermal perturbations, which is today settled towards the adiabatic explanation. For adiabatic perturbations, we obtain a closure equation (assuming an ideal gas for simplicity). As $P\rho^{-\gamma}$ is constant, where γ is the adiabatic index: $\rho_0\delta P - \gamma P_0 \delta\rho = 0$. Therefore, taking the derivative of the last equation with time gives:

$$\frac{\rho_0}{\gamma P_0}\frac{\partial^2 \delta P}{\partial t^2}, -\Delta\delta P = 0 \tag{2.16}$$

which is the equation of a wave travelling at the speed $c_s = \sqrt{\gamma P_0/\rho_0} = \sqrt{\gamma R T_0}$, called the sound speed. In a lot of cases in planetary science, the motion of the fluid is slow compared to the sound speed. Then, the fluid can be considered as incompressible: a perturbation in the density will be instantaneously smoothed away by sound waves, that is considering that the sound speed is infinite. Even if the fluid has a characteristic velocity comparable with the sound speed, as will be seen for hot Jupiters in the last chapters, incompressibility can still apply as the global motion will mostly act as a Doppler shifting of the sound wave for an external observer (at the Equator, the Earth spins faster than the speed of sound in the air). Acoustic waves are of more importance when there is an obstacle in the flow or significant speed differences, eventually leading to shocks (see notably Fromang et al. [2016] for a discussion on acoustic shocks in hot Jupiter).

Gravity waves

As stated above, gravity can also act as a restoring force for propagating waves. They exist in planetary fluid dynamics in the form of shallow water gravity waves or internal gravity waves. The best examples of shallow water gravity waves are oceanic waves: the propagation of a perturbation between two fluids of different density. The derivation of their dispertion relation is similar to that for an acoustic wave and one can show that they are transverse wave: a parcel of fluid in the ocean moves vertically but the wave propagates horizontally. If H is the height of the unperturbed fluid, one can show that they propagate at a constant speed

$$c_{sw} = \sqrt{gH}, \tag{2.17}$$

called the shallow water wave speed (see discussion in Holton [1992] chapter 7.3.2). As stated by Holton, these waves can actually propagate at more than 200m.s^{-1} if the wavelength is big enough and the ocean deep enough. This is not a plausible solution for wind driven waves, but tsunamis, triggered by Earth quakes, can still be thought of as extreme shallow water gravity waves. In a stratified atmosphere, it has been shown in Wu et al. [2000] that in some cases one can decompose the propagating wave with the formalism of shallow water gravity waves and the use of different effective heights. In that regard, shallow water gravity waves do have their importance in the study of atmospheric dynamics.

The internal gravity waves on the other hand *only* exist in a stratified atmosphere, where density changes with height. First, let's assume a simple vertical displacement of a parcel in a hydrostatic atmosphere. The displacement δz will verify the equation

$$\frac{\mathrm{D}^2}{\mathrm{D}t^2}(\delta z) = -g - \frac{1}{\rho}\frac{\partial p}{\partial z} \tag{2.18}$$

where p and ρ are the pressure and density of the parcel. In the following, we assume that the parcel adapts its pressure instantaneously which, as stated by Holton [1992] or Vallis [2006], must be true if the parcel does not alter the overall pressure field. Then $\mathrm{d}P/\mathrm{d}z = -\rho_0 g$ with ρ_0 the density of the environment and therefore:

$$\frac{\mathrm{D}^2}{\mathrm{D}t^2}(\delta z) = g\frac{\rho_0 - \rho}{\rho} = g\frac{\theta(\delta z) - \theta_0(\delta z)}{\theta_0(\delta z)}, \tag{2.19}$$

where we have used the result from the ideal gas equation: the potential temperature is equal to $1/\rho$ times a function of P only. As pressure adjusts instantaneously, the functions of P cancel in the fraction. Assuming an adiabatic perturbation, from the definition of potential temperature it means that the potential temperature of the parcel is conserved through its displacement, whereas the environment can be stratified in potential temperature. Therefore: $\theta(\delta z) = \theta_0(0)$ and directly:

$$\frac{\mathrm{D}^2}{\mathrm{D}t^2}(\delta z) = -g\frac{\mathrm{d}\ln\theta_0}{\mathrm{d}z}\delta z\ . \tag{2.20}$$

Naming $N = \sqrt{g\mathrm{d}\ln\theta_0/\mathrm{d}z}$ the Brunt-Väisälä frequency, or buoyancy frequency, the equation of motion of the parcel simplifies to:

$$\frac{\mathrm{D}^2}{\mathrm{D}t^2}(\delta z) = -N^2\delta z\ . \tag{2.21}$$

This equation is simply solved: if N^2 is positive, then the parcel oscillates around its original position with a characteristic frequency being the buoyancy frequency. If N^2 is zero, the parcel is statically stable: it will simply continue rising with its initial speed or stay still if it has no velocity. If N^2 is negative, then the stratification of the atmosphere is unstable: any rising parcel will continue its motion with an exponential increase in time, with a characteristic growth timescale being $\sqrt{-N^2}$. This is the case for convection in Jupiter, as will be seen in section 2.2.2. Otherwise said, if the potential temperature increases with height, the atmosphere will be stable. If it decreases, convection can take place. It must be noted that this applies for dry air, and moist convection, carrying latent heat of water within the convective motion, does not verify the same equations.

This case of one dimensional buoyancy wave is very simplified: there is no reason a gravity wave could not propagate in the horizontal direction as well. In this case, applying the same method of linear perturbation on a cartesian plane (we choose not to consider one of the horizontal coordinates for simplicity), an equation for the vertical perturbation speed w is obtain (as in Holton [1992], we could add a global mean horizontal wind in a general case but restrict here to simpler considerations):

$$\left[\left(\frac{\partial^2}{\partial x^2}+\frac{\partial^2}{\partial z^2}\right)\frac{\partial}{\partial t^2}+N^2\frac{\partial^2}{\partial x^2}\right]w=0\ . \tag{2.22}$$

Seeking solution in the form $w = Wexp[i(kx + mz - \omega t)]$ we obtain the dispersion relation for gravity waves:

$$\omega^2=\frac{k^2N^2}{k^2+m^2}\ . \tag{2.23}$$

We see that the phase of these waves depends on height, and in that regard they are called internal waves. As in the 1D case, the value of N^2, hence the stratification of the atmosphere, determines whether gravity waves can become unstable. If $m = 0$, hence no dependency on the phase with height, we recover the frequency of a vertical, non propagating buoyancy wave but with a new horizontal dependency. We show the characteristic shape of a gravity wave on Figure 2.2 inspired from Holton [1992] figure 7.9

An interesting aspect of gravity waves is that, contrary to simple 1D buoyancy wave, they can propagate energy through great distances much larger than the oscillation of an individual parcel. Notably, they are thought to be involved in the maintenance of the Quasi biennal oscillation (Holton and Lindzen [1972]), a periodic change in the direction of the winds in the equatorial stratosphere with a period of about 2 years. Excited by convective overshoot at the bottom of the atmosphere, gravity waves could propagate through the stratosphere and deposit their energy to maintain this circulation. In gaseous planets, there are observations of oscillations on cycle of 4 years for Jupiter and 15 years for Saturn (see e.g., Orton et al. [1991] and Fouchet et al. [2008]), which are thought to be similar to the quasi biennal oscillations. Unfortunately, numerically speaking, it requires a very high resolution to account properly for upward propagating gravity waves, and we are only getting to the point where we might resolve such oscillations on global scale simulations of gaseous planets and brown dwarfs (the first simulation of this kind is reported in Showman et al. [2018]). For hot Jupiters, the understanding of the acceleration of superrotation (which we discuss in depth in the last chapters) rather involves internal Rossby and Kelvin waves. However, it has been proposed that there should be a correction in the GCM studies of hot Jupiters because of the inaccurate treatment of gravity wave and the energy they carry with low resolution [Watkins and Cho, 2010]. Finally, gravity waves can also be altered by the effect of rotation, and discussion on this point can be found in any planetary hydrodynamics text book.

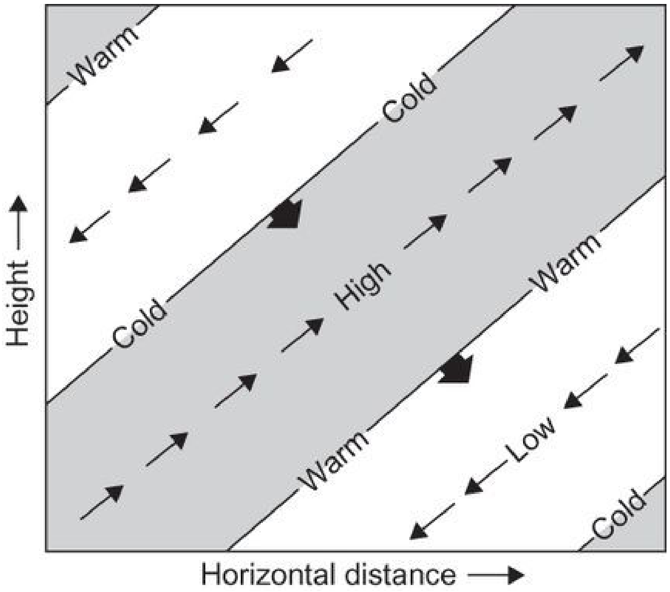

Figure 2.2: Ideal cross-section of an internal gravity wave, taken from Holton [1992], showing phases of pressure, temperature and velocity perturbation. Thins arrows indicate the perturbation velocity field, blunt solid arrows the phase velocity. Shading shows region of upward motion.

Kelvin waves

A particular type of gravity waves must be mentioned, as they are used extensively in chapter 7: Kelvin waves. They arise in the considerations of shallow water waves, with a rigid boundary (for example, a coastal line or in other words, a beach) and the presence of rotation, making the f-plane shallow water formalism particularly adapted to study these waves. If we assume that this boundary is located at $y = 0$, harmonic solutions are not allowed anymore and it is quite natural to look for waves with no meridional velocity perturbation, $\delta v = 0$ [Vallis, 2006]. In the shallow water formalism, the amplitude of Kelvin waves is calculated in chapter 3.7.3 of Vallis [2006] for $y > 0$:

$$\delta u = e^{-y/L_d} G(x - ct), \tag{2.24a}$$

$$\delta v = 0, \tag{2.24b}$$

$$\delta h = \sqrt{\frac{H_0}{g}} e^{-y/L_d} G(x - ct), \tag{2.24c}$$

where $L_d = \sqrt{gH_0}/f_0$ is the deformation radius, δh the height perturbation of the shallow water system and G the initial perturbation that propagates at characteristic speed c. Clearly, these waves decay away from the boundary on a typical lengthscale L_d and propagate to the East of the initial perturbation, as shown by the $x - ct$ term. There is a particular type of Kelvin waves which are equatorial Kelvin waves, and arise from the change of sign of the Coriolis parameter at the equator, acting like a solid boundary. They are easily highlighted through the use of the quasi geostrophic equations, as was done by Matsuno [1966] (we detail this paper and the decomposition into different waves in the first section of chapter 7). These waves are known to have a major effect on the spin-up and equilibration of superrotation for hot Jupiter (Showman and Polvani [2011] or Tsai et al. [2014]), and we will study their propagation and dissipation with care again in chapter 7.

Rossby waves

We finish our discussion on waves with those that are of most interest for large scale atmospheric processes: Rossby waves. We first need to introduce the vorticity ω:

$$\vec{\omega} \equiv \vec{\nabla} \wedge \vec{v} \ . \tag{2.25}$$

From the Navier Stokes equations in a non rotating frame, and considering that all the external body forces can be gathered into a term $\vec{F}$, an equation for $\vec{\omega_\rho} = \vec{\omega}/\rho$ is obtained (see e.g., Vallis [2006] chapter 4.2):

$$\frac{\mathrm{D}\vec{\omega_\rho}}{\mathrm{D}t} = (\vec{\omega_\rho} \cdot \vec{\nabla})\vec{v} + \frac{1}{\rho^3}(\vec{\nabla}\rho \wedge \vec{\nabla}p) + \frac{1}{\rho}\vec{\nabla} \wedge \vec{F} \ . \tag{2.26}$$

In the following, we assume that the curl of $\vec{F}$ is zero, which is verified in the rest of this thesis anyway. Then two situations might arise: for barotropic flows, where $\rho = \rho(P)$, the gradients of P are colinear with the gradients of ρ, hence the second term of the right hand side of equation (2.26) is zero and the equations simplifies to:

$$\frac{\mathrm{D}\vec{\omega_\rho}}{\mathrm{D}t} = (\vec{\omega_\rho} \cdot \vec{\nabla})\vec{v}. \tag{2.27}$$

If the flow is also incompressible, then $\vec{\omega_\rho}$ can be changed by $\vec{\omega}$, the usual vorticity. From there, a few conservation laws can be derived through the use of the Kelvin circulation theorem, which state the circulation around a closed curve remains constant with time, and using that the circulation is the line integral of the velocity, hence the surface integral of the vorticity. However, a general conservation law can be derived, both for barotropic and non barotropic (baroclinic) flows. In a fixed spherical frame of coordinates, the velocity can be written $\vec{v} = \vec{v}_r + \vec{\Omega} \wedge \vec{r}$ where $\vec{v}_r$ is the relative velocity in the rotating frame. Hence, similarly, one can define a relative vorticity $\vec{\omega_r}$ and an absolute vorticity $\vec{\omega_a}$ related by: $\vec{\omega}_a = 2\vec{\Omega} + \vec{\omega}_r$. Then, for adiabatic, inviscid flows, it can be shown in the general case that there is a conservation law for *potential* vorticity (we refer the reader to Vallis [2006] or Holton [1992] for further details):

$$\frac{\mathrm{D}}{\mathrm{D}t}(\vec{\omega}_{a,\rho} \cdot \vec{\nabla}\theta) = 0, \tag{2.28}$$

where $\vec{\omega}_{a,\rho} = \vec{\omega}_a/\rho$ and θ is the usual potential temperature. Therefore, the potential vorticity of a parcel of fluid in an unforced, inviscid atmosphere is always conserved, as was first realised by Rossby [Rossby, 1936]. This is the phenomenological origin of Rossby waves.

For a barotropic flow on a beta-plane, the potential vorticity is simply the absolute vorticity, and the conservation of absolute vorticity writes:

$$\frac{\mathrm{D}}{\mathrm{D}t}(\xi + \beta y) = 0, \tag{2.29}$$

where $\xi = \vec{\nabla} \wedge \vec{u}$ is the curl of the horizontal velocity. Therefore, suppose that there are some displacement around an initially stationary material line, the northward displacements will lead to the generation of negative relative vorticity whereas the southward displacements will generate positive vorticity perturbations. The existence of Rossby wave is therefore inherent to the variation of the Coriolis parameter with latitude: if β were 0, only the global vorticity would be conserved and northward or southward displacement would not alter vorticity locally.

The dispersion relation of Rossby waves is easily obtained by linearising equation (2.29) for an incompressible flow, as in Vallis [2006] chapter 5.7.1. Using the streamfunction ψ defined as:

$$u = \frac{\partial \psi}{\partial y} \quad \text{and} \quad v = -\frac{\partial \psi}{\partial x}, \tag{2.30}$$

and looking for plane wave solutions $\psi = \tilde{\psi}\exp(i(kx + ly - \omega t))$, non trivial solutions are obtained when

$$\omega = Uk - \frac{\beta k}{K^2}, \tag{2.31}$$

where U is the background horizontal velocity (if any) and $K^2 = k^2 + l^2$. It is also easily verified that the perturbation of u and v have perpendicular phases, hence when δu is maximum δv is 0 and conversely. This leads to the rotating aspect of the Rossby waves: as stated above, small displacement generate vorticity, hence rotating fluids. More generally, for an initial perturbation of finite scale, one can link the perturbation of the velocity to the gradient of pressure, and obtain the classical view of Rossby waves as rotating clockwisely around a maximum of pressure in the Northern hemisphere and inversely in the Southern hemisphere, because of the change of sign of the Coriolis parameter. Phenomemologically, it is only another representation of the conservation of potential vorticity. Notably, the potential vorticity conservation in the shallow water system on a beta-plane can be written as:

$$\frac{\mathrm{D}}{\mathrm{D}t}\left(\frac{\xi + \beta y}{h}\right) = 0 \ . \tag{2.32}$$

From this expression, we recover the connexion between the gradients of relative vorticity ξ and pressure or temperature, represented by the height h in the shallow water system.

On Earth and rapidly rotating planet, Rossby waves are mostly generated in the region where the gradient of the Coriolis parameter is the strongest: the mid latitudes. As shown in Vallis [2006] chapter 12 and particularly Figure 12.3, this has stringent effects on the global motion of the atmosphere: one can link the propagation of Rossby waves to a convergence of Eastward momentum, due to stirring of the lines of relative vorticity, and the dissipation of these same waves to a region of divergence of momentum. In other words, Rossby waves carry westward momentum that they deposit when they break. This is one of the causes of the Eastward jet in the mid latitudes of the Earth's stratosphere, and of the alternating Eastward and Westward mid latitudes jets on both Jupiter and Saturn. On hot Jupiter though, this phenomena is not thought to occur. Because of the slower rotation, Showman and Polvani [2011] have shown that the radius of deformation of Rossby waves is of the order of the size of the planet: Rossby wave do propagate, but they don't break at the equator or pole as on Earth. Their impact on global motions of the atmosphere is more subtle, and detailed in depth in Showman and Polvani [2011], inspired mainly form Matsuno [1966], Gill [1980] and Wu et al. [2001]. Based on this theoretical framework, the work of this thesis regarding atmospheric dynamics of hot Jupiters extends the understanding of propagation and decay of Rossby waves, in order to assess the phenomena leading to the equatorial superrotation of hot Jupiters. This is the point of the last chapters, and we have now detailed all the necessary fundamental background.

2.2 Structure of a giant planet

2.2.1 The gravitational moments

The other work in this thesis is the derivation of the structure of Jupiter. In order to constrain the interior of a giant planet, one needs external observable quantities that relate to the density structure of the planet. One of such quantities are the gravitational moments. Basically, a satellite orbiting the planet will have a trajectory that is different from the perfect ellipse predicted by Kepler's law if Jupiter was a point mass. The measurement of these differences are the proxy to evaluate the planet's gravitational field. Let's consider a spherical frame of coordinates with the planet at the center, r is the distance from the center of the planet, θ is the angle from the rotation axis of the planet defined as 0 in the equator (the latitude) and ϕ the longitude. The gravitational potential felt by a satellite exterior to the planet can be expressed as:

$$\phi(\vec{r}) = -\int_0^R \int_{-\pi/2}^{\pi/2} \int_0^{2\pi} \frac{G\rho(\vec{r})}{||\vec{r}-\vec{r'}||} r'^2 \sin(\theta') d\phi' d\theta' dr', \tag{2.33}$$

where $\vec{r}$ is the vector to the satellite, $\vec{r'}$ is the vector to a point (r', θ', ϕ') of the planet, $\rho(\vec{r'})$ is the density of the planet at (r', θ', ϕ'), G is the gravitationnal constant and R is the radius of the planet (which could actually be any celestial object). We can write:

$$\frac{1}{||\vec{r}-\vec{r'}||} = \frac{1}{r} \frac{1}{\left(1 + \left(\frac{r'}{r}\right)^2 - 2\frac{\vec{r}\cdot\vec{r'}}{r}\right)} = \frac{1}{r}\frac{1}{(1+x^2-2x\cos(\lambda))}, \tag{2.34}$$

where $x = r'/r$ and λ is the angle between $\vec{r}$ and $\vec{r'}$. Because $x < 1$ we recognise the generating function of the Legendre polynomials:

$$\frac{1}{||\vec{r}-\vec{r'}||} = \frac{1}{r}\sum_{k=0}^{\infty} \left(\frac{r'}{r}\right)^k P_k(\cos\lambda) \ . \tag{2.35}$$

With the use of the cosine rules in spherical geometry, we have:

$$\cos\lambda = \cos\theta\cos\theta' + \sin\theta\sin\theta'\cos(\phi-\phi') \ . \tag{2.36}$$

We can define the origin of the longitude to be at the point where the satellite is, so $\phi = 0$ and $\cos(\phi - \phi') = \cos\phi'$. Now there is a convenient formula for the Legendre polynomials, which is only valid if $0 < \theta, \theta' < \pi$. To be completely rigorous we would either need to change the latitude by the colatitude or to separate the hemispheres, but we will later use North-South symmetry so we can consider this inequality to be valid. The formula yields:

$$P_k(\cos\theta\cos\theta' + \sin\theta\sin\theta'\cos\phi') = P_k(\cos\theta)P_k(\cos\theta') + 2\sum_{m=1}^{\infty}(-1)^m P_k^m(\cos\theta)P_k^{-m}(\cos\theta')\sin m\phi' \ . \tag{2.37}$$

For now we will make the assumption that the planet has an axial symmetry, so ρ doesn't depend on the longitude. Then in the integral on ϕ', the terms in the sum of eqn.(2.37) will be zero. Only a 2π will emerge from the cosine terms, not depending on ϕ. We will also make the assumption that the planet is symmetric around the equator (North-South symmetry), so we can only integrate from 0 to $\pi/2$ and only the even Legendre polynomials will be non zero. By naming $\mu = \cos\theta$ and same for μ' we finally get from eqn.(2.33):

$$\phi(\vec{r}) = \sum_{k=0}^{\infty} -\frac{4\pi G}{r} P_{2k}(\mu) r^{-2k} \int_0^R \int_0^1 \rho(\vec{r'}) r'^{2k+2} P_{2k}(\mu') d\mu' dr' \ . \tag{2.38}$$

In the $k = 0$ term we simply recognize the integral over the planet of the elementary mass, so the total mass of the body M. The other terms can't simplify. In order to compare with the satellite measurements, we usually project on the Legendre polynomials and define $D_{2k} = -4\pi \int_0^R \int_0^1 \rho(\vec{r'}) r'^{2k+2} P_{2k}(\mu') d\mu' dr'$. The dimensionless form of the D_k yields the definition of the gravitational moments of the planet:

$$\boxed{J_{2k} = \frac{D_{2k}}{MR^{2k}} = -\frac{4\pi}{MR^{2k}} \int_0^R \int_0^1 \rho(\vec{r'}) r'^{2k+2} P_{2k}(\mu') d\mu' dr'} \ . \tag{2.39}$$

All in all, the planet's gravitational field writes:

$$\phi(\vec{r}) = -\frac{GM}{r} \left(1 - \sum_{k=1}^{\infty} J_{2k} \left(\frac{R}{r} \right)^{2k} P_{2k}(\mu) \right) \ . \tag{2.40}$$

A satellite orbiting e.g. Jupiter will be able to measure these gravitational moments, and we know their analytical expression. So we just need to be able to calculate them from interior models of Jupiter and compare them with observations. Unfortunately, this calculation is far from easy, and is the point of chapter 3. We just states here that it needs to assume hydrostatic balance, which directly relates the pressure p, the density ρ and the potential inside the planet U (which is the sum of the gravitational potential and the rotationnal potential and possible tidal potentials when the moons are taken into account):

$$\nabla p = \rho \nabla U \tag{2.41}$$

This is the direct equivalent of eqn.(2.5), but eqn.(2.5) is a simplification of the atmosphere behaviour whereas eqn.(2.41) is a very good representation of the stratification inside the planets. We discuss this is section 2.2.3.

2.2.2 Why are giant planets convective?

The knowledge of the gravitational moments of a planet is not sufficient to constrain its interior. We are indeed trying to solve an inverse degenerate problem, with multiple interior structures that could reproduce the same value of the gravitational moments. Additional information must be derived from other information regarding the planet. Before the 1960's giant planets were thought to be solid, cold conductive bodies. However, with the observations of Low [1965], it was understood that giant planets possess an internal flux of heat. On Jupiter, it accounts for 1.6 times the flux the planet receives from the sun. This flux alone would give to the planet an effective temperature of ∼ 120K. We show in this section why this internal flux imposes the need for Jupiter to be a convective hot fluid. This section gathers ideas and equations from Hubbard [1968], Stevenson and Salpeter [1977a], Kippenhahn and Weigert [1990], Hansen and Kawaler [1994] and Guillot et al. [1994] at the least. Hydrostatic balance is assumed, and justified in the following section.

In order for Jupiter to radiate its internal flux, as observed by Low [1965], there must be a physical process of heat transport inside the whole planet. Assuming that no nuclear reaction take place in Jupiter (which will be validated by the following calculation), Jupiter's luminosity can only come from its energy of formation: the planet cools and contracts to balance the radiative losses of energy at the photosphere (naive estimates can show that Jupiter would need to contract by $\sim 2mm$ per year if the whole internal flux comes from gravitational contraction). The transport of heat inside Jupiter can be ensured by three physical mechanisms: radiation, conduction and convection (as will be shown later, convection in Jupiter can be assumed as an adiabatic process). To determine which process is dominating, the stellar and giant planets community often introduces the radiative, conductive and adiabatic logarithmic gradients:

$$\nabla_{\rm rad} = \left(\frac{{\rm dln}T}{{\rm dln}P}\right)_{\rm rad}, \nabla_{\rm cond} = \left(\frac{{\rm dln}T}{{\rm dln}P}\right)_{\rm cond}, \nabla_{\rm ad} = \left(\frac{{\rm dln}T}{{\rm dln}P}\right)_{\rm ad} . \tag{2.42}$$

These gradients represent the temperature-pressure structure that the planet would have if only radiation, diffusion or convection transported heat. For example, if $\nabla_{\rm rad} \ll \nabla_{\rm cond} \sim \nabla_{\rm ad}$, an increase in the pressure would lead to a much larger increase in the temperature if heat is transported by diffusion or convection rather than radiation. Therefore, radiation is much more efficient at transporting heat, and the temperature stratificiation of the planet will be very close to the radiative temperature profile, slightly altered by conductive and convective processes. In this section, we thus want to determine the relation orders between these three gradients (or equivalently, the usual temperature gradients set by each process), to determine which one is the smallest hence what process is controlling the temperature stratification of the planet.

Radiative flux

Let us first consider the case of radiation, carried by photons. We introduce the optical depth $\tau_\nu(r)$, which is a measure of the absorbtion at a given depth and frequency ν. Namely, $\tau_\nu = -\int_0^r \kappa_\nu(r)\rho {\rm d}r$ where κ_ν is the absorption of the medium at frequency ν. If some light at frequency ν penetrated perpendicularly and was only absorbed through a medium of size L, hence no emission occured at this frequency, we can link the incoming and outcoming intensity of the light: $I_{\rm out} = I_{\rm in} e^{-\tau_\nu(L)}$. It can be shown, see notably Hansen and Kawaler [1994] chapter 4.1, that in the limit of high optical depth ($\tau_\nu \gg 1$ hence far from the surface of the planet or the star) and assuming local thermodynamic equilibrium, the flux transported by radiation at frequency ν and optical depth τ_ν is:

$$\mathcal{F}_\nu = \frac{4\pi}{3}\frac{\partial B_\nu(T(\tau_\nu))}{\partial \tau_\nu}, \tag{2.43}$$

where B_ν is the planck Function:

$$B_\nu(T) = \frac{2h\nu^3}{c^2}\frac{1}{e^{h\nu/k_{\rm B}T}-1} \ {\rm erg.cm}^{-2}, \tag{2.44}$$

with h the Planck's constant, c the speed of light and $k_{\rm B}$ the Boltzmann constant. Using the definition of τ_ν: ${\rm d}\tau_\nu = -\kappa_\nu \rho {\rm d}r$. Expanding the derivative of B_ν with respect to r as a derivative with respect to T, through ${\rm d}T/{\rm d}r$ and finally introducing the Rosseland mean opacity κ:

$$\frac{1}{\kappa} = \left[\int_0^\infty \frac{1}{\kappa_\nu}\frac{\partial B_\nu}{\partial T}{\rm d}\nu\right]\left[\int_0^\infty \frac{\partial B_\nu}{\partial T}{\rm d}\nu\right]^{-1}, \tag{2.45}$$

we obtain for the total flux, integrated over frequencies:

$$\mathcal{F}(r) = -\frac{4\pi}{3}\frac{1}{\kappa\rho}\frac{\mathrm{d}T}{\mathrm{d}r}\int_0^\infty \frac{\partial B_\nu(T)}{\partial T}\mathrm{d}\nu \ . \tag{2.46}$$

Finally, the integral over the frequency of the Planck function is known, and the integral in the above expression is simply equal to acT^3/π, where $a = 8\pi^5 k_\mathrm{B}^4/(15c^3h^3)$ is the radiation constant. We then obtain the radiative flux:

$$\mathcal{F}_\mathrm{rad}(r) = -\frac{4ac}{3}\frac{1}{\kappa\rho}T^3\frac{\mathrm{d}T}{\mathrm{d}r} \ . \tag{2.47}$$

The really interesting aspect of this expression is the dependence on $\mathrm{d}T/\mathrm{d}r$: it is reminiscent of the Fourier's law of conduction.

Convective flux

More precisely, the flux of heat carried by conduction is:

$$\mathcal{F}_\mathrm{cond}(r) = -\lambda\frac{\mathrm{d}T}{\mathrm{d}r}, \tag{2.48}$$

where λ is the thermal conductivity. Redefining:

$$\kappa_\mathrm{cond} = \frac{4acT^3}{3\lambda\rho}, \tag{2.49}$$

the conductive flux of heat can be written as:

$$\mathcal{F}_\mathrm{cond}(r) = -\frac{4ac}{3}\frac{1}{\kappa_\mathrm{cond}\rho}T^3\frac{\mathrm{d}T}{\mathrm{d}r} \ . \tag{2.50}$$

Total diffusive flux

Therefore, conduction and radiation can be coupled into a "diffusive flux", that takes into account diffusion by radiation and thermal diffusion:

$$\mathcal{F}_\mathrm{diff}(r) = -\frac{4ac}{3}\frac{1}{\kappa_\mathrm{tot}\rho}T^3\frac{\mathrm{d}T}{\mathrm{d}r}, \tag{2.51}$$

with

$$\frac{1}{\kappa_\mathrm{tot}} = \frac{1}{\kappa_\mathrm{rad}} + \frac{1}{\kappa_\mathrm{cond}} \ . \tag{2.52}$$

This is particularly useful as it allows to determine directly which phenomenon is mostly carrying the flux when convection is ignored. If the radiative opacity is much larger than the conductive opacity, $\kappa_\mathrm{tot} \approx \kappa_\mathrm{cond}$ then the majority of the flux is carried by conduction. Said differently, the thermal gradient that would be imposed by radiation is too high to be sustainable: conduction is more efficient, and will reduce the thermal gradient.

It must be noted that, if conduction is the leading mechanism, then one can estimate the central temperature T_c of the planet. As the flux is constant (no heat production):

$$T_c \approx T_0 + \mathcal{F}_{\text{ext}} \frac{R_J}{\lambda}, \tag{2.53}$$

where $\mathcal{F}_{\text{ext}}$ is the external flux as observed by Low [1965]. Following Hubbard [1968], the conductivity of metallic hydrogen, that composes most of the interior of the planet (see below), is at the first order $\lambda \approx 10^3 \text{W.m}^{-1}.\text{K}^{-1}$. This yield a central temperature of $\sim 10^5$K. The central pressure of a self gravitating, hydrostatically balanced (see next section) celestial body is well approximated by $P_c \approx 0.1\mathcal{G}M^2/R^4$ where $\mathcal{G}$ is the gravitational constant, M the mass of the object and R its radius. For Jupiter, this gives $P_c \approx 10^{12}Pa = 10Mbar$. With any equation of state for hydrogen, at these temperatures and pressure hydrogen is in a fluid form, and not a solid form. This has two consequences: the thermal conductivity would be lower, implying an even hotter central temperature, and convection cannot be ignored.

Convective flux

We are now left with the calculation of the convective gradient, which is more subtle. We can picture it this way: contrary to the gravity wave case, a parcel that is displaced adiabatically will be unstable and continue rising (or sinking) on large distances. Assuming it rises on a distance l and with a speed w, the convective flux simply is the amount of energy it deposits at dissolution:

$$\mathcal{F}_{\text{conv}} = \rho w c_{\text{P}} \Delta T, \tag{2.54}$$

where c_{P} is the specific heat at constant pressure and ΔT the temperature difference between the parcel and its surroundings when mixing. We must then calculate both w and ΔT.

Let's consider that the medium has a stratification in temperature $T(P)$ or $T(r)$, probably due to diffusive processes. We will consider that a parcel which is moved adiabatically adjusts instantaneously to the surrounding pressure, which corresponds to saying that the hydrodynamic timescale is much less than the diffusion timescale (which is the case in Jupiter). Therefore, at the altitude $r + \mathrm{d}r$, where r is the original position of the parcel and $\mathrm{d}r$ its displacement, the temperature of the parcel will be $T'(r+\mathrm{d}r) = T(r) + (\mathrm{d}T/\mathrm{d}r)_{\text{ad}}\mathrm{d}r$ where the "ad" subscript means adiabatic, whereas the surrounding temperature is $T(r + \mathrm{d}r) = T(r) + (\mathrm{d}T/\mathrm{d}r)\mathrm{d}r$. As the pressure of the parcel and its surrounding are equal, the difference in density of the parcel only depends on the difference of temperature: if the temperature of the parcel is higher, the density will be lower and the parcel will experience a net buoyancy force directed upwards. Then, if the parcel is displaced upwards ($\mathrm{d}r < 0$), the parcel will keep rising if $T' > T$ or:

$$\left(\frac{\mathrm{d}T}{\mathrm{d}r}\right)_{\text{ad}} \mathrm{d}r > \left(\frac{\mathrm{d}T}{\mathrm{d}r}\right) \mathrm{d}r,$$

hence

$$\left(\frac{\mathrm{d}T}{\mathrm{d}r}\right)_{\text{ad}} < \frac{\mathrm{d}T}{\mathrm{d}r} \ . \tag{2.55}$$

With some simple transformations, it is easily shown that this is equivalent to $\nabla > \nabla_{\text{ad}}$ where $\nabla = \mathrm{dln}T/\mathrm{dln}P$. From there, Hansen and Kawaler [1994] in chapter 5.1.2 show that the evolution of $\Delta T = T' - T$ can be written as follows:

$$\frac{\mathrm{D}\Delta T}{\mathrm{D}t} = \left(\left(\frac{\mathrm{d}T}{\mathrm{d}r} \right)_{ad} - \frac{\mathrm{d}T}{\mathrm{d}r} \right) w - \frac{\nu_T}{l^2} \Delta T, \tag{2.56}$$

where ν_T is the thermal diffusivity. This is easily understood phenomenologically: if the surrounding gradient was the adiabatic gradient, the temperature difference would not change when the parcel rises, and the parcel would just keep rising with its initial velocity. The first term on the equation simply expresses the rate of change of the temperature difference because of the surrounding temperature structure of the planet. The second term represent the diffusive leakage: on a distance l, the thermal diffusivity smoothes away the temperature difference with a characteristic time ν_T / l^2.

In a similar manner, the evolution of the velocity of the parcel w is driven by the buoyancy forces:

$$\frac{\mathrm{D}w}{\mathrm{d}t} = \frac{\rho - \rho'}{\rho} g \ . \tag{2.57}$$

Introducing the thermal expansion $\mathcal{Q} = -\left(\mathrm{dln}\rho / \mathrm{dln}T\right)_P$ it is easily rewritten as:

$$\frac{\mathrm{D}w}{\mathrm{D}t} = \frac{\mathcal{Q} g}{T} \Delta T \ . \tag{2.58}$$

Finally, a combination of the Equations (2.56) and (2.58) would yield a second order differential equation, hence ΔT and $w \propto e^{\sigma t}$ where σ is defined by the relation:

$$\sigma^2 + \sigma \frac{\nu_T}{l^2} + N^2 = 0, \tag{2.59}$$

where N^2 is, as in the case of gravity waves, the Brunt Väisälä frequency defined here as:

$$N^2 = -\frac{\mathcal{Q} g}{T} \left(\left(\frac{\mathrm{d}T}{\mathrm{d}r} \right)_{ad} - \frac{\mathrm{d}T}{\mathrm{d}r} \right) \ . \tag{2.60}$$

In the case of efficient convection, when the diffusive losses are small, it is quite clear that convection happens when $N^2 < 0$, and we again obtain that the temperature gradient in the atmosphere must be larger than the adiabatic temperature gradient for convection to occur. Additionaly, the assumptions of the mixing length imposes that the parcel dissolves after travellind a distance l. If σ is real and positive, this basically states that dissolution is limiting the exponential increase of w and ΔT, which must then occur on a time $1/\sigma$. Now we can therefore evaluate an order of magnitude for w:

$$w \approx \sigma l, \tag{2.61}$$

which is the characteristic distance over the characteristic time.

For ΔT, we recall that the time evolution of w and ΔT is in the Lagrangian framework, so $\mathrm{D}T/\mathrm{D}t = \sigma T$. Hence, using equation (2.56) and with a bit of straightforward transformations:

$$\Delta T = \frac{\sigma^2 l T}{\mathcal{Q} g} \ . \tag{2.62}$$

We can now compute the convective flux. In the limit of no diffusion, $\sigma = \sqrt{-N^2}$ and using equations (2.54), (2.60), (2.61) and (2.62):

$$\mathcal{F}_{\mathrm{conv}} = \frac{\rho c_{\mathrm{P}} l^2 T g^{1/2} \mathcal{Q}^{1/2} \left(\nabla - \nabla_{\mathrm{ad}}\right)^{3/2}}{H_{\mathrm{P}}^{3/2}}, \tag{2.63}$$

where H_{P} is the pressure scale height, which allows to change the gradient to the logarithmic gradient: $\mathrm{d}T/\mathrm{d}r = -(T/H_{\mathrm{P}})\mathrm{dln}T/\mathrm{dln}P = -(T/H_{\mathrm{P}})\nabla$. Therefore, for convection to transport a heat flux $\mathcal{F}$, the logarithmic thermal gradient in the planet ∇ must be greater than the adiabatic gradient ∇_{ad}. The problem of the theory is obvious in the definition of $\mathcal{F}_{\mathrm{conv}}$: what is the value of l? Unfortunately, there is no theoretical, absolute answer to this question, and this value must be chosen with other a priori knowledge (usually, it is a fraction of the pressure scale height as this is the scale on which thermodynamic quantities are properly estimated as constant). In the case of low diffusion, as noted by Hansen and Kawaler [1994], this problem is less stringent as a whole range of l will still imply a small departure from the adiabatic gradient.

Heat transport in Jupiter

With this theoretical framework, we can now answer the question: what is the leading heat transport phenomenon in Jupiter? We have obtained three heat fluxes, all expressed as a function of the thermal gradient in the planet. Our question is therefore equivalent to: which of the heat transport process yields the minimal temperature gradient for carrying the internal flux of Jupiter? This question is highly non trivial, and we answer it with theoretical studies starting in the 1960's.

In molecular Hydrogen, hence in the outermost part of the planet, Stevenson and Salpeter [1977a] have shown that the Rosseland opacity is much smaller than the conductive opacity. In that regard, heat transport by diffusion can be neglected, and the competition is between radiation and convection. In the atmosphere, where the optical depth is low, radiation is the leading heat transport mechanism but the equations we have derived in this section are not applicable. The issue of radiative transfer in atmospheres is a complicated one, as is noted in the exoplanet community (see notably Amundsen et al. [2014] and Amundsen et al. [2016] in the case of the Unified Model), and we will not enter into the details. Our main interest here is to understand the temperature-pressure structure from the bottom of the atmosphere, where $\tau \gtrsim 1$ to the centre of the planet.

The extensive discussion in the thesis of Stevenson [1976] shows that there can only be a radiative window in Jupiter for temperatures between 400 and 700K, and Stevenson and Salpeter [1977a] conclude that a small amount of heavy elements, increasing the radiative opacity, would probably erase the possibility of a radiative window. This possibility was made contemporary again in Guillot et al. [1994]: the new calculations of opacities at that time allowed the refinement of the radiative gradient and comparison to the adiabatic gradient. Rearrangements of Equation 2.47 performed in Hansen and Kawaler [1994] show that:

$$\nabla_{\mathrm{rad}} = -\frac{L(r)}{4\pi r^2}\frac{3\rho P}{4\pi a c T^4}\kappa_{\mathrm{rad}}\left(\frac{\mathrm{d}P}{\mathrm{d}r}\right)^{-1}, \tag{2.64}$$

whereas the adiabatic gradient is simply $\nabla_{\mathrm{ad}} = (\mathrm{dln}T/\mathrm{dln}P)_{S=cte}$, with S the specific entropy. Assuming that the luminosity is constant throughout the molecular hydrogen region, so the outgoing flux is the observed internal flux, one can estimate both these gradients through the use of an equation of state. It was performed with the SCvH equation of state Saumon et al. [1995] in Guillot et al. [1994], and they observed indeed that some regions of the planet exhibited $\nabla_{\mathrm{rad}} < \nabla_{\mathrm{ad}}$: a part of the outermost layers of Jupiter could be radiative (above $\sim 97\%$ of the radius). However, further improvements on the opacities and especially on the shape of the absorption rays of heavy elements (mostly due to observations of browns dwarfs, see Burrows et al. [2000] and Guillot et al. [2004]) have confirmed the original proposition of Stevenson and Salpeter [1977a]: there cannot be a radiative window in the external part of Jupiter if the abundance of **heavy elements** is at least solar. As it happens, the abundance of heavy elements is largely super solar in the outer layers of the planet: the molecular region of Jupiter is convective.

Deeper in the planet, at higher temperature, the increasing abundance of free electrons increases the opacity notably of H_2^- and H^-, and in any case radiative gradients become greater than convection gradients: convection is the leading mechanism. If one follows the adiabatic gradient from the observed value of $165K$ and 1 bar in the deep atmosphere by Galileo, the density at 1Mbar is of the order of $0.8\mathrm{g.cm}^{-3}$. This leads to a mean interatomic distance which is:

$$a_d = \left(\frac{3m_{\mathrm{H}}}{4\pi}\right)^{1/3} \rho^{-1/3} \sim a_0, \tag{2.65}$$

with m_{H} the mass of an hydrogen atom and a_0 is the Bohr radius. Therefore, the mean interatomic distance if of the order of the size of an atom: the orbitals of the electrons of hydrogen overlap. As was first intuited by Wigner and Huntington [1935], and confirmed since by numerous theories and claimed by some experiments (Saumon et al. [1995] for example on the theoretical side and Knudson et al. [2015], Celliers et al. [2018] for the experiments), hydrogen becomes similar to a metal in these conditions (justifying its classification in the alkali metals column of the Mendeleev table). This pressure and density occur at a depth of about 10000km: the inner 90% of Jupiter are composed of metallic, monoatomic hydrogen, and not dihydrogen.

Within metallic hydrogen, the radiative opacity becomes extremely large as the absorbtion from the free electrons is very effective. On the other hand, the thermal conductivity strongly increase, hence the conductive opacity dominates the total opacity. According to Stevenson and Salpeter [1977a], this conductivity can be approximated by:

$$\lambda = 0.3\rho^{1/3}\mathrm{cm}^2.\mathrm{s}^{-1}. \tag{2.66}$$

Nonetheless, the work of Hubbard [1968] and Stevenson and Salpeter [1977a] show that the adiabatic gradient is much less than the diffusive gradient: the internal heat flux observed at the surface is transported throughout the planet by convection. Discussions on the temperature of melting of hydrogen also show that the thermal structure obtained are compatible with a fluid state for hydrogen, necessary to ensure convection.

Therefore, estimates of the heat transport mechanisms, coupled with the microphysics of molecular and metallic hydrogen, have led us to the picture of a mostly convective planet. Additionally, within the limits of the mixing length theory which we have used to derive the convective flux, any reasonable estimate shows that convection is very efficient at transporting Jupiter's internal heat flux. In other words, the actual temperature gradient is very close to the adiabatic temperature gradient, and the thermal losses are only a negligible correction to the adiabatic gradient. In the absence of heat generation within convective zones (no nuclear processes nore latent heat generation), the convection can be considered as both adiabatic and reversible. Hence, in a very good approximation, the convective zones in Jupiter are isentropic (this is also true in the convective regions of star, see notably the extensive discussion on departure from usual mixing length theory and adiabatic gradients in Ireland and Browning [2018]).

Still, Jupiter could be composed of a fluid, outer convective molecular hydrogen and an inner, solid diffusive core. The core would be close to isothermal, transporting almost no flux and the luminosity of Jupiter would only arise from the convective transport through the outermost region. The condition for this to happen is that equations of state allow for a solid inner core (a solid hydrogen core is today excluded but minor constituents can gather into a smaller core in the very centre of the planet), and it would have strong implication on the cooling of the planet. Indeed, as less mass is available for carrying the convective flux in a case of a partially convective planet than in the case of a completely convective planet, the loss of internal energy (neglecting contraction) from luminosity can be written as:

$$L = -\frac{\mathrm{d}U}{\mathrm{d}t} \approx M_{\mathrm{av}} C_v \frac{\mathrm{d}\bar{T}}{\mathrm{d}t}, \tag{2.67}$$

where L is the luminosity, U the internal energy, M_{av} the available mass for convection, $\bar{T}$ an estimate for the mean temperature of the planet and C_v the specific heat at constant volume, supposed constant through the planet. This yields a characteristic cooling time scale (at a given luminosity):

$$\tau_{\mathrm{cool}} \approx \frac{1}{L} M_{\mathrm{av}} C_v \bar{T} \ . \tag{2.68}$$

Clearly, a smaller available mass yields a shorter timescale for the cooling of temperature, assuming that the luminosity is constant between the two models (at any rate, the present luminosity is the observed luminosity).

This picture of a fully convective Jupiter with eventually a small core persisted through a good part of the 20th century, from the papers of Peebles [1964] and Hubbard [1968] to the models of Chabrier et al. [1992], where multi layers models of the planet were introduced for the first time (although the idea was inherent to the two papers of Stevenson and Salpeter in 1977). In chapter 4 however, we are showing that the improvements on observations and theory have changed our understanding of the planet, towards a more complicated structure: some regions must exhibit a strong departure from an isentropic structure. The convective zones of the planet remain isentropic, as we have seen, but the value of the specific entropy changes within the planet. Hydrostatic balance, on the other hand, remains a very good approximation in the whole planet, as we show in the next section.

2.2.3 Hydrostatic balance

Hydrostatic balance, or equilibrium, is used almost ubiquitously in geophysics and astrophysics. The underlying idea is that, in a state of rest, there is a differential force between two parcels of material at different height because of the change in the gravity field. This force must be compensated by another one to prevent the collapse of the fluid: the pressure forces. The downward increasing gravity creates an increase in the pressure, hence an outward force from the high pressure fluid to the low pressure fluid. Let's take two simple examples. First, the Earth's atmosphere. Because of its small mass compared to the planet ($\lesssim 10^{-6}\times$ the mass of the Earth), we can neglect its self-gravity and suppose that the gravity field is generated by the terrestrial materials only. Hence, studying a small region of Earth so that Cartesian coordinates are a good approximation, the gravitational acceleration (neglecting rotation) writes:

$$\vec{g}(x,y,z) = -\frac{\mathcal{G}M_\odot}{(R_\odot + z)^2}\vec{k}, \tag{2.69}$$

where (x,y,z) are the local cartesian coordinates, $\mathcal{G}$ the gravitational constant, $M_\odot$ and $R_\odot$ the mass and radius of Earth respectively and $\vec{k}$ is the vertical unit vector directed away from the Earth. As the size of the atmosphere is $\sim$ 100km, one 60th of the Earth radius, $|\vec{g}|$ can be considered as constant as a good approximation. Taking a slice of the atmosphere (Figure 2.3) of section S, vertical extent dz and density ρ, the gravitational force $\vec{F_g}$ exerted on the slice is $\vec{F_g} = m\vec{g} = -\rho S \mathrm{d}z g\vec{k}$ and the differential pressure force is $\vec{F_p} = (Sp(z) - Sp(z+dz))\vec{k}$. In order for the slice of atmosphere to be stable, the forces must cancel and we obtain the hydrostatic balance:

$$\frac{\mathrm{d}p}{\mathrm{d}z} = -\rho g\ . \tag{2.70}$$

Now, if we assume that the variations of temperature are small compared to the variation of pressure (which is a good approximation close to the surface), with the ideal gas equation $P = \rho RT$ we obtain:

$$P = P_0 e^{-gz/RT}, \tag{2.71}$$

where P_0 is the surface pressure. In the limit of hydrostatic balance, the pressure stratification of the atmosphere exhibits a characteristic height of variation $H \sim RT/g \approx 8$km. This explains the change in pressure with altitude and the need to adapt when climbing summits, and is a very good approximation in the first layers of the Earth's atmosphere.

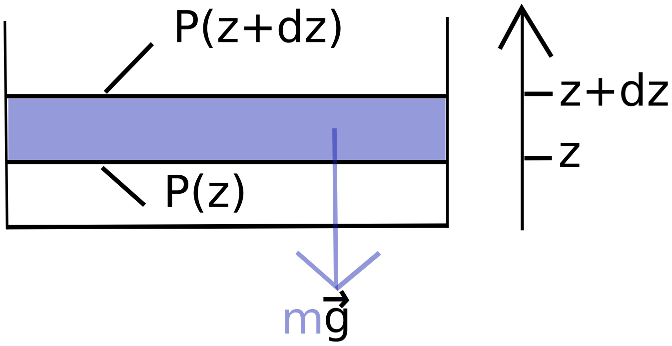

Figure 2.3: Hydrostatic balance: the pressure gradient must compensate the gravity exerted on the selected slice of the atmosphere.

Hydrostatic balance also applies for rocky bodies such as asteroids or terrestrial planet. The gravitational force depending only on the radial coordinate, gravity tends to form only spherical structures, with properties such as density depending only on the radial distance from the centre. As can be seen in the solar system, there exists a plethora of non spherical small bodies, but only spherical planets (neglecting the deformation due to rotation). This shows that when dust particles conglomerate to form pebbles and eventually asteroids, planetesimals and planets, there is a minimum size (or mass?) when gravity becomes the dominant force compared to the structural cohesion of the objects.

Such objects, exhibiting an almost spherical shape, are then considered to be in hydrostatic balance. The International Astronomical Union's definition of a planet actually requires that it is a celestial body in hydrostatic equilibrium. In the solar system, the smallest body confirmed to be in hydrostatic equilibrium is the dwarf planet Ceres, with a radius of 945 km, whereas the largest body known to not be in hydrostatic equilibrium is the icy moon of Saturn Iapetus, at 1,470 km, showing that different composition of asteroids lead to different internal stresses that oppose gravitational forces.

Finally, hydrostatic balance also applies in the interior of giant planets. To be stricto censu applicable, there would need to be no wind acceleration whatsoever in giant planets. This is impossible, as we have shown above that Jupiter is dominated by convective motion, and the outgoing or ingoing convective plumes must turn over eventually. However, if the planet is in a globally equilibrated state (a planet is never truly in equilibrium as long as it radiates more flux than it receives from the sun), then the internal motions must average out overall. In that case, although locally this assumption can break, we have globally $\mathrm{d}P/\mathrm{d}r = -g\rho$. This does not prevent the emergence of winds, but it supposes that this balance is instantaneously recovered if there is the slightest change: the pressure structure smoothes away any deviation. Said differently, any local perturbation will always be at the pressure of its surrounding, and other thermodynamic quantities (density and temperature mainly) will adjust more slowly. Globally, it means that the speed of sound is much larger than any other characteristic velocity in the interior of giant planets.

Hydrostatic balance in giant planets can be understood further. Let's assume that the gravity acceleration is not compensated by the pressure gradients. Necessarily, the winds are the only other phenomena that can prevent the star from collapsing (see the Navier-Stokes equation for the vertical momentum). With order of magnitude estimates, one would obtain that the global vertical motion must be, in absolute value, of the order of a few km.s^{-1} to ensure equilibrium. The question is: what is the physical mechanism sustaining such winds? Any reasonable viscous or energetic timescale study would lead to the dissipations of such winds much quicker than a billion years (see e.g., the timescale approach in the first chapters of Kippenhahn and Weigert [1990]). In Jupiter, we have shown that if the heat flux is transported by diffusion, the central temperature is less than 10^5K, if it is transported by convection then the wind speed is of the order of a few cm.s^{-1} leading to a central temperature of the order of 10^4K (similar estimate is obtained by a naive application of the Virial equation, assuming that the kinetic energy is only due to thermal motions). If the winds must reach km.s^{-1} values and heat transport is ensured by convection, the central temperature would be further decreased. At any rate, such a low temperature gradient in the planet cannot accelerate these winds. Finally, if there were global breaking of hydrostasy, it cannot be spherically symmetric or we would see global oscillations of Jupiter to conserve the mass. One would therefore need to explain how to sustain extremely asymmetrical motions in Jupiter without forcing terms nor observational evidence.

To conclude, we stress that the hydrostatic equilibrium is therefore a global, average property, used as an excellent approximations in many cases. As in Kippenhahn and Weigert [1990], let's assume a perturbation from hydrostatic equilibrium in equation 6.1c. If pressure terms were negligible, we obtain a characteristic time of free fall of Jupiter under gravity:

$$t_{\text{ff}} \approx \sqrt{\frac{R_J}{g}} \tag{2.72}$$

Similarly, we can define an explosion timescale over which a parcel would be expelled if gravity were to disappear. It is mainly the speed of sound integrated over the whole planet:

$$t_{\text{expl}} \approx R_J \sqrt{\frac{\bar{\rho}}{\bar{P}}} \tag{2.73}$$

where $\bar{\rho}$ and $\bar{P}$ are the mean density and pressure. A simple view of hydrostatic equilibrium states that the free fall and explosion timescales must be comparable: a perturbation that falls under the effect of gravity must be restored by pressure forces on similar timescales. Using the external value for $g = \mathcal{G}M_J/R_J^2$ as a proxy, this leads to the definition of the hydrodynamical timescale:

$$t_{\text{hydro}} \approx \left(\frac{R^3}{\mathcal{G}M}\right)^{1/2} \tag{2.74}$$

For Jupiter, this timescale is about 30 minutes. Therefore, if the planet is in hydrostatic equilibrium, a perturbation will be smoothed away in an hour. This is much less than any other timescale we will study for the evolution of Jupiter, and the hydrostatic approximation is very appropriate. Obviously, this does not mean that locally, both in space and time, hydrostasy is always verified, but it confirms what we stated above: there can be some deviations from the hydrostatic equilibrium, and accelerations of the winds, but almost instantaneously the balance is restored. Notably, we have shown that the typical convective speed in Jupiter is about 10cm.s^{-1}, which corresponds to a covered distance of 360 meters in an hour. Any study of Jupiter structure on larger lengthscale can be accuratly considered as hydrostatically balanced.

2.3 Short summary

In this chapter, we have first introduced the equations for describing the motions of fluid in a planetary case. This was followed by a discussion on the nature of the waves that can propagate in an atmosphere. The most important in the large scale dynamics of atmospheres are gravity waves and Rossby waves, with the Rossby wave being particularly important in the study of hot Jupiters equatorial dynamics as will be shown in the last chapters.

We have also introduced the gravitational moments, that will allow us to constrain the interior structure of Jupiter, provided we have a priori knowledge of the physical conditions in the interior and a method to evaluate the gravitational moments. The most simple priors have been introduced in this section: Jupiter is a convective, isentropic planet. This simple view will be extended in chapter 4, showing that additional processes are needed to understand the interior of the planet. The method to calculate the moments has to be exposed and tested first. This is the point of the next chapter.

Chapter 3

Calculation of Jupiter's gravitational field: testing the Concentric Maclaurin Spheroid method

> *Qu'est-ce que vous faites mercredi prochain?*
>
> *Pierre Brochant*

As stated in the introduction, the quality of the observations of Juno requires to have a very precise method to evaluate the gravitational moments of a Jupiter model from its pressure-density profile. The Concentric Maclaurin Spheroid (CMS) method, developed in Hubbard [2012] and Hubbard [2013], provides an ideal framework in the context of Juno. In this chapter, we will first present this method and study its limitations as was done in Debras and Chabrier [2018]. The various quantities relevant for Jupiter are given in table 3.1. Through this chapter, we compare the precision of the method with the first observations of Juno, reported in Bolton et al. [2017]. The later observations of Iess et al. [2018] are much more precise than the intrinsic precision of the method derived here. At the present date however, other physical unknowns (imperfect equations of state, dynamical effects (see next chapter)) exhibit comparable or bigger errors than the intrinsic ones we calculate for the CMS method.

3.1 Brief overview of the CMS method

As shown in Section 2.2.1, the gravitational moments are powerful quantities to constrain the density structure of a planet. However, the rotation of the planet changes the gravitational potential and the angular function of the potential inside the planet is impossible to calculate analytically for realistic equations of state. Therefore, the pressure-density profile of the planet cannot be accurately calculated without numerical methods: tt is not possible to express the density as an analytical function of r' and μ' in eqn.(2.39). Three main approaches have been created to evaluate the integrals in eqn.(2.39):

- The most famous is the theory of figures, as detailed for example in Zharkov and Trubitsyn [1978]. It is a perturbative method that allows a development of the potential in the power of q, the ratio of rotational

Table 3.1: Values of the planetary parameters of Jupiter.

Quantity	Parameter	Value
Gravitational constant	G^a (global parameter)	$6.672598 \times 10^{-11} \pm 2 \times 10^{-17}$ $\mathrm{m^3 kg^{-1} s^{-2}}$
Mass	M_J	1.89861×10^{27} kg
Standard gravitational parameter	$G \times M_J{}^b$	(126686533 ± 2) $\times 10^9 \mathrm{m^3 s^{-2}}$
Equatorial radius	$R_{eq}{}^c$	71492 ± 4 km
Polar radius	$R_{polar}{}^c$	66854 ± 10 km
Rotation rate	ω^d	1.7585324×10^{-4} $\pm 6 \times 10^{-10}$ $\mathrm{s^{-1}}$
Mean density	$\bar{\rho}$	$1326.5\ \mathrm{kg\,m^{-3}}$
	$m = 3\omega^2/4\pi G\bar{\rho}$	0.083408
Rotational distortion	$q = \omega^2 R_{eq}^3/GM_J$	0.0891954
Second gravitational moment	$J_2 \times 10^6$	14696.572 ± 0.014^e , 14696.514 ± 0.272^f
Fourth gravitational moment	$-J_4 \times 10^6$	586.609 ± 0.004^e , 586.623 ± 0.363^f
Sixth gravitational moment	$J_6 \times 10^6$	34.198 ± 0.009^e , 34.244 ± 0.236^f
Eigth gravitational moment	$-J_8 \times 10^6$	2.426 ± 0.025^e , 2.502 ± 0.311^f
Tenth gravitational moment	$J_{10} \times 10^6$	0.172 ± 0.069^e

R_{eq} and R_{polar} are observed at 1 bar. The value of the pulsation is chosen following Archinal et al. [2011]. (a) Cohen and Taylor [1987] (b) Folkner et al. [2017] (c) Archinal et al. [2011] (d) Riddle and Warwick [1976] (e) Iess et al. [2018] (f) Bolton et al. [2017] (previous values) potential over gravitational potential. It has been extensively used to derive models of Jupiter (e.g. Chabrier et al. [1992], Hubbard and Marley [1989] or Zharkov and Gudkova [1991]). Unfortunately, the higher the precision and the order of the gravitational moments to calculate the more cumbersome the calculations. With Juno precision and the need to evaluate of $J_{k>8}$, this method is rather unappropriate although it can be adapted as was done in e.g., Guillot et al. [2018]. From J_8 on however, quantitative conclusions cannot be drawn (see their Table 2 of the extended data for the polytrope eos).

- Wisdom [1996] has presented a non perturbative approach that reproduced with a tremendous accuracy the results for polytropic equation of state. Unfortunately, it has not been adapted yet to realistic equations of state, and it is not obvious whether this method can deal easily with discontinuities. Still, it allows comparisons in order ot benchmark other method, such as in Wisdom and Hubbard [2016].
- The concentric Maclaurin Spheroid method developed in Hubbard [2012] and Hubbard [2013] (H13). It is a non perturbative, numerical scheme that decomposes the planet in concentric spheroids, which we further detail in this chapter. A schematic view of the method is provided in Figure 3.1.

The CMS method consists of a numerical hydrostatic scheme which decomposes a rotating celestial body into N concentric spheroids of constant density (the well-known MacLaurin spheroid would correspond to the case $N = 1$). For $N > 1$, one needs to picture it as spheroids of different radii, the bigger one being the outermost one with planetary radius and the innermost one is the smallest, that pile up to create a density profile in the planet being the sum of the density of each spheroid. The spheroids are labeled with index $i = 0, N-1$, with $i = 0$ corresponding to the outermost spheroid and $N-1$ to the innermost one. The method requires two inputs. First, (i) the planet rotational distortion, $q = \omega^2 a^3/GM$, where ω denotes the angular velocity, a the equatorial radius, M the planet's mass and G is the gravitational constant. The factor q represents the ratio of the rotational over gravitational potentials, as in the theory of figures (Zharkov and Trubitsyn [1978] or Chabrier et al. [1992]). Second, (ii) a barotrope (P,ρ) representing the equation of state (eos) of the planet and its composition.

For a given density profile, we can calculate the gravitational potential of each spheroid (which is constant on the spheroid), and then calculate self-consistently the radius of each spheroid as a function of latitude. The obtained radii give different values for the potential of the spheroids, and successive iterations lead to convergence of both shape and potential of the spheroids (see Hubbard [2012] and H13). With the density and potential of each spheroid, one easily obtains the pressure from the hydrostatic equilibrium condition. More precisely, H13 shows that we can express the potential U_i at the equator of the i^{th} spheroid as the sum over the different layers of three quantities: $J_{i,k}$ the external gravitational moment of order k of the i^{th} layer only, J''_{i-1} the external moments of the sphere of radius r_i with the density of the $(i-1)^{th}$ spheroid and $J'_{i-1,k}$ the internal moment due to the $(i-1)^{th}$, leading to:

$$U_j = -\frac{1}{\lambda_j}\left(\sum_{i=j}^{N-1}\sum_{k=0}^{\infty} J_{i,2k}\lambda_j^{-2k}P_{2k}(0) + \sum_{i=0}^{j-1}\sum_{k=0}^{\infty} J'_{i,2k}\lambda_j^{2k+1}P_{2k}(0) + \sum_{i=0}^{j-1} J''_i\lambda_j^2\right) + \frac{1}{2}q\lambda_j^2 \tag{3.1}$$

where λ_j is the ratio of the equatorial radius of the spheroid over the equatorial radius of the planet and the P_{2k} the Legendre polynomials as in chapter 2. As the surfaces of the spheroids are equipotentials, the shape of the spheroid is just obtained by saying that the potential at any μ must be equal to U_j of eqn .(3.1), being the potential at the

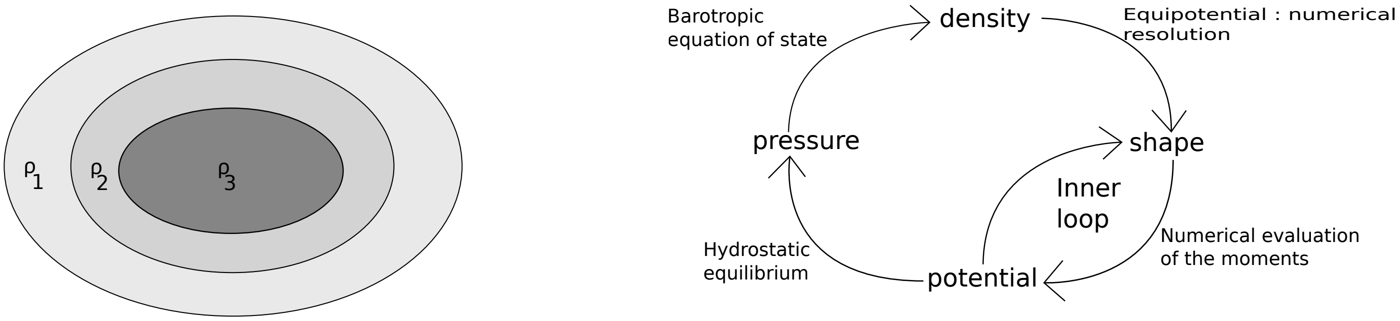

(a)

(b)

Figure 3.1: Schematic view of the CMS method. (a) Discretization of the density structure inside the planet. One must remembers that these are concentric spheroids and not successive layers. (b) Iteration procedure of the method.

equator.

After this first stage of convergence, it is necessary to verify whether the obtained (P,ρ) profile of the planet is in agreement with the prescribed barotrope. Since generally it is not, an outer loop is necessary to converge the density profile for the given eos.

At last, once the radii, potentials and densities of the multi-layer spheroids have been obtained consistently with the required numerical precision, one obtains a discretized profile of these quantities throughout the whole planet. We can then calculate the gravitational moments, to be compared with Juno's observations. By additivity, equation (2.39) simplifies to:

$$J_k = \sum_{i=0}^{N-1} J_{i,k}, \tag{3.2}$$

and, using the fact that the i^{th} spheroid has constant density $\delta\rho_i$:

$$J_{i,2k} = -\frac{4\pi\delta\rho_i}{MR^{2k}(2k+3)} \int_0^1 r_j(\mu)^{2k+3} P_{2k}(\mu') d\mu' \tag{3.3}$$

In this chapter, we first evaluate analytically the discretization errors of the CMS method with a polytropic equation of state in section 3.2, showing that 512 spheroids are not enough to match Juno's error bars, and that the repartition of spheroids is an important parameter in the evaluation of the errors. We confirm these results by numerical calculations in Section 3.3. We then apply our method with a realistic eos in Section 3.4, which shows the need to improve the basic CMS method. In Section 3.5, we study the impact of the outer boundary condition, as proposed in Wahl et al. [2017]. Section 3.6 is devoted to the conclusion.

3.2 Evaluation of the uncertainties of the CMS method

3.2.1 Analytical evaluation

As we have seen, the CMS discretises the planet in successive spheroids. A discretisation error will stem from this decomposition, which needs to be evaluated it order to ensure sure that the method is precise at the Juno level. The first thing to note is that eqn.(3.2) implies that the uncertainties of each spheroid are added up, so a small error on the radius, potential or density can lead ultimately to a significant error once summed over all the layers.

As explained in H13, for a given piecewise density profile, the evaluation of the gravitational moments is extremely precise, with an error around 10^{-13}. The main sources of error, apart from the uncertainties on the barotrope, then arise from the finite number of spheroids and from the approximation of constant density within each spheroid, leading potentially to an incorrect evaluation of the radii and potential of the layers.

Evaluation of the errors with 512 spheroids

In order to evaluate the errors analytically, we have considered a polytrope of index $n = 1$, $P \propto \rho^2$. We call ρ_2 the discretized version of ρ in the CMS model.

If we assume longitudinal and north-south symmetry, only the even values of the gravitational moments are not null. Therefore, we were able to express the difference between the analytical value of the potential and the value obtained with the CMS method on a point exterior to the planet with radial and latitudinal coordinates ($r, \mu = cos(\theta)$, where θ is the angle from the rotation axis), as:

$$\Delta\phi = -\frac{4\pi G}{r} \sum_{k=0}^{\infty} P_{2k}(\mu) r^{-2k} \times \int_0^1 \int_0^{a_J} \left[\rho(r') - \rho_2(r')\right] r'^{2k+2} P_{2k}(\mu) dr' d\mu, \tag{3.4}$$

where P_{2k} is the Legendre polynomial of order $2k$ and a_J is Jupiter's equatorial radius. Our first assumption here was that the CMS method prefectly captures the shapes of the spheroids. In reality, this is the case only for an infinite number of spheroids, but we have neglected this first source of error which is difficult to evaluate analytically.

Since the masses of the two models must be the same, the $k = 0$ term must cancel. In terms of gravitational moments J_{2k}:

$$J_{2k} = -\frac{4\pi}{M a_J^{2k}} \int_0^1 \int_0^{a_J} \rho(r') r'^{2k+2} P_{2k}(\mu) dr' d\mu. \tag{3.5}$$

By construction we can write $\rho_2(r) = \rho_i,\ r_{i+1} < r \leq r_i$. So the difference on the gravitational moment between the exact and the CMS models from Eq.(3.5) is:

$$\Delta J_{2k} = -\frac{4\pi}{M a_J^{2k}} \sum_{i=0}^{N-1} \int_0^1 \int_{r_{i+1}(\mu)}^{r_i(\mu)} \left[\rho(r') - \rho_i\right] \times r'^{2k+2} P_{2k}(\mu) dr' d\mu. \tag{3.6}$$

This formulation is exactly the same as in H13 (Eq.(10)), except that we used ρ_i instead of $\delta\rho_i$. The analytical expression of the density of a rotating polytrope at first order in m as a function of the mean radius l of the equipotential layers and of the planet mean density $\bar{\rho}$ is given by (Zharkov and Trubitsyn [1978]):

$$\frac{\rho(l)}{\bar{\rho}} = A\frac{sin(\alpha\frac{l}{l_0})}{(\frac{l}{l_0})} + \frac{2}{3}m, \tag{3.7}$$

$$\text{with } A = \frac{\pi}{3}\left(1 - \frac{2}{3}m\left(1 - \frac{6}{\pi^2}\right)\right) \text{ and } \alpha = \pi\left(1 + \frac{2m}{\pi^2}\right), \tag{3.8}$$

where l_0 is the outer mean radius.

At this stage, our method implied an important approximation, namely that ρ_2 followed perfectly the polytropic density profile of Eq.(3.7) on each layer, if evaluated at the middle of the layer: $\rho_i = \rho_{poly}\left(r_i + r_{i+1}\right)/2$. The errors we calculated are thus smaller than the real ones since we did not take into account those arising from the departure from the exact density profile.

In Appendix A.1, we show how to get rid of the dependence on the angular part, μ, in Eq.(3.6). As detailed in Appendix A.2, for a linear spacing of the spheroid with depth, $\Delta r = a_J/N$, we obtained:

$$|\Delta J_{2k}| \sim (2k+3)\frac{\pi}{12}\frac{< P_{2k} >}{N^3}\sum_{i=0}^{N-1}\left(1 - \frac{1}{N}\left(i + \frac{1}{2}\right)\right)^{2k+2}, \tag{3.9}$$

$$\text{with } < P_{2k} >= \left|\int_0^1 \left(\frac{1}{1+e^2\mu^2}\right)^{k+1} P_{2k}(\mu)d\mu\right|. \tag{3.10}$$

It is interesting to note that the relative error of each layer is a decreasing function of i: the external layers lead to larger errors on the gravitational moment than the inner ones. Figure 3.2 displays the contribution to J_2 of the outer layers of the planet in the polytropic case (we have numerically integrated the expression for J_2 from Eq.(3.5), Eq.(3.7) and Eq.(A.4)).

To quantify the error, we focused on J_2, the case $k = 1$. As detailed in Appendix A.3, one gets:

$$|\Delta J_2| \times 10^6 \sim \frac{\pi}{12}\frac{< P_2 >}{N^2} \times 10^6 \approx \frac{9.4 \cdot 10^3}{N^2}. \tag{3.11}$$

With $N = 512$ (as used in H13), we get $|\Delta J_2| \times 10^6 \sim 3.6 \times 10^{-2}$. The first data from Juno after three orbits gave an uncertainty of 2.72×10^{-1} on $J_2 \times 10^6$. We are under these error bars by a factor of eight, but in these analytical calculations, we have made several restrictive approximations. Notably, we have supposed that the numerical method can find perfectly the shape and the density of each spheroid, and we have neglected the factor $\alpha^3/3 \sim 2 - 10$ in Eq.(A.28). As mentioned earlier, it is hard to evaluate a priori the errors due to the wrong shapes and densities of the spheroids, but combined with the neglected factor, we expect the real numerical errors to become larger than Juno's error bars. This is confirmed by numerical calculations in the next section. Therefore, even in this ideal case, the CMS method in its basic form is intrinsically not precise enough to safely fulfill Juno's constraints. Calculations

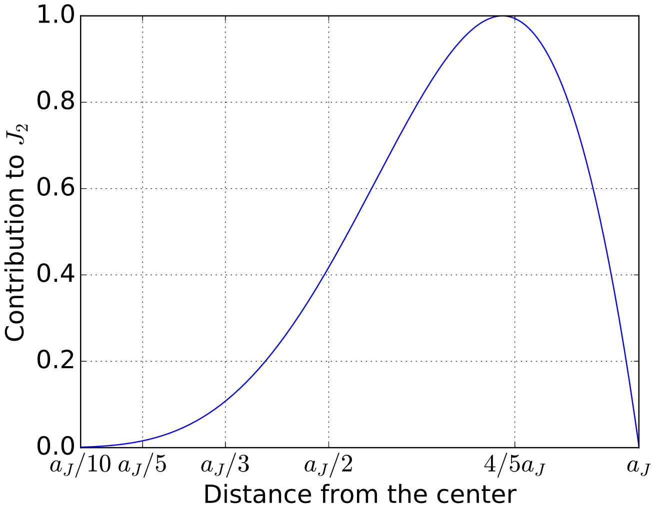

Figure 3.2: Contribution of each part of the planet to the total value of J_2, normalized to its maximum value, for a polytrope of index $n = 1$.

with 512 MacLaurin spheroids with a linear spacing cannot safely enter within Juno's error bars.

HM16 proposed a better spacing of the spheroids, with twice more layers above 50% of the radius than underneath. As shown in Appendix A.3.2, the new error for 512 spheroids becomes:

$$|\Delta J_2| \times 10^6 = \frac{9}{256}\frac{\pi < P_2 >}{N^2} \times 10^6 \approx 1.51 \times 10^{-2}. \tag{3.12}$$

This is about 2.5 times better than with the linear spacing. But once again, when considering the factor of ten neglected in Eq.(A.28) in nearly the entire planet and the strong approximation of perfect density and perfect shape of the discrete spheroids, it seems very unlikely to reach in reality a precision well within Juno's requirements. Again, this is confirmed numerically in §3.3. We note in passing that the difference between the errors obtained with the above two different spacings shows the strong impact of the outermost layers in the method.

In conclusion, these analytical calculations show that, at least with 512 sheroids, the CMS method, first developed in H13 and improved in HM16, leads to a discretization error larger than Juno error bars. Increasing the number of spheroids would give a value of J_2 outside Juno's error bars and would thus require a change in the derived physical quantities (core mass, heavy element mass fraction ...). We investigate in more details the uncertainties on these quantities in §3.4.3.

It should be mentioned that Wisdom and Hubbard [2016] calculated similar errors by comparing their respective methods, finding (their Eq. (15)):

$$\log_{10}|\frac{\Delta J_2}{J_2}| \simeq 0.7 - 1.81\log_{10}(N), \tag{3.13}$$

while we get

$$\log_{10}|\frac{\Delta J_2}{J_2}| \simeq -0.6 - 2\log_{10}(N). \tag{3.14}$$

The 0.7 constant term is about 20 times the value obtained in Eq.(3.12). This confirms that, indeed, we underestimated the errors in the analytical calculations, as mentioned above.

These expressions show that one needs to use at least 2000 spheroids to reach Juno's precision, as can already be inferred from Wisdom and Hubbard [2016]. These authors, however, suggest that 512 spheroids can still be used to derive interior models, because a slight change in the density of one spheroid could balance the discretization error. A change in one spheroid density, however, will affect the whole planet density structure, because of the hydrostatic condition. Changing the density of each spheroid (within the uncertainties of the barotrope itself) can thus yield quite substantial changes in the gravitational moments.

Even more importantly, if the method used to analyze Juno's data has uncertainties due to the number and repartition of spheroids larger than Juno's error bars, this raises the question of the need for a better precision on the gravitational data, since the derived models depend on the inputs of the method itself. It is thus essential to quantify precisely the uncertainties arising from the discretization errors, as we do in §3.4 and 3.5.

Another option would be to use Wisdom's method (Wisdom [1996]), which has virtually an unlimited precision. Table 3 of Wisdom and Hubbard [2016] indeed shows that its accuracy is greater than anything Juno will ever be able to measure. In its present form, however, it is not clear whether this method can easily handle density, composition or entropy discontinuities; it is certainly worth exploring this issue. The CMS method, in contrast, is particularly well adapted to such situations, characteristic of planetary interiors. As for the standard perturbative theory of Figures, it becomes prohibitively cumbersome when deriving high-order (fifth even order for J_{10}) moments (see e.g., Nettelmann [2017]). For these reasons, the CMS method appears to be presently the most attractive one to analyze Juno's data. As mentioned above, it is thus crucial to properly quantify its errors and examine under which conditions it can be safely used to derive reliable enough Jupiter models.

3.2.2 Spacing as a power of k

As shown in Appendix A.3.3, for a cubic distribution of spheroids as a function of depth, we obtained the error on J_2:

$$|\Delta J_2^{cubic}| \sim \frac{\pi}{12}\frac{< P_2 >}{N^2}. \tag{3.15}$$

This is the same result as Eq.(3.11). We checked that we get the same results for a quadratic spacing or with a spacing of power of four (it is probably easy to prove that this holds for any integer power of n). This is interesting for several reasons.

First, these types of spacings have more points in the high atmosphere region, where the neglected factor of Eq.(A.28) is closer to two than ten. The global neglected factor is then smaller than for a linear spacing. Second, we studied where the cubic spacing is equal to the linear one. Using Eq.(A.43), we got:

$$\begin{aligned}\Delta r_i^{\text{cubic}} = \Delta r &\Longleftrightarrow \frac{\Delta i^3}{N^2} = 1 \\ &\Longleftrightarrow 3i^2 + 3i + 1 = N^2 \\ &\Longrightarrow i \sim \frac{N}{\sqrt{3}}. \end{aligned} \tag{3.16}$$

More generally, with a spacing of power k, Δr_i^k is smaller than the linear Δr for $i \leq N/k^{\frac{1}{k-1}}$, and larger for larger values of i. That means that above $r_i = a_J \left(1 - 1/k^{\frac{1}{k-1}}\right)$ the radius, potential and density of the spheroids are better estimated than in the linear case and less well below this radius. And the stronger the exponent in the spheroid distribution, the larger the external gain (internal loss) on the spheroids because the more (less) tight the external (internal) layers.

With a quadratic spacing, the spheroids are closer than in the linear case above 75% of the radius of the planet while inside this limit the spacing is worse than in the linear case. With a cubic spacing the precision in the spheroids repartition is better than in the linear case down to only 80% of the radius, while for a power of 4 the limit is 85%. As shown and explained in §3.3.1, the cubic spacing ends up being the best compromise.

There is one remaining problem with a cubic spacing: for $N > 512$, the sizes of the first (outermost) layers are extremely small, well below the kilometer, with densities smaller than 10^{-3} kg m^{-3}. It is thus mandatory to have an eos accurate enough in this regime; if not the errors will be very large. The other solution, that is discussed in §3.5 is to impose a non zero density as outer boundary condition.

3.2.3 Exponential spacing of the layers

Here, we examine an exponential repartition of spheroids. The details of the calculations are given in Appendix A.3.4, and the repartition functions of the spheroids are displayed in Figure 3.3.
For the exponential repartition, the value of the error is:

$$|\Delta J_2^{exp}| \times 10^6 \simeq \frac{\pi < P_2 >}{252} \times \frac{\gamma^2}{N^2} \times 10^6 \approx 449 \left(\frac{\gamma}{N}\right)^2, \tag{3.17}$$

where $\gamma \in [5, 10]$ is a parameter which determines how sharp we want the exponential function to be. A large value of γ leads to a steep slope in the innermost layers and a very small Δr_i in the exterior. With $N = 512$:

$$|\Delta J_2^{exp}| \times 10^6 \in [1.54 \times 10^{-2}, 1.6 \times 10^1]. \tag{3.18}$$

As seen, the smaller γ the smaller the error, but also the larger the range of outer layers which is a problem, as examined in §3.3. Note also that the neglected factor of Eq.(A.28) in the analytical calculations is much smaller because of the very large number of spheroids in the outermost part of the envelope (see Figure 3.3). Compared to Eq.(3.12), we see that the exponential error is always larger for $\gamma > 3$. As discussed in the next section, however, the impact of the first layers becomes very important with this type of spheroid repartition.

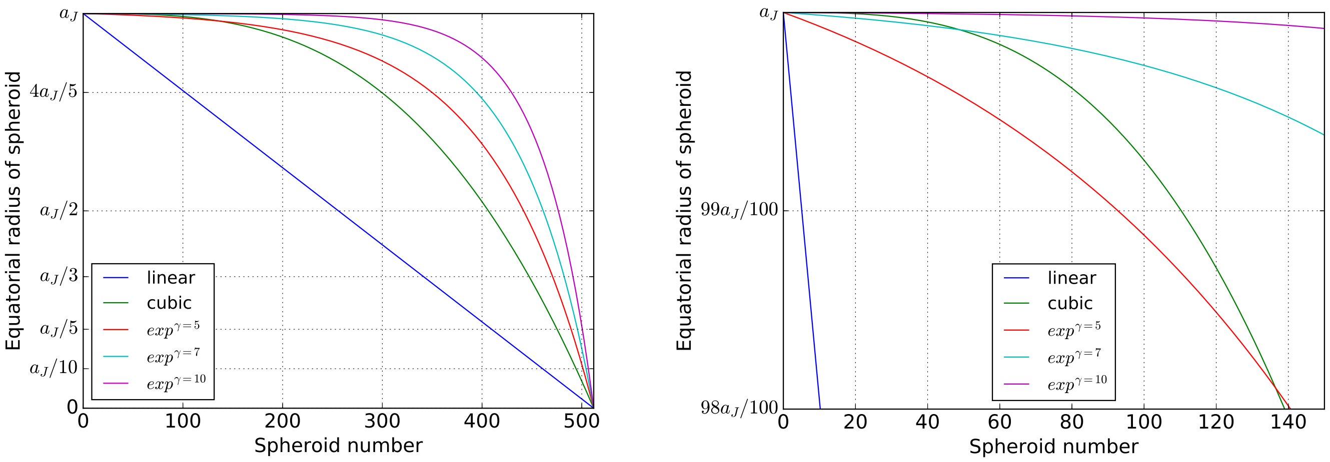

(a)

(b)

Figure 3.3: Equatorial radius as a function of the spheroid number for various functional forms for the repartition of the spheroids. (a): from 0 to a_J; (b): zoom of the external layers.

In summary, in this section, we have shown analytically that 512 layers spaced linearly is not enough to obtain sufficient accuracy on the gravitational moments of Jupiter to safely exploit Juno's data. Indeed, the theoretical errors are within Juno's error bars but the simplifying assumptions used in the calculations (in particular perfect shape and density of the spheroids) suggest that the real calculations will not match the desired accuracy. As explained in §3.2.1, the method, mathematically speaking, is precise up to 10^{-13} for a piecewise density profile, but the errors due to the discretization, as derived in this section, are of the order of $\sim 10^{-7}$. Using a better repartition of spheroids yields, at best, an error of the order of Juno's error bars but, in any case, remains insufficient with 512 spheroids. The impact of such an error on Jupiter's derived physical quantities is discussed in §3.4.3.

According to this analytical study, using a minimum of 1000 spheroids spaced cubically, quadratically or exponentially seems to provide satisfying solutions. That may sound surprising since the spacing used in HM16, with their particular first layer density profile, gives a smaller uncertainty in Eq.(3.12) than the cubic or square one in Eq.(3.15). To explain this apparent contradiction, we need to explore more precisely how the error depends on the different spacings by comparing numerical calculations with the analytical predictions. This is done in the next section.

3.3 Numerical calculations

3.3.1 How to match Juno's error bars

In this section, we explore two main issues: how does the error depend (i) on the number of layers and (ii) on the spacing of the spheroids. Another parameter we did not mention in the previous section is the repartition of the first layers. This is the subject of the next section.

To study this numerically, we have developed a code similar to the one developed by Hubbard, as described in H13. The accuracy of our code has been assessed by comparing our results with all the ones published in the above papers. In the case of constant density, we recovered a MacLaurin spheroid up to the numerical precision, while for a polytrope of index $n = 1$, we recovered the results of Table 5 of H13, as shown in Table 3.2 (the differences are due to the fact that the published results were not converged to the machine precision. With the very same conditions, our code and Hubbard's agree to 10^{-14}). We have also performed several tests of numerical convergence with different repartitions of spheroids. We have compared our various numerical evaluations of the errors, double precision with 30 orders of gravitational moments and 48 points of Gauss-Legendre quadrature, to a quadruple precision method with 60 orders of moments and 70 quadrature points, from a couple of hundred spheroids to 2000 spheroids. The differences are of the order of 10^{-13}, negligible compared with Juno's error bars. Finally, as explained in Hubbard et al. [2014], we have implemented an auto exit of the program if the potential diverges from the audit points.

Table 3.2: Difference between the values calculated with our code and the results from Hubbard [2013].

Quantity	Theoretical value	H13	Our Code
$J_2 \times 10^6$	13988.511	13989.253	13989.239
$-J_4 \times 10^6$	531.82810	531.87997	531.87912
$J_6 \times 10^6$	30.118323	30.122356	30.122298
$-J_8 \times 10^6$	2.1321157	2.1324628	2.1324581

Figure 3.4 displays the difference between the expected and numerical values of J_2 for a polytrope of index $n = 1$, for different spacings with 512 layers. The first thing to note is that, whatever the repartition, the numerical errors are always larger than Juno's error bars: 512 spheroids are definitely not enough to match the measurements of the Juno mission with sufficient accuracy, as anticipated from the analytical calculations of the previous section.

The second and quite important problem is the difference between calculations using a density $\rho = 0$, as in HM16, or $\rho \neq 0$ in the first layer. With 512 spheroids spaced as in HM16, the first layer is 50 km deep. Imposing a zero density in this layer is equivalent to decreasing the radius of the planet by 50 km, which is larger than the uncertainty on Jupiter's radius. As seen in the Figure, if one does so, the error on J_2 is more than 100× Juno's error bar. Specifically, for the HM16 spacing, when the first layer has a non-zero density, its impact on the value of $J_2 \times 10^6$ is $\sim 5 \times 10^1$. We discuss that in more details in §3.3.2.

Figures 3.5 and 3.6 display the behavior of the error as a function of the number N of spheroids for a cubic, square and a few exponential repartitions, respectively. As mentioned earlier, we see in Figure 3.5a that only for $N > 1000$ spheroids do we get an error smaller than Juno's error bar. Importantly enough, we also see that the first spheroid ($N = 0$) makes no difference on the result when the layers are cubically spaced (Figure 3.5b). This contrasts with the results obtained with the HM16 spheroid repartition, where we see that the first spheroid has a huge impact

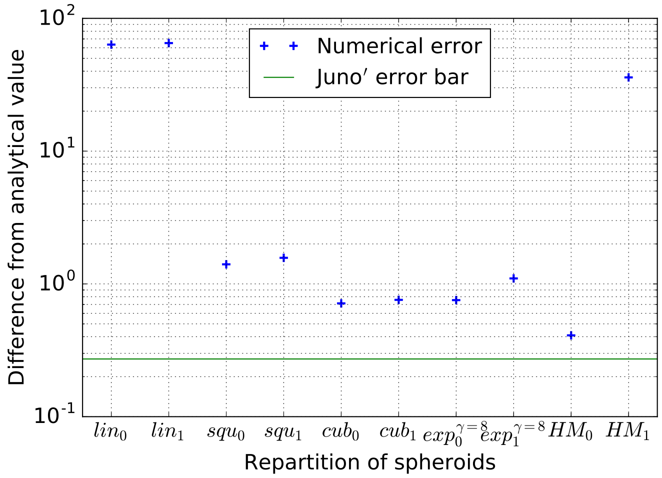

Figure 3.4: Absolute value of the difference between the expected and numerical results on $J_2 \times 10^6$ for different spacings of the spheroids with N=512. Lin, squ and cub are repartitions of spheroids following a power law of exponent 1, 2 or 3, respectively; $exp^{\gamma=8}$ is the exponential repartition with our favored value $\gamma = 8$. HM is the method exposed in HM16, explained in Appendix A.3.2. The subscript 1 means that the first layer has a non-0 density while the subscript 0 means zero density in the first layer.

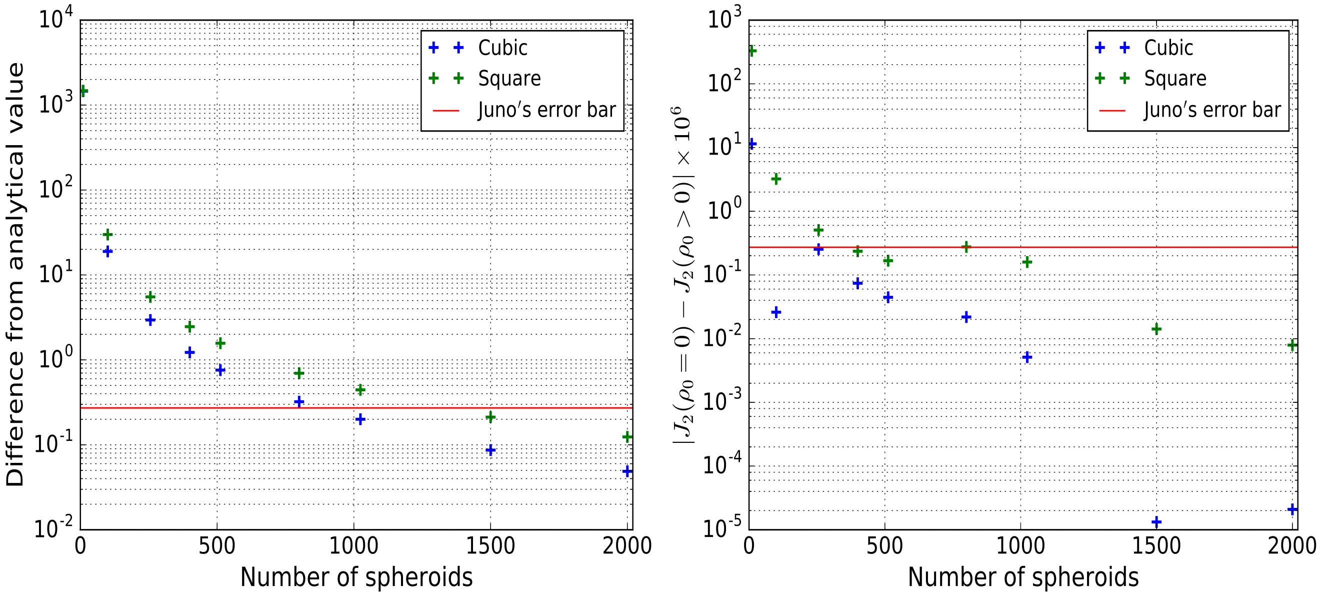

(a) (b)

Figure 3.5: Numerical error as a function of the number of spheroids for the cubic and square repartitions. (a): error between the analytical and measured $J_2 \times 10^6$; (b): difference on $J_2 \times 10^6$ when the first layer has 0 or non-0 density.

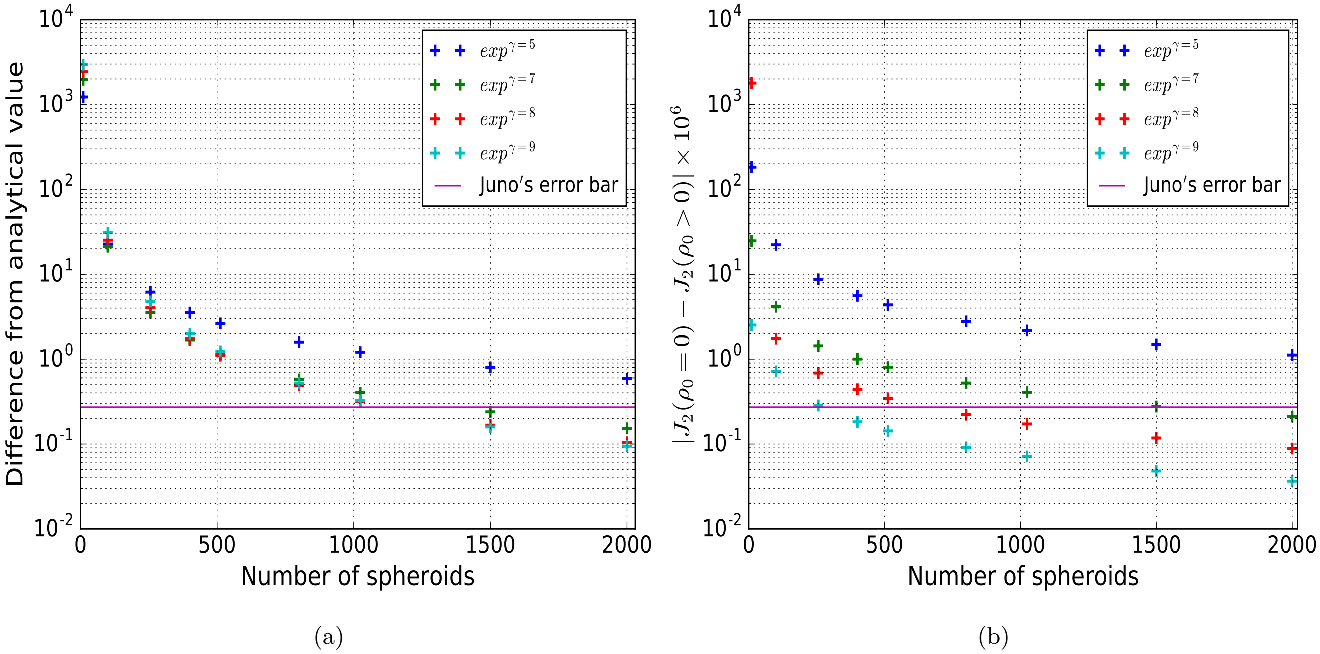

Figure 3.6: Numerical error as a function of the number of spheroids for exponential repartitions. (a): error between the analytical and measured $J_2 \times 10^6$; (b): difference on the $J_2 \times 10^6$ when the first layer has 0 or non-0 density.

on the final result (Figure 3.4). The cubic spacing with at least 1000 spheroids thus matches the constraints, with both an uncertainty within Juno's error bars and a negligible dependence on the first layer. As mentioned in the previous section (and shown later in Figure 3.7*b*), however, with the cubic spacing the densities of the first layers are orders of magnitude smaller than 10^{-3} kg m^{-3}, questioning the validity of the description of the gas properties by an equilibrium equation of state. For this reason, it is preferable to use a square or exponential spacing in the case of a zero pressure outer boundary condition. The effect of changing this boundary condition is discussed in §3.5.

As seen in Figure 3.5a, the square spacing requires at least 1500 spheroids to be under the error bars of Juno with reasonable accuracy. For 1500 or 2000 spheroids, the first layers have densities around 10^{-2} kg m^{-3}. In Figure 3.5b, we confirm that, in that case, having a zero or non-zero density outer layer changes the value under the precision of Juno.

For the exponential spacing, we recall that the higher the γ value the smaller the first layer, which can become a problem (see §3.3.2). Considering Figures 3.6a and 3.6b, the best choices for γ are $\gamma = 8$ or $\gamma = 7$, because it does not require too many spheroids to converge and at the same time the obtained values for the densities of the first layers are comparable to the ones obtained with the square repartition (slightly larger for $\gamma = 7$).

Globally, we conclude in this section that we need at least 1500 and preferentially 2000 spheroids spaced quadratically or exponentially to fulfill our goals of both high enough precision for Juno's data and densities high enough to justify the use of an equilibrium eos. Having two different repartitions that match Juno error bars brings some confidence in results that are obtained with a realistic eos instead of a polytrope. Furthermore, with such choices of repartition, we do not need to impose a first layer with zero density. In §3.5, however, we show that the cubic repartition can also be used, with a different boundary condition.

3.3.2 Importance of the first layers

As explained in HM16, these authors improved the spacing of their spheroids by adding up a first spheroid at depth $a_J - \Delta r/2$, instead of Δr, which has zero density: $\rho_0 = 0$. Although this could seem quite arbitrary, it has an analytical justification emerging from the linear dependence of the density with radius (Hubbard, priv. com.). The obtained result is indeed closer to the analytical value of Hubbard [1975], but it has two downsides. First, it decreases arbitrarily the radius by 50 km (see discussion above). For example, for a cubic spacing with 512 spheroids, decreasing the radius by 50 km leads to $J_2 \times 10^6 = 13961.23$ with an error of 2.7×10^1 according to the analytical calculation, 100× Juno's uncertainty. Furthermore, there is no guarantee that this repartition will still be valid with a realistic eos, with an exponential dependence of the density upon the radius. In order to assess the robustness of the results and of the CMS method, one needs to confirm that different repartitions yield similar values and that the results are not only correct for one given spheroid repartition.

More generally, a key question is: why are the first layers so important in the CMS method? Going back to Figure 3.2, we see that the region outside 90% in radius contributes as much to J_2 as the region within the inner 50%. The problem is the slope of the moment: it is much steeper in the outside region. Consequently, the behavior of a layer in the outermost region yields a much larger error than the contribution from the inner layers. This simply reflects the fact that most of the planet angular momentum is in its outermost part.
Another issue is that, in the first layers, the change in density represents at least 10% of the density itself and can even become comparable to this latter. In contrast, in the internal layers, even a large Δr yields a relative change of density from one spheroid to another less than 1%. Then, the error due to the inevitable mistake on the true shape of the spheroids is much more consequential in the external layers, where the relative density change is significant. Another source of error stems from the fact that the pressure is calculated iteratively from the hydrostatic equation, starting from the outermost layers. A small error in the first layers will then propagate and get amplified along the density profile.

Equation (10) of HM13 gives the explicit expression of J_2 for each layer. With the notation of the paper:

$$J_i^2 = -\left(\frac{3}{5}\right) \frac{\delta\rho_i \int_0^1 d\mu P_{2k}(\mu)\xi_i(\mu)^5}{\sum_{j=0}^{N-1} \delta\rho_j \int_0^1 d\mu \xi_i(\mu)^3}, \tag{3.19}$$

$$\delta\rho_i = \rho_i - \rho_{i+1} \text{ if } i > 0,$$

$$\delta\rho_0 = \rho_0, \tag{3.20}$$

$$\xi_i(\mu) = r_i(\mu)/a_J. \tag{3.21}$$

To illustrate our argument, we said that every spheroid has the same shape and that $\delta\rho_i$ is the same as in the rest case, given by a slight modification of Eq.(63) of HM13:

$$\delta\rho_i = \rho_c \times \delta\lambda_i \left(\frac{\cos(\pi\lambda_i)}{\lambda_i} - \frac{\sin \pi\lambda_i}{\lambda_i^2} \right), \tag{3.22}$$

$$\lambda_i = \xi_i(0) \text{ and } \delta\lambda_i = \lambda_i - \lambda_{i+1}. \tag{3.23}$$

Then, the only different terms for each layer stemmed from the numerator: $\delta\rho_i \times \lambda_i^5$. We plot this value for different spacings of the spheroids in Figure 3.7.

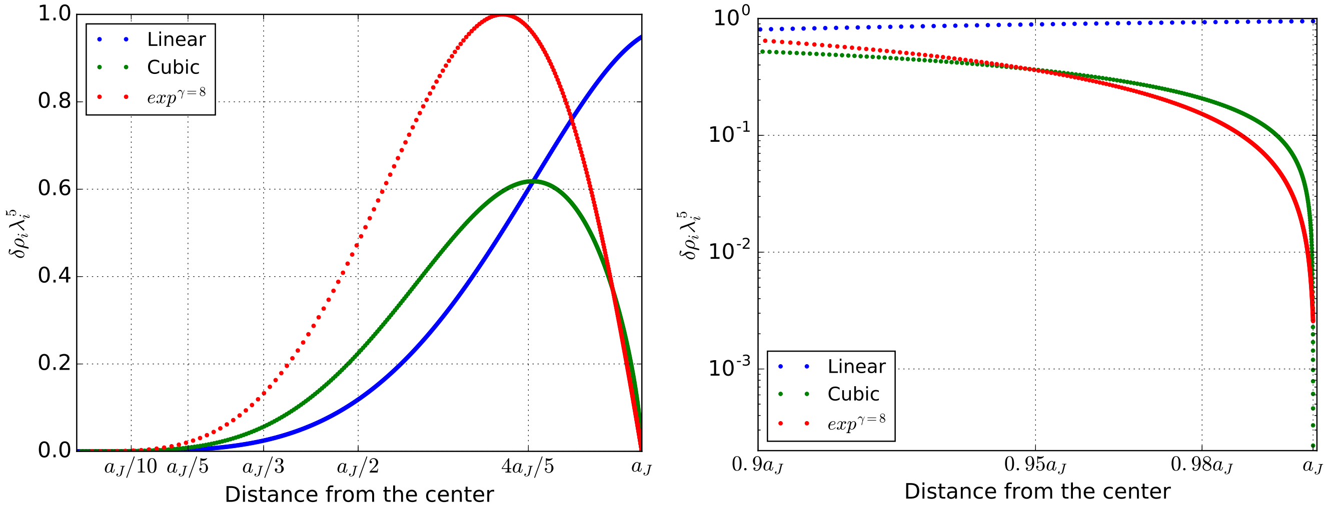

(a)

(b)

Figure 3.7: Normalized value of $\delta\rho_i\lambda_i^5$ as a function of altitude for linear, cubic and exponential ($\gamma = 8$) repartitions of spheroids. (a) From center to exterior; (b) zoom on the external layers

As seen, the linear spacing is much less precise than the other ones in the external layers because of the very small number of layers; it will thus greatly enhance the numerical errors. The cubic spacing is much better but has so many points in the outermost layers that it is oversampling the extremely high part of the atmosphere. The exponential spacing is the worst one in the lower part of the envelope (see Figure 3.7), but provides a nice cut-off between linear and cubic spacings in the uppermost layer region.

An appealing solution would be to take a combination of all these spacings to always have the most optimized one in each region of the planet. We have tried this, with a great number of spheroids, and the conclusion remains the same: the limiting effect on the total errors is the precision on the external layers (above $\sim 95\%$ of the radius). Having simply an exponential repartition of spheroids throughout the whole planet or the same exponential in the high atmosphere and then a cubic repartition when this latter becomes more precise, and then square and linear repartitions (such a repartition almost doubles the number of spheroids) yield eventually the same error. To obtain results within Juno's precision (see Figures 3.5 and 3.6), we need the external layers to be smaller than 1 km.

To conclude this section, we want to stress that the main limiting factor in the CMS method is the number of spheroids in the outmermost layers (above $\sim 0.95 \times a_J$) and the proper evaluation of their densities. If we do not want to impose a first layer with 0 density, with consequences not predictable in general cases, we must be able to describe this region of the planet with sufficiently high accuracy. This requires an optimized trade-off between the number of spheroids in the external layers and the value of the smallest densities. As shown in §3.4.3, the treatment of these layers in the CMS method is the largest source of error in the derived physical quantities of the planet.

One could argue that if the outermost layers can not be adequately described by an eos, a direct measurement of their densities would solve this issue. Unfortunately, beside the fact that, by construction, Mac Laurin spheroids imply constant density layers, there is an additional theoretical challenge: in the high atmosphere, the hydrostatic balance barely holds. The isopotential surfaces are not necessarily in hydrostatic equilibrium, as differential flows are dominating. The time variability in these regions is an other problematic issue. At any rate, the treatment of the high atmospheric layers is of crucial importance in the CMS method, because it determines the structure of all the other spheroids. An error in the description of these layers will propagate and accumulate when summing up the spheroids inward, yielding eventually to large errors. In Section 3.5, we examine the solution used in Wahl et al. [2017] to overcome this issue.

3.3.3 1 bar radius and external radius

So far, Jupiter outer radius in the calculations has been defined as the observed equatorial radius at 1 bar, $R_{1\text{bar}} = 71492$ km (see Table 1). A question then arises: does the atmosphere above 1 bar have any influence on the value of the gravitational moments?

When converging numerically the radius at 1 bar to the observed value, we obtained a value for the outer radius $R_{ext} = 71505$ km. Integrating Eq.(3.5) from $R_{1\text{bar}}$ to R_{ext} by considering a constant density equal to the 1 bar density, with the simplifications of Appendix A.1, yields a contribution of the high atmosphere $J_{2_{<1bar}} \times 10^6 \simeq 1 \times 10^{-2}$.

It thus seems reasonable to use the 1 bar radius as the outer radius with the current Juno's error bars. In §3.5, however, we examine in more detail this issue and quantify the impact of neglecting the high atmosphere layers in the calculations, as done in Wahl et al. [2017]. In the next section, we now examine if the conclusions of §3.3 still hold when using a realistic eos.

3.4 Calculations with a realistic equation of state

We recall that the aim here is not to derive the most accurate Jupiter models or to use the most accurate eos, but to verify (i) under which conditions is the CMS method appropriate in Juno's context, (ii) which spheroid repartition, among the ones tested in the previous sections, is reliable when using a realistic eos to define the barotropes, and (iii) whether the high atmosphere is correctly sampled to induce negligible errors on the moment calculations. For that purpose, we have carried out calculations with the Saumon, Chabrier, Van Horn eos (1995, SCvH). This eos perfectly recovers the atomic-molecular perfect gas eos, which is characteristic of the outermost layers of the planet

(Saumon et al. [1995]).

3.4.1 Impact of the high atmospheric layers on the CMS method

Concerning the last of the three aforementioned questions, the SCvH eos yields much better results than the polytrope. The polytropic densities in the high atmosphere are much larger than the realistic ones, yielding an overestimation of the contribution of the external layers. Figure 3.8 illustrates the contribution to J_2 of the outermost spheroids with the SCvH eos. Even though, as mentioned earlier, the very concept of an equilibrium equation of state becomes questionable at such low densities ($P < 100$ Pa $= 10^{-3}$ bar corresponds to $\rho < 10^{-3}$ kg m^{-3}), this clearly illustrates our purpose.

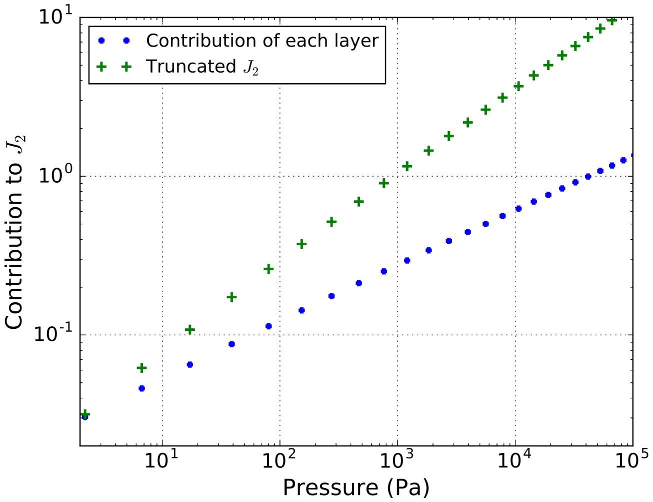

Figure 3.8: Contribution of each spheroid to the total value of $J_2 \times 10^6$ and to the truncated $J_2 \times 10^6$, i.e., the sum of the contributions of the layers from 1 to 10^{-5} bar, for a square spacing with the SCvH eos with 1500 spheroids.

Figure 3.8 shows that, when using a realistic perfect gas eos, using only 1 spheroid up to 10^{-3} bar seems to be adequate to fulfill Juno's constraints. Unfortunately, the real problem is more complex: if we use only one spheroid of 8 km (a few 10^{-3} bar) as a first spheroid, even though its own influence is indeed negligible, as if we divide it into many spheroids, the total value of $J_2 \times 10^6$ is changed by $\sim 1 - 2$, ten times Juno's error ! The reason is that the whole density profile within the planet is modified by the inaccurate evaluation of the first layers. Indeed, remember that the CMS method decomposes the planet into spheroids of density $\delta\rho$. Therefore, a wrong evaluation of the first layers is propagated everywhere since the density at one level is the sum of the densities of all spheroids above that level. We verified that any change in the size of the first layer, from less than 1 km to 35 km significantly changes the value of J_2.

We have also tried a solution where we converged the 1 bar radius to the observed $R_{1\text{bar}}$ value, in order to avoid this modification in the structure, but the result still holds: it is not possible to reduce the global contribution of the first layers, and the densities of the first layers are too small to be realistically described by an equilibrium equation of state. Clearly, with the CMS method, it is not possible to diminish the size of the first layers without significantly affecting the gravitational moments. This, again, is examined in detail in §3.5.

Table 3.3 gives the results for an exponential repartition of 1500 spheroids using the SCvH eos, with no core (in that case, the size of the first layer is 0.6 km). Clearly, varying the size of the first layers yields changes of the J_2 value larger than Juno error bars. A quadratic repartition yields similar results with differences on $J_2 \times 10^6$ that are $< 3 \times 10^{-1}$. It is not clear, however, whether the induced errors stem from the iterative calculations of the pressure from the hydrostatic equation or from the error on the potential determination. Therefore, we confirm with a realistic eos the results obtained in Section 3.3.2: a very accurate evaluation of the first layers is mandatory in order to properly converge the CMS method.

Table 3.3: Value of $J_2 \times 10^6$ for an exponential $\gamma = 7$ spacing with 1500 spheroids and the SCvH eos with no core. Left column: the outer radius is taken as Jupiter's radius; right column: the radius at 1 bar is taken as Jupiter's radius

First layer(km)	$J_2 \times 10^6$	
	R_{ext} =71492km	R_{1bar} =71492km
0.6 (unchanged)	14997.24	15046.34
3	14999.03	15046.71
6	15001.11	15047.46
15	15012.00	15051.85
35	15035.41	15061.54

3.4.2 Errors arising from a (quasi) linear repartition

In order to assess quantitatively the errors arising from an ill-adapted repartition of spheroids, we have carried out 3 test calculations. One without a core, where we changed the H/He ratio (i.e., the helium mass fraction Y) to converge the CMS method (as explained in HM16, that means having a factor $\beta = 1$ in H13). A second one where we imposed Y and the mass of the core but allowed the size of the core to vary (we have verified that imposing the mass or the size leads to the same results). And, finally, one where Y and the mass of the core could change and we converged J_2 to the observed value. These models were not intended to be representative of the real Jupiter but to test the spacings of the CMS explored in the previous sections. All these tests used the observed radius as the outer radius, $R_{eq} = 71492$ km. The results are given in Table 3.4.

The difference on $J_2 \times 10^6$ between the square and exponential spacings with 1500 spheroids are $< 2 \times 10^{-1}$, as expected from Figures 3.5a and 3.6a. In contrast, the HM16 method, which is linear in Δr, though with a different spacing in the high and low atmosphere, respectively, leads to differences 100× larger. These values were obtained

Table 3.4: Difference between square, exponential $\gamma = 7$ and HM16 spacing for 3 different tests with 1500 spheroids.

Moment	Test 1: no core			Test 2: Y = 0.37, M_c= $4M_T$			Test 3: fit on J_2		
	Square	$\text{Exp}^{\gamma=7}$	HM16	Square	$\text{Exp}^{\gamma=7}$	HM16	Square	$\text{Exp}^{\gamma=7}$	HM16
$J_2 * 10^6$	14997.42	14997.24	15025.89	14636.63	14636.47	14680.96	14696.51	14696.51	14696.51
$-J_4 * 10^6$	604.21	604.19	606.49	586.44	586.42	589.47	589.21	589.21	590.08
$J_6 * 10^6$	35.79	35.79	35.99	34.62	34.62	34.87	34.80	34.80	34.90

with a HM16 spacing with 1500 spheroids; with 512 spheroids the differences from square and exponential are a factor ten larger. This demonstrates that the square and exponential repartitions remain consistent, confirming the results obtained for the polytropic case, whereas the HM16 spacing diverges completely. As expected, the idea of using a first half layer of zero density fails when using a realistic eos.

Another proof is the difference, with the HM16 repartition, between 512 and 1500 spheroids: in the polytropic case the difference on $J_2 \times 10^6$ was found to be around 2×10^{-1}. Indeed the HM16 repartition with 512 spheroids led to results very close to the theoretical value. In our first test case, the value of $J_2 \times 10^6$ we obtained for the HM16 spacing with 512 spheroids is 15075.52. When we compare to Table 3.4, the difference is 5×10^1: the discretization error on the gravitational moments with this spacing is way off Juno's precision. Moreover, we see that the order of magnitude of the error is similar to the one in the linear case of Figure 3.4. Indeed, if one does not use a polytrope, the HM16 spacing behaves as badly as a linear spacing, as expected from the quasi linear shape of this repartition.

Figure 3.9 summarizes graphically the uncertainties arising from using an ill adapted repartition of spheroids. As stated above, the errors on J_2 from the bad handling of the high atmosphere reach almost 100× Juno's error bars, as shown in Figure 3.9a. On the other hand, when fitting J_2, Figure 3.9b shows that the errors on J_4 and J_6 are comparable or inferior to Juno's. Nonetheless, we show in §3.4.3 that this leads to significant changes in the physical quantities, hampering the determination of interior models in the context of Juno. These changes can be considered as negligible compared to the uncertainties on the various physical quantities in the models but they are significant when one aims at matching Juno's measurements and thus take full advantage of the Juno mission.

What we have shown so far in the present study is that the CMS method, when taking into account the entire atmosphere above 1 bar, relies on uncontrolled assumptions that can change significantly the value of J_2. The whole purpose of the method, however, is to constrain with high precision Jupiter's internal structure (mass fraction of heavy elements, mass of the core ...). Therefore, we need to assess the impact of these assumptions on such quantities.

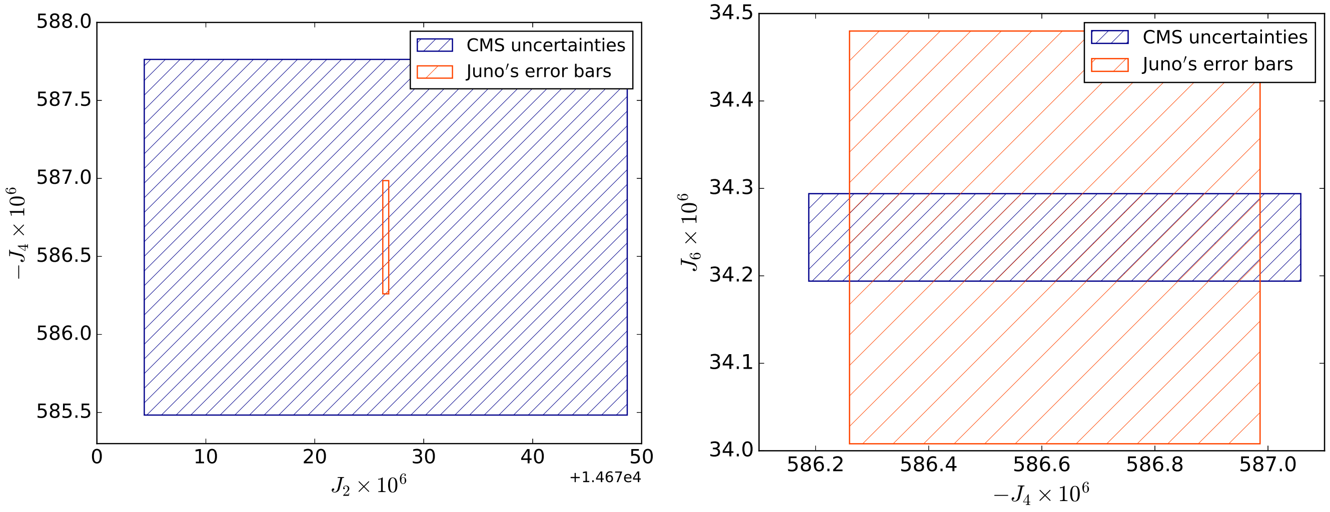

(a)

(b)

Figure 3.9: Comparison of the errors of the CMS method from quadratic and HM16 repartitions with Juno's error bars, shifted to be centered on the observed J_n. (a) $-J_4 \times 10^6$ vs $J_2 \times 10^6$ from test 1; (b) $J_6 \times 10^6$ vs $-J_4 \times 10^6$ from test 3, when J_2 is fit.

3.4.3 Intrinsic uncertainties on the Jupiter models

In this section, we derive interior models that match both J_2 and J_4 from the first Juno data (Bolton et al. [2017]) and determine how they are affected by the number of spheroids and their repartition. Ideally, one would like the final models not to depend on the method used to derive them. We recall that the purpose of this chapter is not to derive the most accurate Jupiter models but to determine the impact of the uncertainties in the CMS method upon these models, in the context of the Juno mission. Therefore, we used the SCvH eos with an effective helium mass fraction (Y′) which includes the metal contribution (see Chabrier et al. [1992]). We supposed that the core was a spheroid of constant density $\rho_{core} = 20000$ kg m^{-3}, the typical density of silicates at the pressure of the center of Jupiter. At 50 GPa, we imposed a change in the effective Y′ at constant temperature and pressure, thus a change in entropy, to mimic either an abrupt metallization of hydrogen or a H/He phase separation. Inward of this pressure, the value of the effective helium mass fraction is denominated Y_2'. All the models were converged to the appropriate J_2 and J_4 values with a precision of 10^{-8}, within Juno's error bars.

Table 3.5 gives the values of Y', Y_2' and the core mass for different repartitions and numbers of spheroids. We considered a quadratic repartition with an unchanged first layer or with a first layer of 10 km, and the HM16 repartition. With HM16, the change on the effective helium mass fraction is of the order of 5%, consistent with the expectations from the results of the previous sections. This confirms that the HM16 repartition of spheroids is not suitable to exploit Juno's data. When we used the Y' and core mass fraction obtained with 512 spheroids to a case with 1500 spheroids, the value of $J_2 \times 10^6$ became 14647.9, which leads to an error of 5×10^1, a hundred times Juno error bars.

Table 3.5: Effective helium mass fraction above (Y$'$) and underneath (Y_2') the entropy jump, and mass of the core (M_c in units of $10^{24}kg$) for different repartitions and numbers of spheroids. Quadratic is a power law spacing of exponent two, Quadratic 10 is the same with a first layer of 10 km and HM16 corresponds to the repartition used in Hubbard and Militzer [2016].

N		Quadratic	Quadratic 10	HM16
512	Y$'$	0.34622	0.34451	0.32297
	Y$'_2$	0.37379	0.37368	0.37215
	M_c	9.9241	9.8952	9.6819
800	Y$'$	0.34698	0.34496	0.33168
	Y$'_2$	0.37386	0.37372	0.37276
	M_c	9.9227	9.8928	9.7677
1500	Y$'$	0.34742	0.34506	0.33840
	Y$'_2$	0.37390	0.37372	0.37323
	M_c	9.9193	9.9000	9.8453

With the quadratic repartition, using the values obtained with 512 spheroids in the 1500 spheroid calculations yields an error on $J_2 \times 10^6$ of 4×10^0, ten times Juno's error bars (which confirms the necessity to use at least 1500 spheroids and this type of repartition). When correctly fitting J_2 and J_4 with this repartition, the change on Y' from 512 to 1500 spheroids is about 0.5 %, about the same as the difference between using a $<$ 1 km or a 10 km first layer. For the core mass, increasing the number of spheroids is useless as the difference is negligible compared to the one due to changing the size of the first layer. Therefore, the uncertainties due to the description of the first layers are the dominant sources of limitation in the determination of Jupiter's physical quantities like Y' or the core mass fraction.

In reality, the limitation is even more drastic. First, with a 10 km first layer, the outer density is $\simeq 3 \times 10^{-3}$ kg m^{-3}. This is too low to use an equilibrium equation of state. If we use instead a 20 km first layer, increasing the density to more acceptable values, the uncertainties on Y' are about 1-2% and $>$ 5% on M_c . Virtually any model leading to such an uncertainty can fit J_2 and J_4. Indeed, given the impact of the first layers on the gravitational moments, they could be used, instead of Y' and M_c, as the variables to fit models with the appropriate gravitational moments. Slightly changing these layers (mean density, size,..) can yield adequate models. Therefore, no model can be derived within better than a few percent uncertainties on Y', thus the heavy element mass fraction, and on the core mass.

The calculations carried out in this section yield three major conclusions:

1. It is not possible to use a linear repartition, especially with a zero density first layer, as the values of the

moments would be changed by 100× the value of Juno's error bars when increasing the number of spheroids.

2. The results obtained with a square or an exponential repartition with 1500 spheroids yield consistent errors, no matter the size of the first layer, and can thus be considered as reliable spheroid repartitions. The size of the first layer, however, remains the major source of uncertainty in the CMS method when taking into account the high atmosphere above the 1 bar level.

3. When deriving appropriate internal models of Jupiter, the CMS method such as used in HM16 can not allow the determination of key physical quantities such as the amount of heavy elements or the size of the core to better than a few percents. Changing the size and/or density distribution of the first layers yields a significant change in the values of the gravitational moments. This degeneracy unfortunately hampers the derivation of very precise models.

In the light of these conclusions, the CMS method, such as used so far in all calculations, needs to be improved. To do so, Wahl et al. [2017] propose to neglect the high atmosphere, and define the outer boundary at the 1 bar level. We examine this solution in the next section.

3.5 Taking the 1 bar level as the outer boundary condition

3.5.1 Irreducible errors due to the high atmosphere region (less than 1 bar)

According to their second appendix, Wahl et al. [2017] impose the 1 bar level as the outer boundary condition in their CMS calculations. As shown with a polytropic eos in §3.3.2, the atmosphere above this level, called here the high atmosphere, has a contribution to $J_2 \times 10^6 \simeq 1 \times 10^{-2}$. With a realistic eos, converging the 1 bar radius on the observed value yields a high atmosphere depth of ~ 70 km but a smaller outer density than the polytrope. The contribution to J_2 is then about the same.

The high atmosphere, however, also alters the evaluation of the potential inside the planet and thus the shape of the spheroids in the CMS method. In Appendix A.4, we evaluated the first order neglected potential ϕ_{neg} on each spheroid due to the omission of the high atmosphere. We showed that it is a constant value, which does not depend on depth or angle:

$$\phi_{neg} \simeq 2.87 \times \frac{GM}{a_{1bar}} \left(\frac{\rho_{ext}}{\bar{\rho_S}}\right) \left(\frac{\Delta a}{a_{1bar}}\right), \tag{3.24}$$

where ρ_{ext} is the (constant) density of the high atmosphere, $\bar{\rho_S}$ is the mean density of Jupiter if it was a sphere of radius $a_{1bar} = 71492$ km, and Δa is the depth of the high atmosphere.

As mentioned above, $\Delta a \simeq 70$ km and we know that $\bar{\rho_S} \simeq 10^3$ kg m^{-3}. Taking the outer density in a range $(0.01 - 1) \times \rho_{1bar}$, and the conditions of Jupiter, $\rho_{1bar} \simeq 0.17$ kg m^{-3}, yields:

$$\phi_{neg} \in [5 \times 10^{-9}; 5 \times 10^{-7}] \times \frac{GM}{a_{1bar}}. \tag{3.25}$$

This is clearly a first order correction since the potential on each spheroid, given by the CMS method, ranges from GM/a_{1bar} in the outermost layers to $2GM/a_{1bar}$ inside.

The neglected potential does not depend on the layer, so the hydrostatic assumption (using the gradient of the potential) remains valid. The main source of change comes from the shapes of the spheroids. We calculated the impact of this change in Appendix A.4 with the use of equation (40) of H13 and obtained the following result:

$$\frac{\Delta J_{2,0}}{J_{2,0}} \simeq 287 \times \left(\frac{\rho_{ext}}{\bar{\rho_S}}\right)\left(\frac{\Delta a}{a_{1bar}}\right). \tag{3.26}$$

Within the above range of outer densities we get:

$$\frac{\Delta J_{2,0}}{J_{2,0}} \in [5 \times 10^{-7}; 5 \times 10^{-5}]. \tag{3.27}$$

Since the potential is smallest in the outside layers, we expect the relative change in $J_{2,i}$ of the i^{th} spheroid to decrease with depth. Nevertheless, we have seen that the CMS method requires a large number of spheroids in the high atmosphere (a point which is validated in the next section). We thus expect the change in the $J_{2,i}$ in the outer layers, which have the largest impact on J_2, to be comparable to Eq.(3.27).

If we make the bold assumption that every layer contributes equally and choose for the outer density $\rho_{ext} = 0.03$ kg m^{-3}, which is the value that corresponds to mass conservation in the high atmosphere, we get:

$$\Delta J_2^{ext} \times 10^6 \simeq 8 \times 10^{-6}(J_2^{ext} \times 10^6) \simeq 1 \times 10^{-1}. \tag{3.28}$$

This is approximately 1/2 Juno error bars. Even though this relies on several assumptions, mainly that we can approximate the outer layers by a constant density spheroid and that the error is the same on each spheroid, it gives a reasonable estimate of the impact of neglecting the high atmosphere on J_2.

From the evaluation of J_4 and J_6 in Appendix A.4, we calculated that:

$$\Delta J_4^{ext} \times 10^6 \simeq 6 \times 10^{-2}, \tag{3.29}$$

$$\Delta J_6^{ext} \times 10^6 \simeq 2 \times 10^{-2}. \tag{3.30}$$

We see that the agreement with Juno's error bars improves with higher order moments, although it stabilizes around 10^{-2} from J_6 onward. In order to derive physical information from the high order moments, however, one needs to have confidence in the evaluation of the first moments. Moreover, these estimations rely on many assumptions and give only orders of magnitude.

As in Figure 3.9, we show graphically these uncertainties in Figure 3.10. We see that we are now able to reach Juno's precision, but the analysis of future, more accurate data will remain limited by these intrinsic uncertainties.

If we were able to perform rigorously the calculations of Appendix A.4, we would probably find that the errors on the J_n's are correlated, decreasing the aforederived uncertainties. Unfortunately, a rigorous derivation of these errors would require to relax many assumptions and would imply very complicated theoretical and numerical calculations. Until this is not done, the determination of the J_n are inevitably blurred by the neglected potential, up to half Juno's error bars, as shown in Figure 3.10.

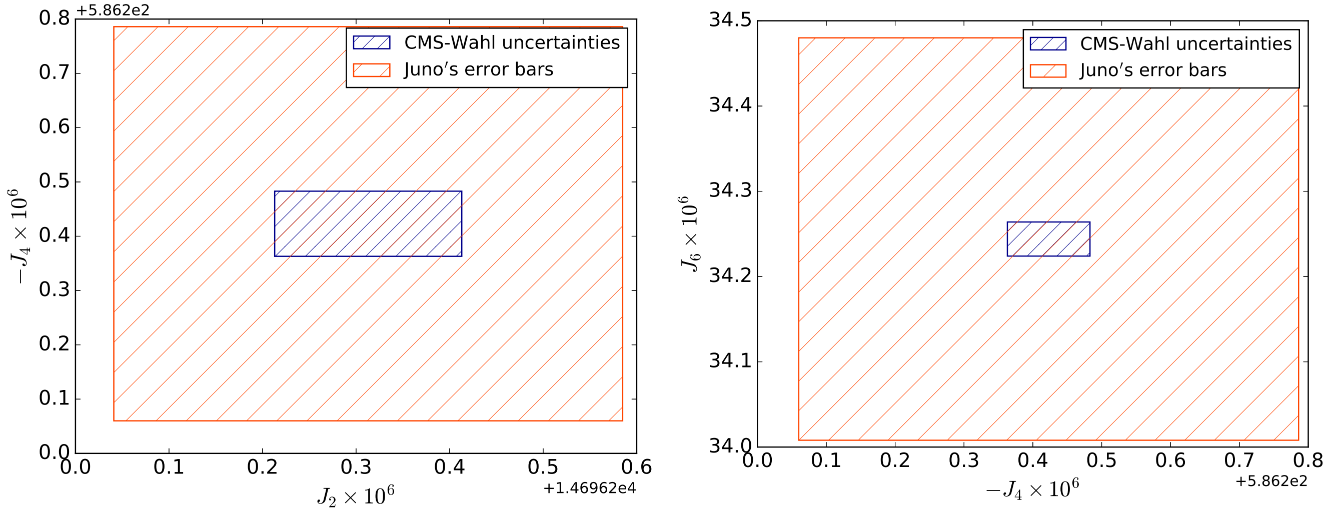

(a)

(b)

Figure 3.10: Comparison of the errors of the CMS arising from neglecting the high atmosphere with Juno's error bar, shifted to be centered on the observed J_n. (a) $-J_4 \times 10^6$ vs $J_2 \times 10^6$; (b) $J_6 \times 10^6$ vs $-J_4 \times 10^6$.

In conclusion, we have shown in this section that the neglected potential due to the high (<1 bar) atmosphere region leads to an error of about half Juno error bars. Globally, neglecting the atmosphere above 1 bar in the CMS method leads to an irreducible error on $J_2 \times 10^6$ of the order of 10^{-1}. Although such an error level is smaller than Juno's present precision, this will become an issue if the precision improves further.

It must be stressed that this irreducible error is not arising from uncertainties in any physical quantity, such as for example the radius determination or the eos. It stems from neglecting the high atmospheric levels in the CMS method itself, and in that regard cannot be removed; indeed, as we have shown in the previous sections, including the high atmosphere leads to huge uncertainties. Said differently, even with a perfect knowledge of Jupiter radius, internal eos, etc., the error, intrinsically linked to the method, remains. Semi analytical integrations show that, globally, this error is of the order of 10^{-2} for higher order moments. Therefore, the $J_k \times 10^6$ cannot be determined within better than a few 10^{-2}. On J_{10} and higher order moments, in particular, this error can be close to the order of magnitude of the moments themselves. One must keep that in mind when calculating values of these moments with the CMS method, as in Wahl et al. [2017].

3.5.2 Error from the finite number of spheroids

Now that we have estimated every possible source of error and showed that the method used by Wahl et al. [2017] is applicable with the current error bars of the Juno mission, we need to examine how the uncertainties depend on the number of spheroids and verify whether the conclusions of §3.3 are affected or not by the change of outer boundary condition. Figure 3.11 displays the dependence of the error upon the number of spheroids for different spheroid repartitions in the present case.

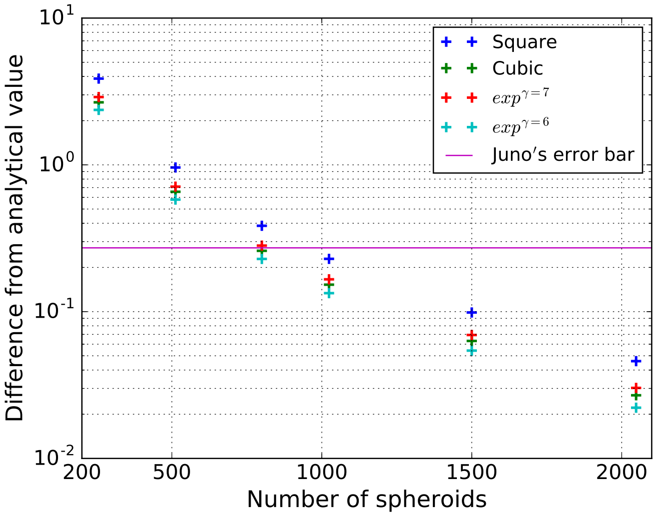

Figure 3.11: Numerical error as a function of the number of spheroids when neglecting the high atmosphere for a polytropic eos.

Interestingly, the exponential $\gamma = 6$ repartition happens to provide the best match to the analytical results. More importantly, we show that some of the different repartitions give the same results, a mandatory condition to use the method with confidence with a realistic eos, as mentioned earlier.

We see, again, that 512 spheroids are not enough to satisfy Juno's precision. As mentioned previously, even though the CMS values are precise at 10^{-13}, the discretization error dominates. Depending on the spheroid repartition, this error can become quite significant. Unfortunately, Wahl et al. [2017] do not mention which spheroid repartition they use exactly. As shown in the Figure, however, this needs to be clearly specified when deriving Jupiter models in the context of Juno to verify their validity.

When neglecting the high atmosphere, the calculations are not hampered by any degeneracy due to the first layers since the densities, which are larger than $\rho_{1bar} \simeq 0.17$ kg m^{-3} are well described by the eos. Therefore, the only errors on the derived quantities of interest come from the discretization errors. As in §3.4.3, we give in Table 3.6 the values of Y', Y_2' and M_c obtained when matching J_2 and J_4 in the same conditions. One might notice that these results are different from the ones in Table 3.5; this is only due to the fact that in Table 3.5 the outer radius is 71492 km, instead of the radius at 1 bar. We checked that if the external radii are consistent, the derived physical quantities are within the range of uncertainties of §3.4.

The differences from 512 to 1500 spheroids are of the order of 0.3% on the physical quantities. Because of the

Table 3.6: Same as Table 3.5 when neglecting the high atmosphere.

N		Quadratic	Cubic
512	Y′	0.3210	0.3211
	Y'_2	0.372001	0.372015
	M_c	9.6849	9.6709
1500	Y′	0.3218	0.3218
	Y'_2	0.372098	0.372090
	M_c	9.6546	9.6624

Table 3.7: Same as Table 3.6 except that $J_2 \times 10^6$ and $J_4 \times 10^6$ have been changed by $\pm 1 \times 10^{-1}$. +1-1 means that we add 1×10^{-1} on J_2 and remove it from J_4, -1+1 is the opposite.

N		Cubic +1-1	Cubic -1+1
512	Y′	0.3212	0.3225
	Y'_2	0.372155	0.372024
	M_c	9.5297	9.8015
1500	Y′	0.3212	0.3225
	Y'_2	0.372149	0.372022
	M_c	9.5374	9.8053

degeneracy of models leading to the same external gravitational moments (by e.g., changing the pressure of the entropy jump, the amount of metals, etc..) we do not expect to derive a unique model with such a precision on the core mass, so, in this context, 512 spheroids can be considered as sufficient to derive accurate enough models of Jupiter. When using the physical quantities obtained with 512 spheroids in calculations done with 1500 spheroids, we get an error on $J_2 \times 10^6$ of ~ 1, 10× Juno error bars. Therefore, even though one can derive a precise enough model with 512 spheroids, it is highly recommended, as a sanity check, to verify with 1500 whether Juno precision can be reached with only a slight change of the derived physical quantities.

We still have to evaluate the errors coming from neglecting the high atmosphere. To evaluate the largest possible uncertainty, we added 1×10^{-1} to $J_2 \times 10^6$ and removed it from $J_4 \times 10^6$. We stress again that this must be done because the value of both J_2 and J_4 can not be trusted under the aforederived intrinsic irreducible error of the method, due to the omission of the high atmosphere, even when fitting to observed values at much higher precision. The results are given in Table 3.7. The differences between Table 3.6 and 3.7 show that neglecting the high atmosphere yields an uncertainty on the physical quantities of a few parts in a thousand, even up to 2 to 3% on the core mass.

This is the irreducible error of the CMS method when neglecting the levels of the high atmosphere (<1 bar). An improvement in the precision of Juno cannot change this uncertainty. In that regard, using more than 1500 spheroids would be a second order correction on the method uncertainty.

3.6 Conclusion

In this chapter, we have examined under which configuration the CMS method can be safely used in the context of the Juno mission. We have first derived analytical expressions, based on a polytropic eos, to evaluate the errors in the calculation of the gravitational moments with the CMS method in various cases. These analytical derivations relied on simplifying approximations and thus represent lower limits of the errors. When applied to calculations based on 512 spheroids, as done for instance in the works of Hubbard and Militzer [2016] these expressions show that it is not possible to match the Juno's constraints because of the discretization error. To verify the analytical calculations, we have developed a code based on the method exposed by Hubbard [2013]. The numerical calculations confirmed the analytical results and also showed that the external layers of the planet have a huge impact of the determination of J_2 and need to be described with very high accuracy. At first, this appeared to be the biggest limitation of the CMS method: for a precise evaluation of the gravitational moments of Jupiter, this method requires layers in the high atmosphere smaller than 1 km. However, this implies densities so low that the very concept of an equilibrium equation of state to describe these layers becomes questionable, while density profiles fit from observations would not solve this issue (as explained at the end of §3.3.2).

We have shown, with a polytrope $n = 1$, that one needs a quadratic or exponential repartition of at least 1500 spheroids to reach precise enough values of the moments to match Juno's constraints, which implies densities of the order of a few 10^{-2} kg m^{-3} for the outermost layers. With such specifications, the CMS method can in principle reach precisions better than Juno's uncertainties.

When these calculations are performed numerically with barotropes prescribed from an appropriate eos for the external layers, the above conclusions were confirmed: the CMS method requires a square, cubic or exponential spacing of at least 1500 spheroids. None of these calculations, however, was able to get a satisfying description of the first layers. Indeed, even though each of these individual layers contributes negligibly to J_2, a small change in the density structure of these regions leads eventually to unacceptable changes in the total value of J_2. Furthermore, when fitting J_2 and J_4, we have shown that the description of these layers leads to a degeneracy of solutions which hampers the determination of physical quantities such as the heavy element mass fraction or the mass of the core to better than a few percents.

In order to overcome this issue, Wahl et al. [2017] propose to neglect the high atmosphere and impose the 1 bar pressure as an outer boundary condition. We have evaluated the errors coming from this assumption, and showed that they are of the order of half Juno error bars. In principle, the CMS method with this boundary condition can thus be applied to derive Jupiter models within the precision of Juno from Bolton et al. [2017], with an irreducible uncertainty arising from the neglected high atmosphere. This uncertainty is of the order of 0.1 on $J_2 \times 10^6$. The remaining sources of errors on the physical quantities, however, stem from discretization errors, and 512 spheroids can give results with a precision of a few parts of a thousand. Considering the degeneracy of models that could fit with Jupiter's observed gravitational moments, this can be considered as an acceptable uncertainty. However, we show that, due to the aforementioned irreducible error of the method, increasing Juno precision will not enable us to derive more precise models. Therefore, when deriving interior models of Jupiter, it is not realistic to reproduce the observations of Iess et al. [2018] within their error bars. Quantitatively, the irreducible errors yield global uncertainties on the physical quantities derived in a model close to 1%.

The conclusion is that the Concentric MacLaurin Spheroid method such as used in HM16 could not satisfy Juno's constraints and needed to be improved to derive accurate enough Jupiter model. First, a larger number of spheroids with a better repartition is mandatory. Second, there is no satisfying solution to safely take into account the impact of the high atmosphere region above 1 bar. We have shown that imposing the 1 bar radius as the outer boundary condition, as done in Wahl et al. [2017], is acceptable, although it leads to irreducible errors of a few parts of a thousand on the derived physical quantities, increased by an eventual discretization error. Although such a precision can be considered as satisfactory, given all the other sources of uncertainty in the input physics of the model, this shows that the observations have already reached the maximum precision of the CMS method in its current form.

Chapter 4

New models of the interior of Jupiter

> *There was a solid rocky core to the planet, a spherical mass of about ten Earth-sized planets buried under seventy thousand vertical kilometres of hydrogen, helium and ice, and there were purists who would call the transition region between that stony kernel and the high-temperature, highpressure water ice above it the planet's surface. But you had to be a real nit-picker even to pretend to take that definition seriously. Beyond the water ice - technically ice [...] but at over twenty thousand degrees, confusingly hot for the human image of what ice was supposed to be like – came over forty thousand vertical kilometres of metallic hydrogen, then a deep transition layer to the ten-kilo-klick layer of molecular hydrogen which, if you were of an especially imaginative turn of mind, you might term a sea.*
>
> *Ian M. Banks* - The Algebraist

WITH the method presented in the previous chapter, we are able to construct models of the interior of Jupiter with precision comparable to what was required from the Juno spacecraft after three orbits (as we will see in this chapter, this precision is anyway limited by physical uncertainties). The next step is to understand the physical processes at stake in the interior of the planet, in order to derive structures as physically motivated as possible, with the observational data as a guide to constrain our structure and not the departure point of our models.

With almost no observational resources, only the knowledge of the Kepler laws and a small telescope, one can infer the mass, the radius and eventually the oblateness of Jupiter. From these quantities, a mean density can be estimated, of the order of 1300kg.m^{-3}. Such a low mean density compared to the pressure that exists in the center of the planet can only be explained by a composition dominated by light elements, and particularly hydrogen. Although liquid in the interior of the planet, the very low mean density of Jupiter compared to terrestrial planets and the high extent of the gaseous layers due to the high abundance of hydrogen and helium gave to these planets the name of "gas giants". This simple view can be pushed a bit forward, but gaining knowledge on the interior of Jupiter needs further observational and theoretical resources. Therefore, during the twentieth century, the knowledge of the interior of Jupiter improved step by step with the refinement of observations and theoretical physics, towards the global understanding of the planet we have nowadays.

In this chapter, we will present our new models of Jupiter in the context of Juno and Galileo, submitted for revision in the Astrophysical Journal. We first explain historically what brought us to our current knowledge of the planet in section 4.1. We then expose the method and the different physical inputs of our models in Section 4.2. In Section 4.3, we demonstrate the need to have several different regions in Jupiter's interior by exploring different simple models and showing that they fail to reproduce the observations. In Section 4.4, we show that a locally *inward decreasing abundance of heavy elements* in the Mbar region is the favored solution to resolve this discrepancy. We explore in details the possibility to have such an element distribution.

In Section 4.5, we present our final series of models. We first show that, without the presence of a sharp entropy increase somewhere within the gaseous envelope, the values of J_6 to J_{10} are too large compared with Juno's ones, which implies to invoke an unplausibly large amount of differential rotation. Indeed, a strong entropy increase in the region of hydrogen metallisation (around 1 Mbar) yields higher internal temperatures, allowing a larger amount of heavy elements in the central region (§4.5.2). This in turn affects the high order gravitational moments and enables us to derive Jupiter models which satisfy both the Juno and Galileo observational constraints. We examine in detail the possible physical mechanisms leading to this type of internal structure and discuss their implications for the physics of hydrogen pressure ionization. In Section 4.6, we summarize and examine the validity of the major physical assumptions that have been made throughout this chapter. Section 4.7 is devoted to the conclusion.

4.1 A brief history of Jupiter

In the twentieth century, our understanding of the structure of Jupiter has dramatically improved. This improvement was due to two main reasons: theoretical advances on the physical properties of hydrogen and helium under Megabar pressures and unprecedented observations of the planet. In 1924, Menzel et al. [1926] carried out the first survey of Jupiter in a radio band, in a gap of the water spectrum in the Earth's atmosphere. This work allowed to measure the effective temperature of Jupiter around 130K. Assuming a grey atmosphere, hence an absorption that does not depend on the wavelength, one could show that the effective temperature if Jupiter only radiated away the energy absorbed by the sun would be close to 109K. Necessarily, Jupiter must possess an inner source of power, which accounts for around 60% of the observed luminosity of the planet: Jupiter alone produces more energy that it receives from the sun. However, the radio band is a limited observation of the planet, and it was only forty years later, with infrared observations, that the luminosity excess was linked to an internal source of energy.

During these forty years, many models have tried to couple the mass and radius of the planet, known for centuries, and the theoretical knowledge in the physics of hydrogen. A few works have had particular importance: in 1938, Wildt [1938] and Kothari [1938] independently proposed that the giant planets were probably composed of metallic hydrogen in their deeper layers, which is nowadays a certitude. The review by Öpik [1962] is an interesting read to grasp the idea of Jupiter at the beginning of the 1960's. Although a lot of our current knowledge of Jupiter has already been inferred, there are a few misthoughts led by observational or theoretical limits. On the observational side, the atmosphere of Jupiter is thought to have a dominant helium composition, in accordance with the high observed molecular weight. Additional ground and sattellite observations will change that idea in the next decade, confirming that even the atmosphere of Jupiter is dominated by hydrogen. On the theoretical side, the helium and hydrogen in the deepest part of the planet are thought to be in the solid state, which are now known to be in a liquid state in the interior of Jupiter. Of particular interest is the discussion on how to explain the high amount of helium in the atmosphere, which sets a theoretical understanding of an erroneous observation. It is a reminder that a model is only but a representation of a physical object at a given epoch, limited by observations and current knowledge of the underlying theoretical physics.

A major change happened a couple of years later, driven by the work of Peebles [1964]. Extending on the planetary model of Demarcus [1958], which was based on a modification on the current equations of state for hydrogen under the assumption of a cold interior, hence a solid hydrogen-helium interior, Peebles [1964] has shown with the first extensive use of "electronic-computer" that the interior of Jupiter and Saturn were likely to be hot, hence in a fluid state, providing constraints on their elemental abundances and first gravitational moments. Motivated by the recent infrared observations of Low [1965], that allowed to evaluate with certainty the luminosity excess of the planet, Hubbard [1968] completed the work of Peebles [1964] and have provided a thorough examination on the heat transfer processes happening in Jupiter. The conclusion, as detailed in chapter 2 section 2.2.2, is of particular importance and remains to date a strong constraint: most of the interior of Jupiter is convective. Because of the low thermal conductivity of metallic hydrogen and the strong energy flux that needs to be transported to ensure the luminosity of the planet, convection is the only viable mechanism. If adiabatic processes were already expected to be predominant in Jupiter, the work of Hubbard [1968] was the confirmation of their extent and importance in the planet.

Without a doubt, major change in our understanding of giant planets were brought by the two seminal papers of Stevenson and Salpeter in 1977 (Stevenson and Salpeter [1977a] and Stevenson and Salpeter [1977b]), which, forty years later, have still not been exploited to their full potential nor infirmed by later, more numerically and experimentally advanced studies. The first paper, Stevenson and Salpeter [1977a], details all the possible configuration that can happen in a mixture of hydrogen and helium in the conditions of a giant planet. Of particular importance is the treatment of demixtion and phase transitions, that can considerably alter the energy or entropy budget of an hydrogen-helium mixture. The second paper, Stevenson and Salpeter [1977b], applies the obtained phase diagrams to giant planets. If phase properties are determining the physical structure and evolution of a planet, gravity also has its influence. As in a glass of water and oil, the two phases separate but the lighter one will always be on top for stability. This second paper therefore considers the influence of gravity, convection, rain-out, bubble growth and stability aginst eddy disruption in giant planets for a mixture of hydrogen and helium. Amongst other conclusions, these papers provide an explanation for the high luminosity of Saturn compared to its present age with the prediction of helium "rains" inside the planet, slowing down the inner cooling.

In the two following decades, the first direct data were obtained. The Voyager and Pioneer spacecrafts flew by Jupiter a few times, gathering elemental and gravitational observations of the planet, reported in Campbell and Synott [1985]. With a thorough theoretical work on the equation of state of hydrogen and helium, now known as the Saumon-Chabrier-vanHorn (SCvH) equation of state (Saumon et al. [1995]), Chabrier et al. [1992] constructed the first multi layers models of Jupiter and Saturn, able to reproduce the two first observed gravitational moments. These models comprised two isentropic zones in the planet of separate composition, and a compact core in the center surrounded by a liquid icy core. These models have been the template for successive models of Jupiter (Fortney and Hubbard [2003],Nettelmann et al. [2012], Saumon and Guillot [2004], ...). The observations of Galileo in 1995, reanalysed by Wong et al. [2004], which sent an entry probe in the atmosphere of the planet confirmed this multi layers models: the atmospheric helium abundance is 20% smaller than the expected cosmogonic abundance (Anders and Grevesse [1989] and von Zahn et al. [1998]). In order to ensure that the composition of Jupiter is primordial, the helium content must increase somewhere inside the planet. Within the framework of these models, Saumon and Guillot [2004] were able to derive constraints on the heavy elements (defined as everything but hydrogen and helium) abundance and the mass of the core.

The 2010's have witnessed another leap in our understanding of Jupiter. Four things happened within a few years:

1. Hubbard [2012] and Hubbard [2013] have detailed a new, much more powerful way to calculate the gravitational moments of a rotating barotrope: the Concentric MacLaurin Spheroid method, as detailed in the previous chapter. Analysed in Wisdom and Hubbard [2016] and Debras and Chabrier [2018], it is both a simpler concept and a more precise method than the theory of figures that was used thus far (see the extensive work of Zharkov and Trubitsyn [1978] and the latest upgrade of Nettelmann [2017].

2. New equations of state have been derived. Although the REOS-2 [Nettelmann et al., 2012] and the equation of state from Miguel et al. [2016] have later been shown to have limitations or errors, the works of Militzer and Hubbard [2013] and Chabrier et al. [2018] notably have set a new basis for state of the art hydrogen helium equations of state in planetary conditions.

3. Leconte and Chabrier [2012] have detailed the physical mechanisms that can happen at a region of composition and entropy change inside a giant planet. Within the framework of double diffusive convection and mixing length theory (MLT), they have highlighted the possible emergence of layered convection, altering the heat transport inside the planet and other possible explanation of the luminosity of Saturn [Leconte and Chabrier, 2013]

4. The Juno spacecraft reached Jupiter, and measured the gravitational field of the planet with extreme precision (Bolton et al. [2017] and then Iess et al. [2018]). This spacecraft also observed the magnetic field (Connerney et al. [2018]) and the ammonia abundance [Li et al., 2017] as never been done before. These results allowed for first conclusions on the structure of the planet, showing the need for a diluted core (Wahl et al. [2017]), constraining the depth of the winds from the odd gravitational moments (Kaspi et al. [2018]) and the strength of differential rotation from the even gravitational moments (Guillot et al. [2018]).

The work of this thesis is incorporated within this global, thrilling and rapidly evolving environment. As shown in the previous chapter, a complete study of the method used to derive Jupiter structures was needed and has been performed in Debras and Chabrier [2018]. More generally, a few questions remain unanswered and one of the most puzzling is the discrepancy between the observations of Galileo (Wong et al. [2004]) and Juno (Iess et al. [2018]). The trouble indeed is to reconcile the low value of Juno's even gravitational moments of order 4 and more, J_4 to J_{10}, and the high value of helium and heavy elements observed by Galileo, Y_{Gal} and Z_{Gal}. The higher the order of a gravitational moment, the more sensitive it is to the outermost part of the planet. Hence, the most important physical parameters to determine the values of J_4 to J_{10}, for a given mass and J_2, are the abundances of helium and heavy elements in the external envelope of the planet. Had equations of state not been improved, this would not be an issue and Jupiter models would only need to be slightly adjusted. However, using state-of-the-art equations of state, the density of a mixture of hydrogen and helium at 1 Mbar following an isentrope from the atmospheric conditions of Jupiter is much higher, meaning that the heavy elements abundance must be sharply decreased. Therefore, it is much more complicated to adjust the density distribution inside the planet to balance the weight of the outer regions, with high abundance of heavy elements, compared to SCvH equation of state. Our work, detailed in the rest of this chapter, intends to explain this apparent discrepancy.

4.2 Method

4.2.1 Concentric MacLaurin Spheroids

Our Jupiter models are calculated with the Concentric Maclaurin Spheroid method (Hubbard [2012], Hubbard [2013]). As demonstrated in the previous chapter, in order to yield valid models, the method must fulfill several mathematical and numerical constraints, in terms of *numbers and spacing* of the spheroids and of the treatment of the outermost spheroids. Accordingly, the spheroids implemented in our calculations are spaced exponentially, their equatorial radius is $\lambda_i = 1-(\mathrm{e}^{i\beta}-1)/(\mathrm{e}^{N\beta}-1)$ with N the number of spheroids, i ranging from 0 to $N-1$, $\beta = 6/N$ and the upper atmosphere is neglected[1]. In this chapter, we seek to examine which kind of model is compatible with Juno's observations, providing the difference can be explained by the *maximum* allowed amount of differential rotation, i.e. differential rotation penetrating down to 10,000 km (see Guillot et al. [2018] and Kaspi et al. [2017]). Said differently, we want the uncertainty on the J values obtained for an acceptable model to be smaller than the one due to this maximum possible level of differential rotation. At this level, we checked that 512 spheroids yield a sufficient precision and that using 1000 spheroids or changing the β parameter does not significantly affect the conclusions. Deriving more precise models, fullfilling precisely all Juno's and Galileo's constraints with smaller levels of differental rotation, however, requires *at least* 1000 spheroids to ensure that the discretisation error is negligible compared with the other sources of error on the evaluation of the gravitational moments. The various parameters used for Jupiter throughout this work are the same than in the previous chapter, reported in Table 3.1.

4.2.2 Equations of state

Our models are based on the new equation of state (EOS) for H/He mixture recently derived by Chabrier et al. [2018], which combines semi-analytical models in the low (molecular/atomic) and high (fully ionized) temperature-density domains and quantum molecular dynamic (QMD) calculations in the intermediate pressure dissociation/ionization regime. As shown in the aforementioned paper, this new EOS fullfills all available experimental constraints and first-principle simulations and, besides pressure, density and temperature, provides the entropy, a quantity of prime importance in the present context. This EOS, however, is based on the so-called "Additive Volume Law" (AVL), which does not take into account the interactions between the hydrogen and helium species, neglecting then in

---

[1] This implies an irreducible error of the order of 10^{-7} on J_2 and a few 10^{-8}on higher order moments, which is negliglible compared to the possible impact of differential rotation (Debras and Chabrier [2018], Kaspi et al. [2017])

particular the non-ideal mixing entropy. As shown in Chabrier et al. [2018], however, the contribution of the H-He interactions, although small, becomes important for cool entropy values, such as the one characteristic of Jupiter's present adiabat. Therefore, we have combined this new H/He EOS with the simulation data points calculated by Militzer and Hubbard [2013] (MH13) in their available density-temperature domain, characteristic of the hydrogen pressure ionization regime. By construction, the MH13 simulations do take into account interactions between H and He species. We recall that the MH13 EOS recovers outside its domain of validity the SCvH EOS, as the Chabrier et al. [2018] one. As in Miguel et al. [2016], we have first calculated a pure H table by calculating, at each P-T point:

$$\begin{aligned}\frac{1}{\rho_{\mathrm{MH13}}} &= \frac{X_{\mathrm{MH13}}}{\rho_H}+\frac{Y_{\mathrm{MH13}}}{\rho_{\mathrm{He,New}}} \Rightarrow \frac{1}{\rho_{\mathrm{H}}} = \frac{1}{X_{\mathrm{MH13}}}\left(\frac{1}{\rho_{\mathrm{MH13}}}-\frac{Y_{\mathrm{MH13}}}{\rho_{\mathrm{He,New}}}\right), &(4.1)\\ S_{\mathrm{MH13}} &= X_{\mathrm{MH13}}S_{\mathrm{H}}+Y_{\mathrm{MH13}}S_{\mathrm{He,New}}+S_{\mathrm{mix}} \Rightarrow S_H = \frac{1}{X_{\mathrm{MH13}}}\left(S_{\mathrm{MH13}}-Y_{\mathrm{MH13}}S_{\mathrm{He,New}}-S_{\mathrm{mix}}\right), &(4.2)\end{aligned}$$

where ρ_H is the mass density for pure hydrogen, ρ_{MH13} the density derived from MH13 by spline procedures, $\rho_{\mathrm{He,New}}$ the helium density in the Chabrier et al. [2018] EOS, S_H the sought pure hydrogen specific entropy, S_{MH13} the splined specific entropy from MH13, $S_{\mathrm{He,New}}$ the helium specific entropy in the new EOS, all at the same (P,T), and $X_{\mathrm{MH13}} = 0.7534$, $Y_{\mathrm{MH13}} = 0.2466$ the mass fractions of hydrogen and helium in the MH13 simulations. Finally, S_{mix} is the mixing specific entropy defined as:

$$\frac{S_{\mathrm{mix}}}{k_b} = \frac{1}{M_{\mathrm{H,He}}}\left[N_{\mathrm{H}}\ln\left(1+\frac{N_{\mathrm{He}}}{N_{\mathrm{H}}}\right)+N_{\mathrm{He}}\ln\left(1+\frac{N_{\mathrm{H}}}{N_{\mathrm{He}}}\right)\right], \tag{4.3}$$

with N_{H} the number of H particles, N_{He} the number of He particles, $x_i = N_i/(N_H + H_{He})$ the number fraction of species i (H or He), $M_{\mathrm{H,He}} = \bar{A}m_H$ the total mass of H+He, $\bar{A} = \sum_i x_i A_i$ the mean atomic number and $m_H = 1.660 \times 10^{-27}$ kg the atomic mass unit. This "mixed" (Chabrier et al./MH13) pure hydrogen EOS is then combined with the new pure helium one (Chabrier et al. [2018], Soubiran et al. (in prep)) to obtain a complete EOS for the H/He mixture at any given helium mass fraction Y. For densities above $500\,\mathrm{kg\,m^{-3}}$, the pressure ionization domain in Jupiter, and temperature-pressure conditions relevant for Jupiter, we have verified that the difference between our mixed EOS and MH13 results is always $< 0.5\%$, which is less than the numerical error in MH13. It is clear that, even though the MH13 calculations do include the non-ideal H/He mixing entropy, eqns. (4.1)-(4.3) are based on the AVL mixing equations. The derivation of the pure H EOS is thus not fully consistent and not entirely satisfactory. Carrying out ab-initio QMD simulations such as in MH13 over a large enough (T, ρ) domain to provide a consistent H/He EOS covering the required domain for astrophysical applications for various values of Y (as required to derive Jupiter interior models), however, remain illusive with present day computer capacities. The present derivation is thus the best, or least bad possible way to somehow take into account the impact of H-He interactions on the thermodynamic quantities of the mixture, notably in the important Mbar region.

For the heavy elements in the H/He rich envelope, composed essentially of volatiles (H_2O, CH_4, NH_3), we use a recent EOS for water, based on QMD simulations at high density (Licari [2016], Mazevet et al. [2018]). Here also, this EOS has been shown to adequately reproduce available Hugoniot experiments [Knudson et al., 2012]. Given the small number fraction of CH_4 and NH_3 compared with H, He and even H_2O, we do not expect the assumption to generically treat all the volatiles with the water EOS to be consequential on the results. When considering a *diluted* core, we combine the above water EOS with the the Sesame "drysand" one [Lyon and Johnson, 1992] to take into account additional heavy elements such as silicates and iron. Finally, when including a central *compact* core, we use a 100% "drysand" EOS. We verified that using e.g. an EOS for pure iron instead of the drysand one for this region does not make noticeable difference. Note that ab initio simulations have shown that, under the characteristic temperature and pressure conditions typical of Jupiter deep interior, water is in a liquid state and is fully soluble in metallic hydrogen [Wilson and Militzer, 2012a]. Similarly, solid SiO_2 and MgO, representative examples of planetary silica and rocky material, are also found to be soluble in H^+ under similar conditions (González-Cataldo et al. [2014], Wilson and Militzer [2012b], Wahl et al. [2013]). These thermodynamic considerations, in passing, support a core erosion for Jupiter typical central conditions.

As shown by Soubiran and Militzer [2016], the inclusion of heavy elements in a H/He/Z mixture under Jupiter-like internal temperature and density conditions can be performed with the AVL providing we use an *effective* volume (density) for the heavy species. In the completely dissociated limit, $H_2O \rightarrow 2H + O$, we verified that, when calculating the volume of O by using the AVL approximation from a combination of our water and pure (Chabrier et al./MH13) H EOS's, respectively, we recover Soubiran and Militzer [2016] effective volumes for O within at most a few percents. Given oxygen low number abundance in Jupiter, such a difference is well acceptable. Although the abundance of oxygen w.r.t. H becomes more important in the diluted core (at high pressure and temperature), Soubiran and Militzer [2016] showed that for high pressure and temperature the effective volume of a species in the mixture is equal to the volume of the pure species, a limit we indeed recover. In other words, our water EOS can be safely used as the equivalent of a combined H+O EOS calculated with Soubiran and Militzer [2016]'s *effective* AVL in the 2H+O (high pressure) dissociated domain. This water EOS, as representative of volatiles in Jupiter, can thus be used throughout the entire T-ρ domain from Jupiter's atmosphere to the center. Jupiter models using an other water EOS must verify this important point. Indeed, as shown by Soubiran and Militzer [2016], using an EOS for H_2O which yields a volume for O in the H/He/O mixture different from the effective one found by these authors can yield errors larger than several percents on the density, a consequential issue when trying to fullfill Juno's constraints.

For H/He/Z mixtures, our EOS are then combined at each given (P, T) point throughout the AVL:

$$\frac{1}{\rho} = \frac{1 - Z_{\mathrm{water}} - Z_{\mathrm{drysand}}}{\rho_{\mathrm{H,He}}} + \frac{Z_{\mathrm{water}}}{\rho_{\mathrm{water}}} + \frac{Z_{\mathrm{drysand}}}{\rho_{\mathrm{drysand}}} \qquad \text{at } (P,T) = \text{constant}, \tag{4.4}$$

where $\rho_{\mathrm{H,He}}$, ρ_{water} and ρ_{drysand} are the densities of the H/He mixture, water and drysand, respectively, and $Z_{\mathrm{water}} = M_{\mathrm{water}}/M$, $Z_{\mathrm{drysand}} = M_{\mathrm{drysand}}/M$ the mass fractions of water and drysand, respectively, with M the mass of the planet. Note that the accuracy of the AVL for the hydrogen/water mixture under the relevant conditions for Jupiter interior has been verified with QMD simulations Soubiran and Militzer [2015].

Given the small number fraction of heavy elements compared with H and He, the P and T used to calculate the densities in the H/He/Z mixture are the ones obtained with the H/He mixture only. Similarly, the entropy of heavy elements can be neglected (see Soubiran and Militzer [2016]) and even when their mass fraction becomes $Z \gtrsim 0.2$, they affect the total mixing entropy by at most 2%, which represents a few per thousands of the total entropy. Moreover, this occurs only in the deepest part of the planet, with little impact of the gravitational moments. Hence, the total entropy is evaluated as the entropy of a pure H-He mixture with effective hydrogen and helium mass fractions $X^{\text{eff}} = X/(1-Z)$ and $Y^{\text{eff}} = Y/(1-Z)$, respectively, with $X^{\text{eff}} + Y^{\text{eff}} = 1$, and $X = M_H/M$, $Y = M_{He}/M$, and $Z = M_Z/M = Z_{\text{water}} + Z_{\text{drysand}}$.

4.2.3 Galileo constraints on the composition

For the outer element abundances, the observations of Galileo give

$$\frac{Y_{\text{Gal}}}{(X_{\text{Gal}} + Y_{\text{Gal}})} = 0.238 \pm 0.005,$$
$$Z_{\text{Gal}} = 0.0167 \pm 0.006,$$

where X_{Gal} and Y_{Gal} are the observed mass abundances of hydrogen and helium, respectively. Z_{Gal} is the abundance of heavy elements in the high envelope measured by Galileo, but the real abundance of heavy elements should be larger. This implies that Y_{Gal} and X_{Gal} are only defined relatively to each other and that $X_{\text{Gal}} + Y_{\text{Gal}} + Z_{\text{Gal}}$ can be larger than 1 in the planet. In all the following models1, except if stated otherwise, we impose the external atmosphere to have helium and heavy element mass fractions:

$$Y_{\text{ext}} = 0.23$$
$$Z_{\text{ext}} = 0.02,$$

which corresponds to $Y_{\text{ext}}/(X_{\text{ext}} + Y_{\text{ext}}) = 0.2347$.

As just mentioned, this Z value is most likely a lower limit for the heavy element content in the external envelope of Jupiter (see §4.5.2 for a detailed exploration of this issue). Forgetting Galileo's constraints, i.e. reducing the observed amount of heavy elements, drastically reduces the constraints on the models and allows the derivation of a large range of models compatible with Juno's data. Relaxing these constraints thus drastically simplifies the calculations of valid models consistent with only Juno's observations. Such simplifications, as done in all recent studies (Guillot et al. [2018], Wahl et al. [2017], except when using an ad-hoc modification of their EOS), however, can hardly be justified (see §4.6).

4.3 Simple benchmark models

In this section, we show that traditional homogeneous, adiabatic 2 or 3 layer interior models for Jupiter are excluded by the new observations and that the planet must consist of several different regions.

4.3.1 Homogeneous adiabatic gaseous envelope

We first calculate an isentropic model, composed of one homogeneous convective isentropic gaseous envelope and a spherical compact core of constant density. The helium fraction in the convective envelope is fixed to the protosolar value, $\bar{Y}/(\bar{X} + \bar{Y}) = Y_\odot = 0.275$ (see e.g., Anders and Grevesse [1989]), and the total heavy material content (only water in the present model for sake of simplicity) is determined to obtain the correct mass of the planet. This model reproduces the J_2 observed value within 10^{-7}, the maximum intrinsic precision of the CMS method [Debras and Chabrier, 2018]. The J_4 and J_6 values are compared to Juno's ones in Figure 4.1 under the labels "Isentrope". The differences between the observed and calculated values for these moments are about 3% and 6%, respectively, well above any numerical source of error.

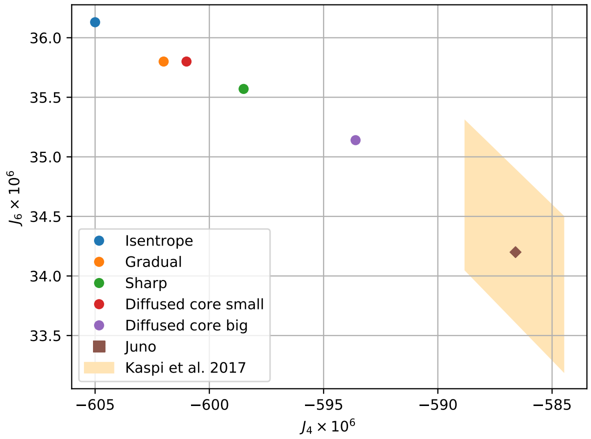

Figure 4.1: $J_4 \times 10^6$ vs $J_6 \times 10^6$ for different models (see text) and Juno's values [Iess et al., 2018] with the error bars too small to be seen on this Figure. The shaded area correspond to the uncertainty on the graviational moments arising from differential rotation shallower than 10000 km, as evaluated by Kaspi et al. [2017].

The only possibility to reconcile the observed and theoretical values would be the presence of strong differential rotation affecting the calculation of the gravitational moments, not implemented in the CMS calculations. However, the results of Kaspi et al. [2017] show that with various flow profiles extending more than 10000 km within the planet, the change in J_4 is at most 0.7% (see their Figure 4). Furthermore, the study of Cao and Stevenson [2017] excludes such a deep differential rotation.

- This yields the first robust conclusion: *Jupiter's interior is not isentropic.*

4.3.2 A region of compositional and entropy variation within the planet

The next step in increasing complexity is to change the composition, then the entropy, somewhere in the planet. There are two physically plausible domains: a diluted core extending throughout a substantial fraction of the interior and/or a region of either layered convection, hydrogen metallisation or H/He phase separation somewhere within the envelope.

Two possible locations

A diluted core or a region of layered convection further up in the planet can emerge during the evolution of the planet or can be inherited from the formation process (see e.g. Stevenson [1985], Chabrier and Baraffe

[2007] and references therein, Helled and Stevenson [2017]) and is characterized by a compositional gradient $\nabla\mu = (\partial\mu/\partial r) \propto \nabla Z = (\partial Z/\partial r)$, thus an entropy gradient $\nabla S = (\partial S/\partial r)$. For hydrogen metallisation, 1^{st}-principle numerical simulations suggest it could occur through a first-order phase transition (usually denominated plasma phase transition, PPT, or liquid-liquid transition, LLT) in a domain $P_c \sim$ 1-2 Mbar, for temperatures below the critical temperature $T \leq T_c \simeq$ 2000-5000 K (Morales et al. [2010] , Lorenzen et al. [2011], Morales et al. [2013b], Knudson et al. [2015], Mazzola et al. [2018]). Experiments on liquid deuterium, D_2, seem to be consistent with these figures, even though significant differences still persist between various experiments (see e.g. Knudson et al. [2015], Celliers et al. [2018]). Until this issue is resolved definitively, an entropy discontinuity, ΔS, due to hydrogen pressure ionisation in Jupiter can thus not be excluded.

In a similar vein, H/He phase separation, also a first-order transition, will also yield an entropy discontinuity, providing the local temperature is lower than the critical one for the appropriate He concentration (see below). Last but not least, a regime of double-diffusive layered convection could develop somewhere within the planet interior, triggered either by one of these two transitions (or by any phase separation involving some heavy component insoluble in metallic hydrogen) and/or simply by a local compositional gradient [Leconte and Chabrier, 2012]. Phase transitions, indeed, notably endothermic ones, are suspected of enforcing layered convection, for instance in the Earth's mantle (Schubert et al. 1975, Christensen and Yuen [1985]). The physical reason is the release of latent heat at the transition, which leads to thermal expansion and temperature advection which tend to hamper convection. It is interesting to note that, due essentially to the larger entropy in the plasma phase than in the molecular one, a PPT is an endothermic transition, i.e. $dP/dT < 0$ along the transition critical line, according to the Clausius-Clapeyron equation, $dP/dT \propto -\Delta S/\Delta\rho$. As for the H/He immiscibility, ab initio simulations, while still differing substantially, seem to suggest a critical temperature for $x_{He} = 0.08$ in the range $\sim$ 2000-8000 K for $P \gtrsim 1$ Mbar (100 GPa), with a weak dependence upon pressure in the T, P domain relevant for Jupiter, suggesting $dP/dT \sim 0$ for the protosolar helium value (Lorenzen et al. [2009], Morales et al. [2009], Morales et al. [2013a]) (see Fig. 13 below).

The entropy variation in the gaseous envelope could then occur either within a region of layered convection due to compositional gradients [Leconte and Chabrier, 2012] or because of either a PPT or a H/He phase separation (see Stevenson and Salpeter [1977a] or Chabrier et al. [1992]). Needless to say, not only these three physical processes are not exclusive but they are likely to be tightly linked and thus to take place in the same more or less extended hereafter denominated "*metallization boundary region*" near the Mbar.

Continuous or sharp entropy variation

Following up on the above discussion, we examine two types of entropy variation. Either (i) a gradual (continuous) one, δS, only due to a change in composition ($\nabla Y, \nabla Z$, see §4.2.2) over a more or less extended region. Such a continuous entropy change is expected from core dilution/erosion and/or weakly super adiabatic layered convection (see §4.6). Or (ii) a sharp entropy variation, hereafter denominated ΔS for identification, due to a first-order transition or a strongly super adiabatic layered convection.

- In the case of the models with a diluted core, we consider two possibilities: either (i) a jump in composition between two spheroids in the CMS method at the core-envelope boundary, and thus two isentropic zones in the planet, namely the outer gaseous envelope and the inner diluted core, or (ii) a gradual change of composition, thus of entropy throughout the core. In this latter case, we just consider that P, T at the limit between two spheroids are constant but that Y, Z, S increase from one spheroid to the next one as a constant piecewise radial function. In both cases, the change of entropy can be either gradual or sharp, as mentioned above. In all cases, the total helium content in the planet is the protosolar value, $\bar{Y}/(\bar{X}+\bar{Y}) = Y_\odot = 0.275$. In these calculations, we allow the diluted core to extend up to 75% of the planet's radius (about $P \sim 3$ Mbar), for sake of exploration.

In the case of a diluted core unstable to double diffusive behaviour, Moll et al. [2017] showed that a central seed could survive to erosion longer than the lifetime of Jupiter. The fact that, under Jupiter central T and P conditions, iron and silicates are under a solid form (see e.g., Musella et al. [2018]) tends to favor the presence of such a central seed. We thus consider the presence of a compact core at the very center of the planet.

- For the entropy variation within the gaseous envelope, with or without central compact core, we have proceeded similarly by considering either a gradual or an abrupt change in composition at the metallisation boundary, extending between at most 0.1 and 3.0 Mbar. In case of a gradual (continuous) change, which implies a continuous molecular H_2 to metallic H^+ transition and no H/He phase separation, the smooth change in entropy is simply due to a composition change (see eqns. (2)-(4)). In case of a first order molecular-metallic transition, the abrupt change in entropy ΔS is given by the Clausius-Clapeyron relation:

$$\frac{\Delta S}{\Delta(1/\rho)} = \frac{\mathrm{d}P_c}{\mathrm{d}T}, \tag{4.5}$$

where P_c denotes the critical pressure of hydrogen metallisation. Analytical calculations suggest that the entropy jump along the critical line is about $\Delta S \simeq 0.5\, k_B/\mathrm{proton}$ [Saumon and Chabrier, 1992]. However, given the lack of exact determination, ΔS will be used as a free parameter, discretized over a certain number of spheroids.

In case of a diluted core alone with *weak* layered convection, continuous H_2-H^+ transition and homogeneous H/He mixture in the envelope (no PPT or H/He separation), since the average helium content must be protosolar, the only free parameters are (i) the gradual change in heavy element abundance, δZ, thus δY and δS, (ii) the pressure range within which this change takes place, and (iii) the piecewise function of pressure describing this change. Somehow, these 3 parameters determine the gradients of entropy and composition in the region of concern. In models considering a first order transition in the hydrogen metallisation boundary or *a strongly super adiabatic* layered convection, the entropy jump ΔS is also a free parameter, as mentioned above.

The two types of models with entropy and compositional changes *either in the central region or in the gaseous envelope*, are illustrated schematically in Fig. 4.2 and the obtained J values are given in Fig. 4.1. For the models with a change of composition in the gaseous envelope, the typical values of J_4 and J_6 for a gradual increase δS and a sharp increase ΔS are plotted under the labels 'Gradual' and 'Sharp', respectively. As seen, smooth increase or a jump in composition yield similar results and the important parameter is the corresponding change in entropy. For the models with a change of composition in the central region, the size of the diluted core, somehow related to the entropy change and the repartition of heavy elements with depth (gradual increase or jump in composition) is the determinant parameter. The labels 'Diffused core small' and 'Diffuse core big' represent diffuse cores extending up to the 10 and 3 Mbar region, i.e. $\sim 50\%$ to 75% of the radius, respectively, and roughly bracket the range of accessible values in the $J_4 - J_6$ plan with this type of model.

In all cases, none of these two types of models, whatever the type of change of composition and entropy, sharp or gradual, was found to be able to yield J_4 and J_6 values sufficiently close to the observed ones (labeled 'Juno') to be explained by differential rotation or deep winds.

Another "simple" possible interior structure model is the one suggested by Leconte and Chabrier [2012]: the entire planet would be made of alternating convective and diffusive layers. However, it is known that the large scale dipolar magnetic field of Jupiter is not a fossil one but is due to a dynamo action. Even though dedicated numerical simulations are needed to explore this issue, it seems difficult to generate such a field in the absence of a large enough convective zone within the planet (see §4.6). Leconte and Chabrier [2012], however, pointed out that this entire double-diffusive interior model for Jupiter could be replaced by a model with a localized double-diffusive buffer in the envelope, surrounded by large scale convective envelopes (see their §4.3), similar to the type of model explored above, which is found to be excluded. We will return to this point in §4.5.2 and 4.6.

This yields the following conclusions:

- *Conclusion 1*: The first conclusion of this section is that models of Jupiter displayed in Figure 4.2(a) and 4.2(b) cannot fulfill both Juno and Galileo observational constraints. One needs a mix of these two types of models: Jupiter is at least composed of an envelope split in two parts (an outer molecular/atomic envelope with Galileo element composition and an inner ionized one) separated by a region of compositional change, *and* a diluted core extending throughout a significant fraction of the planet. A compact core can also be present at the center of the planet.

- *Conclusion 2*: Another key result of the analysis carried out in this section is that, in the absence of a sharp entropy increase ΔS, typical models of Figure 4.2(a) cannot even reproduce the J_2 value of Jupiter if the inner envelope has a larger amount of heavy elements than the outer one. Therefore, either ΔS must be substantial (an issue explored in §4.5) or *the heavy element content must decrease with depth in the outer part of the planet*. This local decrease of Z is balanced by an increase of Y so that the density (and the molecular weight, see §4.6), of course, increases with depth. As mentioned in the introduction, one of the most stringent constraints on the models are the Y and Z values observed by Galileo, which are surprisingly high for the observed values of the high order gravitational moments. *A local inward decrease of the metal content in some region of the planet's gaseous envelope appears to be the favored solution to resolve this discrepancy.* This is examined in detail the next Section.

It is essential at this stage to stress the crucial role played by the H/He EOS. Using the SCvH EOS, Chabrier et al. [1992] and subsequent similar models, which fullfilled Galileo and Voyager observational constraints, could relatively easily fullfill as well the Juno ones. This is entirely due to the SCvH EOS (or, similarly, the R-EOS one [Nettelmann et al., 2012], see Fig. 11 of Militzer and Hubbard [2013] or Fig. 27 of Chabrier et al. [2018]): for a given entropy, this latter has a lower density (pressure) in the ~Mbar region than our new EOS, enabling a larger amount of heavy element repartition in Jupiter interior, relaxing appreciably the constraints on possible models. The constraints become much more stringent with stiffer, state-of-the-art EOS's.

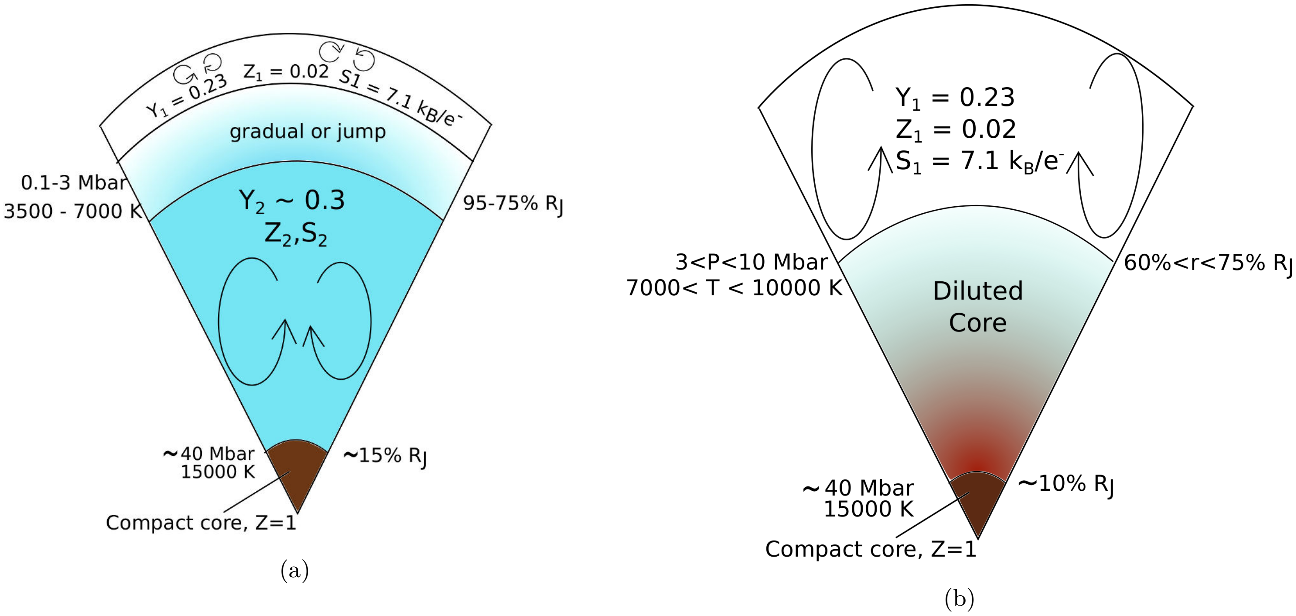

(a)

(b)

Figure 4.2: Simple structures of Jupiter with an internal entropy variation either in the envelope (left) or in the core (right) (see §4.3.2). None of these models can match the observations of both Juno and Galileo.

4.4 Locally inward decreasing Z-abundance in the gaseous envelope

4.4.1 Inward decreasing abundance of heavy elements in some part of the outer envelope

Two physical processes can lead to a locally decreasing abundance of heavy elements with depth in Jupiter's outer envelope, i.e. a locally positive gradient $\nabla Z > 0$: a "static" one, based on thermodynamic stability criteria, and a "dynamic" one, which involves non-equilibrium processes. For sake of completeness, a third, more "exotic" process, involving external events, is also discussed.

Thermodynamic stability

Salpeter [1973] and Stevenson and Salpeter [1977a] (see also Stevenson [1979]) suggested the occurence of helium differentiation in giant planet interiors, either in the same or in a different region that the H_2-H^+ pressure metallisation of hydrogen. These authors suggested that minor constituents, namely the heavy elements, could suffer differentiation in a similar or even larger way as helium. Unfortunately, phase diagram calculations of two or more components under the typical relevant conditions for Jupiter (about 1 Mbar and 5000 K) are scarce, or even inexistent, so finding out which element, under which molar concentration, prefers the H^+-rich or He-rich phase remains to be determined. The only existing study is the one by Wilson and Militzer [2010]. Ab initio simulations by these authors suggest that Ne association with He is thermodynamically favored, while the opposite is true for Ar, which is found to be more soluble with H^+. The underlying physical reason is the argon atom additional electron shell which increases its effective volume with respect to He due to the Pauli exclusion principle. If this explanation is correct, Kr and Xe should likewise be soluble in metallic hydrogen, which is consistent with their observed nondepletion in Jupiter's atmosphere.

It is indeed intuitively appealing to think that in case some species, Z_i, is pressure ionized, it might become immiscible with neutral helium, as for H^+/He, due to the strongly repulsive pseudo-potential, as in the case e.g. of alkali metals [Stevenson, 1979]. For some element (atom or molecule) to differentiate in the midst of some mixture, one needs its interaction energy in the mixture, typically the molecule or electron binding energy, to be larger (in absolute value) than the ideal mixing entropy, $-k_B T \ln x_Z$. Since the most abundant heavy elements have a number fraction $x_Z \simeq 0.1\%$, this yields near the metallization boundary, $\sim$ 5000 K, $|E_b| \gtrsim 0.5$ eV, a condition rather easy to fullfill. As mentioned above, all heavy elements, however, do not necessarily behave similarly. As shown by Wilson and Militzer [2010], heavy noble gases, indeed, are more likely to form compounds (Hyman [1964] Blackburn [1966]), suggesting that species like neon, acting like helium, and argon, have a different behaviour in the H^+/He mixture.

In case of element differentiation, according to the Gibbs phase rule, $x_{II} = x_I \exp\{-\Delta G(P,T)/k_b T\}$, where x_i denotes the number abundance of a given species in phase I or II (H^+-rich/poor, conversely He-poor/rich in the present context) and ΔG is its excess mixing enthalpy in the mixture, the differentiation of a given heavy element can be similar or opposite to that of helium, yielding an increasing (resp. decreasing) abundance with depth in the former (resp. latter) case. In all cases, this yields a gradient of abundance ∇Z within some part of the planet envelope, with $\nabla Z > 0$ for some heavy elements.

If H-He immiscibility, leading to a depletion of helium in the outer envelope, is triggered by the metallisation of hydrogen, the fact that hydrogen metallisation in a H/He mixture is found to occur at lower pressures with decreasing helium fraction (e.g. Mazzola et al. [2018]) implies that the pressure range of immiscibility will extend with time because of both the planet's decreasing internal temperature and the decreasing abundance (depletion) of helium in the upper layers. The region of immiscibility can thus be relatively broad in Jupiter's interior, depending on when it started. Note in passing that, if H/He differentiation occurs and is at least partly responsible for the redistribution of heavy elements in Jupiter's envelope, this excludes the H/He diagrams suggested by Morales et al. [2009] and Schöttler and Redmer [2018] which predict no immiscibility within present Jupiter. This point will be discussed in detail in §4.6.1.

Upward atomic motions

As explored thoroughly by Stevenson and Salpeter [1977a] in the case of a first-order hydrogen pressure ionization (PPT) and a H/He phase separation occuring in the same region, the following process might occur. At the onset of hydrogen metallisation, characterized by a pressure P^+, latent heat release will lead to the superposition of a overheated (resp. supercooled) H^+-rich (resp. H_2-rich) layer, thus less (resp. more) dense than the surrounding medium, underneath (resp. above) the metallization boundary (see Fig. 2 of Stevenson and Salpeter [1977a]). Under such conditions, nucleation of bubbles might occur. Concomitantly, He atoms will differentiate from H^+. If such H^+-rich/He-poor bubbles form, they will absorb heat by thermal diffusivity and will be lighter than the surrounding gas. The bubbles will then rise by buoyancy, up to a pressure P less than the metallisation pressure, $P < P^+$. They will then break and H^+ will recombine to form H_2, depleting little by little the upper envelope in He by mixing this convective region with H^+-rich bubbles while enriching the lower envelope in He. Consequently, the heavy elements which, for chemical and/or thermodynamic reasons, have a preference for these H^+-rich/He-poor bubbles, rather than for the He-rich/H^+-poor surrounding medium, will be transported upwards and be depleted little by little in the deep envelope whereas the opposite will be true for species favoring association with helium atoms. Somehow, this is similar to an ongoing distillation process in the sense that the redistribution of elements arises from a physical separation rather than a chemical reaction and mass is not *locally* conserved underneath the uppermost convective envelope. This occurs only if the heavy elements do not affect significantly the density of the bubbles, which must remain lighter than the surrounding gas. In the typical conditions of Jupiter's outer envelope, there are about 500 times more atoms of hydrogen than of heavy elements. Therefore, for a typical atomic weight ratio $\bar{A}_Z/A_H \sim 15/1$ (average between C, N and O atoms), such a process is possible. Heavier molecules (such as iron) being even more rare compared to H, gravitational considerations are still consistent with this scenario.

Such a scenario has further theoretical support. First, noble gases have been known to be almost insoluble in metals since the end of the 19th century (Ramsay and Travers [1897] or Blackburn [1966] for a review, and Wilson and Militzer [2010] for the case of neon and argon). On the other hand, at high pressure, hydrogen can form complex polyhydrides molecules very efficiently, with many different atoms (sulfur, lithium, sodium, iron, ...; see e.g. Ashcroft [2004] or Pépin et al. [2017]). Therefore, at metallisation, non inert heavy elements tend to form polyhydrides within metallic H^+-rich bubbles. If, as discussed above, the density of these bubbles is less than the one of the surrounding gas, these heavy elements will be transported upwards, enriching Jupiter's outer envelope while depleting the inner one. One of the unknowns in this process is the impact of temperature upon the formation of polyhydrides, only probed experimentally so far up to ~ 1500 K [Pépin et al., 2017] while, assuming an isentropic profile from the $P = 1$ bar down to $P \simeq 0.5\,\mathrm{Mbar}$, about the onset of metallisation, the temperature is $T \sim 4500K$. Further numerical or experimental work on the formation of polyhydrides at high pressures and temperatures would help assessing the validity of this process.

Concomitantly with hydrogen metallization, and the formation of polyhydrides, we also expect reduction-oxydation (redox) reactions to occur. The loss of its $1s$ electron at hydrogen metallization makes H^+ prone to react with other heavy elements through electron transfer. The H^+ bubbles could then trap e.g. N, O or other elements, participating also to en enrichment (resp. depletion) of these elements in the upper (resp. lower) envelope.

As shown by Stevenson and Salpeter [1977a], we recall that bubble nucleation requires dynamical motions, such e.g. as gravity waves, upward plume penetrations etc... along the ionization critical line. In the absence of such variations, the amount of overheating due to a PPT would be insufficient to yield homogeneous nucleation. In that case, or in the absence of PPT within Jupiter's envelope, even though He-rich dropplets can still form and drown if H/He differentiation occurs, no upward motion of heavy element takes place and the enrichment of the upper envelope can only be due to the type of phase diagram discussed in §4.4.1.

We can try to assess more quantitatively this upward transport of heavy elements, if it occurs. As will be shown in §5 (see Fig. 4.5), in our most favored models, the diluted core extends up to about 65% of the planet's radius and the outer envelope, including the region of composition change, extends from $R \gtrsim 0.8 \times \mathrm{R_J}$ upward. Denominating Y_{bubble} the He mass fraction in the bubbles before they disolve in the upper convective envelope, and given the fact that in this latter $Y_{\mathrm{ext}} = Y_{Gal} = 0.238$, today external envelope is composed of a fraction α of the helium initial protosolar value $Y_{\odot} = 0.275$:

$$0.275\,\alpha + Y_{\mathrm{bubble}}(1-\alpha) = 0.238 \Rightarrow Y_{\mathrm{bubble}} = \frac{0.238 - 0.275\alpha}{1-\alpha}. \tag{4.6}$$

Necessarily, $Y_{\mathrm{bubble}} < 0.238$ and is expected to be much smaller because of helium strong diffusivity [Stevenson and Salpeter, 1977a]. This also implies $\alpha < 0.238/0.275 = 0.87$ in order to have $Y_{\mathrm{bubble}} > 0$. As will be shown below, the mass of the outer envelope, $R \geq 0.8 \times \mathrm{R_J}$, is of the order of $57\,\mathrm{M_\oplus}$ while the one of the inner envelope, $R_{core} \approx 0.65 \times \mathrm{R_J} < R < 0.8 \times \mathrm{R_J}$, where R_{core} is the upper limit of the diluted core, is about $137\,\mathrm{M_\oplus}$. The total mass transported upwards by the bubbles is thus $M_{\mathrm{up}} = (1-\alpha) \times 57\,\mathrm{M_\oplus}$, with a helium mass fraction $Y = Y_{\mathrm{bubble}}$. If a mass M_{Z} of heavy elements is trapped in the bubbles, which by mass conservation corresponds to the depleted mass of heavy elements in the inner envelope, the mass fraction of metals in the bubbles is $Z_{\mathrm{bubble}} = M_{\mathrm{Z}}/M_{\mathrm{up}}$. The global balance thus yields: $Z_{\mathrm{bubble}} = M_{\mathrm{Z}}/[57(1-\alpha)]$.

As an example, let us take an initial protosolar heavy element composition, $Z \approx 0.02$, in both envelopes. In that case, the inner envelope is thus composed of $M_Z \approx 0.02 \times 136 = 2.72\,\mathrm{M_\oplus}$ of heavy elements. Significantly decreasing the metal content underneath the metallization region thus requires to transport upwards about 2 $\mathrm{M_\oplus}$ of heavy elements, yielding

$$Z_{\mathrm{bubble}} = \frac{0.035}{1-\alpha}. \tag{4.7}$$

At $R = 0.8\,\mathrm{R_J}$, the isentropic external condition yields $P \simeq 2$ Mbar, $T \simeq 6500$ K. For these values, the H/He and water EOS's give for the densities of hydrogen, helium and heavy elements (assumed here to be mostly water for sake of simplicity): $\rho_{\mathrm{H}} = 850\,\mathrm{kg\,m^{-3}}$, $\rho_{\mathrm{He}} = 2060\,\mathrm{kg\,m^{-3}} = 2.42\,\rho_{\mathrm{H}}$ and $\rho_{\mathrm{Z}} = 5084\,\mathrm{kg\,m^{-3}} = 5.98\,\rho_{\mathrm{H}}$ considering a pure oxygen atom with its effective volume, as explained in §4.2. According to the AVL and Eqns.(4.6)-(4.7), the density of the bubble is then:

$$\frac{1}{\rho_{\mathrm{bubble}}} = \frac{1}{\rho_H}\left(\frac{1-(Y_{\mathrm{bubble}}+Z_{\mathrm{bubble}})}{1.0} + \frac{Y_{\mathrm{bubble}}}{2.42} + \frac{Z_{\mathrm{bubble}}}{5.98}\right)$$

$$\alpha = 1 - \frac{0.00749}{0.838 - \rho_H/\rho_{\mathrm{bubble}}}. \tag{4.8}$$

For a protosolar He and Z composition, $Y_{\odot} = 0.275$, $Z_{\odot} = 0.02$, the density at this (P,T) point is $\rho = \rho_{\odot} = 1038\,\mathrm{kg\,m^{-3}} = 1.22\,\rho_{\mathrm{H}}$. In order for the bubble to rise, we need $\rho_{\mathrm{bubble}} < \rho_{\odot}$ and, in order to ensure that $0 < \alpha < 1$, the above equation implies a minimum density: $0.838 - \rho_H/\rho_{\mathrm{bubble}} > 0.00749$, which gives $\rho_{\mathrm{bubble}} > 1.204\,\rho_H$.

We then get as a final balance of the upward motions of H^+-rich/He-poor bubbles: $1.204\,\rho_H < \rho_{\rm bubble} < 1.22\,\rho_H$, which yields $0 < \alpha < 0.62$, $0.035 < Z_{\rm bubble} < 0.09$ and $0.178 < Y_{\rm bubble} < 0.238$. Note that Stevenson and Salpeter [1977a] verified that such bubbles can rise fast enough to circumvent convective motions.

These calculations are obviously very approximate and should be taken with due caution, but show that upward motions of bubbles in a region of H^+/He immiscibility in the vicinity of a PPT is a plausible process to enrich Jupiter's outer envelope in heavy elements. We see that, even though the range of change for the density is quite small (about 1%), it corresponds to a significant range of change for $Y_{\rm bubble}$ and $Z_{\rm bubble}$. Most importantly, it shows that Jupiter's today outer envelope composition can be a mixture of a primordial envelope and a process of rising bubbles, composed of less than $\lesssim 60\%$ of the primordial helium fraction with a significant increase of heavy element. With the above estimates, the upper envelope would be roughly composed (in mass) of 23.3% of helium and 5% of (water-like) heavy elements, and the lower envelope of 29.5% of helium and 0.5% of water.

The present analysis provides a plausible explanation for the observations of Galileo (see Wong et al. [2004]) that indicate that today real ratio of heavy elements to the protosolar value in the upper envelope of Jupiter could be as high as $Z/Z_\odot > 2.5$. This enriched (resp. depleted) abundance of heavy elements in Jupiter's upper (resp. lower) envelope can thus be explained by dynamical differentiation at the onset of hydrogen metallization and H/He phase separation in the planet. However, for the afore "rising bubble" process to take place, this requires hydrogen molecular-metallic transitions to occur through a first-order transition, leading to a local release of latent heat. As mentioned in §3.2.1, although a PPT is indeed found in some modern ab initio numerical simulations, its critical temperature remains to be determined precisely, being predicted within the range $2000 \lesssim T_c \lesssim 5000$ K for a critical pressure $1 \lesssim P_c \lesssim 2$ Mbar. Interestingly enough, a critical temperature $T_c \simeq 5000$ K around ~ 1 Mbar would be consistent with a PPT in the outer part of Jupiter. In the absence of a PPT in the envelope, H^+/He phase separation can possibly still occur but the outer observed oversolar abundance of heavy elements can not be due to upward bubble motions. Phase separation of these elements with He, as discussed in §4.4.1, will thus be the favored explanation.

Accretion

Finally, the overabundance of heavy elements in Jupiter's upper envelope can have a third explanation, namely one or several giant impacts [Iaroslavitz and Podolak, 2007] or, similarly, ongoing accretion of planetesimals (e.g., Bézard et al. [2002]). This scenario, however, implies that global internal convective motions must be inhibited somewhere in Jupiter, preventing the extra accreted material to be redistributed homogeneously throughout the planet. Indeed, a global Z abundance throughout the planet equal to the Galileo value would yield low-order gravitational moments inconsistent with observations. If convection inhibition is due to H/He immiscibility, this latter must already have started when the external event took place. This in turn puts an important constraint on the H/He phase diagram, notably on the critical P, T values for $x_{He} = 0.08$, Jupiter helium protosolar concentration. If inhibition is due to hydrogen metallization, it implies that this latter must be a 1^{st}-order phase transition (yielding an entropy jump). Convection can also be inhibited by the onset of double diffusive convection, either as an enhanced diffusive process (oscillatory convection) or, more likely under the present conditions, as layered convection, a process indeed possibly triggered by extensive planetesimal accretion (e.g. Stevenson [1985], Chabrier and Baraffe [2007] and references therein).

We can estimate the amount of accreted heavy material. Assuming, as in the previous section, that the external envelope extends down to $\sim 80 \times \mathrm{R}_J$, with an average density $\rho_{\text{ext}} = 450\,\mathrm{kg\,m^{-3}}$ to obtain a mass of $\sim 57\,\mathrm{M}_\oplus$, the "enriched" mass of heavy elements in this envelope, M_{excess}, compared to the protosolar value is roughly (assuming sphericity and a primordial protosolar composition):

$$M_{\text{excess}} \approx \frac{4\pi}{3}\rho_{\text{ext}} R_{\mathrm{J}}^3 (1 - 0.8^3)(Z_{\text{Gal}} - Z_\odot). \tag{4.9}$$

To explain the Galileo value, $Z_{Gal} \simeq 2.5 \times Z_\odot$, the impact embryo (or the sum of the planeteismals) must have a mass $M_{\text{excess}} \approx 1.5\ \mathrm{M}_\oplus$, a significant but not unplausible value.

4.4.2 Constraints from the evolution

To be considered as plausible, our models with a region of locally inward decreasing abundance of heavy elements must be consistent with what is known of Jupiter's long term evolution. If, as expected, Jupiter formed through core accretion [Pollack et al., 1996], the primordial abundance of heavy elements in the planet should be increasing with depth (see Fig.4.3). As explored by, e.g., Leconte and Chabrier [2013], Vazan et al. [2018], the differential core-envelope cooling of the planet leads to a redistribution of heavy elements with time, yielding an increasing heavy element content in the gas rich envelope. To explain our $\nabla Z > 0$, a physical process must have inhibited convection within the envelope and prevented a homogeneous redistribution of elements. Three possibilities have been discussed in the previous subsections: 1^{st} order metallisation, immiscibility and accretion. We examine whether they are compatible with the evolution of the planet.

If a first order metallization (PPT) stopped the convective motions, our discussion on the bubbles in §4.4.1 shows that it is possible to deplete the inner envelope and enrich the outer one. This would be in adequation with any evolutionary scenario.

In the case of immiscibility between hydrogen and helium the discussion of §4.4.1 shows that the outer envelope will lose part of its helium content because of H/He phase separation and the onset of helium sedimentation (Stevenson and Salpeter [1977a]). The enrichment in $Z = M_Z/M$ in the outer envelope is at least partly due to the mass decrease in this region. In contrast, since the mass of the inner envelope is much larger than the one of the outer envelope (as confirmed in §4.5), the increase of mass of the inner envelope will not dilute significantly the heavy element content: the decrease of Z in the inner envelope is thus necessarily much smaller than its increase in the outer envelope. More importantly, in order to obtain a locally steep enough gradient of heavy elements $\nabla Z > 0$ between the outer, Z-enriched, and the inner, Z-depleted, envelopes, the He-rich falling dropplets must be as Z-poor as possible. This implies limited miscibility between some Z-components and He, as discussed in §4.1.1, in addition to H and He, and a typical Z/He phase diagram with very low concentations of heavy elements in He-rich dropplets. Under such conditions, it is possible to preserve (and even increase) a positive Z-gradient with time.

Finally, in the case of accretion of planetesimals or giant impacts, if it is combined with a PPT or a phase sep-

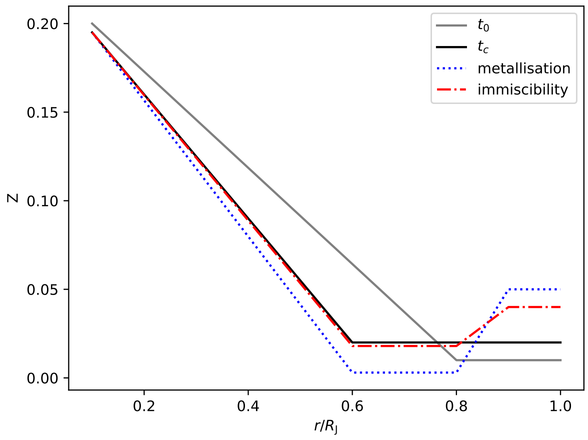

Figure 4.3: Typical evolution of the heavy element content Z as a function of the radial distance r with time, assuming that a first order phase transition (PPT) or immiscibility will occur during the cooling history. At $t = t_0$ Jupiter just formed. A small convective external envelope is connected to a gradually diluted planet, structure inherited from the core accretion. At $t = t_c$, immiscibility or first order metallisation is about to happen. The convective zone has somewhat expanded, redistributing the metal content in the planet. Later on ('metallisation' curve), the rising bubbles have enriched the outer envelope in heavy elements while depleted the inner one. If immiscibility takes place ('immiscibility' curve), the outer envelope will eventually lose part of its mass because of drowning helium dropplets, increasing the heavy elements mass fraction in the outer envelope whereas the dilution of these elements in the inner envelope is almost negligible.

aration, the above conclusions apply. In the other case, if triggered layered convection is the only reason for the difference of composition between the outer and inner envelopes, it must have persisted since the accretion event(s). As discussed in detail in §4.5.2 and §4.6 and in Leconte and Chabrier [2012], this implies strong constraints on the physical characteristics of the layered convection. Although, as examined in §4.6.2, these constraints are fullfilled by the present models, whether they could persist during Jupiter's cooling history, or in fact during any gaseous planet cooling history [Chabrier and Baraffe, 2007] is not clear and needs to be explored with extreme care (e.g. Rosenblum et al. [2011], Mirouh et al. [2012], Wood et al. [2013], Kurokawa and Inutsuka [2015]). Evolutionary calculations show that the long stability of layered convection could persist during Saturn's cooling history (Leconte and Chabrier [2013]). For Jupiter, a dedicated analysis of this issue with the interior structures presented in this chapter, provided the physical processes at play are handled with great accuracy, would certainly allow to reduce the range of possible models. Multi-dimensional *time implicit* simulations of convection [Pratt et al., 2017] are a promising avenue to explore this exciting problem, of prime importance for planetary science.

To conclude this section, we should mention that recent evolutionary calculations (e.g. Vazan et al. [2018]) converge to a structure profile for present Jupiter with a monotonically outward decreasing compositional gradient, $\nabla Z < 0$, at odd with our suggestion of a local $\nabla Z > 0$. These models, however, use the SCvH EOS. As discussed in §4.3.2, this latter yields a too hot thermal structure along an adiabat (see Militzer and Hubbard [2013] or Fig. 27 of Chabrier et al. [2018]), favoring convection and allowing larger metal fractions. These Jupiter internal structure models are excluded by the present Juno+Galileo analysis and thus can not be used as reliable evolutionary constraints. Further evolutionary calculations with the proper physics, including a proper treatment of double diffusive convection and of H/He phase separation are needed to verify the consistency of the present models with Jupiter's thermal history. As just mentioned, however, properly handling such complex physical processes is a task of major difficulty (see §4.6.5).

4.5 Models with at least 4 layers and an entropy discontinuity in the gaseous envelope

As shown in §4.3, Jupiter interior structure must entail at least four different regions, namely two outer and inner homogeneous adiabatic envelopes, separated by a region of compositional, thus entropy variation, and a diluted core, also harboring a more or less extended domain of compositional/entropy change near the envelope boundary, and potentially a solid rocky seed. One of the unknowns in these models is the amount of entropy change in the envelope.

4.5.1 No entropy discontinuity

We first explore models for which the entropy and composition change within the gaseous envelope is *continuous*, e.g. only due to a change in composition, for instance due to the onset of weakly super adiabatic layered convection. At given (P,T) at the interface between two spheroids, a change in Y naturally leads to a difference of entropy between the layers (§2.2). As shown previously, the possibility to fullfill both Juno and Galileo observational constraints in that case is an inward *decreasing* metal abundance at/near the metallization boundary, around 1 Mbar. There are two possibilities.

In the first one, we suppose that, whatever the physical process occuring in this region, it does not lead to a strong enrichment of helium in Jupiter *present day* inner envelope, with typically $Y \simeq 0.25$ in this region. In order to ensure an average protosolar helium content, $\bar{Y} \approx 0.275$, this implies a helium enrichment in the diluted Z-rich core. At first glance, this seems to be counterintuitive, given the smaller diffusivity of He compared to H. Recent ab initio simulations, however, suggest the formation of stable He-rich compounds, e.g. FeHe, at pressures $P \gtrsim 40$ Mbar and temperatures $T \simeq 20000$ K, typical of the central core conditions [Monserrat et al., 2018].

The second possibility, on the opposite, supposes a strong differentiation between He and H and thus a strong He enrichment in the inner envelope between the inner edge of the metallization or H/He demixion boundary and the upper one of the diluted core. Typically, $Y \simeq 0.3$ in the inner envelope. This, in turn, implies that He does not diffuse efficiently in nor mixes well with the strongly Z-enriched diluted core, and thus Y decreases with depth in the central part of the planet.

Among these two types of models, only the first one, where the differentiation of helium at the Mbar region is small, allows to significantly decrease the J_4 and higher order moment values compared to the simple cases explored in

§3. We show the schematic representation of our optimised model in Figure 4.4. The smallest value of J_4 we could obtain lies within the limit of what can be explained by differential rotation shallower than 10000 km [Kaspi et al., 2017]. The higher order moments, however, remain much too large.

- *Conclusion:* Models with no entropy discontinuity in the Mbar region seem to be excluded as possible Jupiter internal structure.

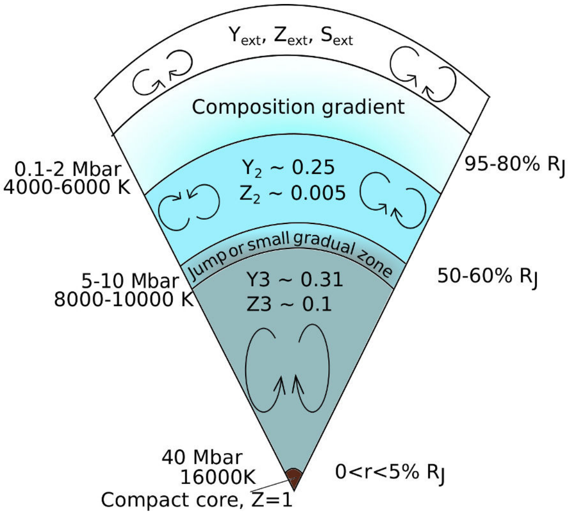

Figure 4.4: Models with a continuous change of entropy within the envelope only due to a change in composition compatible with Galileo's constraints and Juno's J_2 and J_4 values, assuming a strong differential rotation. The higher order moments are incompatible with Juno.

4.5.2 Entropy discontinuity in the gaseous envelope

In the previous series of model, the (modest) change of entropy δS throughout the gas rich envelope is a direct consequence of the change in Y and Z within the hydrogen pressure ionization boundary layer, due e.g. to the onset of weakly super adiabatic layered convection. In this subsection, the inward increase of entropy in the boundary layer is now used as a free parameter in the calculations, and is discretised throughout a certain number of spheroids across the ionization boundary region, i.e. we assume an entropy gradient $\nabla S = \Delta S / \Delta R < 0$ within the pressure range of interest.

Physical expectations

A brutal inward increase of S can have several physical foundations. Assuming that Jupiter's outermost thermal profile is isentropic (because of adiabatic convection in this region), the observed condition, $T = 165$ K, $P = 1$ bar corresponds, according to our EOS, to $T \simeq 5000$ K at 1 Mbar. As mentioned above, recent 1^{st}-principle simulations [Mazzola et al., 2018] predict a critical temperature for the metallisation of hydrogen in the range $T_c \simeq$ 2000-5000 K at $P \simeq 1$ Mbar. Both simulations (Soubiran et al. [2013], Mazzola et al. [2018]) and experiments [Loubeyre et al., 1985], however, suggest that, even for a low helium concentration like in Jupiter ($x_{He} < 0.1$), the critical pressure increases while the critical temperature decreases with increasing helium concentration. If this behaviour is confirmed, it probably excludes a PPT in Jupiter. However, given the present uncertainties in these determinations, we still explore the possibility of a first order phase transition (PPT) between molecular and metallic hydrogen in Jupiter. According to Saumon and Chabrier [1992] and Chabrier et al. [1992], the increase of entropy associated with such a transition is about

$$\Delta S_{\text{metallization}} \sim 0.5\,\mathrm{k_B}/\text{proton}. \tag{4.10}$$

Since, as mentioned above, the temperature in this region of Jupiter's interior should be close to T_c, we expect ΔS to be less than this value.

If hydrogen pressure ionization does not occur through a first order transition inside Jupiter (because the local temperature at the ionization pressure is larger than the PPT critical temperature, $T > T_c$), a sharp entropy change can be due to H/He phase separation (also a 1^{st}-order transition). As shown by Stevenson and Salpeter [1977a], drowning nucleated helium dropplets lead to a release of gravitational energy and, even though their analysis suggest that most of this energy is radiated away, part of it contributes to heating up the inner part of the planet (see detailed discussion in §4.6.5).

The shape of the H/He phase diagram is a major uncertainty in the present study. The rather limited helium depletion w.r.t. the solar value in Jupiter's external envelope suggests that the variation ΔY in the immiscible region should be modest (about $\sim 10\%$), so the equilibrium number fraction of helium today in the outer (low pressure) part of the demixing region is still close to $x_{He} \simeq 0.1$. In that case, according to Morales et al. [2013b] Fig. 2, the mixing entropy should depart only slightly from the ideal mixing entropy, by $\sim 0.03\,k_B$/at at 5000 K for $x_{He} = 0.1$. Since the maximum value of the ideal mixing entropy, for a concentration $x_{He} = 0.5$ is $S^{id}_{mix}/N = -[x \ln x + (1-x)\ln(1-x)] = 0.7\,k_B$/at (about $0.3\,k_B$/at for $x_{He} = 0.1$), we see that the entropy jump due to H/He immiscibility should be $\lesssim 0.5\,k_B$/proton. The entropy change due to helium dropplet sedimentation is more difficult to evaluate and requires numerical explorations. Guidance is provided by the calculations of Fortney and Hubbard [2003] for the case of Saturn. In the case of a maximum temperature gradient in the inhomogeneous region and no formation of a helium layer atop the core (both the most likely present situation), these authors find that a change of composition $Y = 0.21 \rightarrow 0.36$ corresponds to a global increase of entropy $\Delta S \sim 0.3\,k_B$/proton. For Jupiter, we expect helium sedimentation (i) to have occured, if ever, more recently than for Saturn, (ii) to encompass a much smaller fraction of the planet (see §4.6.1) and thus to induce a much smaller entropy variation. Adding up these two contributions, it seems difficult to justify an entropy jump arising from H/He phase separation much larger than $\sim 1\,k_B$/proton.

Clearly, more experimental and numerical exploration of hydrogen pressure metallisation and of the H/He phase diagram and He sedimentation process are strongly needed to help constraining these processes.

Finally, if the mean molecular weight gradient due to the change of composition is large enough to hamper adiabatic convection, a regime of layered convection can develop and lead to a super adiabatic temperature structure similar, at least in some part of the planet, to the oned derived in Leconte and Chabrier [2012] . As shown in Figure 4 of their paper, this can increase the central temperature of Jupiter by a factor ~ 1.5 compared to the adiabatic central temperature. As discussed in §4.3, whereas a fully layered structure throughout the planet is probably difficult to reconcile with a large scale magnetic field generation, localised regions of layered convection can affect similarly the temperature structure of the planet. According to the study of Leconte and Chabrier [2012] (see also §4.6), layered convection can occur in Jupiter if $10^{-5} \lesssim \alpha \lesssim 10^{-4} - 10^{-2}$, with $\alpha = l/H_p$ the ratio of the size of a convective layer over the pressure scale height. If $\alpha \ll 10^{-5}$, convection is completely inhibited and the flux is transported by diffusion, which is not compatible with the thermal history of Jupiter. If $\alpha \gg 10^{-4}$, the diffusive layers can not persist for more than a billion year and large scale adiabatic convection sets up throughout the whole planet. This in turn constrains the range of super adiabaticity induced by persistent layered convection (see eqn. (21) of Leconte and Chabrier [2012]): strong departure from adiabaticity will break the convective zones, which is not allowed, whereas a small departure will not persist and adiabatic convection will prevail.

The detailed treatment of layered convection in our calculations is presented in §4.6.2. Varying the location and extent of layered convection between 0.1 Mbar and 2 Mbar, i.e. in the vicinity of hydrogen pressure ionization, we obtain numerically a maximum entropy increase from layered convection:

$$\Delta S_{\text{layered}} \lesssim 0.6\,\mathrm{k_B}/\text{proton}, \tag{4.11}$$

with a decreasing metal abundance, i.e. $\nabla Z > 0$, in this region. An increasing metal abundance in this region yields higher values of ΔS but in that case $\alpha \lesssim 10^{-7}$ (see §4.6). This implies the presence of a diffusive buffer, or a regime of turbulent diffusion within the ionization boundary layer. Although detailed calculations are lacking, it seems difficult to reconcile such a structure with Jupiter's thermal history. Let aside the fact that, as mentioned previously, such models are hard to reconciliate with the values of J_6 to J_{10}.

In summary, if either a first order transition and/or layered convection is present within some part (most likely around the Mbar) of the planet gas rich envelope, an inhomogeneous zone where the total increase in entropy can reach $\sim$ 0.5-1 $\mathrm{k_B}$/proton is expected. Note that if layered convection develops above the location of hydrogen pressure ionization, the induced temperature increase could inhibit the PPT or the H/He phase separation in Jupiter's present interior.

Figure 4.5 portrays the typical structure of our final Jupiter models. They all share the following features:

- an outer homogeneous convective envelope characterized by the Galileo helium and heavy element abundances and the adiabat condition at $T = 165$ K, $P = 1$ bar;
- an inhomogeneous region between ∼0.1 and ∼2 Mbar associated with (i) a change in composition, very likely characterized by an *inward decreasing metal abundance* ($\nabla Z > 0$) and (ii) a non negligible entropy ($\gtrsim 5\%$) and temperature increase. These gradients stem from layered convection and/or H-He immiscibility, even though a PPT can not be totally excluded for now;
- an inner homogeneous convective envelope lying on a warmer isentrope than the outer region, with an average larger helium fraction and, most likely, a lower metal fraction than in the outermost region. Indeed, even

though a larger Z fraction in this region than in the outer one is not entirely excluded, it requires an uncomfortably large entropy increase, $\Delta S \gtrsim 1.4\, k_B$/proton (case (c)), according to the aforederived estimates. As shown below, there is a degeneracy between the entropy jump in the inhomogeneous region and the helium and metal fractions in the inner envelope. The larger Y and Z in the inner envelope, the larger ΔS needs to be.

- a diluted (eroded) core extending throughout a significant fraction of the planet. A small entropy jump in the inhomogeneous region, $\Delta S \lesssim 0.5\, k_B$/proton (case (a)), yields an inward increasing helium abundance in the core, while a larger value (case (b)) implies an inward decreasing helium abundance in the core.
- most likely a central compact, solid core.

A quantitative analysis of these models is given in the next subsection.

Quantitative results on the gravitational moments

The results of our optimized models with an entropy discontinuity $\Delta S \in [0-2]\mathrm{k_B}$/proton in the ionization boundary region, projected in different J_k - J_{k+2} plans, are displayed in Figure 4.6 for two values of external heavy element abundance, namely $Z_{\text{ext}} = Z_\odot$ and $Z_{\text{ext}} = 2 \times Z_\odot$. The first obvious conclusion from this figure is that our range of models consistent with Juno's observed gravitational moments differs from the one derived by Guillot et al. [2018] with 200 000 models (see their Fig. 1 of the Extended Data, reported as a hashed area in Fig. 4.6). We have verified that this is not a discretisation issue: with interior structures calculated with 1000 spheroids, this conclusion is unaltered. Even though the difference between the two analysis should partly stem from the different EOS used by these authors, it arises essentially from our different representation of the planet interior. Indeed, we recall that these authors do not take into account the constraint from Galileo on the outer heavy element abundances. Therefore, if Galileo's observations are correct, Fig. 4.6 shows that the qualitative conlusions on the differential rotation obtained by Guillot et al. [2018] could be altered.

- *Impact on the low-order moments ($\leq J_4$).* We found out that the entropy change, ΔS, is strongly affected by the composition in the inner convective envelope, i.e. the region between the inhomogeneous one and the diluted core. Therefore the size and composition of the diluted core, the composition of the inner envelope, and the entropy change ΔS in the region of compositional variation are intrinsically linked. To better understand this result, we must recall that the major issue of the models is to decrease J_4 at constant J_2. Figure 4.7 portrays the value of the contribution function $J_2 - J_4$ in the planet as a function of pressure.

This figure shows that, in order to decrease J_4 with respect to J_2, one needs to enrich the planet deeper than $\sim 2\,$Mbar, and the region around $\sim 10\,$Mbar is where it is most efficient. Therefore, an enriched inner envelope decreases J_4 at constant J_2 (see the pressure range in Figure 4.7), but enriching the inner envelope implies a steeper compositional gradient in the boundary region between the outer and inner envelopes, which has the opposite effect on J_4 compared to J_2. Furthermore, this boundary region between ∼0.1 and 2 Mbar has a much stronger contribution on J_2 and J_4 than the deeper region. This stems from the fact that this region has a high mean radius, hence the mass of a spherical shell is much larger than in the 5 Mbar region, and the impact on J_2 and J_4 is enhanced. In

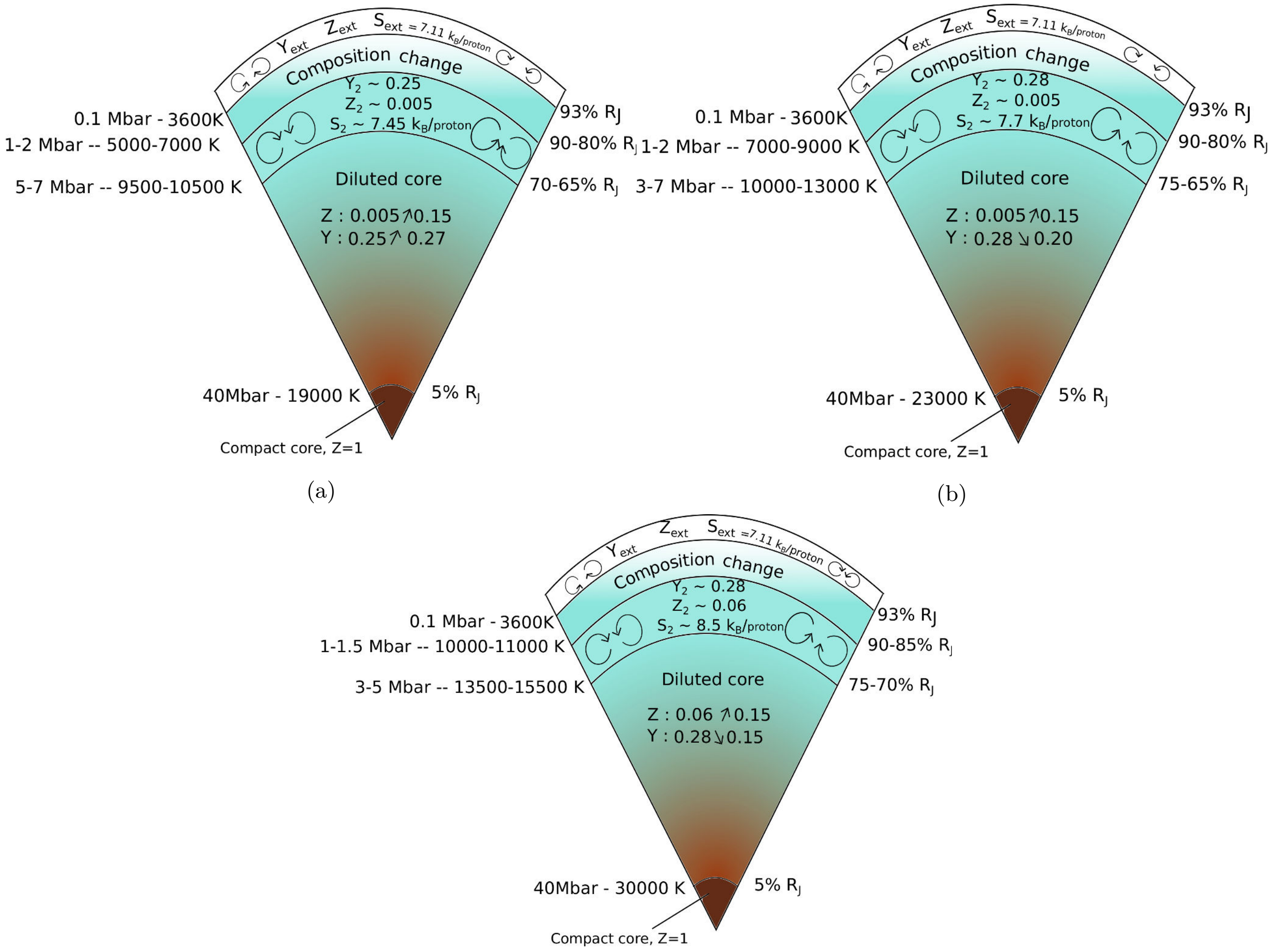

(a) (b)

(c)

Figure 4.5: Schematic internal structure of our final Jupiter models. $Y_{\text{ext}} = 0.23$, $Z_{\text{ext}} = 0.02$ as stated in the text. (a) The modest entropy increase between the outer and inner envelopes yields a moderate helium increase in this latter, and an inward helium enrichment in the diluted core (see text). (b) The larger entropy increase in the inhomogeneous boudary region yields a supersolar helium fraction in the inner envelope, but then the helium abundance decreases in the diluted core. (c) Our least favored model. An increase of both helium and heavy element abundances in the inner envelope requires a strong entropy increase, at the limit of what is physically achievable. A mixture of structures (a) and (c) is also possible, with a small increase in both helium and heavy elements. The required ΔS would be comparable to (b).

consequence, a small change in the $\sim 0.1-1$ Mbar region must be compensated by a strong change in the diluted core.

- *Impact on the high-order moments ($> J_4$).* Concerning the high order gravitational moments, they strongly depend on the value of J_4, as shown by Guillot et al. [2018]. For a given J_4, the other parameters affecting these moments are the external abundance of metals (as expected), and the mass of the central compact core. Changing

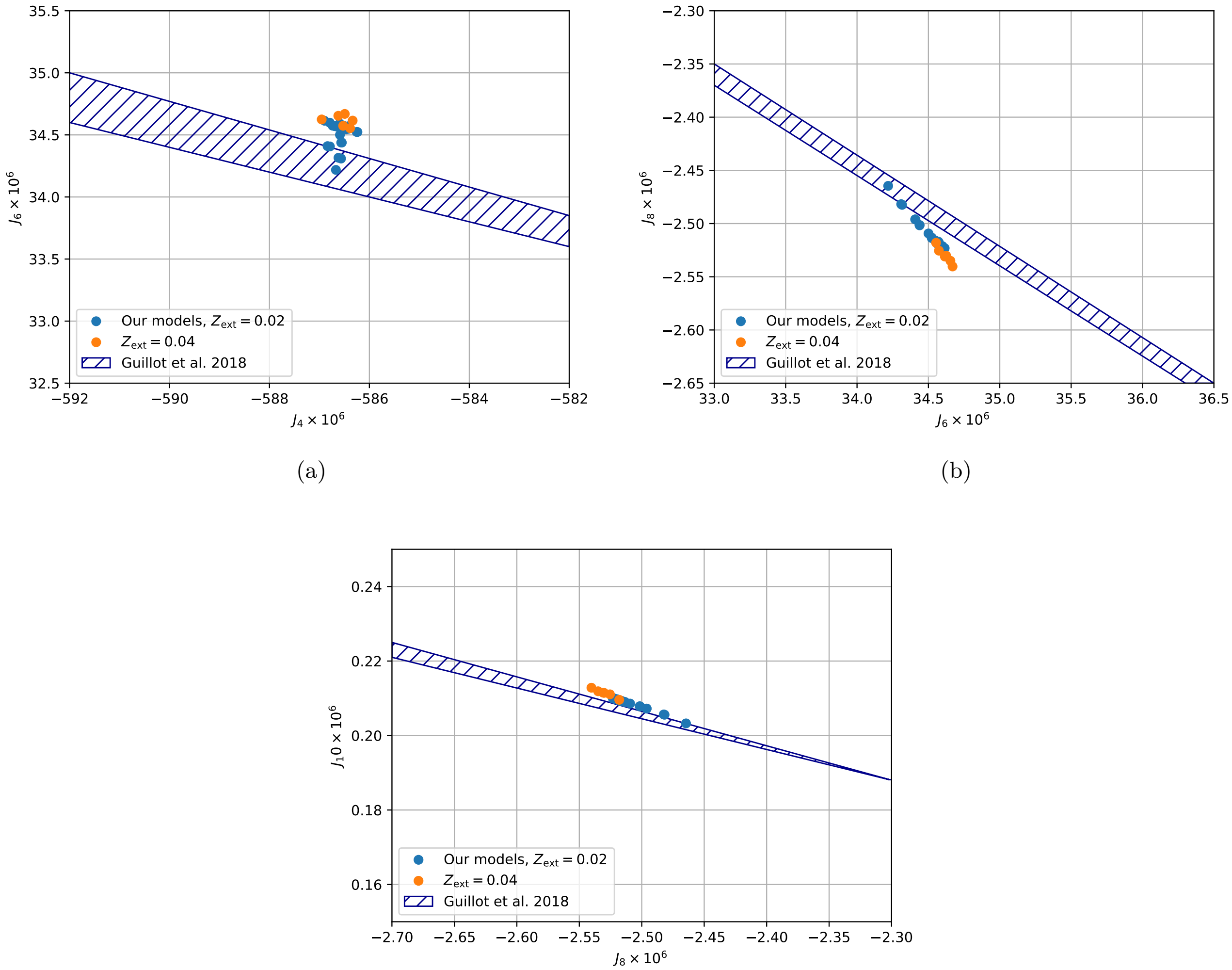

(a)

(b)

(c)

Figure 4.6: Gravitational moments we obtain with various models in the $J_k - J_{k+2}$ plans, for two values of $Z_{\rm ext}$. All the values are multiplied by 1×10^6 as done in e.g., Guillot et al. [2018].

the helium content within the inner convective envelope has almost no impact, as there is a trade-off between the inner abundances of helium and heavy elements and the entropy increase, without affecting the high order gravitational moments. Similarly, the position and extent of the boundary region of compositional change is a second order correction to the J_6 to J_{10} values. As a whole, we found out that the J_6 to J_{10} values are not much affected by the composition in the inner part of Jupiter, deeper than where the compositional change occurs.

Importantly enough, we found out that it is possible to obtain models with an *inward increase* of heavy elements in this domain ($\nabla Z < 0$) which fullfill all observational constraints (case (c)) contrary to the ones discussed in §4.3, provided the entropy change in the inhomogeneous region around ~ 1 Mbar reaches values $\Delta S > 1 k_{\rm B}/\text{proton}$.

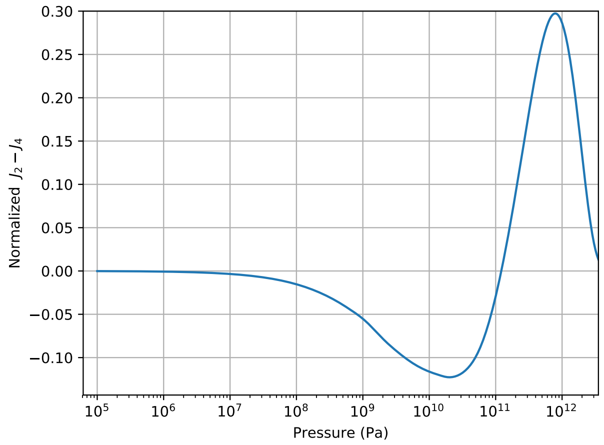

Figure 4.7: Subtraction of the contribution functions for J_2 minus J_4, both normalized to their maxima, with respect to pressure, for an isentropic model.

In contrast, models with an *inward decreasing* abundance of heavy elements ($\nabla Z > 0$) in this region require a more modest entropy change. If models with $\nabla Z < 0$ throughout the entire gas rich envelope ended up being representative of Jupiter's internal structure, this would put strong constraints on the phase diagrams of hydrogen and helium. They require a strong entropy discontinuity induced either by a PPT for $T \simeq 4500$ K (which implies a critical point at larger temperature) or by H/He differentiation and sedimentation, as layered convection alone cannot yield such an entropy jump. Therefore, *although not entirely excluded, models with $\nabla Z < 0$ throughout the envelope are rather uncomfortable.*

The fact that, surprisingly, the mass of the *compact* core affects the high order moments can be explained as follows. Since we consider the central compact core as spherical, it has no direct influence on the gravitational moments. However, with a massive central core, the rest of the planet must satisfy the J values with less available mass. Since the outer envelope composition is constrained by Galileo, one can only enrich the inner envelope or the *diluted* core to compensate. Fig. 4.7, however, shows that if there is a too large increase of density deeper than 2 Mbar, the increase of J_2 is larger than the one of J_4 (and even larger than the increase of the higher order moments, not shown). This leads to

- *Conclusion 1*: *for given J_2, a central compact core tends to decrease the moments of order $\geq J_4$ compared to a model with only a diluted core.*

Aditionally, increasing the mass of the compact core, the diluted core and the inner envelope implies to add more heavy elements in the inner regions of the planets, and the larger the amount of heavy elements in the deep layers the larger the required entropy jump ΔS between the outer and inner envelopes. This, in turn, has consequences on the high order moments: a model with a high entropy jump in the metallisation region implies a higher temperature, and thus a lower density for a given composition at given pressure in the Mbar region than a model with a small entropy change. The lower density means that this region has a smaller contribution to the gravitational moments than in the case of a small ΔS. Although, for J_2 and J_4, this can be balanced by a higher contribution of the internal layers (deeper than a few Mbars), this is not the case for the higher order moments.

To illustrate this result, we show in Figure 4.8 the differences ΔJ_n in the contribution functions J_2 to J_8 between a model with a small entropy change, $\delta S < 0.1\,\mathrm{k_B}$/proton, in the ionization boundary region, only due to a composition change, and a model with a total entropy discontinuity $\Delta S = 0.9\,\mathrm{k_B}$/proton. We see that the region of the outer (molecular) envelope has always a stronger contribution to the J's when the entropy change is small, as expected, whatever the order of the moment. On the other hand, the inner region of the diluted core has much more impact on J_2 than on the other moments. A strong ΔS thus requires more heavy elements in the diluted core to preserve J_2 while the high order moments will be almost insensitive to the enhanced composition in the diluted core. This leads to

- *Conclusion 2: an entropy jump in the envelope tends to decrease the value of the high order moments at a given J_2.* And a large enough entropy change is necessary to preserve the correct balance between the moments.

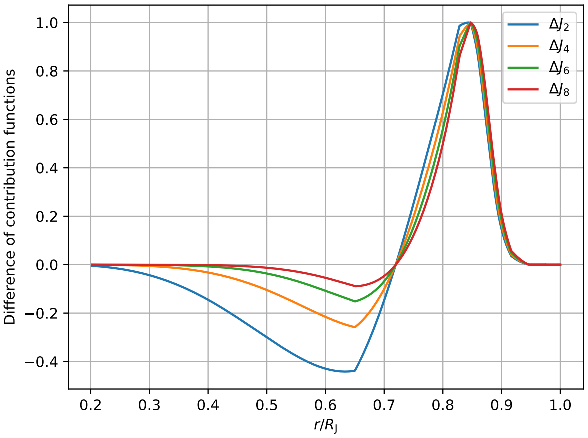

Figure 4.8: Normalized difference of contribution functions for J_2 to J_8 between a model with a small entropy change, δS, and a model with strong entropy change, ΔS.

This latter effect, however, is limited by the possible increase of entropy in the metallization boundary region allowed by physics principles. For central compact cores larger than $\gtrsim 5\,\mathrm{M}_\oplus$, one needs an entropy increase $\Delta S > 1\,\mathrm{k_B}$/proton, which, as discussed above, seems to be hardly possible at these temperatures. Figure 4.9 displays the values of the high order gravitational moments as a function of the entropy jump ΔS. Small (absolute) values of J_6, J_8 or J_{10} always require a very strong ΔS, except if we decrease the atmospheric Z_{ext}, violating in that case the Galileo constraint, as done in all recent studies. Models with no entropy jump in the gaseous envelope thus seem to be excluded, confirming the conclusion reached in §4.5.1.

As seen in Fig. 4.9, none of our models can match the 3σ error bars on J_6 for $\Delta S < 1\,\mathrm{k_B}$/proton when considering the contribution from the winds derived in Kaspi et al. [2018]. This is particularly true if the external abundance of heavy elements Z_{ext} is supersolar (see §4.5.2). When considering the dynamical correction from Kaspi et al. [2017], however, flows extending down to 3000 km are sufficient to explain the discrepancy with the observed gravitational moments. Therefore, either the ΔJ_6 correction due to the wind contribution in Kaspi et al. [2018] is underestimated, because of an erroneous estimation of the winds or the presence of North-South symmetric zonal flows which will affect the even gravitational moments, or the entropy increase must reach at least $\sim 1.5\,\mathrm{k_B}$/proton. In any case, a continuously increasing heavy element mass fraction with depth, i.e. $\nabla Z < 0$, in the Mbar region is hard to justify (on Fig. 4.9, such models all have $\Delta S \gtrsim 1\mathrm{k_B}$/proton).

As shown in Fig. 4.5, the valid models predict a size for the metallization boundary region, $l_b \approx 15\%$ of Jupiter's radius. Clearly, this is orders of magnitude larger than any possible interface due to a PPT. It can, however, be consistent with the size of the inhomogeneous H/He region, as this latter keeps expanding during the planet's cooling. Finally, as shown in §4.6.2, this region, characterized by a compositional gradient, is prone to layered convection, by itself characterized by a significant superadiabaticity and thus by its own entropy variation, to be added up to the one issued from a phase transition and thus contributing to the total ΔS.

Optimized Jupiter models

Figure 4.10 portrays the thermodynamic and composition profiles of our models consistent with all Galileo and Juno constraints, taking into account for this latter the correction due to differential rotation from Kaspi et al. [2017] and Kaspi et al. [2018], respectively. Profiles for an isentropic interior structure, inconsistent of course with the observed gravitational moments, are shown for comparison. The blue curves represent our favored models, with J_6 compatible with Kaspi et al. [2017] but not with Kaspi et al. [2018] while the red curves are the profiles obtained from a model with a lower J_6, at the limit of what can be reached according to Kaspi et al. [2018]. Globally, the pressure and density profiles differ by a few percents at most from the ones of the isentropic model, bearly seeable on the figure.

However, it is worth stressing that the density of the optimized model is smaller in the Mbar region than the one of the isentropic model whereas the opposite is true in the central regions (diluted and compact core). This is a direct consequence of the constraints arising from the gravitational moments. In contrast, the temperature departs from the isentropic profile for $R \lesssim 0.9 \times R_J$, i.e. within most of the interior, by a difference $\Delta T \simeq +1000$-2000 K. Interestingly enough, this temperature increase agrees very well with the value obtained by Fortney and Hubbard [2003] in the H/He inhomogeneous layer for a helium enrichment in the interior from $Y = Y_\odot$ to $Y = 0.35$, and a temperature gradient leading to overstable convection. As a consequence, the specific entropy increases from the outer to the inner envelope. This increase is steeper for the model with a lowered J_6. For this latter, the inner isentropic envelope occupies a very limited fraction of the planet, $0.89 \times R_J \lesssim R \lesssim 0.92 \times R_J$, and the diluted core extends up to 85% of the planet.

Within the diluted core, the specific entropy decreases drastically due to the strong increase in heavy elements (Figure 4.10(b)). We do not show the specific entropy and compositional profiles in the diluted core because of the degeneracy between helium and heavy element distributions in this region, which yield similar results for the gravitational moments. Not mentioning the fact that the entropy profile is of no real interest in this region. The

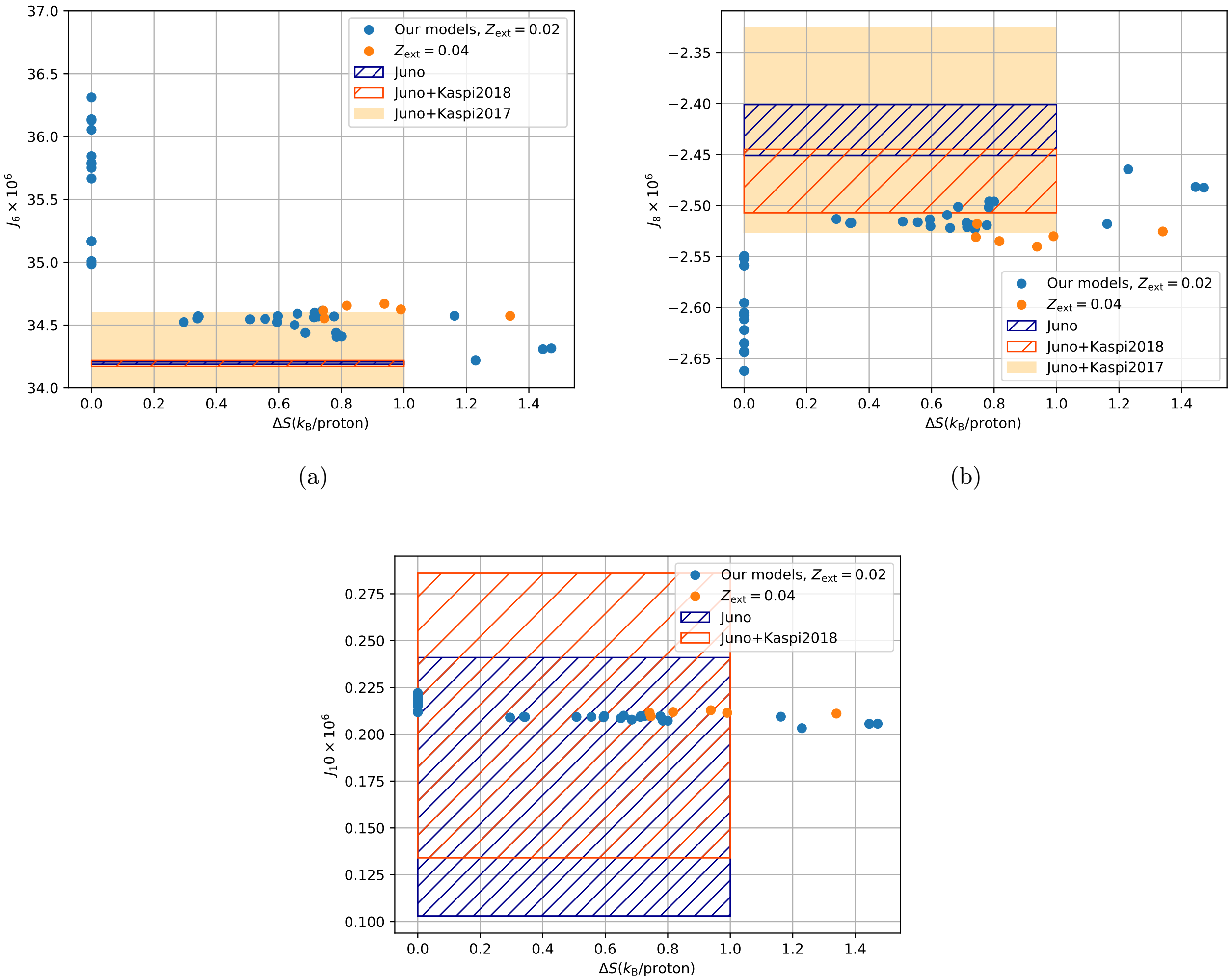

(a)

(b)

(c)

Figure 4.9: High order gravitational moments as a function of the entropy jump ΔS in the envelope. All these models have J_2 and J_4 values within the allowed range from Juno's observations with the Kaspi et al. [2018] correction , except those with $\Delta S = 0$ for which we could not even match J_4 (see §4.5.1). The Z_{ext} value is the atmospheric Z, 'Juno' corresponds to the observations of Juno with the 3σ error bars, 'Juno + Kaspi2018' are the observations corrected by the winds estimated in Kaspi et al. [2018], and 'Juno + Kaspi2017' includes the correction to the observed gravitational moments due to a differential rotation shallower than 3000 km, from Kaspi et al. [2017]. While several models are compatible with Juno's observations when taking into account the corrections due to differential estimated by Kaspi et al. [2017], this becomes much more difficult when considering the correction derived from the odd gravitational moments by Kaspi et al. [2018]. Note that, in this latter case, none of the models with $\Delta S = 0$ or $\nabla Z < 0$ can reproduce the gravitational moments of Jupiter.

only important parameter is the steepness of the gradient of composition between the inner envelope and the diluted core. The steeper the gradient, the smaller the diluted core needs to be to obtain the correct J_2, despite the decrease in density in the Mbar region (compared to an isentropic profile) that allows to decrease the J_4 to J_{10} values. The mean heavy element mass fraction is displayed in Fig. 4.10(b). As discussed in the text, Z is decreasing between the outer and inner envelopes ($\nabla Z > 0$). As mentioned earlier, although models with a continuously increasing Z ($\nabla Z < 0$) in the envelope can not be excluded, they require a very large entropy jump ($\Delta S > 1 k_{\rm B}$/proton), which seems difficult to reconcile with the examined physical processes (§5.2.1). Future work in this direction is certainly needed to help clarifying this issue.

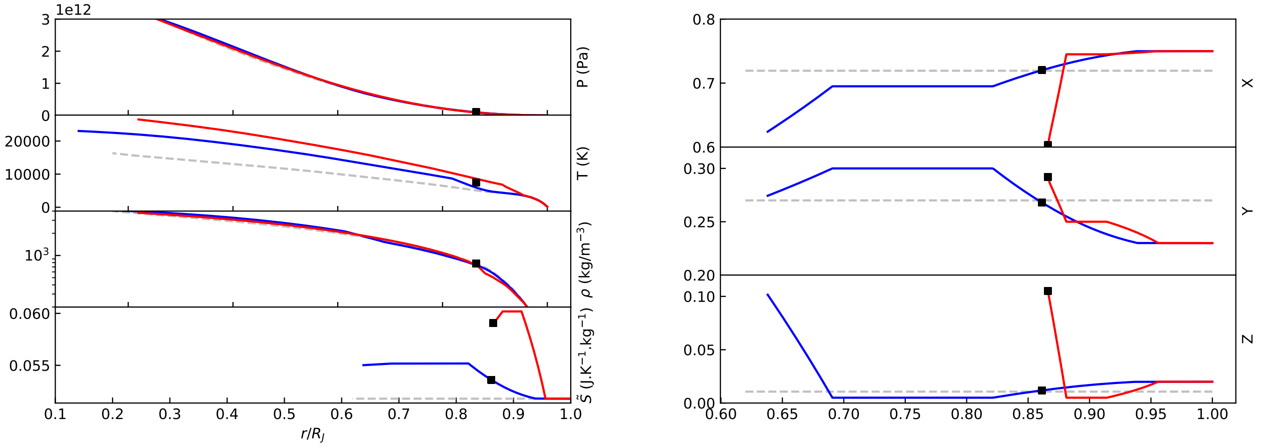

(a)

(b)

Figure 4.10: (a) Pressure, temperature, density and specific entropy as a function of radius for an isentropic (dashed gray) structure of Jupiter, a model with a high J_6 value (blue) and a model with J_6 compatible with Kaspi et al. [2018] (red). (b) Hydrogen (X), helium (Y) and heavy element (Z) mass abundances for the same models. The black crosses correspond to $P = 1$Mbar, about the region of hydrogen pressure dissociation/ionization.

Figure 4.11a portrays the mass profile of our typical optimized Jupiter interior structure fullfilling Juno and Galileo constraints with the wind correction of Kaspi et al. [2017]. An isentropic profile is shown for comparison. The black circle indicates the inner limit of the outer convective zone while the two crosses bracket the inner convective zone and the diamond corresponds to the limit of the compact core if present. The zoom on the right hand side shows the inner convective zone, encompassing around 30% of the mass of the planet. The heavy element distribution is displayed in Fig. 4.11b. For models wit no central compact core, the total amount of heavy elements in the planet is M_Z = 25-30 $M_\oplus$. Adding up a compact core yields up to M_Z = 40-45 $M_\oplus$.

Supersolar atmospheric abundance of heavy elements

As discussed in §4.3, we have taken a very conservative *lower limit* for the true average metal content in the atmosphere, $Z_{\rm ext}$, in our calculations. We have taken a solar value, while Galileo measured abundances of individual

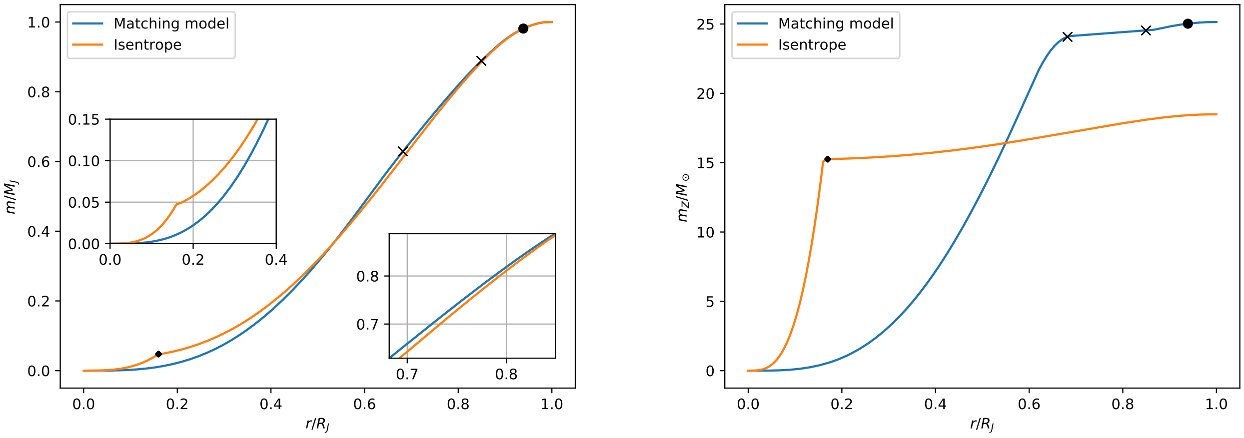

(a)

(b)

Figure 4.11: (a) Normalized mass as a function of radius for a model matching observational constraints and an isentropic model. (b) Mass of heavy elements (in Earth masses) as a function of radius for the same models.

heavy elements, excluding oxygen and neon, rather yield $Z_{\rm Gal}^{true} \approx (2-3) \times Z_{\odot} \approx$ 0.04-0.06. Interestingly, such a highly oversolar value seems to be supported even for oxygen by the latest observations of the great red spot [Bjoraker et al., 2018]. Increasing $Z_{\rm ext}$ for a given structure increases $|J_6|$ - $|J_{10}|$ and thus implies either a very strong differential rotation or a very large ΔS to preserve the moments. If $Z_{\rm ext} \simeq 0.05$, models with an inward increase of Z in the metallization boundary region lead to a ΔS much larger than the aforederived 1 k_B/proton maximum value consistent with physical estimates. This reinforces our previous conclusion: *Jupiter internal structures with an inward increase of heavy elements within the Mbar boundary region imply uncomfortable physical constraints:* the entropy jump or amount of differential rotation required to be compatible with the high order gravitational moments need to be very large. In contrast, *models with a locally decreasing abundance of heavy element within Jupiter's metallization boundary region fullfill all constraints with acceptable levels of entropy variation and differential rotation.*

Figure 4.9 portrays five models with $Z_{\rm ext} > Z_{\odot}$ (orange circles). We see that, for a given ΔS, these models have higher $|J_6|$ to $|J_{10}|$ values than models with $Z_{\rm ext} = Z_{\odot}$. Although some of these models are compatible with the correction due to differential rotation estimated in Kaspi et al. [2017], they are more difficult to reconcile with the observations when considering the correction to the even gravitational moments estimated in Kaspi et al. [2018]. We recall that the models of Figure 4.9 have J_2 and J_4 values consistent with Kaspi et al. [2018]. Because of the strong correlation between J_4 and J_6, further decreasing $|J_4|$, consistent in that case with Kaspi et al. [2017] but not with Kaspi et al. [2018], would allow us to decrease the $|J_6|$ and higher order moment values, expanding the range of plausible models.

4.6 Discussion

In this section, we examine in details the reliability of the various assumptions used in the models.

4.6.1 Hydrogen pressure metallization and H/He phase separation

First, following the nomenclature of Stevenson and Salpeter [1977a], we have assumed that Jupiter had a "hot start", meaning that the initial inner temperature of the planet was higher than the critical temperature of both hydrogen metallization, $T_c(H-H_2)$, and H/He demixion, $T_c(H-He)$ (for $x_{He}=0.08$). According to all existing numerical simulations aimed at exploring these issues, this is quite a safe assumption. Further work on the metallisation of hydrogen and the H/He phase diagram will enable us to discriminate between the sectors I, II and III of Figure 1 of these authors, namely:

- Sector I: if $T_c(H-H_2) < T(P) < T_c(H-He)$, where $T(P)$ is the local temperature at pressure P, but hydrogen is pressure ionized at this pressure, hydrogen metallisation is occuring smoothly but probably triggers H/He or Z_i/He immiscibility. The only possibility to deplete (resp. enrich) the inner (resp. outer) envelope in metals is to invoke the 2- or 3-body phase separations mentioned in §4.4.1.
- Sector II: $T_c(H-H_2) \sim T_c(H-He)$ is a simple reduction of the Sector I case. In both cases, an inhomogeneous region forms which is depleted in He and some Z-components, but in that case there is a possibly of H^+-rich bubble nucleation and thus uplifting He-poor, Z-rich bubbles and dropping He-rich dropplets (§4.4.1).
- Sector III: if $T_c(H-H_2) > T_c(H-He)$, H/He demixion has not started yet, the redistribution is due to the aforementioned H^+-rich, He-poor bubbles. Regarding the current work on metallisation and immiscibility of hydrogen and helium, this is probably the most unlikely situation.

These situations are imposed by the necessity to globally increase the metal content of the upper envelope (and conversely deplete the lower one) to fullfill Galileo's constraints, $Z_{\rm ext}=Z_{\rm Gal}$, but also to enrich the inner helium content, Y, to balance the Z decrease. As explored in §4.4, this implies to invoke either upward motions of H^+-rich bubbles associated with some heavy elements, or 2-body or 3-body immiscibility phase diagrams between partially pressure ionized heavy elements Z^{n+} (probably with $n\sim 1$) and neutral He, similar to what is occuring for H^+-He. Note that if, as found in all dedicated numerical simulations, hydrogen (or any heavy component) ionization triggers immiscibility with He atoms (or He-like ones), the Sector I case is the most likely one. This urges the need for numerical explorations of this type of diagram and, more generally, of the stability of H/He/Z mixtures under Jupiter internal conditions.

Noticeable differences still exist between modern ab-initio calculations aimed at characterizing the H/He phase diagram. Figure 4.12 portrays the immiscibility region predicted by some of these calculations with the T-P profiles obtained with our favored models fullfilling all Galileo and Juno constraints, taking into account either the Kaspi et al. [2018] (low J_6) or Kaspi et al. [2017] (high J_6) correction due to differential rotation. Figure 4.12(a) corresponds to interior structures with strongly superadiabatic layered convection occuring at $P \geq 0.1$ Mbar. Figure 4.12(b) displays two models (labeled 'Morales' and 'Lorenzen', respectively) for which the change of entropy is only due to the H/He phase separation, i.e. occurs at the corresponding critical pressures, without any layered convection above this layer. A Jupiter isentropic profile is shown for comparison. As seen in the figure, while, according to the Lorenzen et al. [2009] calculations, H/He phase separation could take place in some fraction of our favoured Jupiter interior models, it is not the case with the results of Morales et al. [2013b] (or Schöttler and Redmer [2018], not shown) which predict no H/He immiscibility in present Jupiter. For the models with no layered convection above the phase separation (dash dotted lines in Fig. 4.12(b)), the temperature gradient is probably too high for overstable modes to persist, and convection will prevail (see e.g., Figure 3 of Stevenson and Salpeter [1977a]). Although the lack of excess (non-ideal) mixing entropy in Lorenzen et al. [2009] calculations casts doubt on the reliability of their phase diagram, it is worth noting that a $\sim$ 200-800 K underestimation of the critical temperature in the 1-2 Mbar domain by Morales et al. [2013b] (no temperature error bar is shown in these calculations) would be consistent with immisciblity for our model with $Y_2 = 0.25$. Therefore, Jupiter's present internal structure could entail a region of layered convection region starting around $\sim$ 0.1 Mbar, associated with some change in composition, and a (probably small) region of H/He (most likely H/He/Z) immiscibility at deeper levels. Although more numerical exploration of this major issue is certainly needed, key diagnostics on H/He phase separation under the relevant conditions might be provided by existing experiments [Soubiran et al., 2013].

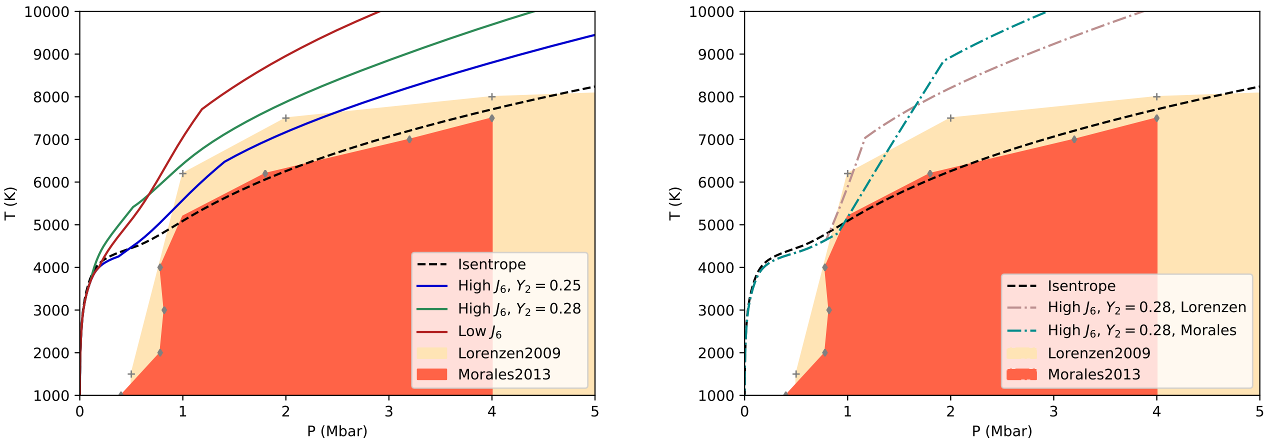

(a) (b)

Figure 4.12: Temperature-pressure profiles of different Jupiter models, overplotted on the immiscibility diagrams of Lorenzen et al. [2009] (pale yellow area) and Morales et al. [2013b] (orange area). All models (except isentrope) have J_2 and J_4 matching the Juno values corrected by the estimated differential rotation of Kaspi et al. [2018], and a mass abundance of heavy elements in the inner envelope $Z_2 = 0.005$. The Y_2 value is the mass abundance of helium in the inner envelope, as in Figure 4.5. 'Isentrope': fully isentropic structure, with $Y = 0.275$. 'High J_6': models with J_6 compatible with Kaspi et al. [2017] but not Kaspi et al. [2018]. 'Low J_6': model with J_6 compatible with Kaspi et al. [2018]. This latter model seems difficult to justify physically (se text). (a) Models with layered convection fo $P \geq 0.1$ Mbar. (b) The 'Morales' and 'Lorenzen' profiles are isentropic up to the onset of immiscibility according to the two related phase diagrams (see text).

As seen in Figure 4.12, it seems difficult to reconcile a H/He phase separation, according to the most recent calculations, with a model reproducing the Kaspi et al. [2018] J_6 value. Furthermore, the required entropy increase for this model leads to such a steep temperature gradient that unstable convection will prevail. It is thus very difficult to justify the very large entropy change ΔS in Jupiter's gaseous envelope required in this model on physical grounds. This suggests either a revision of the Kaspi et al. [2018] analysis, or the presence of North-South symmetric winds which are inconsequential for the odd gravitational moments, but would increase the correction to the even gravitational moments, rejoining the corrections obtained in Kaspi et al. [2017].

4.6.2 Layered convection

As found out in the previous sections, fulfilling both Galileo and Juno constraints, while preserving a global mean helium protosolar value $\bar{Y} = Y_{\odot}$ and a physically acceptable entropy increase ΔS in the hydrogen metallization region requires an inward decrease of heavy element abundance in this region, i.e. a locally positive gradient, $\nabla Z > 0$. We verified that, because of the $\sim 1/40$ heavy element to helium number ratio, this region still exhibits a positive molecular weight gradient, $\nabla \mu > 0$. In that case, large scale adiabatic convection can be inhibited and lead to a regime of small scale, suradiabatic double diffusive convection to transport heat. As mentioned previously, although a first order transition is not required to trigger such a process, it strongly favors it, as suggested for instance at the Earth's mantle boundary (e.g. Christensen and Yuen [1985]).

The condition for the onset of double diffusive convection reads (e.g., Stern [1960]):

$$0 < \nabla_T - \nabla_{\mathrm{ad}} < \frac{\alpha_\mu}{\alpha_T} \nabla_\mu, \tag{4.12}$$

where we have adopted the notations of Leconte and Chabrier [2012] ($\alpha_\mu = (\partial \mathrm{ln}\rho / \partial \mathrm{ln}\mu)_{P,T}$ and $\alpha_T = (\partial \mathrm{ln}\rho / \partial \mathrm{ln}T)_{P,\mu}$; note that $\nabla X = \partial X / \partial r$ is the usual gradient of X with depth, which differs from the often used notation $\nabla_X = \mathrm{dln}X / \mathrm{dln}r$). Under Jupiter interior conditions, double diffusive convection rather takes the form of layered convection, i.e. a series of small-scale convective layers of size l separated by diffusive layers, than oscillatory convection (e.g., Rosenblum et al. [2011]). As shown by Leconte and Chabrier [2012], the existence of double diffusive convection is controlled by the parameter α, which is the ratio of the size of the convective layer to the pressure scale height, $\alpha = l/H_P$. From their eqn.(21), we can relate this parameter to the suradiabatic gradient, $(< \nabla_{\mathrm{T}} > - \nabla_{\mathrm{ad}})$, by:

$$< \nabla_{\mathrm{T}} > - \nabla_{\mathrm{ad}} = \epsilon_d \times \left[(\Phi_0 \alpha^4 \epsilon_d)^{\frac{-1}{4(1+a)}} + (\Phi_0 \alpha^4 \epsilon_d)^{\frac{-a}{(1+a)}} \right], \tag{4.13}$$

with layered convection occuring when

$$10^{-9} - 10^{-6} \lesssim \alpha \lesssim 10^{-4} - 10^{-2}, \tag{4.14}$$

with, for Jupiter, the lower bound being more likely 10^{-5} (see Table 1 of Leconte and Chabrier [2012]).
As MacLaurin spheroids have by definition a constant density, layered convection cannot be prescribed very accurately with the CMS method. As for the case of a first order phase transition/separation, we have implemented a sharp entropy and composition change at constant T and P between consecutive layers. We can then verify, for the appropriate models, whether conditions (4.14) and (4.12) are fullfilled or not. Figure 4.13a displays the

values of (α_μ/α_T), calculated with the Chabrier et al. [2018] EOS, for an isentropic profile and for two profiles with an entropy increase in the Mbar region of 0.5 and $1\,\mathrm{k_B}$/proton, respectively. We see that this quantity increases with depth by an order of magnitude, between the ideal gas limit $\alpha_\mu/\alpha_T = 1$ in the external layers and the values prevailing at depth in Jupiter. This is particularly true for models with a small entropy increase. This favors the onset of layered convection deeper than ~ 0.1 Mbar. Figure 4.13b displays the values of α and of the parameter $R_\rho^{-1} = (\alpha_\mu/\alpha_T)\nabla_\mu/(\nabla_T - \nabla_{\rm ad})$ (overstable convection occurs for $R_\rho^{-1} > 1$, see Rosenblum et al. [2011], Mirouh et al. [2012], Leconte and Chabrier [2012]), for a composition change from $(Y_{ext} = 0.23\ , Z_{\rm ext} = 0.03)$ to $(Y_2 = 0.3\ ,\ Z_2 = 0.01)$, with an entropy increase $\Delta S = 0.45\,\mathrm{k_B}$/proton between 0.1 and 1 Mbar. We see that α and R_ρ^{-1} fullfill the conditions for the presence of layered convection in this domain. Models with higher ΔS (of at most $\sim 0.6\,\mathrm{k_B}$/proton, see §4.5.2) require larger ΔY. Globally, we verified that all our favored models do fullfill the conditions for the occurence of layered convection derived in Leconte and Chabrier [2012].

One caveat should be noted: when H_2 dissociates into atomic H^+, the mean molecular weight μ decreases brutally. According e.g. to Nellis et al. [1995], however, the fraction of dissociation is around 10% at 1.4 Mbar, and the molecular weight is roughly insensitive to dissocitation up to this pressure. Therefore, the decrease of μ do to hydrogen dissociation probably happens over a rather localized region between ~ 1.4 and 2 Mbar. It is not quite clear whether layered convection is still present or not in this domain (overshoot might occur) but we consider it localized enough to not significantly modify the aforecalculated temperature profile.

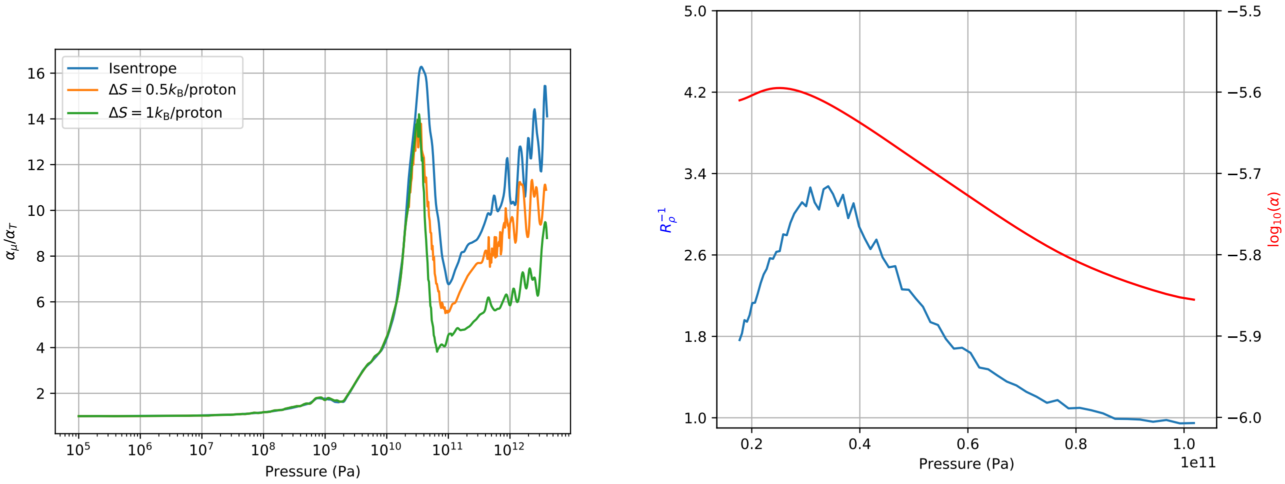

(a) (b)

Figure 4.13: (a) α_μ/α_T as a function of pressure for an isentropic model and two models with $\Delta S = 0.5$ and $1\,\mathrm{k_B}$/proton, respectively. (b) α (eq.4.14) and R_ρ^{-1} (see Leconte and Chabrier [2012]) for the model described in the text.

4.6.3 External impacts, atmospheric dynamical effects

As suggested in §4.4.1, Galileo's high heavy element abundances in the outermost part of the envelope could be due to recent impact or recently accreted material which would not have had time yet to be redistributed within the planet and thus would not affect its gravitational potential. In that case, Juno's contraints could be examined without taking into account the ones from Galileo. Let us examine such a possibility. Using standard equations of the mixing length theory (Kippenhahn and Weigert [1990], Hansen and Kawaler [1994]), it is easy to show that the typical convective velocity in Jupiter scales as:

$$v_{\rm conv} \approx 10 \left(\frac{\nabla - \nabla_{ad}}{10^{-8}}\right)^{1/2} \left(\frac{H_P}{10^6\ {\rm m}}\right)\ {\rm m\,s^{-1}}, \tag{4.15}$$

with $(\nabla - \nabla_{ad})$ ranging from $\sim 10^{-10}$ at the center to $\sim 10^{-6}$ near the surface, yielding $v_{\rm conv} \sim$ a few to about ~ 100 cm s^{-1} from the center to the surface.

This means that, within at most a few years, the external extra material will be mixed throughout most of the planet. It is quite clear that Jupiter has not accreted a few Earth masses of heavy elements in the past 20 years. The only source of uncertainty is Shoemaker-Levy 9. Although its mass is ridiculously small compared to the mass of the envelope, and even to the mass of heavy elements in the envelope of Jupiter, the energy deposited when it crashed onto the planet (end of July 1994) triggered uplifting of deep material (e.g, Bézard et al. [2002] or Moreno et al. [2003]). As Galileo entered Jupiter's atmosphere 1.5 year later (7 December, 1995), the material had probably be mixed again throughout the upper envelope (remember $v_{\rm conv} \approx 1$ m s^{-1} in this region) even though it is not completely excluded that this event has affected somehow Galileo's observations. Therefore, taking into account Galileo's observations of Jupiter's heavy element external abundance seems to be mandatory when trying to recover Juno's gravitational moments.

Atmospheric dynamical effects (for instance a vortex), on the other hand, could have produced a localised maximum concentration of heavy material, not representative of the (lower) average value. Additional information is provided by the Juno microwave instrument [Li et al., 2017] that suggests a rather unexpected amonia vertical profile. However, if we compare the Fig. 4 of these authors with the location where the Galileo entry probe dived (around 5-10° in planetocentric latitude), we see that, compared to the region deeper than 100 bar, Galileo can have only measured a lower limit of the amonia content. Indeed, there seems to be a maximum of amonia concentration in the equatorial regions, followed by a minimum in the mid latitudes. Galileo entry probe dived at the limit between these two regions, and, most importantly, the concentration anywhere above the 25 bar level is smaller than the one deeper than 100 bars, where convective mixing definitely takes place. Therefore it is rather unlikely that the measurements of Galileo, consistent with an increase of ammonia with depth up to 25 bars, are an upper bound of the heavy element composition.

One can also wonder whether the composition varies between $P = 1$ bar and $P = 100$ bar level, affecting the gravitational moments, and then should be parametrized instead of being assumed to be constant. Between two models with $(Y, Z) = (0.23, 0.02)$ and $(Y, Z) = (0.23, 0.04)$ in the external envelope, we get changes in J_2 and J_4, due to the first 100 bar variation, of at most 2×10^{-6} and 2×10^{-7}, respectively, about an order of magnitude smaller than the change due to differential rotation (Fig. 3 of Kaspi et al. [2017]). Variations of composition in the external envelope are thus a second order correction compared to differential rotation.

4.6.4 Magnetic field

Although the magnetic field at the surface of Jupiter has been shown to vary with latitude and longitude within an order of magnitude [Connerney et al., 2018], the leading feature is a dipolar field with moment $M = 4.170 \times 10^{-4}\,\mathrm{T}$. According to numerical simulations, self consistent dynamo action is generally found to start when the convective magnetic Reynolds number, i.e. the ratio of magnetic field production to Ohmic dissipation, $Rm = v_{rms} d/\eta$, where v_{rms}, d and η denote respectively the rms flow velocity, the thickness of the shell and the magnetic diffusivity, exceeds a critical value $Rm \gtrsim 50$ [Christensen and Aubert, 2006]. Using simple scaling arguments (e.g. Chabrier et al. [2007] and §4.6.3), it is easily verified that this condition is well fullfilled at the ionization boundary, located around $P \approx 1\,\mathrm{Mbar}$, where the density is $\rho \approx 800\,\mathrm{kg\,m^{-3}}$, radius $R \approx 0.85 \times R_\mathrm{J}$, and that deeper in Jupiter convective, metallic zone we get $Rm \gg 10^5$. This suggests that the primary dipole-dominated magnetic field is created at depth where Rm is significant, the electrical conductivity high, and the density contrast relatively mild. This is indeed what is found in state-of-the-art numerical simulations which reveal that the combination of a deep-seated dipolar dynamo and a magnetic banding associated with the equatorial jet reproduce Jupiter field geometry with realistic relative axial dipole, equatorial dipole, quadrupole and octupole field contributions [Gastine et al., 2014]. These simulations are also consistent with the suggestion that the mean internal field strength as well as the mean convective velocity scale with the available convective power [Christensen and Aubert, 2006]. Gastine et al. [2014] find that Jupiter's surface magnetic field strength, $B_J \simeq 7$ G, is consistent with a typical rms flow velocity ~ 3 cm s^{-1}, for a shell thickness extending from 0.2 to 0.99 R_J. Such a velocity is largely consistent with the maximum value derived in §4.6.3 around the metallization boundary. Although a dedicated study is necessary to explore this issue in the presence of an outer layered convection region, the rms velocity and the average conductivity should remain large enough for Rm to still exceed the critical value $R_m \approx 50$, and thus for the reservoir of convective power to still contribute appreciably to the dynamo action.

Defining R_{50} as the radius in the planet above which $Rm \lesssim 50$, Duarte et al. [2018] find that $R_{50} \simeq 0.9\,R_J$, due essentially to the big change of conductivity when molecular H_2 fully recombines, while values below $R_{50} \simeq 0.85\,R_J$ seem to be excluded with some confidence. This is consistent with our favorite model (Fig. 6) with or even without inclusion of the region of compositional change.

Interestingly enough, recent observations of the hemispheric difference in Jupiter's field geometry [Moore et al., 2018] are consistent with the superposition of two types of dynamo action, namely a thick shell dynamo, reponsible for the strong axial dipole, occuring at depth in the metallic region, and a thin-shell dynamo, yielding the observed hemispheric asymmetry, occuring further up in the envelope. A region of density gradient/layering between these two regions provides a very plausible explanation for such a separation.

Note that the large-scale field generation also constraints the size and or the magnetic/electric properties of the diluted core. In case this latter is unable to sustain dynamo action, this implies that the inner convective envelope must be sufficiently large to generate the magnetic field, limiting the maximum extension of the diluted core. This in turn limits the maximum mass of the central dense core. Indeed, as shown in the previous sections, the bigger the compact core the smaller (in absolute value) the high order gravitational moments but the bigger the diluted core. If, however, the conductivity in the diluted core is large enough to generate electric currents, flow motions generated by density contrasts (due e.g. to ill-mixed elements) and the Coriolis force resulting from Jupiter's spin might be able to produce magnetic fields and sustain a geodynamo process similar to the one taking place near the Earth iron core. In that case, the diluted core might contribute substantially to the field generation, extending the available domain for global dynamo action. We realyze that at this stage such a discussion is purely speculative and we hope to motivate dedicated explorations of these issues as Jupiter's magnetic field generation can certainly help assessing the reliability of the present structure models.

4.6.5 Evolution

Constraints due to Jupiter's evolution have been briefly aluded to in §4.4.2. Our favored models suggest an entropy jump $\Delta S \approx 0.3$-1 k_B/proton between the outer molecular envelope and the inner metallic one (see Fig. 4.9), which yields a warmer inner temperature for the planet than in the absence of ΔS. This temperature difference, due to the entropy gradient in the inhomogeneous region, will keep increasing with time as either layered convection and/or H/He phase separation and helium sedimentation will keep progressing. This yields a heat release from inside to outside during the planet's evolution. Jupiter's observed luminosity today, however, suggests that, if H/He phase separation does occur in the planet, it must contribute only modestly to its cooling history. This condition can be fullfilled for several reasons. (1) If a significant fraction of this energy is devoted to heating up the interior (keeping the inner convective envelope on a high isentrope), the energy release, whatever its source, remains modest along cooling. Not mentioning the fact that H/He might become miscible again. (2) H/He separation in Jupiter may have started only recently, contributing negligibly to Jupiter's luminosity (power) whatever the He sedimentation energy release. (3) The H/He immiscible region, yielding a temperature gradient, might encompass a relatively modest fraction of Jupiter's interior. (4) More interestingly in the context of our favored models, core erosion, if it occurs, implies that a fraction of the planet's internal energy must be consumed in the redistribution of heavy elements against gravity, and thus be transformed in potential energy (see e.g. Stevenson [1985], Guillot et al. [2004]). This consumption of Jupiter's available internal energy will speed up the cooling of the planet. Even in the presence of layered convection, the final energetic balance might eventually decrease or increase the planet's cooling rate [Leconte and Chabrier, 2013].

In summary, if the present final models are representative of Jupiter's present internal structure and composition, its cooling history should include (i) layered convection, (ii) H/He (or other elements) phase separation plus helium dropplet sedimentation and (iii) core erosion. Finding out what will be the resulting impact of these three processess upon the planet's global cooling history is a higly non trivial task, which can hardly be intuited or inferred with simplistic models.

4.6.6 Does the observed outer condition lie on an adiabat?

In this section, we raise an other issue regarding Galileo's constraints. Galileo's measurements are taken from 1 to about 25 bar and in all existing models, including the ones derived in the previous sections, the temperature profile is supposed to follow an isentrope, starting from the observed value 165 K at 1 bar. It is not obvious, however, that the deeper profile (between say 1 and 100 bars) does follow an adiabat. The measurements of Galileo show an increase of heavy element abundance with depth, indicating that, at $P \simeq 25$ bar, the probe has not reached yet a well mixed region. In case of departure from adiabaticity, the outermost temperature gradient could then be larger than the adiabatic one, implying that the real inner entropy profile lies on a warmer isentrope than the one obtained if one assumes it is given by the $P = 1$ bar, $T = 165$ K condition.

Let us consider, for instance, the possible impact of rotation. There is presently no well defined theory for turbulent convection in the presence of rotation so we can only rely on estimates. At the pressure level $P \simeq 10$ bar in Jupiter external envelope, the optical depth is $\tau \gg 100$, so except for the possible impact of rotation, one can safely assume that the profile is isentropic at this level. This pressure corresponds to $\rho \sim 10^{-3}\,\mathrm{g\,cm^{-3}}$, $g = GM_J/R^2 \simeq 20$ m s^{-2}, $T \sim 200$ K, and thus a typical convective length $l \sim H_P = P/(\rho g) \approx 10^5$ m, about 1% of the planet's radius. Assuming all Jupiter internal flux, $\mathcal{F} \simeq 5.4$ W m^{-2}, is transported by convection and using the usual equations of the Mixing Length Theory [Kippenhahn and Weigert, 1990], this yields a typical suradiabatic gradient $\Delta\nabla T_0 = (\nabla - \nabla_{ad})_0 \approx 10^{-6}$ at this pressure level, i.e. a characteristic convective velocity $v_{conv} \lesssim 1$ m s^{-1}. Since Jupiter angular velocity is $\Omega_J = v_{rot}/R_J = 1.76 \times 10^{-4}$ rad s^{-1}, the ratio of inertial to Coriolis forces, known as the Rossby number, at 10 bars is thus $Ro = v_{conv}/(l\Omega) \gtrsim 0.1$. Convection at the top of the upper envelope, where the Galileo measurements have been made, should thus be only moderately affected by rotation. It is also easily verified that the Coriolis acceleration is much smaller than the gravity, $R_J\Omega^2 \ll g$, which allows to perform a linear stability analysis of the MLT equations in the presence of a Coriolis force, $2\Omega \times v_{conv}$, [Chandrasekhar, 1961]. Additionally, given the value of the Rossby number, this linear analysis can be performed in the strong rotation limit [Stevenson, 1979]. This yields for the suradiabtic gradient in the presence of rotation in the region probed by Galileo [Stevenson, 1979]:

$$\Delta\nabla T \simeq (\Delta\nabla T_0)^{3/5} \left(\frac{\Omega^2 l}{g}\right)^{2/5} \simeq 6 \times 10^{-6}. \tag{4.16}$$

This estimate shows that rotation cannot yield a strong departure from adiabaticity in the outermost envelope layers of Jupiter, as expected from the inferred Rossby number value, in contrast to deep convective regions (see e.g. Chabrier et al. [2007]).

Moreover, at a pressure of 1 bar, the atmosphere is composed of alternative superrotating and underrotating stripes in latitude. Both at the equator, where advection dominates, and in the mid to high latitudes, where geostrophy applies, one can show that the horizontal variation of temperature due to the winds is of the order of a few percents in latitude and longitude, with a maximum at the equator (as confirmed by the observations of Fisher et al. [2016] and the temperature profiles from GCM calculations of Schneider and Liu [2009]). In that regard, the measurement of Galileo are rather an upper bound than a lower bound on the temperature, and the deviations from these measurements are small.

In conclusion, it seems quite safe to assume that the external condition defined by the $T = 165$ K, $P = 1$ bar condition lies on an adiabatic profile.

4.7 Conclusion

In this chapter, we have examined models of Jupiter aimed at fulfilling *both* the most recent Juno observations and the Galileo constraints. Our calculations were carried out with the Concentric MacLaurin Spheroid method with all the necessary mathematical and numerical constraints [Debras and Chabrier, 2018]. Because of the tension due to the high observed abundances of helium and heavy elements in the external envelope and the low values of the high-order gravitational moments, the number of possible interior models is limited. We verified that, even if the 1 bar temperature observed by Galileo departs from an adiabat because of the impact of rotation, the departure remains modest enough to take the $P = 1$ bar, $T = 165$ K observed values as the external isentrope conditions.

We first showed that the new data from Juno cannot be reproduced with conventional 2- or 3- isentropic homogeneous layer models. These latter are not able to match both the values of the gravitational moments and the external abundance of metals. This first conclusion, which confirms the one of Wahl et al. [2017], is that there must be at least two regions of compositional gradient within the planet interior.

Our thorough analysis suggests that the planet should be composed of four main regions, namely, moving inward from the surface: (I) the external isentropic, homogeneous molecular/atomic $\mathrm{H_2}$/He/Z envelope, extending downward to about 93% of the radius of the planet, (II) an inhomogeneous domain around $P \sim 0.1$-2 Mbar, encompassing the region of hydrogen pressure ionization, of size about $\sim 10 - 15\%$ of the radius, characterized by a gradient of composition $(\nabla X, \nabla Y, \nabla Z)$, and an inward positive entropy change, $\Delta S > 0$ (i.e. a locally negative entropy gradient, $\nabla S = (\partial S/\partial r) < 0$), (III) a second inner isentropic, homogeneous, metallic envelope hydrogen, extending from the bottom of region II down to $60 - 70\%$ of the radius, lying on a hotter isentrope than the outer envelope $(S_{III} > S_I)$ with, most likely, a smaller metal mass fraction than in the outer homogeneous enveloped $(Z_{III} < Z_I)$, and (IV) a diluted Z-rich core composed of volatiles, exhibiting a compositional gradient. Potentially, a central compact seed can be present, essentially composed of solid iron and silicates.

A major result of this study is that a substantial entropy increase, $\Delta S \gtrsim 0.3\,\mathrm{k_B}$/proton is necessary in the inhomogeneous region II to fullfill all the observational constraints. If not, one needs to invoke very strong differential rotation to explain the values of the high order gravitational moments, at odds with the estimate of Kaspi et al. [2018] (and even Kaspi et al. [2017] if $\Delta S = 0$). This suggests the occurence of either suradiabatic layered convection and/or a first order phase transition, be it hydrogen pressure ionization or H/He phase separation. If this entropy increase lies in the range $0.3 \lesssim \Delta S \lesssim 1\,\mathrm{k_B}$/proton, which seems to be inferred from various relevant physical processes, the abundance Z of heavy elements in region II must be locally *decreasing*, i.e. exhibiting a *positive gradient of composition*, $\nabla Z > 0$, but an increasing molecular weight i.e. a positive molecular weight gradient, $\nabla \mu > 0$, due to the much larger helium fraction at the bottom of region II. In case of a strong entropy increase in region II, $\Delta S > 0$, it is possible to strongly reduce the value of the high order gravitational moments while still fullfilling Galileo's external metal abundance, by invoking the presence of a central compact core. The first impact of this latter is to restrain the mass domain of Jupiter's interior impacting the moments. Although it is possible to find models with an inward increasing metal abundance within region II, $\nabla Z < 0$, compatible with Juno and Galileo, they require such a large ΔS or amount of differential rotation that it seems hardly possible to justify them on physical grounds.

Note that there is a degeneracy of solutions between the change of entropy ΔS in region II and the outer differential rotation. The stronger ΔS the shallower and weaker the differential rotation, enabling eventually values consistent with the estimate of Kaspi et al. [2018]. In contrast, if differential rotation extends deeper inward and/or is stronger than suggested by these authors, the change of entropy across the boundary region can be significantly lowered. According to the study of Cao and Stevenson [2017], however, the differential rotation cannot extend too deep, as magnetic reconnection eventually occurs deep in the envelope, leading to rigid rotation.

The entropy jump ΔS in region II is also related to, and can be constrained by other conditions. Namely, (i) the mass of the central dense core M_c. Indeed, as shown in the study, the mass of the central core is directly correlated with ΔS (the larger ΔS the larger M_c) and then anti-correlated with the amplitude of the high order gravitational moments. (ii) The gradient of helium and heavy elements within the boundary region II: the larger the increase in Y and Z between region I and III (most probably an increase in Y and a decrease in Z), the larger the ΔS required to reproduce Juno's data. (iii) At last, ΔS is constrained by the physics of dense matter, namely the nature of hydrogen pressure ionization (critical temperature and pressure and entropy discontinuity) and by the miscibility diagram not only of H/He but also of the various dominant heavy elements in metallic hydrogen. Finally, it is worth pointing out that, even in the absence of a first-order transition, region II, characterized by a strong compositional change, is prone to layered convection. As examined in §4.6, the inferred profile is indeed consistent with conditions derived in Leconte and Chabrier [2012] for the presence of layered convection.

The inward decrease of the mean heavy element mass fraction in region II, and thus the oversolar value in the upper envelope inferred from Galileo, can have different explanations. In case the local temperature at the H_2-H^+ metallization pressure P_c is lower than the critical (PPT) temperature ($T < T_c$), nucleation of H^+-rich bubbles can occur, associated with some heavy elements, and move upward across the critical line, enriching continuously the upper envelope I in (some) heavy elements. Since hydrogen ionization immediately triggers H/He phase separation, with the formation of drowning He-rich dropplets, this process yields at the same time an enrichment of He and associated species in the lower envelope III. In case the above temperature condition is not fullfilled, hydrogen pressure ionization occurs smoothly, there is no bubble nucleation. In that case, the only possibility to enrich the upper envelope I in heavy elements - except for an external impact - is immiscibility of some species in the H/He/Z mixture at the relevant temperature and pressure, yielding a large equilibrium concentration of these species in the low pressure, low temperature molecular phase. In case of an external impact, however, some process (PPT, H/He phase separation or layered convection) must have occured during Jupiter's lifetime to prevent homogeneous redistribution of the envelope. As mentioned above, in all cases, it seems difficult to avoid the presence of a first-order transition or persistent superadiabatic layered convection in Jupiter's gaseous envelope around the $\sim$ Mbar region. Accurate calculations of the planet's long term evolution are definitely needed to assess or reject the viability of some of these static models. As mentioned in §4.6.5, however, properly carrying such calculations appears to be a task of enormous complexity.

In conclusion, we have derived in this study interior models of Jupiter able to reproduce *all* the observed stringent gravitational constraints from the Juno mission and the outer helium and heavy element abundances from Galileo. As shown above, however, because of the lack of precise characterization of major physical processes, there is still a degeneracy of possible models. Indeed, neither experimental nor numerical explorations of these processes provide yet definitive information about the related fundamental questions. This illustrates the tight link between fundamental physics and astrophysics. Additional constraints also arise from the differential rotation in the planet. Indeed, high order gravitational moments are essentially only sensitive to the outermost region of the planet, constraining the available level of differential rotation (see notably Hubbard [1999]). As explained above, more constraints on differential rotation will bring strong constraints on the change of entropy in the pressure ionization boundary domain, and subsequently on the mass or even the presence of the central compact core. This issue will be explored in a forthcoming paper. At last, it is worth mentioning that the most favored models able to fullfill both Galileo's and Juno's constraints, according to the present study, are basically the ones, or at least among the ones intuited and explored in great details by Stevenson & Salpeter 40 years ago in their two seminal papers and by Stevenson [1985] !

Chapter 5

From the core of Jupiter to the atmosphere of hot Jupiters

> *This is one corner... of one country, in one continent, on one planet that's a corner of a galaxy that's a corner of a universe that is forever growing and shrinking and creating and destroying and never remaining the same for a single millisecond. And there is so much, so much to see*
>
> *Matt Smith* - Doctor Who

5.1 Introduction

In the previous chapters, we were able to constrain the interior of Jupiter thanks to decades of observations and successive spacecraft missions that have had the opportunity to orbit around the planet. From these models, we would want to be able to give constraints on the interior of Jupiter like planets accross the galaxy, which could yield an unprecedented understanding of the physical phenomena at stake during planetary formation and evolution. However, it is quite obvious that there is not going to be any sattellite orbiting extrasolar planets in the next decades, at best. Therefore, Jupiter has to be used to infer knowledge on extrasolar giant planets, which has to be combined with the maximum information we can extract from the limited observations of these far away worlds.

With the discovery of extrasolar planets, numerous new challenges were to solve. The first exoplanet observed, 51 Pegasus b (Mayor and Queloz [1995]), was in itself a puzzle, as no one really expected to observe a Jupiter like planet 10 times closer to its star than Mercury ! The answer was actually already predicted by the litterature, where 15 years ago Goldreich and Tremaine [1980] had considered the interactions between a disk and a planet, showing that Jupiter should have migrated on less than million of years timescales.

Therefore, the first striking discovery is that the solar system is not a template for planetary systems accross the galaxy. There exists a much wider range of mass, radius, excentricities ... for planets in the Milky Way only. Typically, planets denominated super Earths and mini Neptunes (see e.g., Winn [2018], Mordasini [2018]) are found to be relatively common, although none of them exist around our sun. An important consequence is that comparing exoplanets to the 8 planets we knew of before the 1990's is not enough. With more than 20 years of observations, trends and statistical results can be derived on the repartition of planets accross the galaxy [Santerne, 2018]. Care must be taken when interpreting these observations. Biases are of primordial importance: to date, no Earth-twin planet have been found, as they are probably the most difficult to observe, which does not mean they don't exist. Similarly, with the Kepler surveys we know more transiting planets that non transiting planets (see notably Morton et al. [2016] and Figure 5.1), and the distribution subsequently derived must be decorrelated from the observational preferences, easing the discovery of large, close in planets orbiting small stars.

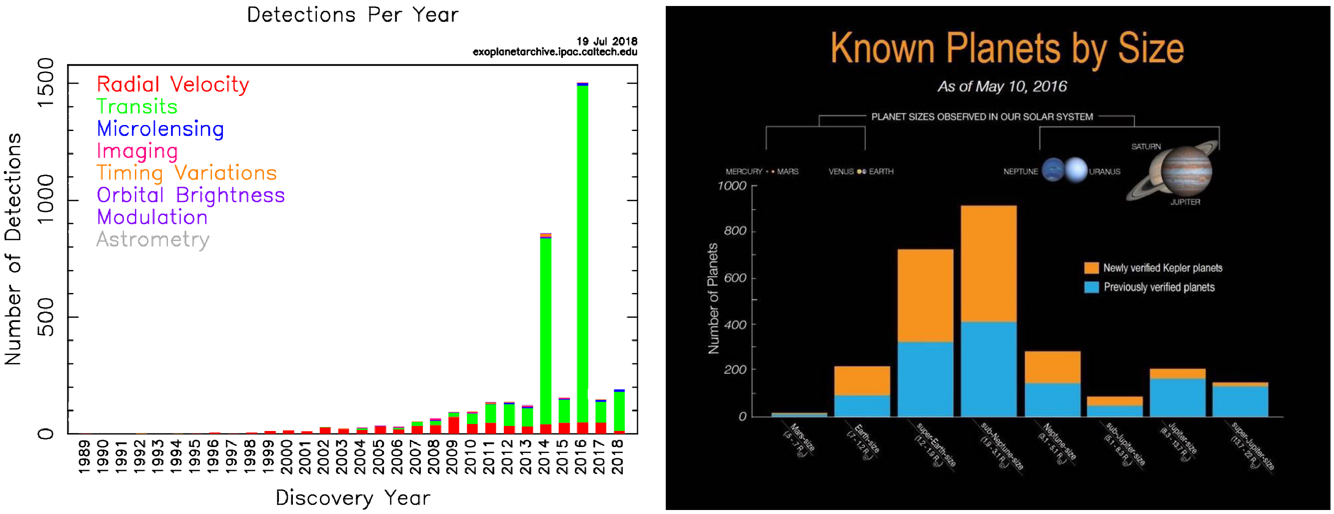

(a)

(b)

Figure 5.1: (a) Number of planets discovered in the last 25 years and their method of discovery. (b) Radius estimation of the discovered planets on the 10^{th} of May 2016, with the announcement of 1284 newly discovered planets from Kepler. Credits: NASA Ames

Among these new worlds, the Pegasi-like planets are of particular importance. Their closeness to their parent star and their size, comparable to Jupiter, make them relatively easy to observe and characterise through both radial velocity technics and transit photometry or spectroscopy. The radial velocity technics relies on the fact that the center of mass of the system star plus planet is not exactly in the center of the star [Wright, 2018]. A spectroscopic analysis will therefore allow to measure precisely the Doppler shifting of the spectral rays of the star due to the motion relatively to the center of mass of the system, and allow for a determination of the mass of the planet given that the mass of the star is known (and the inclination of the orbit of the planet relatively to the observer, the real value is $M \sin i$ where M is the mass and i the inclination). Quite logically, the easiest planets to detect with this technics are the massive planets, far enough from their star to displace sufficiently the center of mass but close enough so that the orbital period of the planet is short and the amplitude of the Doppler shifting is high. The Pegasi-like planets are particularly suited for these observations, and 51 Peg b was actually discovered through Doppler spectroscopy of the star.

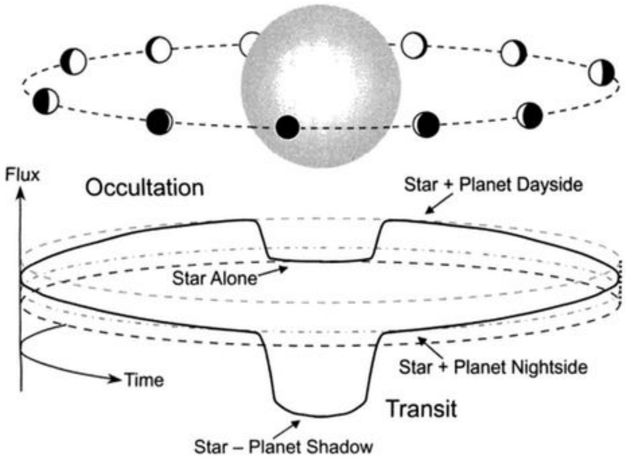

Figure 5.2: Image credit: Josh Winn.

The transit photomotry technics consists in observing the luminosity of a star, and wondering what is the effect of a planet crossing the line of sight of the observer [Deeg and Alonso, 2018]. When the planet passes between the observer and the star, during what is called the primary eclipse, there is a dip in the luminosity of the star which is directly related to the size of the planet compared to the size of the star and the latitude of the transit in the star coordinates. When the star is between the observer and the planet, during the secondary eclipse, there is another dip in the luminosity due to the loss of the reflected light of the star from the planet. A schematic representation of transits is displayed on Figure 5.2. The observations of the luminosity of the star during a full orbital period of the planet is called a phase curve [Parmentier and Crossfield, 2018], and this phase curve contains clues on the radius of the planet and its orbital eccentricity (and on atmospheric dynamics, as shown in the next section). Logically, the easiest planets to detect with this technics are large planets (orbiting small stars) with small orbital distances, and the Pegasi-like planets are therefore particularly suited to transit photometry.

Additionally, the spectroscopy of a transiting planet can be of particular interest. During the secondary eclipse, the only light received by an observer is the emitted light from the photosphere of the star. A spectroscopic analysis of this light allows to characterise the composition of the externalmost layers of the star [Alonso, 2018]. However, during the primary eclipse, a part of the light is completely blocked by the planet, but at the limbs of the planet, the light received from the star can go through the atmosphere and reach the observer (provided the integrated optical depth is less than one). Therefore, if the composition of the atmosphere (or rather of the limbs of the atmosphere) is different from the composition of the star, additional absorption rays will be possible to detect. The transit spectroscopy allows to characterise some regions of the atmosphere of the planet [Kreidberg, 2018].

Because of the unknown on the mass and the uncertainty on the orbit of the potential planet from a phase curve only, detecting a planet through transit photometry needs to be validated by another observation, typically radial velocitiesl. As the Pegasi-like planets are suited for both these technics, they are often characterized through both transiting photometry/spectroscopy and radial velocity. Hence, it is possible to estimate the mass, the radius and have clues on the atmospheric composition of transiting, close-in gas giants. Because of their resemblance with Jupiter but with an orbital radius 10 times smaller than the semi major axis of Mercury thus a much higher received flux from their stars, these planets have been denominated "hot Jupiters".

Our knowledge of the planets themselves though remains quite low, because of the difficulty to understand a planet from very limited observations, at best its mass, its radius and a hint on its atmospheric composition (notably when coupled to atmospheric retrieval methods, Madhusudhan [2018]. To date, because of the reasons above explained, hot Jupiters are the best characterized extrasolar planets. Understanding with precision their propriety and composition could provide clues on their formation and evolution, and globally on the common physical mechanisms at stake in all the stages of the life of a planet. Interestingly, because of their small orbital distances hence strong tidal interactions with their stars, hot Jupiters are expected to be tidally locked (see Baraffe et al. [2010] for a review) as the Moon is to the Earth. Therefore, half of the planet is expected to receive extreme insolation, while the other half never receives any light from the star. There is no such antisymmetrical heating of a deep atmosphere in the solar system, and the understanding of their externalmost layers needed new, comprehensive and extensive studies (see e.g., for a review on radiative trasnfer Heng and Marley [2018] and Heng and Showman [2015] for atmospheric dynamcis). As we have shown in Chapter 4, the external differential rotation, winds and temperature structure has consequences on the internal structure. The dynamics and thermodynamics of the atmosphere of hot Jupiters is therefore a mandatory piece of the puzzle to understand extrasolar planets.

In this chapter, we first expose the issue of the inflated radius in section 5.2, that exhibits the tight link between atmospheric conditions of hot Jupiters and interior structure. This lead us to detail the use of global circulation model to study the evolution of planetary atmospheres in section 5.3. We then detail the understanding of equatorial superrotation of hot Jupiters prior to this thesis in section 5.4. Section 5.5 concludes on the connection between interior models and atmospheric dynamics, and we study further atmospheric dynamics in chapters 6 and 7.

5.2 The inflated radius: a connection between atmospheric dynamics and the interior structure

5.2.1 Observations

In 2000, the star HD209458 was observed both with Doppler imaging and transit photometry (Henry et al. [2000] and Charbonneau et al. [2000]), and HD209458b (hereafter HD209) became the first planet to be characterized by two observation techniques. Although its radius and mean density were coherent with the predictions from the evolution study of Guillot et al. [1996], a more comprehensive work on the atmosphere of strongly irradiated gas giants (Goukenleuque et al. [2000]) showed that the radius of HD209 was too big for its age and mass. Because of the closeness to its parent stars, the atmospheric temperature of HD209 is much higher than Jupiter or Saturn, and one would expect a heated gas to expand, but the degree to which the radius is inflated indicates that the whole planet is substantially heated up compared to Jupiter or Saturn.

More precisely, let us consider that HD209 is composed of a polytropic gas following the equation of state $P = K\rho^\gamma$

(Jupiter is well approximated by a polytrope with $\gamma = 2$, see e.g., Zharkov and Trubitsyn [1978]). From there, the specific entropy s of the planet can be expressed as (see e.g., Hansen and Kawaler [1994]):

$$s = \frac{\mathcal{N}_\mathrm{A} k_\mathrm{B}}{\mu} \ln(K), \tag{5.1}$$

where $\mathcal{N}_\mathrm{A}$ is the Avogadro number and μ the molecular weight, assumed constant for simplification. Chapter 7 of Hansen and Kawaler [1994] detail the link between K, and R, the radius: it can be shown that $K \propto M^{2-\gamma} R^{3\gamma-4}$. Hence, combining it with equation (5.1) and using the fact that the total entropy S_tot is of the order of sM:

$$R \propto \exp\left(\frac{\gamma - 1}{3\gamma - 4} \frac{\mu S_\mathrm{tot}}{\mathcal{N}_\mathrm{A} k_\mathrm{B} M}\right) . \tag{5.2}$$

Hence, for a given mass, the radius of a planet is proportional to the log of the total entropy: a convective planet of the mass of Jupiter with a much hotter interior than Jupiter would have a significantly bigger radius (for adiabatic interiors, a higher temperature at a given pressure is equivalent to a higher entropy).

Considering the discussion of Chapter 4, an isentropic interior of a Jupiter like planet can seem surprising. However, because of the intense stellar irradiation, the temperature at 200 bars, a typical pressure of connection between the atmosphere and the radiatively inactive interior, is of the order of 2000-3000 Kelvin where Jupiter is $\sim$ 800K at the same pressure. Therefore, as we have shown that Jupiter internal temperature might lie at the limit of hydrogen-helium immiscibility and first order metallisation, hot Jupiters are not expected to undergo a first order phase transition/separation, and the only opposition to convection would be persistent layered convection. An adiabatic interior is therefore a rather probable structure.

Almost twenty years after the original discovery of the inflated radius of HD209, numerous hot Jupiters have been observed and their properties questioned, and the problem of the inflated radius remain. We show on Figure 5.3 the radius as a function of the received flux from all the planets from exoplanet.eu that are sufficiently well characterized. Clearly, there is a trend between size of the radius and received flux.

5.2.2 Kinetic or ohmic dissipation

Guillot and Showman [2002] were amongst the first to explore the issue of the **inflated radius** on theoretical grounds. Their main idea is that, considering that hot Jupiters have a convective interior, if a certain amount of stellar energy is able to reach and be deposited at the limit of the convective zone then it would be advected all the way to the center by the convective plumes, heating the interior and puffing the planet up. This is confirmed by the study of Bodenheimer et al. [2001], which showed that the inflation of the radius is independent of location of the deposition of energy within the convective interior.

The key question is: how to bring stellar energy to the convective interior? Previous studies (e.g, Bodenheimer et al. [2001] or Lubow et al. [1997]) suggested that tidal heating or eccentricity damping could lead to a non negligible heating of the interior. However, the timescales to which these phenomena occur make it unlikely for them to be the reason of the present inflated state of hot Jupiters. Guillot and Showman [2002] showed that the stellar flux is

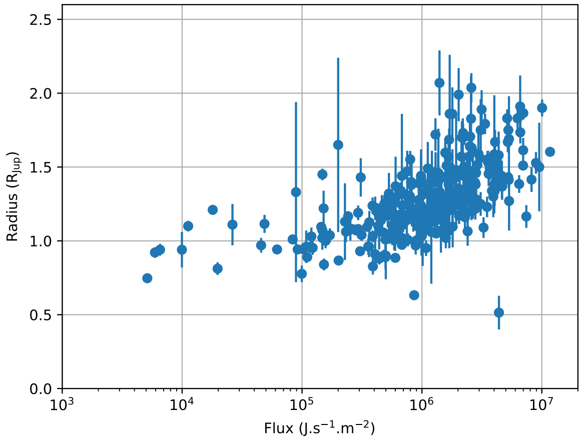

Figure 5.3: Radius as a function of the received flux from all the planets discovered with a radius superior to 0.5 times the radius of Jupiter and a mass between 0.2 and 10 times the mass of Jupiter. Horizontal error bars not displayed for visual aid. Source: exoplanet.eu

unlikely to penetrate deeper than a few bars, and it is quite improbable that this source of energy only would contribute to sufficient heating of the atmosphere. Therefore, their idea is that a part of the stellar flux is transformed into kinetic energy, that can be deposited deeper by the breaking of planetary waves or Kelvin-Helmotz instabilities. According to their analysis, a few percent only on the stellar flux needs to be converted into kinetic energy and dissipated sufficiently deep to explain the inflation of HD209. Earth's atmospheric study (see e.g., Peixoto and Oort [1992]) suggest that this percentage is not impossible, although quite important.

Batygin and Stevenson [2010] proposed another interesting idea, extending on the necessity to heat up the interior. Because of the strong irradiation, one can expect the atmosphere and interior of hot Jupiter to be ionised to a significant level. As alluded to in the previous chapter when refering to Cao and Stevenson [2017], the zonal flows cannot be too strong when the medium is highly ionized as Ohmic dissipation prevents strong differential motions. In the atmosphere of hot Jupiter, the intense forcing and especially the extreme day to night contrast is expected to trigger intense zonal flows. Roughly, assuming that the temperature gradient between the day side, heated by the star, and the night side generates a pressure gradient that triggers longitudinal winds, the gradient of the momentum equation yields:

$$\vec{v} \cdot \vec{\nabla} \left(\frac{v^2}{2} \right) \sim -\frac{1}{\rho} \frac{\mathrm{D}p}{\mathrm{D}t} \; . \tag{5.3}$$

Assuming a simplified Newtonian cooling, where an equilibrium temperature is prescribed as well as a relaxation timescale to converge to the solution (see notably Heng et al. [2011] which details a benchmark Newtonian cooling scheme for hot Jupiter), one can write:

$$\frac{\mathrm{D}T}{\mathrm{D}t} = \frac{T_{\mathrm{eq}} - T}{\tau_{\mathrm{rad}}}, \tag{5.4}$$

hence

$$\frac{\mathrm{D}p}{\mathrm{D}t} = \rho R \frac{T_{\mathrm{eq}} - T}{\tau_{\mathrm{rad}}}, \tag{5.5}$$

where τ_{rad} is the radiative timescale that varies with depth or pressure and we have used the ideal gas equation (2.11f) combined with incompressibility: $\mathrm{D}\rho/\mathrm{D}t = 0$. An order of magnitude for the winds U can thus be estimated:

$$U^3 \sim \frac{LR\Delta T_{\mathrm{eq}}}{\tau_{\mathrm{rad}}}, \tag{5.6}$$

where L is a characteristic distance and ΔT_{eq} the difference between the equilibrium day side temperature and equilibrium night side temperature. Assuming $\tau_{\mathrm{rad}} \sim 10^4$s which is characteristic of the 0.1bar level (Heng et al. [2011] or Showman and Guillot [2002]), $\Delta T_{\mathrm{eq}} \sim 1000$K a plausible differential heating for tidally locked planets, $R \sim 4 \times 10^3 \mathrm{J.kg^{-1}.K^{-1}}$ typical for the composition of hot Jupiters [Mayne et al., 2014a] and L of the order of the distance between the day and night side hence $L \sim \pi R_p$ with R_p the radius of the planet:

$$U \sim 4\mathrm{km.s^{-1}}\ . \tag{5.7}$$

This is most probably an overestimated value as it is about two times the sound speed and would lead to the emergence of Kelvin-Helmotz instabilites (Showman and Guillot [2002] or Fromang et al. [2016]), but shows that the intense heating is prone to generate extreme winds. Ohmic dissipation can thus significantly heat up the interior by converting kinetic energy into heat.

Another limit of the above estimation is that such a differential heating, associated with such strong winds, can lead to a state of equatorial superrotation, as seen on many planets of the solar system: the whole equator would have a roughly constant prograde speed (depending on height), greater than the velocity arising from the rotation of the planet alone, reducing the longitudinal temperature gradients because of the strong advection. This situation was first suggested by Showman and Guillot [2002] for hot Jupiters, and then confirmed by all subsequent studies. Section 5.4 is devoted to the understanding of superrotation, but we detail here another inflation mechanism that relies on these strong winds: the advection of potential temperature.

5.2.3 Advection of potential temperature

Tremblin et al. [2017] have detailed another mechanism for heating up the deep interior of hot Jupiters that does not rely on the direct dissipation of solar energy. Instead, it results of a global balance between the strong zonal winds excited by the stellar heating and the vertical winds that arise from mass conservation. We here assume that superrotation is present at the equator, and justify it in the next section numerically and theoretically in the next chapter.

Anlytically, at the equator, because of North-South symmetry the meridional momentum equation (2.11b) vanishes and solutions cannot be obtained without the prescription of an additional equation. The idea of Tremblin et al. [2017] is to define a depth-dependent ratio factor α that characterizes the importance of meridional mass fluxes relatively to vertical mass fluxes to balance the longitudinal mass fluxes:

$$\frac{1}{r^2}\frac{\partial(r^2\rho w)}{\partial r} = \frac{1}{r\alpha}\frac{\partial(\rho v)}{\partial \phi}\ . \tag{5.8}$$

If $\alpha \to \infty$, then the longitudinal mass fluxes are completely balanced by meridional mass fluxes where they are balanced by vertical fluxes in the case $\alpha \to 0$. Two questions then arise: how to prescribe α, and what does this imply for the atmosphere?

The value of α cannot be constructed from first principles, and although one might try to explore the parameter space the depth dependency of α makes it quite a time consuming task, with hardly meaningful physical results. Instead, Tremblin et al. [2017] decided to evaluate α from 3D numerical simulations with the use of a global circulation model (GCM, see next section). The issue with 3D GCM is that the time to converge to a steady solution for the whole atmosphere (down to a few tens of bars) is extremely long, so the values of α cannot be trusted deeper than $\sim$ 10bars from the simulations used in Tremblin et al. [2017]. Fortunately, the whole effect pictured in the paper is not dependent on the deepest value of α, and tests with different constant values of α between 3 and infinity deeper than 10 bars do not alter the picture.

Qualitatively, α above a few bars is of the order unity, hence the longitudinal mass fluxes lead to non negligible vertical mass fluxes. Once deep enough in the atmosphere, where the differential longitudinal mass fluxes become negligible, the differential vertical mass fluxes must vanish as well, which implies that the vertical speeds must be inversely proportional to ρr^2. Hence, the value of the vertical speed at the connection between the radiatively forced atmosphere, where longitudinal mass fluxes persists, and the quiescent atmosphere determines the motion in the deep atmosphere. This value is intrisically linked to the α profile in the upper atmosphere. Once in the deep atmosphere but not yet in the convective regions (which sets is at $\sim$ 40bars in the absence of radiatively driven vertical velocities [Chabrier et al., 2004], hence probably deeper in our case), Tremblin et al. [2017] have shown that:

$$\frac{\partial \ln \theta}{\partial \ln P} = \frac{\gamma - 1}{\gamma}\frac{H_{\mathrm{rad}} r^2}{\dot{M}_r g}, \tag{5.9}$$

where θ is the potential temperature, H_{rad} the heating rate from the star evaluated with radiative transfer calculations [Amundsen et al., 2016] and $\dot{M}_r = w\rho r^2 = \mathrm{cte}$. Hence when the heating rate becomes small enough compared to the other terms of equation (5.9), between 10 and 100 bars according to Tremblin et al. [2017], the potential temperature is constant with pressure: the structure is that of an adiabatic structure, although the medium is not in a convective state. The depth where this situation begins is inversely proportional to $\dot{M}_r = w\rho r^2$: the larger the vertical velocity at the junction with the radiatively quiescent atmosphere (hence the larger the α profile in the upper atmosphere), the higher the atmosphere reaches this potential temperature conserving structure. Hence, the vertical winds triggered by the stellar heating advect potential temperature in the deep interior. Figure 5.4 shows the equlibrium thermodynamic profile for a case with $\alpha = 2$ or $\alpha = 100$, constant in the upper atmosphere (this second case corresponds to the case with no vertical fluxes, usually obtained with 1D radiative transfer codes). The result is clear: the existence of significant vertical mass fluxes heat up the deep atmosphere of the planet, eventually connecting to a hotter adiabatic structure in the deep interior.

Obviously, none of the processes presented throughout this section are exclusive: Ohmic and kinetic dissipation

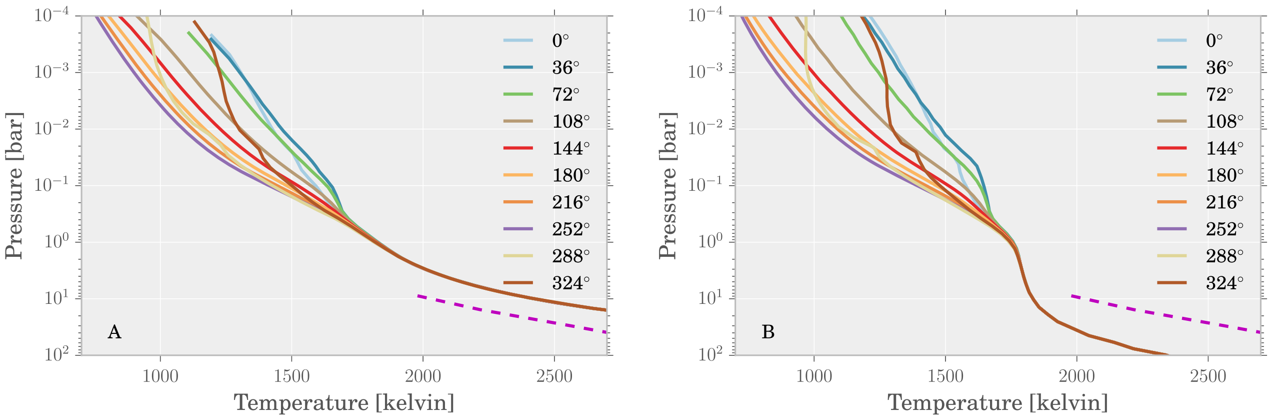

Figure 5.4: Equatorial pressure-temperature structure of the atmosphere at different longitudes for $\alpha = 2$ (A) or $\alpha = 100$ (B) constant in the upper atmosphere. The pink dashed line portrays the thermal profile obtained in the evolutionary models with extra energy of 1% of the stellar luminosity, leading to a radius increased by 40% while the inner adiabat of (A) leads to an increase of 60% in the radius.

can increase the effect of radius inflation by advection of potential temperature, and there is no clear consensus on which is the dominant effect. Nonetheless, these works all show the need to constrain as precisely as possible the dynamics and radiative behaviour of the atmosphere of extrasolar planets. Analytical arguments are not necessarily enough regarding the complexity of the mathematical treatment of the Navier-Stokes and energy equations, and are often driven by the results from numerical simulations. Such simulations are performed with global circulation models.

5.3 Global Circulation Models

As eluded to in chapter 1, the complexity of the Navier-Stokes equations makes them impossible to solve analytically for real three dimensional flows. Additionally, the treatment of radiative transfer is a complicated issue of prime importance in the atmosphere, where the optical depth is small compared to unity [Amundsen et al., 2014, 2016]. The understanding of planetary atmospheres is therefore greatly improved with the use of numerical solvers: global circulation models, although their treatment of the physics is necessarily idealized. We review in the next section the simplifications that can be made in the study of hot Jupiters with GCM, before discussing the level of complexity of the GCM used at the university of Exeter.

5.3.1 Common simplifications

In this section, we detail the physical simplifications performed in different global circulation models. The next section is devoted to detailing the numerical treatment of the equations. Because of the complexity of a planetary atmosphere, global scale study cannot be performed without neglecting or idealising some physical phenomena. For example, if one wanted to correctly treat the dissipation of energy by turbulent processes, one would need to resolve the scale at which kinetic energy is transformed into heat. This scale is, with any reasonable theory, many orders of magnitude smaller than planetary scale on which atmospheric processes happen. Current computational resources are not able to treat both atmospheric flows and turbulent dissipations on timescale relevant for planetary flows evolution, and turbulence is prescribed or diagnosed through dissipative terms as physically motivated as possible. Many such approximations can be performed to include non smaller scale processes or second order correction of physical processes.

The first simplifications that can be made when using GCM are in the Navier Stokes equations themselves (Eqns. (2.11a) to (2.11g)). Most GCMs applied to hot Jupiters solve the primitive equations of meteorology, involving the approximation of vertical hydrostatic equilibrium, and a shallow atmosphere (combining the constant gravity, shallow-fluid and traditional approximations, see Vallis [2006]; White et al. [2005]). Namely, the primitive equations assume:

$$r \approx R_p \text{ and } \frac{\partial}{\partial r} = \frac{\partial}{\partial z}, \tag{5.10}$$

$$\frac{\partial p}{\partial z} = -\rho g \tag{5.11}$$

$$f' = 2\Omega \cos\phi = 0, \tag{5.12}$$

$$\tag{5.13}$$

where z is the local cartesian height and R_p the radius of the planet. This states that the aspect ratio of the atmosphere is small, hence its height is small compared to its width, and allows as well not to take into account the metric terms involving the vertical speed w as well as setting $f' = 0$ as it represents Coriolis accelerations due to vertical motions.

The hydrostatic equilibrium is particularly useful when modelling atmospheres. It states that the pressure is a strictly increasing function of depth: therefore, depth can be replaced by pressure. This is particularly useful for hot Jupiters: at a given height, the pressure between the day side and night side can be so different because of the intense heating experienced in the day side that pressure based coordinates can be more suited to the study of planetary flows. These primitive equations are solved in the context of hot Jupiter by e.g, Cooper and Showman [2005], Rauscher and Menou [2012], or Heng et al. [2011]. However, in the very high atmosphere, hydrostatic balance breaks and this assumption might be too restrictive.

Probably the most restrictive approximation is in the treatment of radiative transfer. A perfect radiative transfer calculation would require to know both the exact composition of the atmosphere with depth and the radiative opacities of all the atoms and molecules. This is obviously out of reach. The first numerical study of hot Jupiters [Showman and Guillot, 2002, Cooper and Showman, 2005] have applied a Newtonian cooling scheme. This consists in prescribing a radiative timescale, representative of the microphysical equilibration to heat transfers, and an equilibrium temperature structure towards which the atmosphere would tend if there were only thermodynamical effects (notably no advection). For hot Jupiters, this mainly implies a hot day side and a cold night side in the upper atmosphere and once the optical depth approaches unity this day-night temperature difference tends to zero. Namely, the energy equation (2.11e) in this approximation writes:

$$\frac{\mathrm{D}\theta}{\mathrm{D}t} = \frac{\theta}{T}\frac{T_{\mathrm{eq}} - T}{\tau_{\mathrm{rad}}} \tag{5.14}$$

where T_{eq} is the 3D equilibrium temperature profile and τ_{rad} the radiative timescale, often prescribed as pressure dependent. The Newtonian cooling allows to treat the radiative transfer in a very simple and efficient way, although the reliability of the results can be questioned. It is therefore a very efficient tool to grasp the essence of the dynamical and thermodynamical evolution of the atmosphere, but cannot provide actual quantitative prediction. Mainly, it has been used in the first GCM studies [Showman and Guillot, 2002, Cooper and Showman, 2005] or for benchmarking [Heng et al., 2011].

Without the use of a complete radiative transfer solver, time and memory consuming for a numerical solver, the thermodynamics of the atmosphere can be simplified with the use of the two stream approximation with grey [Rauscher and Menou, 2012] or average opacity schemes [Dobbs-Dixon and Agol, 2013]. However, this has been shown to yield inaccurate heating rates [Amundsen et al., 2014]. As discussed in [Amundsen et al., 2014], extending on the work of Showman et al. [2009] and Lewis et al. [2010], one needs to couple the two stream approximation with the correlated k-method to obtain accurate fluxes and heating rate for hot Jupiter. We will not detail this any further, and refer to Amundsen et al. [2014, 2016, 2017] and references therein for additional explanation.

Finally, additional physical processes not included in the equations can be approximated by the addition of source or dissipative terms. Turbulence can be prescribed as a rate of conversion from kinetic to thermal energy, as we highlighted in the introduction. We also mentioned gravity waves in chapter 1. According to Watkins and Cho [2010], the damping of the small scale gravity waves should aslo generate a source of heating in the atmosphere. Unfortunately, these waves are not resolved by GCMs, hence their dissipation is not included in the coarsely discretized resolution of the Navier Stokes equations. As for turbulence, one could add the thermodynamical effect of these waves although their dynamical effect is not captured. Quite clearly, there exists numerous other processes not present in the numerical resolution of Navier Stokes equations, but one must also take care not to generate spurious effects while trying to simulate physical effects and looking for a maximum number of corrections to the numerical solver might be misleading. In essence, this paragraph raises the problem of dissipation in a global sense. We detail this further in the next section, with the presentation of the way our own GCM, the Unified Model, solves the Navier Stokes equations.

5.3.2 The Unified Model

There are many numerical ways of solving the Navier-Stokes equations, depending on the context and the dominant physical mechanisms. In this thesis, we have used the GCM of the university of Exeter: the unified model (UM) []. We will therefore focus on the method used by the UM as exposed in Mayne et al. [2014a], although other approaches exist.

The UM is a finite-difference code where the atmosphere is discretised onto a latitude-longitude grid, using a staggered Arakawa-C grid Arakawa and Lamb [1977] and a vertically staggered Charney-Phillips grid Charney and Phillips [1953]. Globally, this states that the values of the physical quantities are calculated at different interfaces of numerical cells, staggered across the 3D grid with regular spacing in longitude, latitude and radial direction. Figure 5.5 shows the shape of the staggered grid.

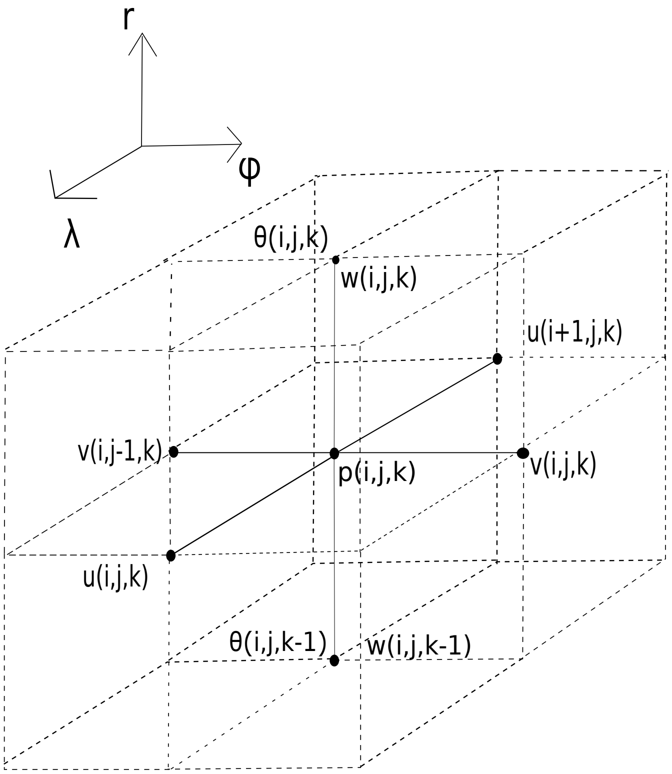

Figure 5.5: Staggered grid for numerical calculation. v goes from the south pole to the north pole thus has one more point in latitude. w and θ go from bottom to top of the atmosphere thus have one more point in height. u is only alternated with other quantities, having the same number of points in longitude. Finally p and ρ are in the middle of the cell, having the same number of points than u

The code is semi-Lagrangian in space and semi-implicit in time: the code employs semi-Lagrangian advection where the values for advected quantities are derived at interpolated departure points, and are then used to calculate quantities within the Eulerian grid. For the semi-implicit scheme the temporal weighting between the ith and the (i + 1)th state is set by the coefficient α which can vary between zero and one, and is set to 0.55 in our simulation for hot Jupiters. For each atmospheric timestep a nested iteration structure is used. The outer iteration performs the semi-Lagrangian advection (including calculation of the departure points), and values of the pressure increments from the inner iteration are back substituted to obtain updated values for each prognostic variable. The inner iteration solves the Helmholtz (elliptical) problem to obtain the pressure increments, and the Coriolis and nonlinear terms are updated.

The ENDGame (Even Newer Dynamics for General atmospheric modelling of the environment) dynamical core (the part of the GCM solving the discretised fluid dynamics equations of motion) of the UM is based on the non-hydrostatic deep-atmosphere equations (Staniforth and Wood [2003, 2008]; Wood et al. 2013), and does not make the approximations incorporated in the primitive equations [White et al., 2005]. The UM also includes a twostream radiative transfer scheme with correlated-k method, but simpler schemes like Newtonian cooling schemes can be used.

An important aspect of the UM as applied to hot Jupiters is the treatment of diffusion. This has been explained in Mayne et al. [2014a], and here we recall the main points. Many astrophysical codes include an artificial viscosity, where the controlling parameter can be altered to set the level of eddy or turbulent dissipation. Correctly formulated, an artificial viscosity includes the conversion of kinetic energy to heat via terms appearing in the momentum and thermal energy equation. For GCMs, and in meteorology, the term dissipation represents a similar scheme where losses of kinetic energy are accounted for in the thermal energy equation. Another scheme also regularly used in GCMs, is termed diffusion, in this case a similar approach is used to remove kinetic energy, but this is not accounted for in the thermal energy equation. Such diffusion can be viewed as a numerical tool to remove grid scale noise. Although the operational version of the ENDGame dynamical core includes no explicit diffusion, in our case, as with many other GCMs, we have incorporated a diffusion scheme. Whichever scheme is used the loss of kinetic energy can affect the characteristic flow and the maximum velocities achieved (Heng et al. [2011]; Li and Goodman [2010]).

Namely, in our working version of the UM, a diffusion operator D is applied to the longitudinal momentum equation in the form:

$$D(u) = \left(\frac{1}{r^2 \cos\phi}\right)\left(\frac{\partial}{\partial\lambda}\left[\frac{K_\lambda}{\cos\phi}\frac{\partial}{\partial\lambda}u\right] + \frac{\partial}{\partial\phi}\left[K_\phi \cos\phi \frac{\partial}{\partial\phi}u\right]\right), \tag{5.15}$$

where K_λ and K_ϕ are diffusion coefficients that depends on the resolution and an absolute diffusion coefficient K. This coefficient cannot be accurately prescribed from physical expectations, and therefore it is chosen to ensure stability in the scheme rather than reproduce the expected flows. If a measure of the maximum speed of the equator of hot Jupiters was observationnally provided, a better constrain on K could be derived.

Contrary to completely Eulerian schemes based on finite volume methods, the UM does not have to solve Godunov schemes: instead, the semi Lagrangian interpolation coupled with diffusion regularizes the solution, preventing the need for solving shocks conditions. This might actually be an issue for hot Jupiters: the flow can reach speeds of $1-2$ times the sound speed, but the low resolution of our simulation coupled with the Lagrangian interpolation would smooth away any situation where a shock should be triggered. That being said, other studies focused on the study of shocks in hot Jupiters [Fromang et al., 2016, Ryu et al., 2018] have shown that the main features of the flow remain correct even without shocks. Same applies for instability: the coupling of interpolation, diffusion and low resolution might prevent the formation of instabilities, particularly any Kelvin-Helmotz instabilities from strong shear flows at the equator. It is definitely worth exploring further these issues, particularly for the most irradiated planets.

Finally, it is worth stating that the code has been benchmarked against classical situation for planetary atmospheres. Notably, in Mayne et al. [2014b] the UM has been shown to qualitatively reproduce the Held-Suarez test [Held and Suarez, 1994] or expected results for tidally locked Earth like planets [Merlis and Schneider, 2010] and a shallow hot Jupiter following [Menou and Rauscher, 2009].

5.3.3 A step further: clouds and disequilibrium chemistry

It must be kept in mind when working on GCMs that incorporating additional physics in a very idealised solver might lead to erroneous and even worse results compared with the real conditions. For example, considering the effects of photodissociation in a GCM where chemistry is highly simplified would make no sense. On the other hand, some physical mechanisms have such dominant effects that not including even a very simplified treatment of them would be too simple an approximation. A very simple example is the atmosphere of Venus: trying to understand the thermal structure of Venus without prescribing clouds is quite a complicated task. The same actually happens for Earth's clouds: the latent heat of evaporation of water is so high that the impact of clouds on the atmospheric dynamics cannot be neglected. However, the precise, microphysical description of clouds and their formation and evolution is far from easy, and an active field of research in the climate science community.

The presence of clouds on extrasolar planets now seems to be confirmed because of the effects on the transmission spectra of the planets. The most famoux example is the comparative study of ten hot Jupiters by Sing et al. [2016], with their observations and fit shown in Figure 5.6. This figure tends to show the diversity of atmospheric cloud coverage, from extremely cloudy where the molecular features are not visible anymore because of cloud opacity to cloud-free where the absorption lines are dominant in the transmission spectrum. Although care must be taken when attributing observations to a single physical effect, especially as reproducing transmission spectra is a complicated, badly constrained inverse problem, the consensus in the community points towards a non negligible importance of clouds in hot Jupiters.

Recently, Lines et al. [2018b,a] have presented their implementation of cloud physics in the UM, and its application for the two planets HD209 and HD189733b. Extending on the work of Lee et al. [2016], the cloud model describes the micro-physics of seed formation (nucleation), surface growth, and evaporation consistently coupled with element conservation, gas phase chemistry, hydrodynamical mixing, and gravitational settling. This model is notably based on the works of Woitke and Helling [2003, 2004], Helling and Woitke [2006]. The very idealised representation of clouds of Lines et al. [2018b] is the most recent model for coupling consistently clouds, dynamics and radiative transfer. It tends to show a quite significant change in the dynamical and mostly thermodynamical structure of the atmosphere, because of cloud absorption, and might help explain elemental observations in peculiar atmospheres [Evans et al., 2016, 2017] or unexpected observed phase curves [Dang et al., 2018].

Finally, it is worth evoking the treatment of chemistry in GCM, as it is a crucial aspect of the thermodynamics of atmospheres, particularly where there exists a high temperature contrast hence a wide range of possible chimical reactions. The simplest inclusion of chemistry is through the minimisation of Gibbs free energy G:

$$G = \sum_{i=1}^{l} \mu_i n_i, \tag{5.16}$$

where l is the number of considered species, μ_i the chemical potential of the ith element and n_i its number of moles. This minimisation is constrained by elemental conservation:

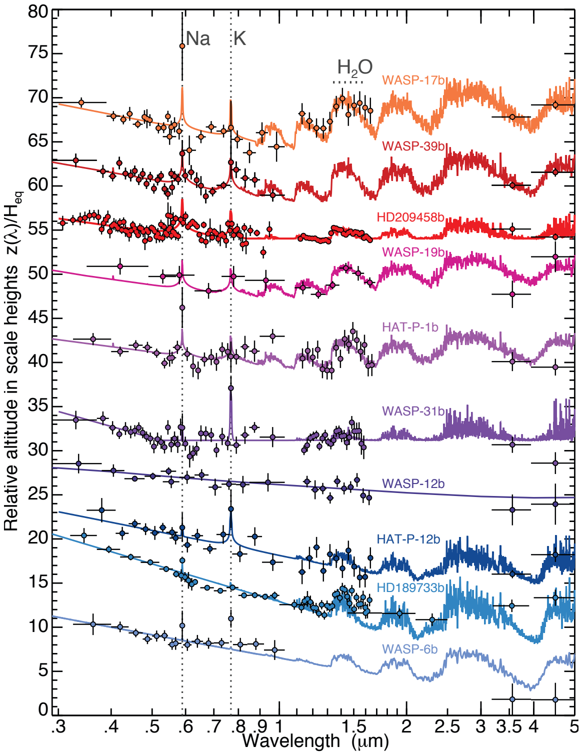

Figure 5.6: Figure and caption taken from Sing et al. [2016]. HST/Spitzer transmission spectral sequence of hot-Jupiter survey targets. Solid coloured lines show fitted atmospheric models with prominent spectral features indicated. Horizontal and vertical error bars indicate the wavelength spectral bin and 1σ measurement uncertainties, respectively. Planets with predominantly clear atmospheres (top) show prominent alkali and H2O absorption, with infrared radii values commensurate or higher than the optical altitudes. Heavily hazy and cloudy planets (bottom) have strong optical scattering slopes, narrow alkali lines and H2O absorption that is partially or completely obscured

$$\sum_{i=1}^{l} a_{ij} n_i - b_j^0 = 0 \tag{5.17}$$

where a_{ij} is the number of atoms of element j per molecule i and b_j^0 is the total number of moles of element j in the mixture. As the chemical potential depends on temperature and pressure, this minimization is usually done in an equilibrium situation: after a dynamical timestep, a snapshot of the thermodynamical profile of the atmosphere is taken, not considering advection or mixing, and the minimisation of the Gibbs energy is performed to update the chemical abundances. The vast majority of GCM calculations applied to hot Jupiter uses this scheme [Cooper and Showman, 2005, Showman et al., 2009, Rauscher and Menou, 2012, Mayne et al., 2014a, Heng et al., 2011,

...]. Although a good approximation and a very efficient numerical method, this scheme supposes that the chemical transformation are instantaneous. It neglects the advection of chemical species by the winds, into a region where they would persist in a disequilibrium state, because advection is more efficient than chemical reactions, as well as photodissociation. In the atmosphere of hot Jupiters, where we have seen that the winds can reach km.s^{-1} values, it is not clear whether equilibrium chemistry is well suited.

The implementation of disequilibrium chemistry has been performed by different groups using GCMs for hot Jupiters [Drummond et al., 2016, Moses, 2014, Agúndez et al., 2014, Tsai et al., 2017, ...]. In Exeter, there has been an extensive works on the effect of disequilibrium chemistry, presented in Drummond et al. [2016, 2018a,c,b]. This tend to shows that, althoug numerically expensive, the treatment of disequilibrium chemsitry for highly irradiated planets can lead to significant changes in the spatial distribution of molecular abundances, with important effect on the phase curves. At any rate, the treatment of disequilibrium chemistry notably due to vertical and longitudinal advection requires a proper understanding of the dynamical processes at stake in the atmosphere of hot Jupiters, which we detail in the next section.

To conclude on this section, we insist on the fact that the understanding of hot Jupiter atmospheres is a highly non trivial task, and that the degree of idealisation included in the models only allows to grasp the dominant qualitative behaviour of extrasolar planets. However, there has been suggestions to link the observation of one molecular species (e.g., H_2O) in the atmosphere to the global atmospheric metallicity of the atmosphere, then the total metallicity of the planet and even formation processes (e.g., Wakeford et al. [2017], Thorngren et al. [2016]). Following the discussion on this chapter and the previous one, these conclusions seem very bold. First, the disequilibrium chemistry (and even badly constrained equilibrium chemistry from inadequate radiative transfer calculations) prevents the direct link between a globally observed abundance of H_2O to an atmospheric metallicity, not even mentioning cloud settling. Then, the internal processes of Jupiter like planets are still not really understood, as we have shown in chapter 4. As their hotter atmospheres yield a higher internal temperature, phase transitions or separation are rather unlikely for hot Jupiters, but double diffusive processes such as layered convection or fingering convection cannot be excluded: the evolution of the atmosphere might be very different from the evolution of the interior of the planet. Without constrains on the density structure of the planet, from gravitational moments or at least Love numbers (which even for the well characterized Jupiter is a difficult task), it seems premature to link our limited observations of hot Jupiters to their evolutionary tracks.

5.4 A deep and robust feature: superrotation

Showman and Guillot [2002] performed the first study of the atmosphere of HD209 using a Global Circulation Model (GCM). As we have shown already, since this work GCMs have been extensively used to characterise hot Jupiters [e.g., Cooper and Showman, 2005, Showman et al., 2008, Heng et al., 2011, Rauscher and Menou, 2012, Dobbs-Dixon and Agol, 2013, Mayne et al., 2014b, Helling et al., 2016]. A common feature emerges from all of these studies: the atmosphere exhibits superrotation [1] at the equator over a certain range of pressures creating

---

[1] We have definded superrotation as a prograde atmospheric wind velocity greater than that arising from the rotation of the planet alone.

Table 5.1: Value of the standard parameters for the temperature forced (TF) and radiative transfer (RT) simulations.

Quantity	TF	RT
Horizontal resolution	144_λ, 90_ϕ	
Vertical resolution, N_z	66	
Dynamical Timestep (s)	1200	30
Radiative Timestep (s)	-	150
Initial inner boundary pressure, p_{max} (Pascals, Pa)	220×10^5	200×10^5
Rotation rate, Ω (s^{-1})	2.06×10^{-5}	
Radius, R_{p} (m)	9.44×10^7	9.0×10^7
Radius to outer boundary, R_{top} (m)	1.1×10^7	9.0×10^6
Surface gravity, g_{p} (ms^{-2})	9.42	10.79
Specific heat capacity (constant pressure), c_{p} ($\mathrm{Jkg}^{-1}\mathrm{K}^{-1}$)	14 308.4	13 000.0
Ideal gas constant, R ($\mathrm{Jkg}^{-1}\mathrm{K}^{-1}$)$^{(1)}$	4593	3556.8
Diffusion setting, K_λ (see Section 5.3 for applied coefficient, K'_λ)	0.158	
Horizontal vector laplacian damping coefficient, $\nu_{\lambda,\phi}$	0.1	0.0
Vertical vector laplacian damping coefficient, ν_{r}	0.0	
Vertical, ‘sponge’, damping coefficient R_w	0.15	
Temperature characterising intrinsic luminosity of the planet (K), T_{int}	-	100

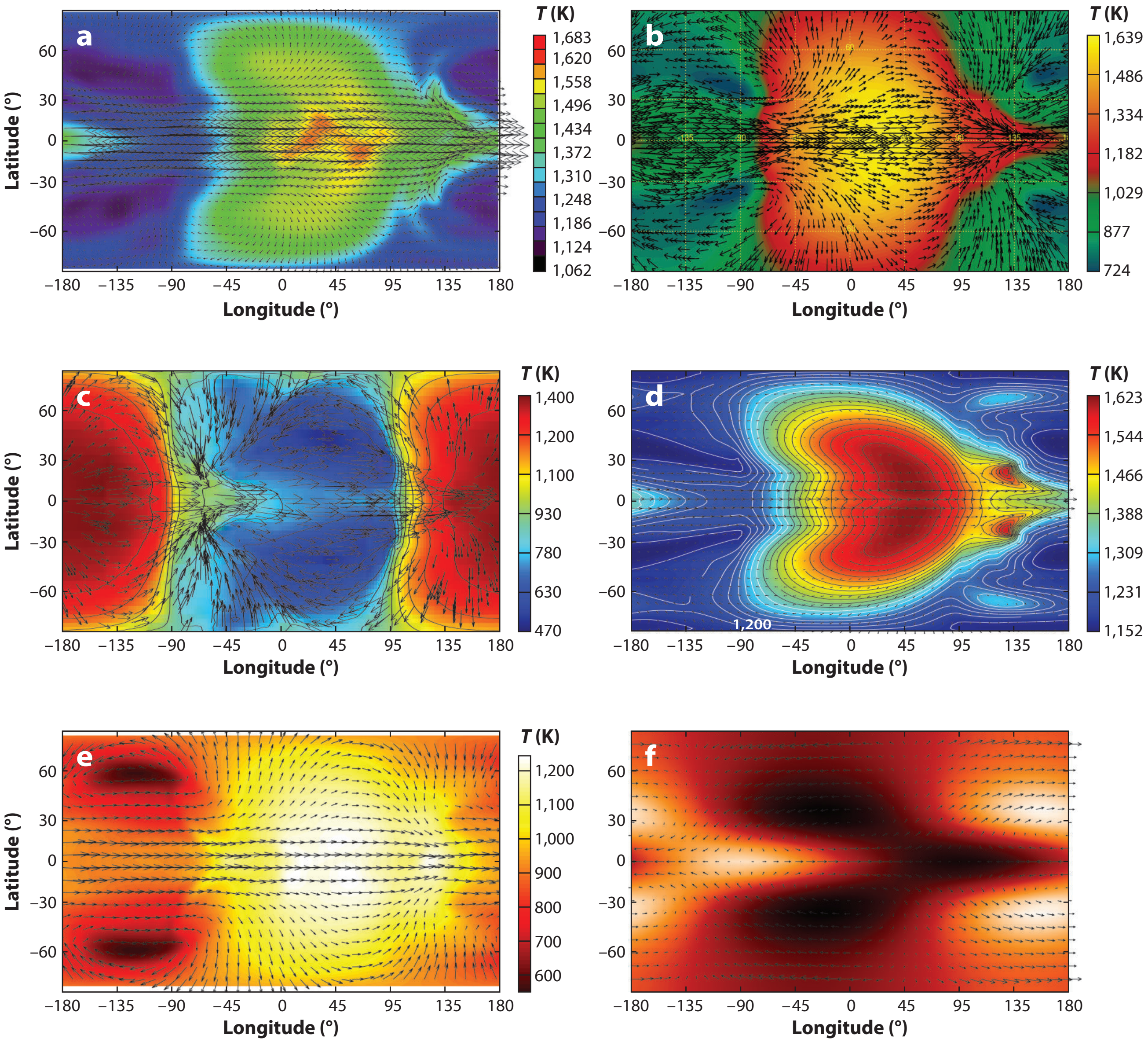

Figure 5.7: Examples of calculations from general circulation models of hot Jupiters. Despite the use of different input parameters, techniques to treat radiation and numerical schemes for atmospheric dynamics, the chevron-shaped feature appears to be a generic outcome of the hot exoplanet regime. Courtesy of Kevin Heng (panel a, using the FMS GCM), Emily Rauscher (panel b, using the IGCM), Ian Dobbs-Dixon (panel c, using a customized code), Nathan Mayne (panel d, using the U.K. Met Office GCM), and Adam Showman (panel e, using the MITgcm). Panel f shows an analytical model from Heng and Workman [2014] , generalized from the works of Matsuno [1966], Gill [1980], Showman and Polvani [2011]. Figure and caption taken from Heng and Showman [2015].

a coherent zonal 'jet'. On Figure 5.7 are gathered the 3D GCM results of different groups, all clearly exhibiting equatorial superrotation. The Figure and caption are taken from Heng and Showman [2015].

Aditionally, observations have detected an eastward shift from the substellar point of the maximum brightness of the atmosphere of hot Jupiters [Knutson et al., 2007, Zellem et al., 2014]. Superrotation would produce such a shift, with the advection of heat by fast winds, and is the best candidate to explain this feature. However, it is worth noting that a recent measurement has inferred an opposite, westward shift for COROT–2b [Dang et al., 2018], suggesting additional complexity.

In this section, we expose the numerical robustness and qualitative aspect of superrotation on hot Jupiters, based on the study we have performed in 2017 [Mayne et al., 2017]. The analytical treatment of superrotation in the particular case of hot Jupiters is studied in the next chapter.

The main idea of Mayne et al. [2017] was to test the robustness of superrotation in the limits of our understanding of the physical conditions prevailing in hot Jupiters. Notably, the treatment of the deep regions of the atmosphere is of prime importance: a change in the initial inner temperatures can affect the convergence of the atmospheric dynamics. We report in Table 5.1 the reference parameters used in the simulations, also used in chapter 7. The 'temperature forced' simulations corresponds to Newtonian heating with the prescription of an equilibrium temperature and a radiative timescale following Iro et al. [2005], whereas the 'radiative transfer' resolves consistently the equations of radiative transfer in the two stream corollated k method [Amundsen et al., 2016].

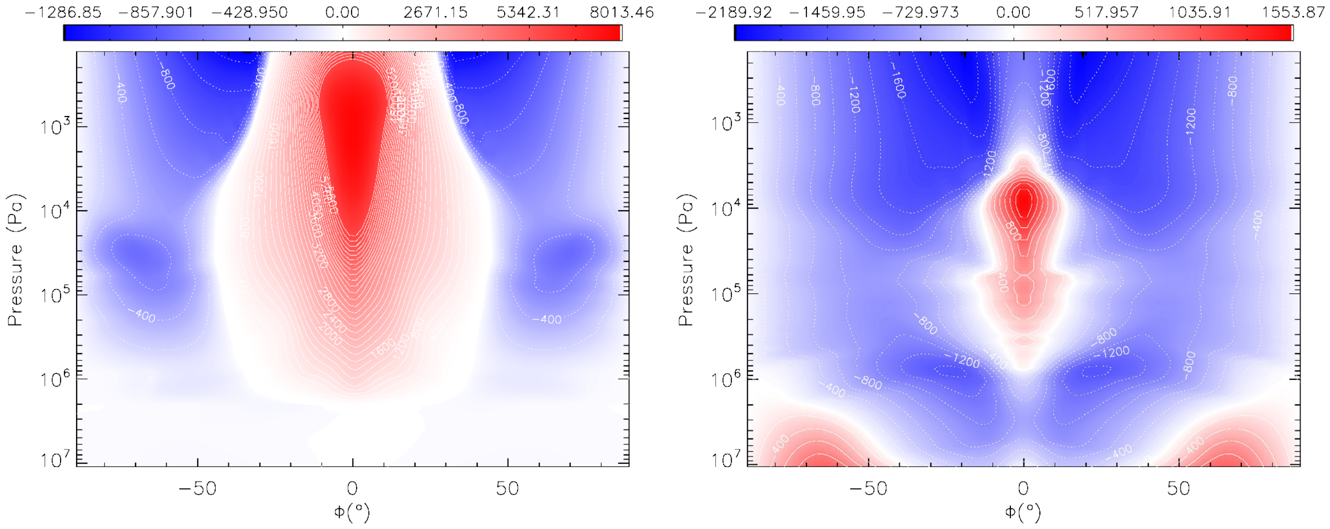

(a)

(b)

Figure 5.8: Zonal average of the density times the zonal average of the zonal velocity, averaged in time between 9000 and 10 000 days as a function of pressure and latitude for (a) an atmosphere initialised with the temperature profile of Iro et al. [2005] and no velocity, (b) an atmosphere initialised with a strong meridional temperature gradient at depth.

The Mayne et al. [2017] paper was willingly a numerical, exploratory paper, hence the main results are the shape of the mean flow under various physical conditions. The first conclusion is that there are qualitative differences between the temperature forced and radiative transfer case: an attempt to compare a thermodynamic structure of a simulated atmosphere to actual observations would need to be done with a consistent treatment of radiative transfer.

Considering superrotation, we have tried without success to suppress superrotation in the atmosphere of hot Jupiters by changing initial conditions and physical parameters (except the diffusion as we know that this parameter is essential in superrotation, see e.g., Komacek and Showman [2016]). The most limiting case is the case with a strong equator to pole temperature gradient in the deep interior. In Figure 5.8, we compare the values of the zonal average of the density times the zonal average of the zonal velocity between an atmosphere initialised with the temperature profile of Iro et al. [2005] and no velocity and an atmosphere initialised with a strong meridional temperature gradient at depth, averaged between 9000 and 10 000 days of simulation.

Clearly, superrotation in a 'usual' case (Figure 5.8a) is much broader and stronger in amplitude than superrotation in the strong temperature gradient case (Figure 5.8b). With constant diffusion and radiative timescale, Figure 5.8b is the less extended and weakest superrotation we could obtain, and we could not suppress superrotating flows in the atmosphere.

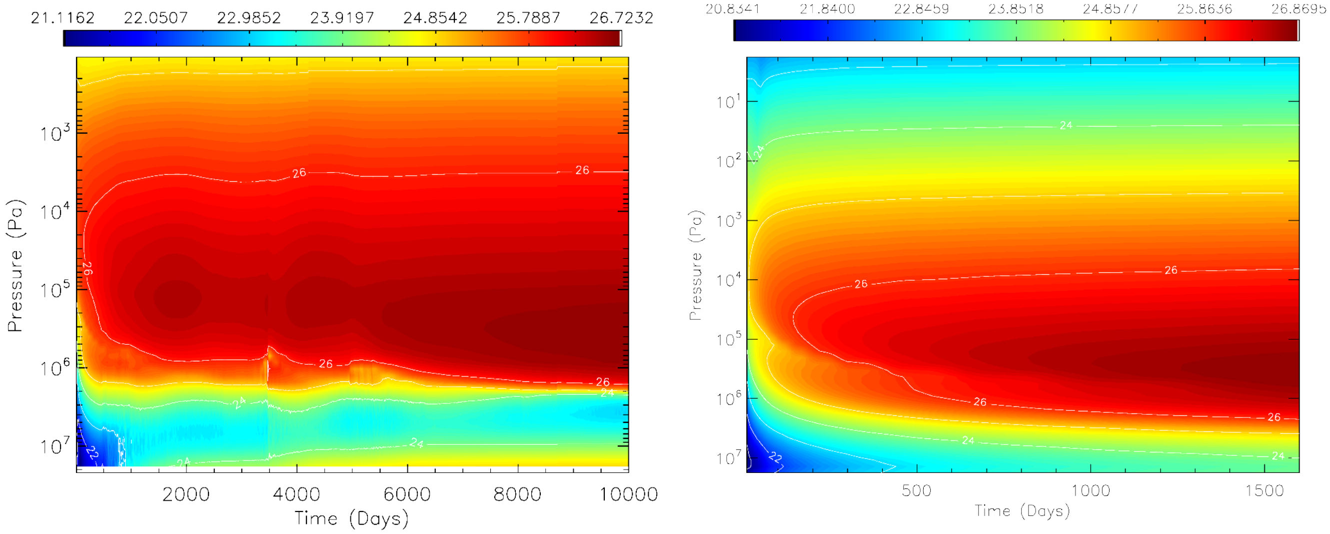

(a)

(b)

Figure 5.9: Zonally averaged equatorial kinetic energy as a function of pressure and latitude for (a) temperature forced simulation and (b) radiative transfer simulations.

Another important question we wanted to adress in Mayne et al. [2017] was the convergence to a steady state of our simulations. In numerous papers it is often stated that some figure are extracted from "a steady state of the simulation". We show in Figure 5.9 the evolution with time of kinetic energy in the temperature forced and radiative trasnfer cases. If the high atmosphere, above 0.1 bar, seems to converge quickly to a state where kinetic energy is constant with time, deeper pressure range are yet not converged after 10 000 days. Notably, the deep atmosphere seems to be converging to an adiabatic structure with time (at least up to a few bars), consistent with the picture of the radius inflation by advection of potential temperature [Tremblin et al., 2017] exposed in the previous section.

To conclude this section, we highlight two other results of Mayne et al. [2017]. First, the equatorial superrotation does lead to an eastward shift of the hot spot, as observed by Knutson et al. [2007], Zellem et al. [2014], and shown in Figure 5.7 d. Although this is not a proof that the hot spot shift is due to superrotation, superrotation can be responsible of this shift. Finally, we have studied the non linear accelerations, to assess whether the balance between vertical and meridional eddy momentum fluxes proposed by Showman and Polvani [2011] indeed happens for steady states (or at converged states in the high atmosphere). The picture from Mayne et al. [2017] seems to be more complex than the simple view proposed by these authors (the work of Tsai et al. [2014] is more relevant for the equilibration of superrotation). We study further the spin up of superrotation in chapter 7.

5.5 Conclusion

In this chapter, we have shown the importance of understanding the atmospheric dynamics of giant planets, and particularly hot Jupiters. From chapter 4, we already knew that the winds can alter the determination of internal structure, because of the variation of density they lead to and therefore the change of the estimated gravitational moments [Kaspi, 2013, Kaspi et al., 2017, 2018]. In this chapter, we have detailed further the connection between atmospheric dynamics and the observed inflated radius of hot Jupiters: dissipative processes such as kinetic energy deposition or ohmic dissipation [Guillot and Showman, 2002, Batygin and Stevenson, 2010] are triggered by the strong dynamical forcing of the atmosphere. The advection of potential temperature on the other hand Tremblin et al. [2017], is a purely dynamical process that links the equatorial superrotation to deep mass fluxes. Globally, the thermal structure of the deep atmosphere is at any rate strongly affected by the external dynamics.

From there, we have exposed the numerical methods to study the atmospheric dynamics of hot Jupiters: GCMs. Numerous GCMs have to date been applied to hot Jupiters, with various level of sophistication from the primitive equations with Newtonian cooling scheme to full hydrodynamics equation with radiative transfer and cloud settling and growth included [e.g., Cooper and Showman, 2005, Menou and Rauscher, 2009, Heng et al., 2011, Dobbs-Dixon and Agol, 2013, Mayne et al., 2014a, Amundsen et al., 2016, Helling et al., 2016, Lines et al., 2018b, Drummond et al., 2018b, , ...]. The various approaches allow to asses the importance and qualitative effect of different physical processes. It seems that the treatment of clouds and non equilibrium chemistry, although a complicated issue, might change parts of our understanding of these far away worlds.

Despite the possible uncertainties, several features are qualitatively, yet robustly reproduced, across most of the GCMs applied to hot Jupiters, in particular the occurrence of a superrotating equatorial jet (coherent zonal flow). This jet is seemingly confirmed by observations of a shift in the brightest part of a hot Jupiter atmosphere away from the substellar point, observed via phase curves and suggested to be caused by winddriven advection [Knutson et al., 2007, Zellem et al., 2014] by a super-rotating equatorial jet. We have detailed the qualitative aspect of superrotation, as well as its robustness as we have done in Mayne et al. [2017].

Superrotation therefore appears as a robust and essential feature to understand conditions prevailing on hot Jupiters. As part of this thesis, I have therefore tried to improve the analytical understanding of equatorial superrotation on Pegasus-like planets, notably in order to assess the validity of the diverse numerical findings. This is presented in chapter 7. In the next chapter however, I detail ECLIPS3D, a code that solves for waves, steady linear circulation and instabilities for 3D planetary atmospheres. The idea behind this code was to test the stability of superrotation, as well as the details of the transition to superrotation. Mainly limited by resolution issues, the use of the code has been less enlightning than expected, but it remains a powerful tool to obtain insight into the linear processes relevant to hot Jupiter conditions, and is used through chapter 7. The numerical and analytical details of ECLIPS3D presented in the next chapter can thus be skipped at first reading.

Chapter 6

ECLIPS3D

Lorsque, la brave machine, dans un éclair de lucidité, a compris combien elle était moche et mal fichue, elle décida courageusement, de se supprimer.
Prunelle - Gaston, Le gang des gaffeurs - *Franquin*

6.1 Introduction

The study of the influence and propagation of waves in planetary atmospheres is often performed under several simplifications, most notably the assumption of a zero or zonally–symmetric and constant initial zonal flow [e.g. Kasahara and Qian, 2000], or restriction to a beta–plane solution [e.g., Lindzen, 1967]. Such simplifications allow analytical prediction of the key wave mechanisms, and in some cases a complete understanding of their structure [even in the mathematical sense, see Matsuno, 1966].

Despite the simplifications, such studies have allowed significant insight into atmospheric dynamics, for example, Wheeler and Kiladis [1999] demonstrate that the propagation of waves can be linked to convective motions in Earth's atmosphere, and the resulting description matches analytical theories [e.g., Vallis, 2006, Holton, 1992] remarkably well. Baroclinic and barotropic instabilities are also known to have an impact on the circulations of planetary atmospheres [see Williams, 2003].

However, for more complex mean flows, or situations where individual terms in the hydrodynamical equations are not clearly dominant analytical treatments rapidly become impractical. Additionally, some wave structures, or modes, are only supported by the full equations, being effectively 'filtered' out by the simplifications. Notably, Wang and Mitchell [2014] numerically identify a Rossby–Kelvin wave mode for a planetary atmosphere that can not be recovered in the quasi–geostrophic equations.

In order to study the wave mechanism at stake during the evolution of hot Jupiter atmospheres, the transition to superrotation and its stability, we have developed a code, ECLIPS3D (Eigenvectors, Circulation and Linear Instabilities for Planetary Science in 3 Dimensions) which we benchmark in this work. More globally, this code can be used in the study of linear stable or unstable modes within any planetary atmosphere from an arbitrary initial steady state. The adaptability of ECLIPS3D makes it easy to change to study such wave mechanisms in other geometries and physical situation (planetary or star interiors, disks, etc...).

We expand upon Thuburn et al. [2002b], who studied propagating wave modes in an axisymmetric atmosphere at rest, to include linear modes in an atmosphere with a steady background flow, in three dimensional spherical coordinates. We detail the structure of ECLIPS3D including the equations solved and the process of obtaining a solution. We detail the different sets of equations implemented (axisymmetric 2D, 3D, two-layer equivalent depth) as well as the time-dependent or independent solutions (waves, instabilities and standing circulation). Finally, we have implemented a posteriori calculation of an energy equation for a given solution. These semi–analytical results allow the verification of the frequency of the modes (and the growth and damping rate for instabilities), as well as isolation of the dominant mechanism providing insight into the physical phenomena driving the instability.

In Section 6.2, we outline the equations implemented in ECLIPS3D (with the full equations detailed in Appendix B.1), and the procedure for solving them, alongside the method of calculating the energy equation. We then benchmark ECLIPS3D against a range of classical calculations of waves, instabilities and circulations in Section 6.3, including a setup similar to Showman and Polvani [2011]. Finally, we draw conclusions and comments on future developments and applications for ECLIPS3D in Section 6.4.

6.2 The algorithm

6.2.1 Linearised equations

Thuburn et al. [2002b] showed that even the simplest atmospheric waves exhibit behaviour that cannot be accurately expressed by separating variables [requiring a height–dependent shift in latitude, see Thuburn et al., 2002b, for details]. Therefore, in the general case, no assumption can be made on the mathematical expression of the wave regarding spatial coordinates. As our steady state is arbitrary, we will linearise the full equations with no simplification. We adopt here the inviscid Navier-Stokes equations, but viscosity or diffusion could be straightforwardly added (as done for example in Section 6.3.5 and Appendix B.1.5). The basic equation set are equations (2.11a) to (2.11g) that we recall here:

$$\frac{Du}{Dt} - 2\Omega v\sin(\phi) + 2\Omega w\cos(\phi) + \frac{1}{\rho r\cos(\phi)}\frac{\partial p}{\partial\lambda} + \frac{uw}{r} - \frac{uv\tan(\phi)}{r} = 0, \tag{6.1a}$$

$$\frac{Dv}{Dt} + 2\Omega u\sin(\phi) + \frac{1}{\rho r}\frac{\partial p}{\partial\phi} + \frac{vw}{r} + \frac{u^2\tan(\phi)}{r} = 0, \tag{6.1b}$$

$$\frac{Dw}{Dt} - 2\Omega u\cos(\phi) + \frac{1}{\rho}\frac{\partial p}{\partial r} + g - \frac{u^2 + v2}{r} = 0, \tag{6.1c}$$

$$\frac{D\rho}{Dt} + \rho\left(\frac{1}{r\cos(\phi)}\frac{\partial u}{\partial\lambda} + \frac{1}{r\cos(\phi)}\frac{\partial}{\partial\phi}\left(v\cos(\phi)\right) + \frac{1}{r^2}\frac{\partial}{\partial r}\left(r^2 w\right)\right) = 0, \tag{6.1d}$$

$$\frac{D\theta}{Dt} = \frac{\theta}{T}\frac{Q}{c_p}, \tag{6.1e}$$

$$p = \rho R T, \tag{6.1f}$$

$$\theta = T \left(\frac{p_0}{p} \right)^{\frac{R}{c_p}}, \tag{6.1g}$$

where u,v and w are the components of velocity in the longitudinal (λ), latitudinal (ϕ) and vertical (r) directions, ρ is the density, p the pressure, T the temperature, θ the potential temperature, p_0 a reference pressure, R is the gas constant, c_p the heat capacity, g the gravitational acceleration (and is a function of r, see Appendix B.1.1), Ω the rotation rate of the planet, r the radial distance from the centre of the planet, λ the longitude, ϕ the latitude and finally Q is the heating rate (if present). Equations (6.1a) to (6.1c) represent momentum conservation, (6.1d) mass conservation, (6.1e) conservation of energy, (6.1f) is the equation of state (here an ideal gas) and (6.1g) defines potential temperature, closing the set. Thuburn et al. [2002b] showed that potential temperature is more appropriate than normal temperature for studies of the linear modes. Finally, D/Dt is the Lagrangian or material derivative and t is time.

Solving for waves or instabilities then requires linearising these equations. We follow the definitions of Thuburn et al. [2002b] for the perturbed variables (this scaling comes from Daley [1988]), which greatly simplify the equations when the steady state is axisymmetric and at rest, and therefore allows for easy comparison with the work of Thuburn et al. [2002a]. Namely, we write:

$$u' = \rho_i \left(u - u_i \right), \tag{6.2a}$$

$$v' = \rho_i \left(v - v_i \right), \tag{6.2b}$$

$$w' = \rho_i \left(w - w_i \right), \tag{6.2c}$$

$$p' = \left(p - p_i \right), \tag{6.2d}$$

$$\theta' = \frac{g \rho_i}{\theta_i} \left(\theta - \theta_i \right), \tag{6.2e}$$

where a prime denotes a linearised variable and an i subscript the initial steady state.

If the heating rate Q is non zero, it has to be properly included in the linearised equations. When solving for waves and instabilities, we simply linearise Q and include it in the left hand side of the equations. This is detailed in Appendix B.1.4. When looking for steady, linear circulation (and not free or forced waves) $Q(r, \phi, \lambda)$ is specified and considered small enough to only trigger a linear response. A dissipative mechanism must also be added in order to reach a linear steady state. This setup is similar to that of Showman and Polvani [2011], which is one of our benchmark cases, and is detailed further in Appendix B.1.5.

Thuburn et al. [2002b] considered the linearised equations for the case where the initial atmospheric state is axisymmetric, in hydrostatic balance and at rest. In the more general case linearisation of each of the terms from Eq.(6.1) must be completed as shown in Appendix B.1, alongside the resulting final equation set Eq.(B.2-B.5). These final, linearised equations are then discretised and solved within ECLIPS3D as detailed in Section 6.2.4. Additionally, we have implemented a two-layer model following Showman and Polvani [2011], based on their equations 9 and 10 (linearised versions of which are given in Appendix B.1.3). Other equation sets (e.g., shallow water, anelastic, ...) and geometries could be implemented within ECLIPS3D with relative ease if required.

6.2.2 Boundary conditions

For inviscid flows, there must be no normal flow at the limits of the domain in order to obtain a well posed problem with complete boundary conditions. Namely, we impose that $v'\cos(\phi)$ tends to zero at the poles, and w' is zero at the top of the atmosphere as a no escape condition. At the inner boundary, we impose a solid boundart with w' equals zero. For hot Jupiters, this requires to the modeled domain to extend to high enough pressures for the atmosphere to reach a quiescent region not involved in the acceleration of superrotation. This inner boundary condition can be easily changed if mass flows or energy transfer with the deep atmosphere need to be considered. If the density of the upper atmosphere is too low, unphysical velocities might arise. In the physical applications of ECLIPS3D so far, we have solved this problem by reducing the extent of the atmosphere but a smoothing of the higher atmosphere could be implemented [as done for example in GCMs, see Mayne et al., 2014a,b].

6.2.3 Energy equation

Following the method of Thuburn et al. [2002b], we calculated an energy equation by combining the linearised Euler equations and integrating them over the whole atmospheric volume with appropriate boundary conditions. We derive this equation in the same context as Thuburn et al. [2002b], with an initially axisymmetric, hydrostatically balanced atmosphere at rest. The general case is shown in Appendix B.2. We assume that the linearised variables X' can be expressed as $X'(r,\phi,\lambda,t) = X(r,\phi)e^{-\mathrm{i}(\sigma t + m\lambda)}$, where the real part of σ is the mode frequency and its imaginary part the growth rate (if nonzero), $X(r,\phi)\in\mathbb{C}$, as explained in 6.2.4, and $m\in\mathbb{Z}$:

$$\begin{aligned}&\int_0^{2\pi}\int_{-\pi/2}^{\pi/2}\int_a^{a+H}\Bigg[2\sigma\rho_i E - F\left(uw^\star + u^\star w\right) + f\left(uv^\star + u^\star v\right) - \frac{m}{r\cos\phi}\left(up^\star + u^\star p\right) - \left(w\theta^\star + w^\star\theta\right)\\&+\frac{1}{r}\left(v^\star\frac{\partial p}{\partial\phi} - + \frac{p^\star}{\cos(\phi)}\frac{\partial}{\partial\phi}\left(v\cos(\phi)\right)\right) + w^\star\frac{g}{c_i^2}p - \frac{N_i^2}{g}wp^\star w^\star\frac{\partial p}{\partial r} - \frac{p^\star}{r^2}\frac{\partial}{\partial r}\left(r^2 w\right)\Bigg]\frac{r^2\cos(\phi)}{\rho_i}drd\phi d\lambda = 0,\end{aligned}\tag{6.3}$$

where * denotes the complex conjugate, with $f = 2\Omega\cos(\phi)$, $F = 2\Omega\sin(\phi)$, a the radius of the planet, H the height of the top of the atmosphere and $E = 1/2\left((|u|^2+|v|^2+|w|^2)/\rho_i + |\theta|^2/\rho_i N_i^2 + |p|^2/(\rho_i c_i^2)\right)$ the sum of the kinetic, thermobaric and elastic energies of the perturbation, with N_i^2 and c_i^2 the initial buoyancy frequency and sound speed, respectively. Using integration by parts we can express:

$$\begin{aligned}\sigma = &-\frac{1}{\int\int\int_V Er^2\cos(\phi)drd\phi d\lambda}\times\int\int\int_V\frac{1}{\rho_i}\Re\Bigg[f\left(uv^\star\right) - F\left(uw^\star\right) - \frac{m}{r\cos\phi}\left(up^\star\right) - \left(w\theta^\star\right) + \frac{1}{r}\left(v\frac{\partial p^\star}{\partial\phi}\right)\\&+\left(w\frac{\partial p^\star}{\partial r}\right) + \frac{g}{c_i^2}\left(wp^\star\right)\Bigg]r^2\cos(\phi)drd\phi d\lambda,\end{aligned}\tag{6.4}$$

with V the volume. This is possible only if $\int\int\int_V Er^2\cos(\phi)drd\phi d\lambda \neq 0$ which is the case when $N_i^2 > 0$. For this work we assume a stably stratified atmosphere ($N_i^2 > 0$). As stated by Thuburn et al. [2002b], Eq.(6.4) shows that σ can only be real in this case and no instability can grow around an atmosphere at rest with no heating and the boundary conditions we have described.

Once the variables $u', v', ...$ are known Eq.(6.4) can then be integrated numerically in ECLIPS3D and be used to verify the obtained frequency and identify the dominant physical processes (e.g., in Section 6.3.1 we show that an acoustic wave is largely dominated by the terms involving the pressure, whereas a Rossby wave is dominated by the f and F terms).

6.2.4 Method of solution

The derived linearised equations of motion can be expressed as:

$$D \begin{pmatrix} u' \\ v' \\ w' \\ p' \\ \theta' \end{pmatrix} = 0, \tag{6.5}$$

where D is a differential linear operator. If we introduce the operator A being:

$$A = \begin{pmatrix} \frac{\partial}{\partial t} & 0 & 0 & 0 & 0 \\ 0 & \frac{\partial}{\partial t} & 0 & 0 & 0 \\ 0 & 0 & \frac{\partial}{\partial t} & 0 & 0 \\ 0 & 0 & 0 & \frac{\partial}{\partial t} & 0 \\ 0 & 0 & 0 & 0 & \frac{\partial}{\partial t} \end{pmatrix}. \tag{6.6}$$

It is clear that A commutes with D as the latter is only time–dependent through the $\partial/\partial t$ terms. Therefore, the vector sub–spaces of D remain stable upon application of A. As A is diagonal the kernel of D can be decomposed on the eigenvectors e_σ of A. Such eigenvectors are well known: $e_\sigma \propto e^{-i\sigma t}$ where $\sigma \in \mathbb{C}$ (the $-$i term is just the convention we choose. The real part of σ is therefore the frequency and the imaginary part the growth rate). Therefore, coupled with appropriate boundary conditions, we can then solve Eq.(6.5) by decomposing them as:

$$\begin{pmatrix} u'(t,r,\phi,\lambda) \\ v'(t,r,\phi,\lambda) \\ w'(t,r,\phi,\lambda) \\ p'(t,r,\phi,\lambda) \\ \theta'(t,r,\phi,\lambda) \end{pmatrix} = \sum_\sigma \begin{pmatrix} \hat{u}(r,\phi,\lambda) \\ \hat{v}(r,\phi,\lambda) \\ \hat{w}(r,\phi,\lambda) \\ \hat{p}(r,\phi,\lambda) \\ \hat{\theta}(r,\phi,\lambda) \end{pmatrix} \exp^{-i\sigma t}, \tag{6.7}$$

with $\hat{u}, \hat{v}, \hat{w}, \hat{p}, \hat{\theta} \in \mathbb{C}$ and remembering that the evolution of the perturbed quantity is then the real part of the above expression. The actual solution is an infinite sum over all σ but the eigenmodes, and therefore the waves, are the individual projections to a single value. It is worth noting that, a priori, σ could take continuous values. For an atmosphere initially at rest, Matsuno [1966] show that only discrete values are solutions, but on the other hand baroclinic waves exhibits a continuous range of frequencies (see e.g., Charney [1947])

Time–dependent solution

From the discussion above, we can re-write our equations as a complex eigenvalue–eigenvector problem:

$$B \begin{pmatrix} u' \\ v' \\ w' \\ p' \\ \theta' \end{pmatrix} = i\sigma \begin{pmatrix} u' \\ v' \\ w' \\ p' \\ \theta' \end{pmatrix}, \tag{6.8}$$

with $B = D - A$. Eq.(6.8) can become difficult or even impossible to solve analytically. However, Thuburn et al. [2002b] discretise this equation using a staggered grid of points, turning the analytical matrix B into a finite numerical matrix. This allows spatial derivatives to be calculated using finite differences. The staggered grid was selected carefully for precision and stability by Thuburn et al. [2002b], where the 2D axisymmetric version is presented. We adopt a staggered grid in ECLIPS3D, shown in Figure 6.1, which resembles the one used in Thuburn et al. [2002b] (and is similar to the one used in the UM, section 5.3) but adapted to 3D and with different staggering of the u and v variables at the poles to simplify the boundary condition.
We have $N_{tot} = N_\lambda(2N_\phi N_r + (N_\phi + 1)N_r + 2N_\phi(N_r + 1))$ points in our grid, with N_λ, N_ϕ and N_r being the number of points in each coordinate, meaning the matrix B will be of size $(5 * N_{tot})^2$ as there are 5 inter–dependent variables. However, each variable at a given point only depends on the values of all variables over the closest points in the grid. Therefore, B is an extremely sparse matrix.

Once the matrix B is filled with discretised values from Eq.(6.8), at the staggered grid points we must find the eigenvectors of this matrix. ECLIPS3D uses the ScaLAPACK[1] library for parallel linear algebra [Blackford et al., 1997]. To express the eigenvectors of a complex matrix we first calculate the upper Hessenberg form of the matrix, then find the Schur decomposition before identifying the eigenvectors themselves [2]. Finally, the eigenvectors are returned to their original form via multiplication with the matrix of transformation.

However, this process of solving for the eigenvectors yields an eigenvector for each row in the matrix. From this set we must select those of interest, representative of physical modes in the atmosphere in question. To identify the interesting eigenvectors we employ two methods. Firstly, for instabilities with positive exponential growth rates, we assume that the modes that will lead the dynamical instability have the highest growth rate, and only select the fastest growing modes. For the case of no instability we first filter out modes arising from numerical errors (e.g., extreme values at the poles), and then manually select modes from the solution set. Analytical expectations then determine the modes of interest.

---

[1] `http://www.netlib.org/scalapack/`

[2] Handled by ScaLAPACK routines PZGEHRD, PZLAHQR and PZTREVC, respectively.

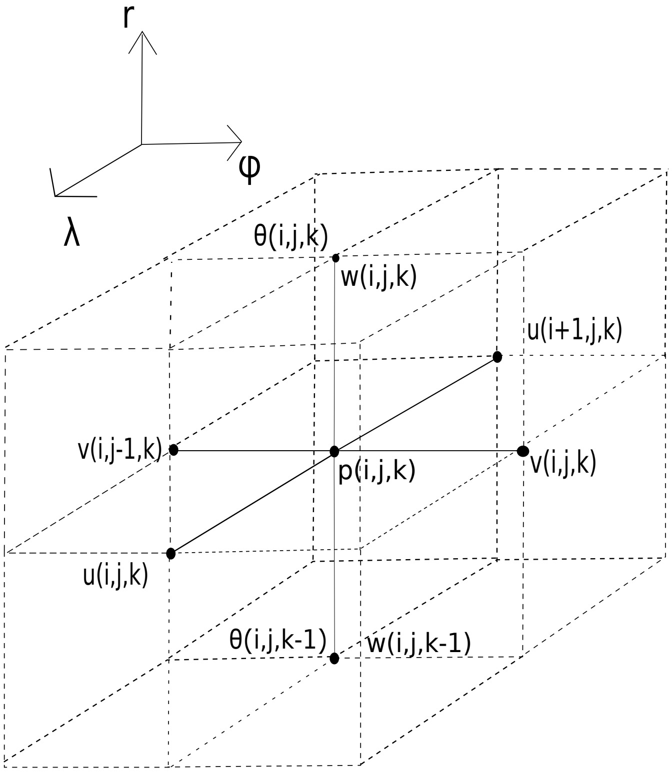

Figure 6.1: Figure showing a cell of the 3D staggered grid adopted in ECLIPS3D, based on Thuburn et al. [2002b]. i discretises the longitudinal variable λ, j the latitude ϕ and k the radial variable r. u and v are staggered in latitude, with v running from the south to north pole and thereby having an additional latitude point. p is staggered in height with w and θ with the latter two variables running from the bottom to the top of the atmosphere resulting in an additional height point.

Time–independent solution

For the case of a steady circulation, without time–dependence and with constant heating rate Eq.(6.5) can be expressed as:

$$C * \begin{pmatrix} u' \\ v' \\ w' \\ p' \\ \theta' \end{pmatrix} = \begin{pmatrix} 0 \\ 0 \\ 0 \\ \gamma R \rho_i \dfrac{Q_i}{c_p} \\ \dfrac{g\rho_i}{T_i}\dfrac{Q_i}{c_p} \end{pmatrix}, \tag{6.9}$$

where C is similar to B in Eq.(6.5) with the inclusion of a drag term if required (see Appendix B.1.5). Solving this problem is much easier than the time–dependent case, as we just need to express C on the staggered grid and invert it to obtain the unique solution to these equations.

6.2.5 Maximum Resolution

Because eigenvectors problems are time and memory consuming and numerically solving for eigenvectors does not behave linearly with the number of points in the matrix, the resolution of ECLIPS3D cannot be very high, at least in its current version. Namely, the 2D problems (axisymmetric, two layer or barotropic equations, see next section) can solve for modes with 100 × 100 points in less than a day of calculation. Unfortunately, the parallelization of eigenvector calculations is still an issue in the computer science community, and increasing the number of processors does not significantly accelerate the calculations. Higher resolution problems therefore take much longer (from the benchmarking we have done, the computational time scales as roughly between N_{tot}^2 and N_{tot}^3). Additionally, using too many processors at some point becomes prohibitive because of the communication delay, and using insufficient processors quickly leads to saturation of the available memory as the memory usage required for the matrix inversion is high (see the ScaLAPACK documentation for details).

These conclusions directly apply to 3D, where the maximum resolution we have used is $25 \times 25 \times 25$ points, although it is not an absolute limit. This resolution on 64 processors took about four days of calculation, showing the limits of ECLIPS3D in its current version. We are working on adapting ECLIPS3D for sparse matrices library (as the matrix to solve is extremely sparse) and are following the developments in computer science research regarding eigenvector calculations.

However, for time-independent solution, hence matrix inversion, the resolution can be much higher because inverting a matrix is well parallelized and not so time nor memory consuming. For example, for $25 \times 25 \times 25$ points it takes less than an hour on 16 processors.

Finally, we stress that the symmetries of the problem can lead us to restrict our study to only one hemisphere, and we therefore solve the problem at the same resolution with half the number of points, reducing the computational cost. In this chapter for example, the modes we present are always symmetric about the equator as this is relevant for hot Jupiters, but ECLIPS3D can solve for both symmetric and antisymmetric modes at the equator, with a slight change in the conditions at the limits of the staggered grid (although the actual boundary conditions remain the same).

6.3 Benchmarking

We have applied ECLIPS3D to five well studied cases from the literature to benchmark the code. These tests are explained in this section. First we reproduce the results of Thuburn et al. [2002b] for a simple, hydrostatically balanced and zonally symmetric atmosphere at rest (Section 6.3.1). This is followed by the case of an unstable jet providing a steady initial circulation as introduced by Wang and Mitchell [2014] (Section 6.3.2). We also present results for the baroclinic instability test of Jablonowski and Williamson [2006], Ullrich et al. [2014] (Section 6.3.3). In order to implement longitudinal variation in the steady state, we study the stability of Rossby-Haurwitz waves [Haurwitz, 1940], as done in Thuburn and Li [2000]. Finally, ECLIPS3D is applied to the case of a linear steady state circulation with atmospheric drag following Komacek and Showman [2016] (Section 6.3.5).

6.3.1 Initial atmospheric rest state

Mode	Acoustic	Acoustic	Gravity	Rossby	Rossby	Kelvin
Thuburn	3.27×10^{-2}	2.87×10^{-4}	1.88×10^{-4}	-1.46×10^{-5}	-3.07×10^{-6}	3.14×10^{-5}
ECLIPS3D	3.28×10^{-2}	2.87×10^{-4}	1.88×10^{-4}	-1.46×10^{-5}	-3.02×10^{-6}	3.08×10^{-5}
Energy equation	3.37×10^{-2}	2.86×10^{-4}	1.88×10^{-4}	-1.46×10^{-5}	-3.08×10^{-6}	3.00×10^{-5}

Table 6.1: Comparison between the frequencies obtained for a sample of different types of waves (see Section 6.3.1) presented in Thuburn et al. [2002b] and those identified in this work using ECLIPS3D. The semi-analytical values from the a posteriori energy equation are also given. All these modes have a longitudinal wavenumber $m = 1$.

We first apply the 2D, axisymmetric version of ECLIPS3D to solve for the eigenmodes of an initially axisymmetric, hydrostatically balanced atmosphere at rest following Thuburn et al. [2002b]. This version of ECLIPS3D needs to assume an integer wavenumber m in longitude, as in Thuburn et al. [2002b]. Table 6.1 shows the frequencies of the modes from both this study and that of Thuburn et al. [2002b] revealing agreement better than 3%, the discrepancies are due to slightly different initialisations and grid staggering. When matching their setup exactly we return matching results to within machine precision. Additionally, our resulting eigenfunctions have the same shape in height and latitude and global values as those found in Thuburn et al. [2002b]. For example, we isolate and present both an acoustic and Rossby wave recovered by ECLIPS3D in Figures 6.2 and 6.3, to be compared to Figures 1 and 2 of Thuburn et al. [2002b].

The difference in the forcing mechanisms between acoustic and Rossby waves, namely the pressure gradient and Coriolis force, respectively, mean we expect their global features to differ. The calculations from our energy equation, shown in Table 6.1, are in excellent agreement with the obtained numerical frequencies. These calculations also allow one to investigate the restoring force. For example, for the Rossby waves the f and F terms of Eq.(6.4) account for 90% of the value of σ, whereas they are negligible compared to the terms involving the pressure, and its derivative, for the acoustic waves.

Although this problem is axisymmetric, it can be used to test the 3D version of ECLIPS3D. In Figure 6.4 we present a single mode from the 3D case, to be compared to Figure 6.2. For this mode (and the other modes not presented explicitly here) we obtain the same height and latitude behaviour. For the additional dimension, longitude, we recover oscillatory modes with an arbitrary integer number, $2m$, of zeros in longitude (corresponding to a wavenumber m). The frequency of the obtained modes again, as with the 2D version of ECLIPS3D, match those of Thuburn et al. [2002b] to better than $\sim 3\%$ (in this case errors are also introduced by the discretisation in longitude).

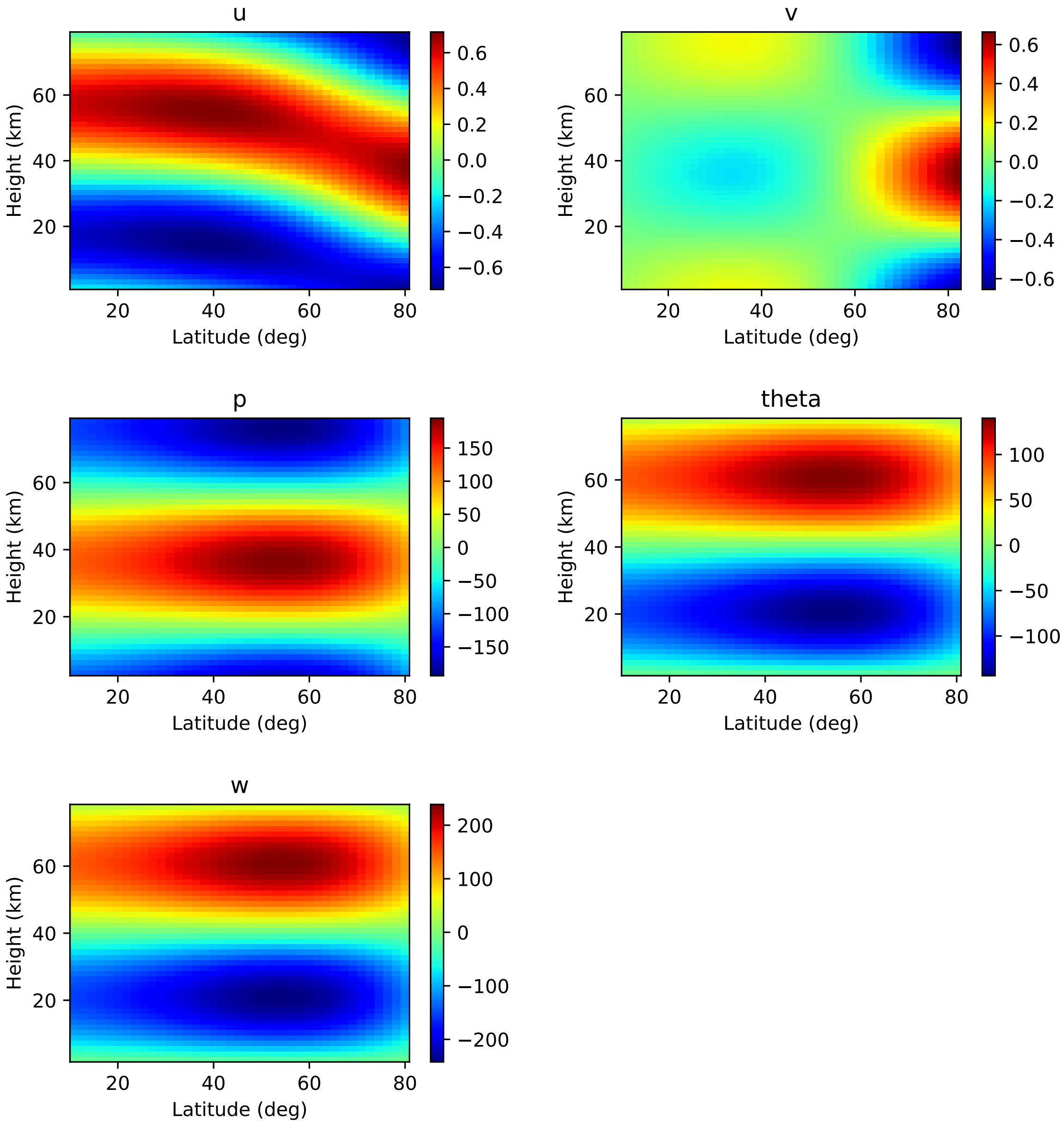

Figure 6.2: Values of the five perturbed variables u',v',p',w' and θ' obtained with ECLIPS3D for an acoustic wave with longitudinal wave number 1, with units proportional to their influence on the energy of the wave (as our solutions are from linear theory all values are defined relative to an unknown proportionality value). This mode is to be compared to Figure 2 of Thuburn et al. [2002b]

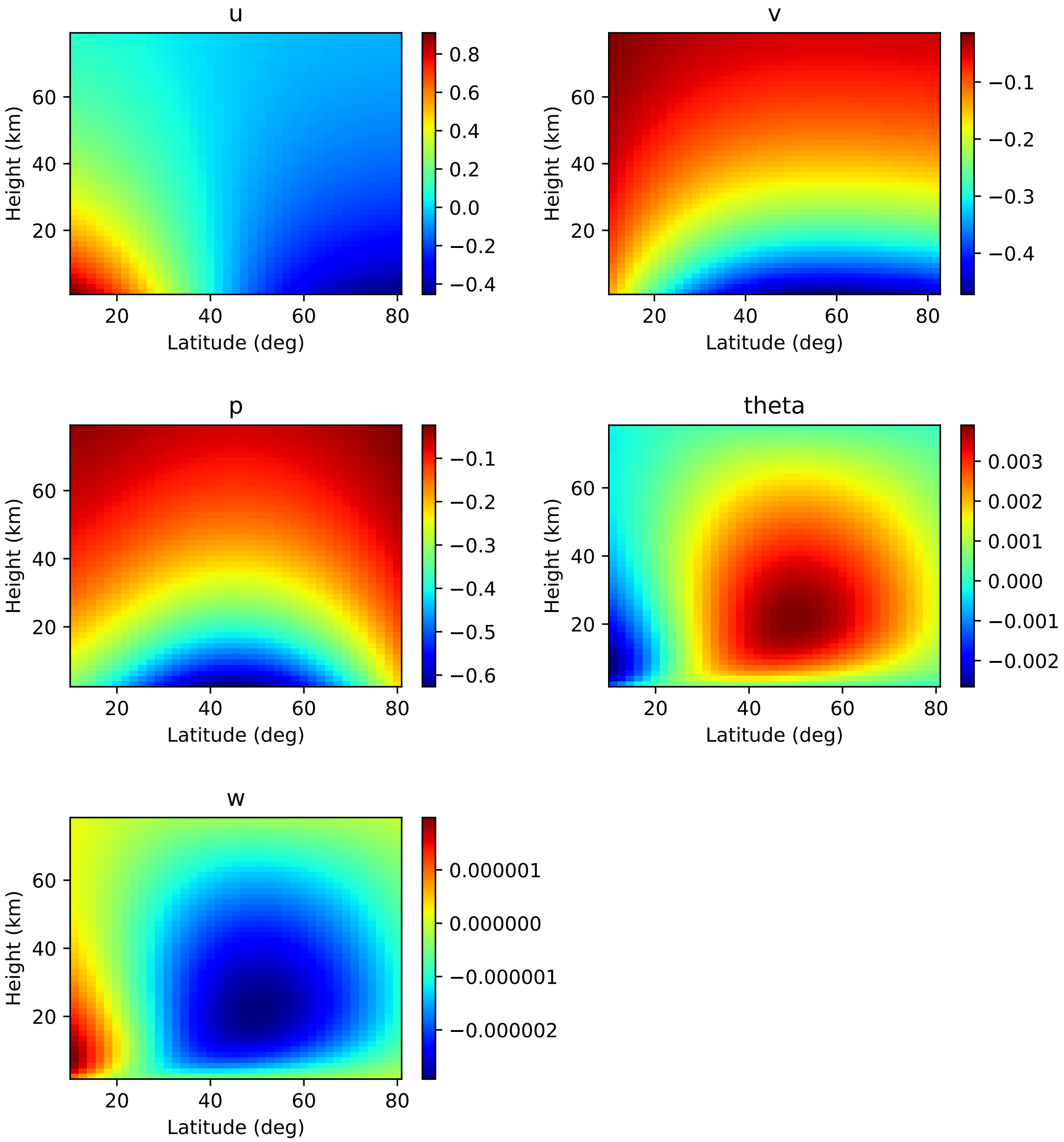

Figure 6.3: Same as Figure 6.2 but for a Rossby wave, to be compared with Figure 1 of Thuburn et al. [2002b].

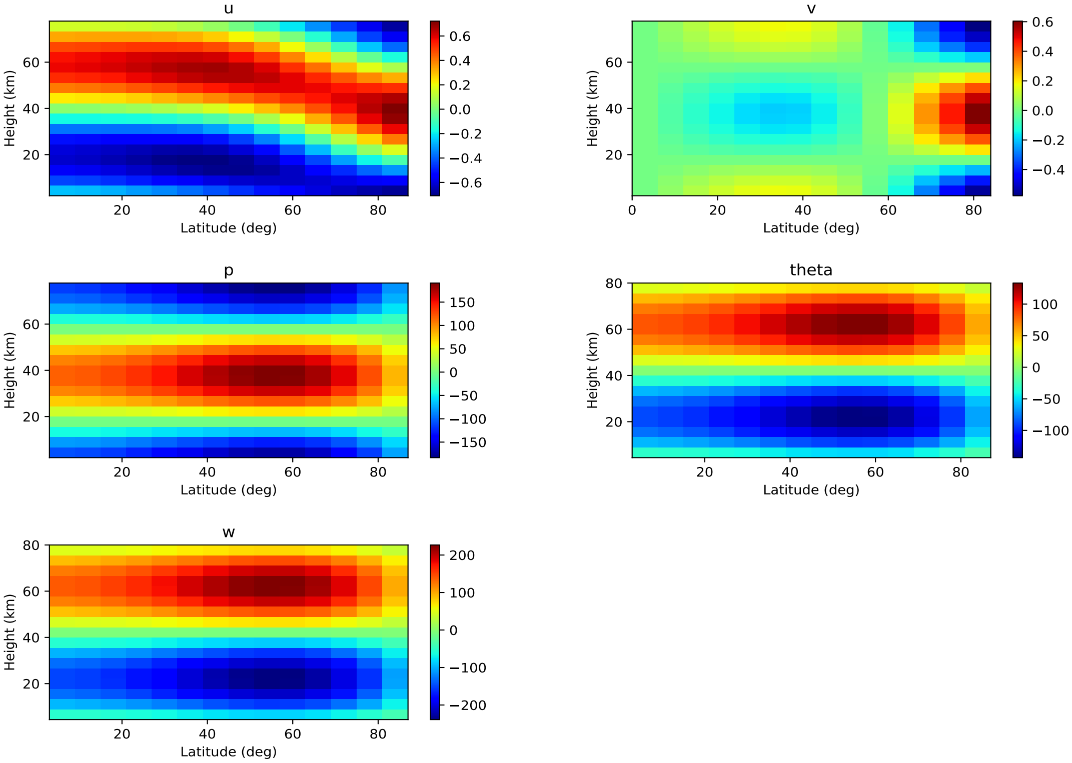

Figure 6.4: Same as Figure 6.2 but from the 3D version.

6.3.2 Steady state circulation: unstable jet

The next benchmark case is a steady state which includes an initial velocity field. Here we follow Wang and Mitchell [2014] who identified an exponentially growing linear mode, bringing eastward momentum to the equator, under axisymmetric forcing. This study essentially identifies unstable modes in an atmosphere similar to Thuburn et al. [2002b] but including a mid–latitude unstable jet. Wang and Mitchell [2014] identify two instabilities, firstly a well–known baroclinic instability (such as studied in Section 6.3.3), and secondly a new instability not captured by analytical treatments under the β–plane approximation. This new mode results in the convergence of eastward momentum at the equator, and is related to the Rossby and Froude numbers. Wang and Mitchell [2014] term this new instability the Rossby–Kelvin instability as it emerges from interaction between the mid–latitude Rossby waves and the Kelvin wave (an equatorially confined gravity wave with zero meridional velocity). In Figure 6.5 we show the characteristics of the mode identified by our own study using the 2D axisymmetric ECLIPS3D, which is to be compared with Figure 1a of Wang and Mitchell [2014]. Figure 6.5 demonstrates the excellent agreement of the structure of the mode found using both ECLIPS3D and that of Wang and Mitchell [2014].

Following Wang and Mitchell [2014] we explore the effect on the most unstable mode of varying the planetary

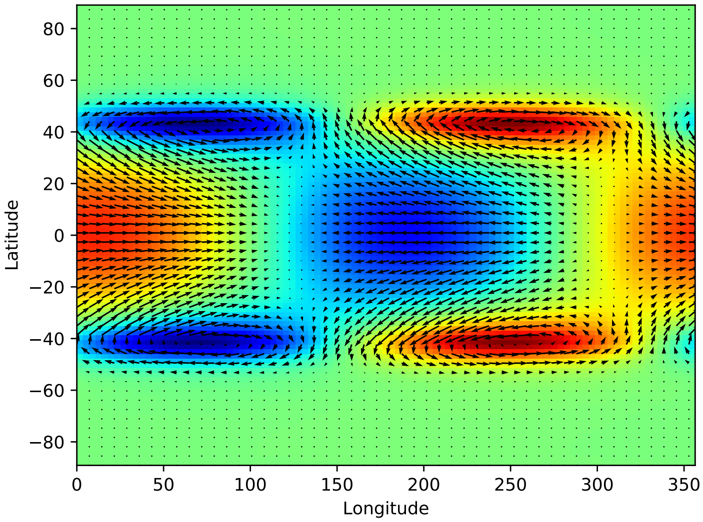

Figure 6.5: Pressure (colour scale) and wind (vector arrows) for the most unstable mode obtained with ECLIPS3D from the setup of Wang and Mitchell [2014], which is to be compared with their Figure 1a.

parameters. Figure (6.6) shows results for different ϕ_0, a characteristic latitude of the initial flow [see Wang and Mitchell, 2014, for definitions] and the Burger number $Bu = ((N_i H)/(2\Omega a))^2$ where H is a characteristic height, revealing a change in the growth rate as H is altered [see Wang and Mitchell, 2014, for more details]. These results are consistent with those presented in Figure 2(a) of Wang and Mitchell [2014].

6.3.3 Baroclinic instability

Jablonowski and Williamson [2006] detail a baroclinic instability test for GCMs using pressure as a vertical coordinate. Ullrich et al. [2014] adapted this test for height–based GCMs. In this test a perturbation to a steady longitudinal wind at mid–latitudes leads to a dynamical instability growing in a few days (for Earth-like conditions). In full 3D GCM simulations many phenomena act simultaneously meaning reproducing an instability with the exact same behaviour and time evolution is unlikely. However, we can expect to reproduce the most unstable modes, which will drive the evolution of the atmosphere in the simulations.

We have implemented the initial state prescribed in Ullrich et al. [2014] in both the axisymmetric 2D and 3D versions of ECLIPS3D [without the prescribed perturbation of Ullrich et al., 2014, as ECLIPS3D intrinsically perturbs steady states]. We only show the 2D results as, similarly to the first test case, 2D and 3D are in excellent agreement. In this test, ECLIPS3D identifies the stable modes of Thuburn et al. [2002b], slightly modified by the mean flow and the angular dependency of pressure and temperature. For the unstable modes, a continuum in frequency is returned (discretised by the numerical precision of the algorithm, controlled by the number of points in the matrix B), as expected from analytical treatment. ECLIPS3D identifies the most unstable mode at $m = 5$ with a growth rate of $6.4 \times 10^{-6} s^{-1}$ (∼2 days) which is presented in Figure 6.7. Figures 4 and 5 of Ullrich et al. [2014] demonstrate

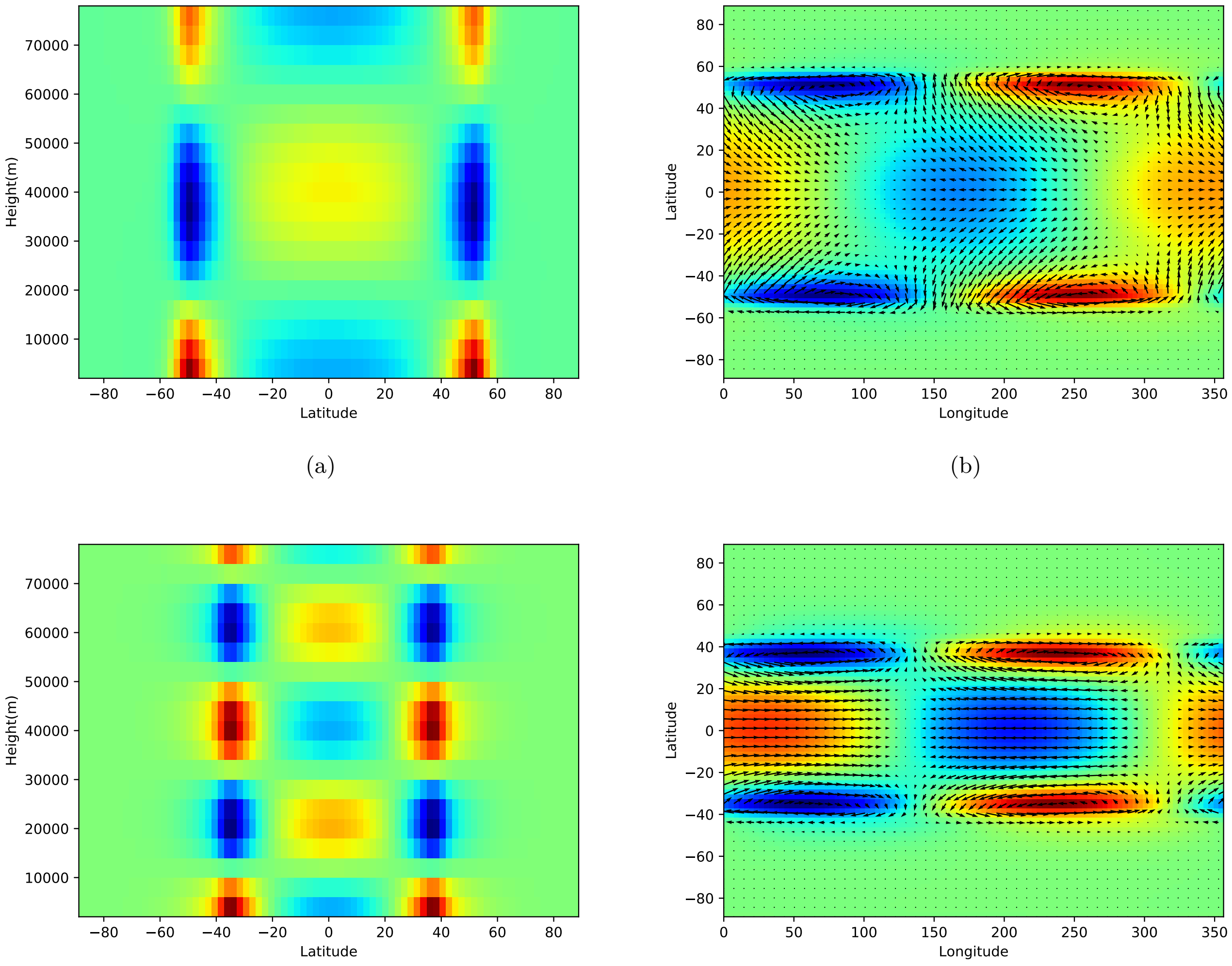

(a) (b) (c) (d)

Figure 6.6: Figures showing pressure perturbations (colour scale) and wind vectors (arrows, (b) & (d) only) for the case of a planet with Earth's radius and rotation rate but an isothermal temperature pressure profile set at $500\,K$.(a) and (c) show latitude against height at a longitude of 200 degrees and (b) and (d) longitude against latitude at a height of 25000 m. We report the values of ϕ_0 and Bu as defined in Wang and Mitchell [2014] and the growth rate σ_{growth}: (a) and (b): $\phi_0 = 50°$, $Bu \sim 0.2$ and $\frac{\sigma_{growth}}{2\Omega} = 0.12$, and (c) and (d): $\phi_0 = 35°$, $Bu \sim 0.05$ and $\frac{\sigma_{growth}}{2\Omega} = 0.026$. These results indicate that the growth rate of the most unstable mode is dependent on the characteristic height of the wave as found in Wang and Mitchell [2014].

that the instability dominates the flow after 8 days, consistent with our growth rate. Additionally, the shape of our instability has similar features to the thermodynamic state of the atmosphere in Ullrich et al. [2014] after 8 days. Our instability indeed exhibits a tilt in the height vs latitude plot (Figure 6.7b) as can be seen in Figure 6 of Ullrich et al. [2014]. The pressure also exhibits a similar sharp decrease just above the surface. One must note here that

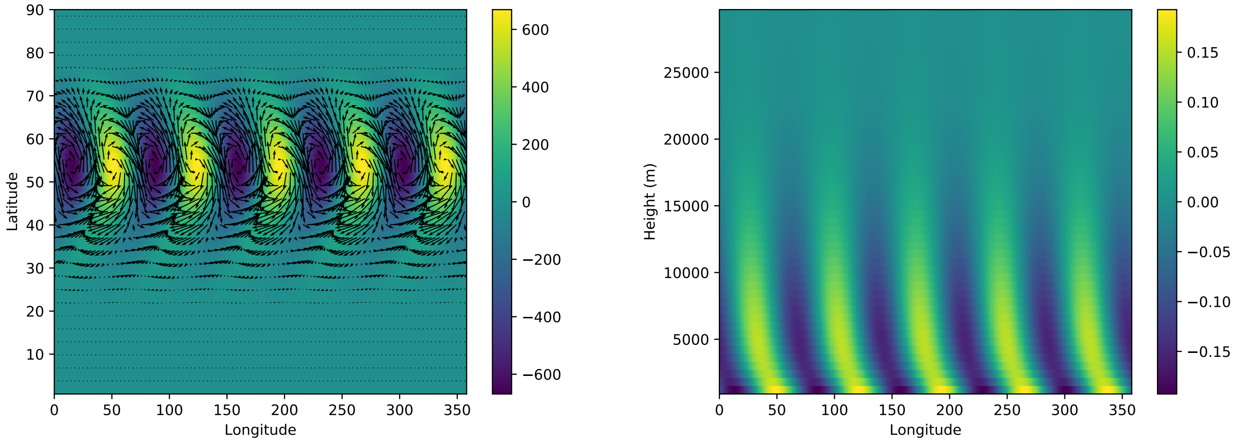

(a) (b)

Figure 6.7: Figures showing pressure (colour scale, pascals) and horizontal winds (arrows figure (a) only) using ECLIPS3D, for the baroclinic instability setup of Ullrich et al. [2014]. Figure (a) shows the near–surface pressure as a function of longitude and latitude. Figure (b) then shows pressure as a function of longitude and height at 50° latitude

our results include an uncontrolled phase in longitude coming from the axisymmetry of our setup.

The only difference between 2D and 3D is the precision due to discretisation. In 3D, ECLIPS3D is limited as the size of the matrix to invert is much bigger than in 2D. Due to the shape of the staggered grid (Figure 6.1), the first point in pressure is not the surface pressure and the sharp decrease is less obvious than in 2D (not shown).

Comparison between the semi–analytical calculation from our a posteriori energy equation and the numerical eigenvalue obtained for this mode reveals close agreement, on the real and imaginary part of σ, within a few percents. As explained in Appendix B.2, we can decompose this energy equation into three components (five in the case with meridional and vertical velocities) comprising the terms coming from the equations at rest with no angular dependency in the thermodynamic variables, the terms arising from the angular dependency of the steady state and the terms coming from the initial zonal velocity. From analytical considerations, we expect the frequency to be dominated by the velocity terms, where the global mean flow excites the modes at specific phase velocity. However, the growth rate should be controlled by the angular dependent terms as the baroclinic instability arises from horizontal gradients in the pressure and temperature [see e.g. Vallis, 2006].

Our energy-based calculation gives a frequency of $1.09 \times 10^{-5} s^{-1}$ where ECLIPS3D finds $9.93 \times 10^{-6} s^{-1}$. In the calculation, the velocity terms account for more than 80% of the frequency, confirming the analytical predictions. The calculated growth rate is $6.63 \times 10^{-6} s^{-1}$, close to the ECLIPS3D value of $6.39 \times 10^{-6} s^{-1}$, with the angular terms accounting for 96%. These results show that our a posteriori energy equation can be a powerful tool to obtain insight in the physics of numerical eigenvectors.

6.3.4 Rossby-Haurwitz waves

The previous steady states we have studied are axisymmetric and include no background velocity (Section 6.3.1) or only a zonal velocity (Section 6.3.2 and Section 6.3.3). Ideally, we would also benchmark ECLIPS3D using a test including meridional velocities as well as a dependency in longitude. Unfortunately, there are no such non–linear steady states in 3D, in which the analytical theory can provide us with predictions to compare with. We therefore consider a 2D non axisymmetric problem, with steady zonal and meridional winds: Rossby-Haurwitz waves.

Rossby-Haurwitz waves are analytical solutions of the non-linear barotropic vorticity equations. They were discovered by Haurwitz [1940] by perturbing the non–divergent equations and solving them non–linearly. If the flow remains incompressible at all times, these waves remain analytical solutions of the full equations and propagate without changing their form at constant speed. With an appropriate choice of parameters, this speed can be 0, and these waves become a stationary, steady solution of the non–divergent barotropic vorticity equations, hence another test case for ECLIPS3D.

The non-divergent barotropic equations are simply Eq.(6.1a) and Eq.(6.1b) with $w = 0$ with an imposed null divergence:

$$\frac{\partial u}{\partial \lambda} + \frac{\partial}{\partial \phi}(v \cos \phi) = 0. \tag{6.10}$$

This last equation does not involve any time derivative, we therefore have to slightly adapt the structure of the code for this set-up. Instead of solving an eigenvector problem, we solve a generalized eigenvector problem where:

$$Bx = \mathrm{i}\sigma C x, \tag{6.11}$$

where x is an eigenvector, B the linearised matrix of equations and C a diagonal matrix with some zeros in the diagonal. The linearisation is straightforward, as the equations are similar to the full set of equations and the divergence equation is already linear.

The interest of this test lies in the stability analysis of these waves. Hoskins [1973] showed that Rossby-Haurwitz waves are stable for longitudinal wave number $R < 5$ and unstable for higher wave numbers. However, in Hoskins' analysis some triad interactions were missing, as simplifications were required to treat the problem analytically. Inspired by Baines [1976], Thuburn and Li [2000] have resolved the issue by showing that a Rossby-Haurwitz wave of wavenumber 4 is unstable, because of an interaction with wave numbers 1, 3 and 5 (see also Lynch [2009]).

ECLIPS3D does not make any assumption on the shape of the perturbation needed to trigger an instability, nor on the instability itself. We therefore expect to obtain unstable modes around a steady $R = 4$ wave. Our set up is similar to the classical benchmarking test of Williamson et al. [1992] and Thuburn and Li [2000], with a vorticity ψ being:

$$\psi = -a\omega^2 \sin \phi + a^2 K \cos^R \phi \sin \phi \cos^R \lambda, \tag{6.12}$$

where K and ω are constants and R is the longitudinal wavenumber. In order to obtain a steady, stationary wave we also must impose [see Haurwitz, 1940]:

$$\frac{2R(\Omega+\omega)}{(R+1)(R+2)} = \omega R. \tag{6.13}$$

With $R = 4$ and $\Omega = 7.29 \times 10^{-5}\text{s}^{-1}$, the Earth rotation rate, this leads to $\omega \approx 5 \times 10^{-6}$, close to the value chosen by Williamson et al. [1992] and Thuburn and Li [2000] $\omega \approx 7.8 \times 10^{-6}$. With $R = 2$, $\omega \approx 1.5 \times 10^{-5}$. In accordance to their set-up, we impose arbitrarily $K = \omega$.

We present the initial steady states for $R = 4$ and $R = 2$ in Figure 6.8. As expected from Thuburn and Li [2000], we obtain a linear instability for the $R = 4$ set-up, displayed in Figure 6.8b. This instability oscillates with a period of ≈ 3 days, with an exponential growth timescale of 6 days. The timescale for instability is globally coherent with the results of Thuburn and Li [2000], which find that the flow becomes significantly altered after day 20. For $R = 2$, we also find an instability, with striking resemblance to the $R = 4$ instability in shape, a period of just under a day and growth timescale of 4 days. This mode is shown in Figure 6.8d, and this result is in accordance with Baines [1976] who shows analytically that all the $R \geq 2$ ($n \geq 3$ in their study, where we have $R = n - 1$ here) Rossby-Haurwitz waves can be unstable. Interestingly, we also found an instability for a $R = 3$ Haurwitz wave but with a growth timescale of more than a hundred days. Such an instability would probably be smoothed out by any source of dissipation or diffusion in a GCM. Globally, our code agrees well with the theoretical study of Rossby-Haurwitz wave, and demonstates the proper treatment of longitudinal dependent steady state and meridional velocities in ECLIPS3D.

6.3.5 Linear steady circulation with drag

As discussed in the introduction our development of ECLIPS3D was largely driven by studies of the acceleration of zonal flows in hot Jupiter atmospheres. For these planets analytical studies have shown linear steady states to be of vital importance [see Showman and Polvani, 2011]. Therefore, we have also implemented the capability to calculate linear steady states in ECLIPS3D (see Section 6.2), which is a much simpler process compared to the identification of eigen modes. To benchmark this section of the code we compare our results to those obtained in the study of Komacek and Showman [2016], in particular the case they present in their Figure 5 where they solve the full Navier-Stokes equations, but with such a low heating rate that only the linear terms contribute. This requires the addition of a linear drag in the linearised equations following the depth dependent behaviour of that adopted by Komacek and Showman [2016]. Additionally, the heating is performed via a Newtonian relaxation with a height–dependent radiative constant. The resulting equation set is shown in Appendix B.1.5. Figure 6.9 then presents the resulting linear circulations obtained using ECLIPS3D 1§ which show excellent qualitative agreement with the results of Komacek and Showman [2016] (see their Figure 5). Komacek and Showman [2016] do not present the vertical structure of their circulation.

6.4 Conclusion

In this chapter we introduced and benchmarked ECLIPS3D: a parallel code for identifying linear instabilities, waves and circulations around a steady state of the Navier–Stokes equations in planetary atmospheres. The linearised equations only omit viscosity and an a posteriori energy equation is used to identify contributions from each component. The time–dependent eigenvector solution or time–independent matrix inversion calculations are performed through discretisation onto a staggered grid and subsequently ScaLAPACK routines.

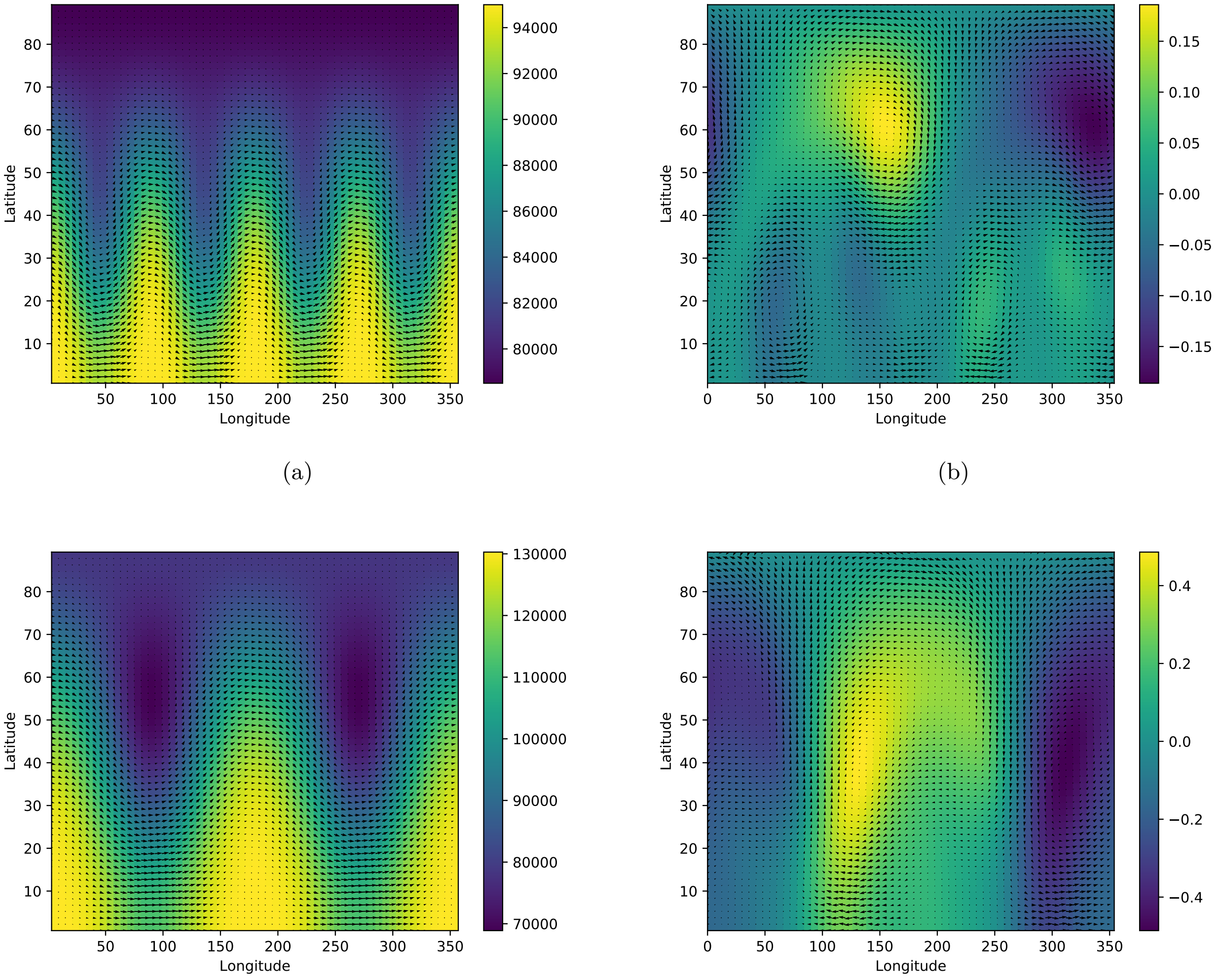

(a) (b) (c) (d)

Figure 6.8: Figures showing pressure (colour scale, (a) and (c) in pascals and arbitrary units for (b) and (d)) and horizontal winds (arrows) for Rossby-Haurwitz waves and most unstable modes. Figures (a) and (c) show the initial steady states for $R = 4$ and $R = 2$ respectively (see text). Figures (b) and (d) are the most unstable mode obtained with ECLIPS3D for the $R = 4$ and $R = 2$ set-up respectively.

The benchmarks cover various well studied wave and instability tests, namely a simple atmosphere at rest [Thuburn et al., 2002b], a Rossby-Kelvin unstable jet [Wang and Mitchell, 2014], a baroclinically unstable jet [Ullrich et al., 2014], an unstable Rossby-Haurwitz wave [Thuburn and Li, 2000] and a linear circulation with atmospheric drag [Komacek and Showman, 2016]. For all these set-ups ECLIPS3D is able to produce excellent, qualitative agreement with the previous works. We demonstrate that our a posteriori energy equation is a viable tool to verify the results and identify the dominant terms. In the next chapter, ECLIPS3D is used to obtain the linear steady states relevant for the study of hot Jupiters, as well as a sanity check in the calculation of the eigenvectors. It has proven in our work to be a powerful tool to grasp the essence of physical mechanisms at stake in the evolution

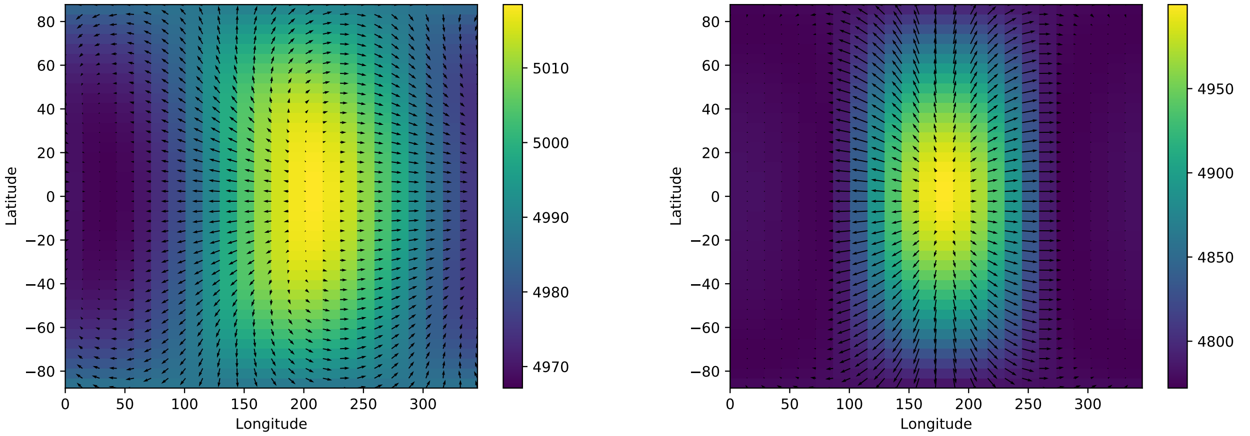

(a) $\tau_{\rm drag} = 10^5 s$ and $\tau_{\rm rad} = 10^4 s$ (b) $\tau_{\rm drag} = 10^3 s$ and $\tau_{\rm rad} = 10^3 s$

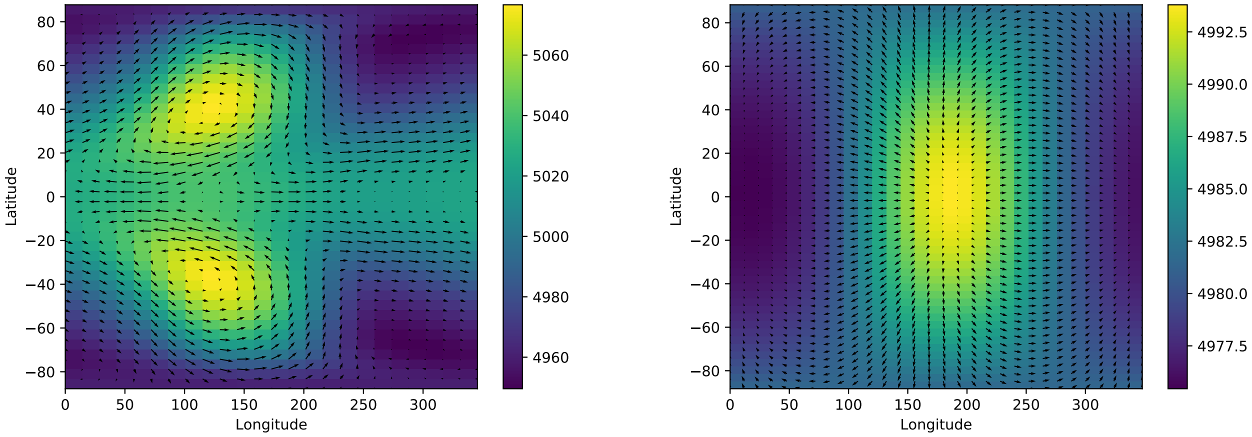

(c) $\tau_{\rm drag} = 10^6 s$ and $\tau_{\rm rad} = 10^4 s$ (d) $\tau_{\rm drag} = 10^4 s$ and $\tau_{\rm rad} = 10^6 s$

Figure 6.9: Figures of the pressure (colour scale, Pascals) and horizontal winds (arrows) as a function of latitude and longitude at a height of 5×10^6m, for a steady state circulation with a forcing of $\Delta T = 100K$ [see Komacek and Showman, 2016, for definition]. Results to be compared to Figure 5 of Komacek and Showman [2016].

of hot Jupiters, and to obtain the qualitative shape of wave processes when the analytic calculations were limitating.

That being said, ECLIPS3D currently has several limitations, primarily its computational efficiency, leading to limitations on resolution, particularly for 3D cases. We are working on several methods to improve this issue for example using libraries adapted to sparse matrices, or splitting the eigenvector solution into several sub–matrices as opposed to a single large matrix (potentially useful as the time taken to solve this type of problem increases faster than linearly with matrix size). This splitting of the matrix may be particularly well suited to a spectral decomposition as we are searching for the most unstable mode, not necessarily trying to capture the entire 'shape' of the mode. This could be done through spherical harmonics in the horizontal or Chebyshev's spectral decomposition in the radial direction.

Despite its limitations, ECLIPS3D in its current version still represents a powerful resource which can be used to study instabilities in 2D situations under axisymmetry or cases where a two–layer model is applicable, or for low resolution 3D problems. The code itself can easily be adapted to different situations, in spherical coordinates, with additional physics or alternative boundary conditions. As the structure of the code is independent of the underlying equations, meaning alternatives can easily be implemented in terms of symmetries and coordinate systems.

Finally, ECLIPS3D could be applied to a wide range of astrophysical problems. The most obvious one, for which ECLIPS3D was designed, is the study of instabilities and linear circulations for planetary atmospheres, but the range of applicability is greater. Asteroseismology for example requires the need to linearise the equations of motion and identify the leading modes, sometimes with complicated circulation or thermodynamic state inside the star. Adapted to cylindrical geometry, ECLIPS3D could be a powerful tool to identify the possible instabilities in protoplanetary disks, where instabilities creating pressure traps are proposed to be a strong way of making planets through core accretion. The addition of a magnetic field in the equations implemented in the code would not pose any theoretical challenge either, which could provide numerous information on the linear behaviour of astrophysical fluids in more general cases.

Chapter 7

Equatorial dynamics of hot Jupiters

Moi j'aime pas ces histoires de Sud-Est, Nord-Ouest, et tous ces machins ! [...]
C'est un coup à se planter ça ! De toutes façons, on dit le Nord ! Selon comme
on est tourné ça change tout.
Perceval – Kaamelott

7.1 Introduction

As we have seen in chapter 5, there are no equivalents of hot Jupiters within our solar system, necessitating the generation of new models, or adaptation of existing frameworks. Notably, due to their proximity to their host star hot Jupiters are expected to be tidally–locked [see review in Baraffe et al., 2010], with a permanent day and night side. This leads to a huge asymmetry in the heating of these planets which, in turn drives the atmospheric dynamics. Numerically, we have detailed the main features of the atmospheric dynamics within chapter 5: a broad equatorial superrotating jet, associated with an eastward shift of the hot spot of the atmosphere from the substellar point.

Analytically, although superrotation in hot Jupiters was first proposed in 2002 [Showman and Guillot, 2002], the understanding of the accelerating mechanism was really put forward by Showman and Polvani [2011] (hereafter SP11). For fast rotating planets, the emergence of jets is often thought a result of Rossby waves convergence and divergence (see section 2.1.5): as shown e.g., by Vallis [2006], the stirring caused by the propagation of Rossby waves generates a convergence of eastward momentum at the latitude where they are excited, and a convergence of westward momentum where they break. In other words, the mid latitudes, where the gradient of the Coriolis parameter is the strongest hence where Rossby waves are mainly triggered, is expected to exhibit a net eastward, prograde momentum excess whereas poleward or equatorward of this region the atmosphere should exhibit a westward momentum excess. This is the case of the Earth's stratosphere. For very slowly rotating planets, like Venus, the whole atmosphere is superrotating, presumably because of diffusion of momentum through meridional circulation [Gierasch, 1975].

Hot Jupiters lie in between these two limits and are extremely heated. The usual understanding of superrotation on solar system planets is therefore not applicable. The main aspect is that the Rossby deformation radius is of the size of the planet: Rossby waves can travel the whole planet both in longitude and latitude without breaking, impeding the usual description of momentum convergence and divergence.

The idea of Showman and Polvani [2011] is that the heating continuously excites, on the day side, planetary Rossby, Kelvin and gravity waves, that lead to a stationary state (of the linear order). This stationary circulation then triggers eastward momentum convergence at the equator of the second order, leading eventually to superrotation. The non–linear equilibrium would then be reached when the transport of meridional and vertical eddy momentum into the region, acting to accelerate and decelerate the jet, respectively, is balanced by the atmospheric drag. This work has been extended to 3D by Tsai et al. [2014] where they include consideration of the resonance of the atmospheric wave response to the presence of a global zonal velocity, as well as the 'tilt' of the vertical component which acts to drive the vertical eddy–momentum transport. Tsai et al. [2014] represents the most advanced study of this process to date, considering the impact of atmospheric waves in the steady state regime. Very recently, Hammond and Pierrehumbert [2018] have extended the work of Tsai et al. [2014] to background shear flows, but only in the 2D beta-plane limit. Perez-Becker and Showman [2013] considered the propagation of waves and the resulting balance for the equilibriated jet to propose diagnostics for predicting the day to night temperature contrast, controlled by the efficiency of the zonal advection. This analysis was later improved upon by Komacek and Showman [2016].

Combining the understanding in the works to date a global, coherent understanding of the formation of superrotation in hot Jupiter atmospheres is developing. However, there are still outstanding questions. Notably, the study of Tsai et al. [2014] is strictly valid in the moderate to strong dissipation limit, and that of Hammond and Pierrehumbert [2018] requires an inital sheared superrotation, but the work of Komacek and Showman [2016] shows that superrotation develops only if the dissipation is sufficiently low (their Figure 4). Therefore, current theories are applicable only once an initial superrotation is set and the further evolution is much slower than the initial triggering of superrotation. Similarly, the explanation of SP11 of the spin up of superrotation requires the linear steady state to be reached before further evolution of the atmosphere, which is not a viable condition when the planet experiences a very high forcing as hot Jupiters do.

In this chapter, we want to assess what is driving the initial spin up of superrotation in hot Jupiters. First, we recall the main assumptions and find the time dependent, linear solution of the beta-plane equations in section 7.2. We also recall the results of SP11, Tsai et al. [2014], Komacek and Showman [2016] that we base our study on. Then, we assess numerically the validity of the formation of the linear stationary state with different longitudinal forcing in section 7.3, showing that as long as there is a differential heating between the day and the night side the exact shape of the forcing is not crucial. In section 7.4, we study the different characteristic time of decay for different waves, that allows us to understand the shape of the linear steady states of the Figure 5 of Komacek and Showman [2016]. These decay times are primordial to determine which processes are dominating in the evolution of hot Jupiters. Finally, in section 7.5 we study the transition to superrotation through eddy mean flow acceleration in different situations, showing the importance of vertical momentum transport with different regimes of drag and newtonian cooling. Globally, the results of this chapter show that the paradigm of equatorial superrotation in hot Jupiter is robust: superrotation is spun-up by an eddy mean flow interaction of the wave structure with the background flow, but also exhibits the importance of wave dissipation timescales and vertical momentum convergence.

7.2 Notations and 2D shallow water equation and solution

7.2.1 Theoretical framework

Through this section, we will work with the 2D shallow water beta plane solutions. Wu et al. [2000] have shown that the 3D structure of beta plane solutions can be decomposed onto an infinite sum of solutions of 2D beta planes with different characteristic heights (see section 2.1.4). The importance of this decomposition regarding hot Jupiter atmospheric dynamics has been emphasized by Tsai et al. [2014], where they see a vertical shift of the wave response when the mean background velocity is changed (their Figure 10). Therefore, we first recall here the most important results of Matsuno [1966], Gill [1980] and Showman and Polvani [2011], that solves for 2D beta-plane solutions.

Following SP11, the nondimensional, linearized equations of motion to the forced problem on a 2D, equatorial beta plane can be written as:

$$\frac{\partial u}{\partial t} - yv + \frac{\partial h}{\partial x} + \frac{u}{\tau_{\text{drag}}} = 0, \tag{7.1}$$
$$\frac{\partial v}{\partial t} + yu + \frac{\partial h}{\partial y} + \frac{v}{\tau_{\text{drag}}} = 0, \tag{7.2}$$
$$\frac{\partial h}{\partial t} + \frac{\partial u}{\partial x} + \frac{\partial v}{\partial y} + \frac{h}{\tau_{\text{rad}}} = Q, \tag{7.3}$$

where u is the zonal velocity, v the meridional, $h = H - H_0$ the height of the shallow water fluid minus the initial, horizontally constant height H_0 and Q the heating function. When spatially decomposing in 3D, the modes are expressed as an infinite sum of modes indexed by m with equivalent depth H_m instead of H_0. The orthogonal base functions are sinusoidal in z, the vertical coordinates, of the form $\cos(mz)$ and the heating has to be decomposed onto these functions (see Tsai et al. [2014], section 2). Keeping H_0 for the rest of this section, the dimensional, characteristic time, length and speed are, respectively:

$$T = \left(\sqrt{gH_0}\beta\right)^{-1/2}, \tag{7.4}$$
$$L = \left(\sqrt{gH_0}/\beta\right)^{1/2}, \tag{7.5}$$
$$U = \sqrt{gH_0}, \tag{7.6}$$

where g is the gravitational acceleration assumed constant, and $\beta = 2\Omega\cos\phi/R$ the derivative of the Rossby parameter with Ω the rotation rate, ϕ the latitude of the beta plane and R the radius of the planet. In this work, we only use $\phi = 0$.

Equations (7.1) to (7.3) form a first order differential equation in time, of the form $\partial X/\partial t = aX + \mathcal{Q}$ where X is a vector $X = (u, v, h)$ of solutions and $\mathcal{Q} = (0, 0, Q)$ the vector form of the forcing. Hence the solutions simply are the sum of a homogeneous and a particular solution.

When neither drag nor heating are considered, Matsuno [1966] has expressed the analytic solutions to the homoegenous equation:

$$\mathrm{i}\omega u - yv + \mathrm{i}kh = 0, \tag{7.7}$$

$$\mathrm{i}\omega v + yu + \frac{\partial h}{\partial y} = 0, \tag{7.8}$$

$$\mathrm{i}\omega h + \mathrm{i}ku + \frac{\partial v}{\partial y} = 0, \tag{7.9}$$

in the form $X = X\exp(\mathrm{i}\omega t + \mathrm{i}kx)$ with ω the frequency of the solution and k the longitudinal wavenumber. Matsuno [1966] showed that one can express a single equation for v:

$$\frac{\partial^2 v}{\partial y^2} + (\omega^2 - k^2 + \frac{k}{\omega} - y^2)v = 0, \tag{7.10}$$

and by analogy with the Schrödinger equation of a simple harmonic oscillator, the boundary conditions $v \to 0$ when $|y| \to \infty$ require

$$\omega^2 - k^2 + \frac{k}{\omega} = 2n + 1, \tag{7.11}$$

with $n \in \mathbb{N}$. As this is a third order equation, the eigenvalues for the frequency were labelled $\omega_{n,l}$ with $l = 0, 1, 2$. Finally, the case where $n = 0$ had to be treated separately, and the important case where v is identically null is similar to a coastal Kelvin wave, with $\omega = -k$. The shape of the solutions in the y direction are finally expressed through the use of the parabolic cylinder functions ψ_n with:

$$\psi_n(y) = H_n(y)e^{-1/2y^2}, \tag{7.12}$$

where H_n is the n^{th} Hermite polynomial. Finally, simple mathematical arguments show that the eigenvalue ω is always real: the homogeneous solutions are only neutral modes. Matsuno [1966] have also showed that the horizontal part of the solutions form a complete, orthogonal set of the 2D beta-plane: any horizontal function on the beta plane can be written as a linear combination of the homogeneous solutions to equations (7.1) to (7.3).

With the inclusion of heating, drag and radiative cooling, Matsuno [1966] and Gill [1980] have obtained the steady solution to the forced equations (hence the particular solution of equations (7.1) to (7.3)). Namely, writing $\tilde{X}_{n,l} = (u_{n,l}, v_{n,l}, h_{n,l})$ the horizontal part of the solutions of the homogeneous equations, their completeness and orthogonality allows one to write:

$$\mathcal{Q} = \sum_{n,l} q_{n,l}\tilde{X}_{n,l}, \tag{7.13}$$

where $\mathcal{Q} = (0, 0, Q)$ and $q_{n,l}$ is the projection of $\mathcal{Q}$ onto $\tilde{X}_{n,l}$. Matsuno [1966] (equation 34) and Gill [1980] have then shown that a steady solution X to the forced problem with $\tau_{\mathrm{drag}} = \tau_{\mathrm{rad}}$ is:

$$X = \sum_{n,l} \frac{q_{n,l}}{\tau_{\mathrm{drag}}^{-1} - \mathrm{i}\omega_{n,l}} \tilde{X}_{n,l}. \tag{7.14}$$

As shown by Showman and Polvani [2011], for conditions relevant to hot Jupiters, hence horizontal wavenumber 1 representing the asymmetric heating, the steady linear solution exhibits a chevron shaped pattern, and has been denominated the Matsuno-Gill solution. The question we raise in the chapter is the pertinence of the study of a linear steady state for hot Jupiters where non linearities are dominant. In that regard, we need the time dependent solution of equations (7.1) to (7.3) in the general case, which we express in section 7.2.3. In the next section however, we recall the results from SP11 and Tsai et al. [2014] that aim to explain the spin up and equilibration of superrotation respectively.

7.2.2 Non linear accelerations from the linear steady state

The main idea of Showman and Polvani [2011] is that the Matsuno-Gill is a linear steady state, but the non linear accelerations from this circulation can trigger an equatorial superrotation. Consider a linear perturbation (a wave or a steady linear circulation of linear order) associated with velocities u', v', w' in the longitudinal, latitudinal and vertical directions respectively. The non linear momentum fluxes per unit mass from this perturbation are given by:

$$\phi_l = \overline{u'v'}, \tag{7.15}$$

$$\phi_v = \overline{u'w'}, \tag{7.16}$$

where ϕ_l is the latitudinal convergence of momentum, ϕ_v the vertical and an overline denotes a longitudinal average. When ϕ_l is positive (negative), there is a net transport of eastward momentum to the North (South). When ϕ_v is positive (negative), there is a net transport of eastward momentum upwards (downwards). For shallow water beta plane, the vertical momentum flux is accounted for by the addition of a coupling term between the bottom, quiescent atmosphere and the dynamically active atmosphere (the R term in SP11, equations (9) and (11)). Therefore, if ϕ_l is negative in the mid latitude of the Northen hemisphere and positive in the Southern hemisphere, there is a net meridional convergence of eastward momemtum (same applies in the vertical coordinates for 3D systems). On Figure 7.1a, we show the shape of the Matsuno-Gill circulation obtained from the 3D linear steady state of ECLIPS3D, in typical conditions for hot Jupiters. For this figure, we follow the definition of Komacek and Showman [2016]: ΔT_{eq}, the equilibrium day side-night side temperature difference, decreases logarithmically in pressure between 10^{-3}bar where $\Delta T_{eq} = \Delta T_{eq,top}$ to 10 bars where $\Delta T_{eq} = 0$. The drag timescale is constant from the outer atmosphere to 10 bars where it can be changed but does not impact the results significantly. Finally, the radiative timescales also decreases logarithmically with pressure between $\tau_{\mathrm{rad}} = \tau_{\mathrm{rad,top}}$ above 10^{-2} bars to $\tau_{\mathrm{rad}} = 10^7$s below 10 bars.

First, as shown in Figure 7.1a the maximum temperature at the equator is shifted eastward from the substellar point (at a longitude of 180 degrees, facing the star), as is seen in observations [Knutson et al., 2007, Zellem et al., 2014]. Then, the meridional circulation exhibits a Rossby wave-type circulation at mid latitudes, with clockwise

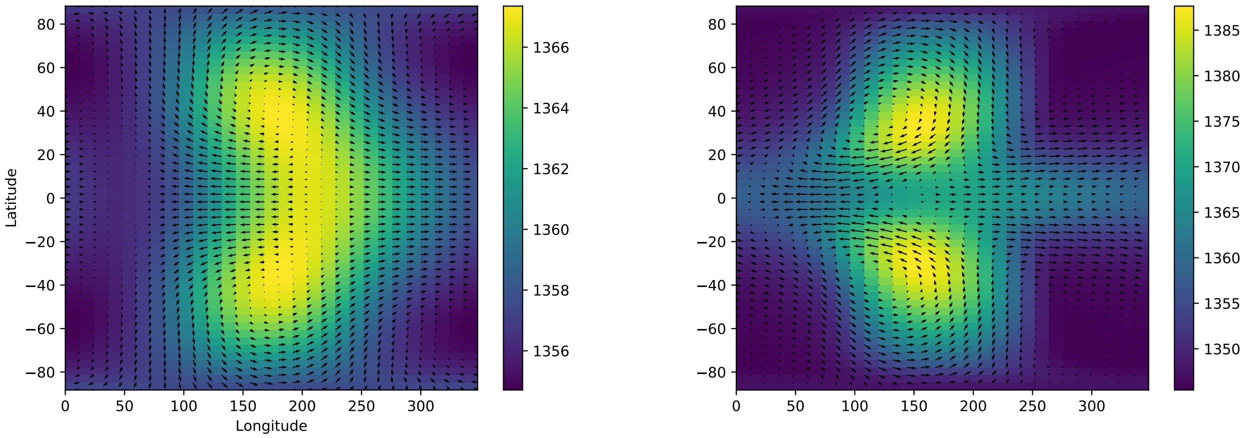

(a) (b)

Figure 7.1: Temperature (colorscale in K) and winds (arrows) at the 40mbar pressure level of the linear steady state (denominated Matsuno-Gill circulation) obtained with ECLIPS3D with heating function, drag and radiative timescales following the definitions of Komacek and Showman [2016]. With their notations: (a) $\Delta T_{eq,top} = 100$K, $\tau_{\mathrm{drag,top}} = 10^5$s and $\tau_{\mathrm{rad,top}} = 10^5$s. The maximum speed at this pressure range is 10m.s^{-1}. (b) $\Delta T_{eq,top} = 100$K, $\tau_{\mathrm{drag,top}} = 10^6$s and $\tau_{\mathrm{rad,top}} = 10^4$s. The maximum speed at this pressure range is 100m.s^{-1}. Note that the maximum speed has been multiplied by ten as the drag timescale has been multiplied by ten.

or anticlockwise rotation around the pressure maxima, and a Kelvin wave type circulation at the equator, with no meridional velocities. The combination of both of these circulations brings eastward momentum to the equator to the East of the substellar point, and advects westward momentum to the mid latitudes to the West of the substellar point. Globally, it is easily shown that ϕ_l is indeed negative in the Northern hemisphere and positive in the Southern hemisphere: there is a net convergence of eastward momentum at the equator. According to SP11, this convergence is associated with a vertical divergence of momentum, and equilibration occurs when both cancel.

Tsai et al. [2014] have further extended this understanding. By considering the vertical coordinates as well, projecting the function onto equivalent height beta plane solutions (see previous section), they have shown that the vertical behaviour of the waves can be linked to the equilibration of the jet (a synonym here for equatorial superrotation). More precisely, they have shown that in the limit of slow evolution, or strong dissipation, their linear development around a steady flow with constant background zonal velocity reproduces extremely well the wave processes occurring in real 3D simulations. In their figure 10, they show that the wave response of the atmosphere is shifted from West to East when the background zonal velocity is increased: they interpret this as a convergence towards a single equilibrium state, where the non linear acceleration from the linear processes cancel. Although very detailed and physically relevant, the results of their paper is, as they state, only applicable to strong or modest damping scenario, which actually is dictated by the fact that the waves must have the time to reach a stationary state before non linearities become significant. Once a primordial jet is settled, the evolution of the atmosphere is slow and their work therefore applies even in the low damping scenario, explaining the evolution of the jet towards an equilibrated state.

The issue, from which our analysis is based on, comes from Komacek and Showman [2016]. In their figure 4 and 5, they compare the steady states from 3D GCM simulations with various τ_{rad} and τ_{drag} with a low forcing, hence a linear steady state, and a strong forcing, hence non linear steady state. In figure 7.1b, we show the shape of the linear steady state they obtain in the case where the non linear steady state exhibits superrotation. When the linear steady state resembles that of Figure 7.1a, the associated non linear steady state is not superrotating. In the explanation of SP11, the stationary wave pattern obtained from the heating supposedly accelerates superrotation. Komacek and Showman [2016] seem to highlight the opposite situation: when the linear steady state accelerates the equator, no superrotation occurs. On the contrary, when the linear steady states takes momentum away from the equator (figure 7.1b), the non linear steady state is superrotating. They acknowledge it themselves: "these phase tilts are the exact opposite of those that are needed to drive superrotation." In order to understand this discrepancy, we need to go a step beyond the sole consideration of linear steady state, and to study the dependency of the linear solution with time. This is the objective of the section 7.2.3 and 7.4.

7.2.3 Time dependent solutions

In this section, we express the time dependent solution to the forced problem. Our main approximation is that the heating function can be decomposed onto the homogeneous solutions of equations 7.17 to 7.19. When $\tau_{\mathrm{drag}} = \tau_{\mathrm{drag}}$, this is a direct consequence of the orthogonality and completeness of the Hermite functions, as shown by Matsuno [1966]. However, when $\tau_{\mathrm{drag}} \neq \tau_{\mathrm{drag}}$, we show in appendix C that the eigenvectors are no more orthogonal. Although they remain linearly independent, a more rigorous proof would need to be provided to show that they still form a complete set of solutions. Physically speaking however, it is quite clear that the heating function will trigger linear waves which are solutions of the homogeneous equation, and such a decomposition of the heating function onto these waves probably exists, although it is not necessarily given by a scalar product (contradicting our equation 7.27). We are working on that point. Finally, we point out that solving $\partial X/\partial t = aX + \mathcal{Q}$ is of no difficulty, except on the calculation of the eigenvalues and eigenvectors of the homogeneous equation, but we decide here to use the Green function as it provides a better physical understanding.

With the addition of a drag timescale τ_{drag} and a radiative timescale τ_{rad}, equations (7.7) to (7.9) are simply modified as:

$$(\mathrm{i}\omega + \frac{1}{\tau_{\mathrm{drag}}})u - yv + \mathrm{i}kh = 0, \tag{7.17}$$

$$(\mathrm{i}\omega + \frac{1}{\tau_{\mathrm{drag}}})v + yu + \frac{\partial h}{\partial y} = 0, \tag{7.18}$$

$$(\mathrm{i}\omega + \frac{1}{\tau_{\mathrm{rad}}})h + \mathrm{i}ku + \frac{\partial v}{\partial y} = 0\ . \tag{7.19}$$

Indexing the solutions by the numbers n and l as in Matsuno [1966], we call $X_{n,l} = (u_{n,l}, v_{n,l}, h_{n,l})$ an eigenvector of equations (7.17), (7.18) and (7.19). We call $\mathcal{O}$ the operator of these equation, such that $\mathcal{O}X_{n,l} = 0$ for all n and l. The general equation is $\mathcal{O}X_{\mathrm{F}} = \mathcal{Q}$ where $\mathcal{Q}$ is the forcing which is only applied on the third equation so $\mathcal{Q} = (0, 0, Q)$ and X_{F} a forced, time dependent solution. A homogeneous solution X_{H} is written in its general form:

$$X_{\mathrm{H}} = \sum_{n,l} \alpha_{n,l} X_{n,l}, \tag{7.20}$$

where $\alpha_{n,l}$ are scalars, and we write:

$$X_{n,l} = \tilde{X}_{n,l}(x,y) e^{(\mathrm{i}\omega_{n,l} - \sigma_{n,l})t} \ . \tag{7.21}$$

When $\tau_{\mathrm{drag}} \neq \tau_{\mathrm{rad}}$, we don't know the analytical expression for $\omega_{n,l}$ and $\sigma_{n,l}$. When $\tau_{\mathrm{drag}} = \tau_{\mathrm{rad}}$, $\omega_{n,l}$ are similar to the $\omega_{n,l}$ of Matsuno [1966] and $\sigma_{n,l} = \tau_{\mathrm{drag}}^{-1}$ for all (n,l). We seek the causal green function $X_{\mathrm{G}}(t,t')$ such that

$$\mathcal{O} X_{\mathrm{G}} = \delta(t-t') F(x,y), \tag{7.22}$$

where $\delta(t)$ is the Dirac distrubution and F is any vector with no time dependency. Taking for F the spatial heating function and writing $\mathcal{Q} = g(t)F(x,y)$ (separating the variable is no trouble in our case), then the global solution of the equations with forcing write

$$X_{\mathrm{F}} = \int_{-\infty}^{\infty} X_{\mathrm{G}}(t-t') g(t') dt' = \int_{-\infty}^{t} X_{\mathrm{G}}(t-t') g(t') dt', \tag{7.23}$$

where the second equality arise from the fact that the Green function is causal. From the definition of the Green function (Eq.(7.22)), for $(t-t') > 0$ we have $\mathcal{O}X_{\mathrm{G}} = 0$. Writing:

$$X_{\mathrm{G}}(t,t') = \Theta(t-t') \sum_{n,l} \alpha_{n,l} X_{n,l}(t-t') \tag{7.24}$$

where $\Theta(t)$ is the heavyside function, null when $t < 0$ and equal to 1 otherwise, it is easily verified that:

$$\begin{aligned}\mathcal{O} X_{\mathrm{G}} &= \delta(t-t') \sum_{n,l} \alpha_{n,l} X_{n,l}(t-t') + \Theta(t-t') \frac{\partial}{\partial t} \sum_{n,l} \alpha_{n,l} X_{n,l}(t-t') + \mathcal{O}_h \Theta(t-t') \sum_{n,l} \alpha_{n,l} X_{n,l}(t-t') \\ &= \delta(t-t') \sum_{n,l} \alpha_{n,l} X_{n,l}(t-t') + \Theta(t-t') \mathcal{O} \sum_{n,l} \alpha_{n,l} X_{n,l}(t-t') \\ &= \delta(t-t') \sum_{n,l} \alpha_{n,l} X_{n,l}(t-t') \end{aligned} \tag{7.25}$$

where we have used the fact that the derivative of the heavyside function is the Dirac distribution, $\mathcal{O} = \partial/\partial t + \mathcal{O}_h$ where $\mathcal{O}_h$ is an operator acting on the horizontal coordinates only and $\mathcal{O}X_{n,l} = 0$. Therefore, if we want to solve the forced problem, we have to project the forcing on the homogeneous solutions and write for $t = t'$:

$$\sum_{n,l} \alpha_{n,l} X_{n,l}(t - t' = 0) = \sum_{n,l} \alpha_{n,l} \tilde{X}_{n,l} = F(x,y) \text{ or} \tag{7.26}$$

$$\alpha_{n,l} = \frac{1}{\left|\left|\tilde{X}_{n,l}\right|\right|^2} \left\langle \tilde{X}_{n,l}, F \right\rangle \tag{7.27}$$

with $<,>$ the scalar product and $||\ ||$ the norm. As in the previous section, we name $\alpha_{n,l} = q_{n,l}$ (they are named b_m in Matsuno [1966] and $b_{m,n,l}$in Tsai et al. [2014] in 3D). In the case of hot Jupiters, the forcing is a constant function of time due to the synchronisation of the orbit and spin of the planet. Therefore, considering that we "switch on" the star at $t = 0$, $g(t) = \Theta(t)$ we obtain the solution to the forced problem:

$$\begin{aligned} X_{\mathrm{F}} &= \int_{-\infty}^{t} \sum_{n,l} q_{n,l} X_{n,l}(t-t')\Theta(t-t')\Theta(t')dt' \\ &= \sum_{n,l} \int_{0}^{t} q_{n,l} \tilde{X}_{n,l}(x,y) e^{(i\omega_{n,l}-\sigma_{n,l})(t-t')}\Theta(t')dt' \end{aligned} \tag{7.28}$$

In this integral form, we see that the solution is the continual excitation (the Θ term) of waves with characteristic frequency $\omega_{n,l}$ and time of decay $\sigma_{n,l}^{-1}$. The amplitude of the excited waves is proportional to their projection in the forcing function Q, as explained by Gill [1980] or Tsai et al. [2014]. Calculating this integral is straightforward:

$$X_{\mathrm{F}} = \sum_{n,l} \frac{q_{n,l}\tilde{X}_{n,l}}{\sigma_{n,l} - i\omega_{n,l}} \left(1 - e^{(i\omega_{n,l}-\sigma_{n,l})(t)}\right) \tag{7.29}$$

Under this form, we simply recover the results of Matsuno [1966], and notably their equation (34) or our equation (7.14):

$$X_{\mathrm{MG}} = \sum_{n,l} \frac{q_{n,l}\tilde{X}_{n,l}}{\sigma_{n,l} - i\omega_{n,l}} \tag{7.30}$$

where X_{MG} is the Matsuno-Gill solution, hence the steady solution to the forced problem. The time dependent part of the solution could have been obtained from a simple first order equation solution. However, the Green function formalism allows to determine that the solution consists of permanently forced waves that are damped with time, and that the shape of the atmosphere is given by the interactions between these waves. Notably, with Eq.(7.28), we can write:

$$X_{\mathrm{MG}} = \lim_{t\to\infty} \sum_{n,l} \int_{0}^{t} q_{n,l}\tilde{X}_{n,l} e^{(i\omega_{n,l}-\sigma_{n,l})(t-t')}\Theta(t')dt' \tag{7.31}$$

This form confirms the interpretation of the stationary solution as an infinite interaction of waves, and also shows that for a given heating function, changing the value of τ_{drag} (but keeping $\tau_{\mathrm{rad}} = \tau_{\mathrm{drag}}$), hence not altering the $\tilde{X_{n,l}}$ and $\omega_{n,l}$ but only $\sigma_{n,l} = \tau_{\mathrm{drag}}^{-1}$, will change the linear steady solution because the excited waves will not propagate to the same length before being damped. This has been realised first by Wu et al. [2001], where they have shown that the zonal decay length is of the order of $\sqrt{\tau_{\mathrm{rad}}\tau_{\mathrm{drag}}}$.

From equation (7.31), we see that the linear solution is altered by three main parameters: the shape of the forcing function ($q_{n,l}$), the global behaviour of the waves (horizontal shape of $\tilde{X}_{n,l}$ and $\omega_{n,l}$) and the dissipation of the waves ($\sigma_{n,l}$). In the next section, we first study whether the simplified prescription of the forcing used by Showman and Polvani [2011] is a limitation to the understanding of the linear processes triggering superrotation in hot Jupiters.

7.3 Insensitivity of Matsuno-Gill to the differential heating

In order to derive analytical results, SP11 had to impose an antisymmetric heating where the night side of the planet is cooled as much as the day side is heated. In this case, the linear steady solution gives rise to the chevron shaped pattern, that they denominated the Matsuno-Gill (MG) circulation. However, if the heating function of hot Jupiters is indeed dominated by the longitudinal wavenumber one, its actual structure is not just a sinusoidal function. Moreover, from Mayne et al. [2017] or Amundsen et al. [2016] we know that there are qualitative differences of the steady state of GCM simulations of hot Jupiters calculated with Newtonian heating or with a more sophisticated radiative transfer scheme. In that regard, the first intuitive idea to test is whether the MG pattern is robust when the heating function is changed. With the addition of the vertical dimension, Tsai et al. [2014] have shown that the linear solution resemble strongly the MG circulation in the high atmosphere. It is not clear whether this holds with realistic, three dimensional heating functions.

From equation (7.14) or (7.31), as $\tilde{X}_{n,l}(x,y) = \hat{X}_{n,l}(y)\exp(ikx)$, we know that the projection of the heating function onto different wavenumbers k can alter the resulting Matsuno-Gill circulation when compared to the simple case of only one wavenumber present in the heating function. To verify this point, we solved for linear steady circulations while prescribing different heating rates. We applied ECLIPS3D (chapter 6, section 6.3.5) with three different forcings: one where there is no cooling on the night side, one where the night side cooling is dominating the day side heating and most importantly one where the heating was chosen as the incoming short wave radiation from our own GCM, the UM (see e.g., Amundsen et al. [2016]) and the cooling the outgoing long wave radiation. The first two cases allow us to test the robustness of the pattern in extreme situations, while the third one mimics the heating in the GCM. Our program calculates the linear steady states by inverting the linear matrix obtained with the full 3D equations. The top boundary condition is a no escape condition (no vertical velocity w), and we have applied an exponential decay in the forcing in the high atmosphere to mimic the vertical sponge used in the UM. At the bottom, a solid boundary ($w = 0$ again) or a no slip condition (no vertical derivatives of the horizontal velocities, u and v) give qualitatively similar results. These conditions are obviously simplifications of the physical situation, but we have changed the range of pressure for boundary conditions and verified that it did not alter qualitatively the solutions. The physical parameter for the planet are the same as in Mayne et al. [2017], given again in the previous chapter, table 5.1.

We show in Figure 7.2 the shape of the MG solutions for these different heating profiles. We have chosen a characteristic drag and radiative timescale of 10^5s, but this affects the shape of the solutions in all cases in a similar way. We see that the shape of the linear steady circulation does not qualitatively depend on the forcing. More precisely, as long as there is a differential heating between the day and the night side, the linear steady solution of the atmosphere exhibits the "chevron-shaped" pattern of the MG circulation (we have verified that a constant heating on the whole planet or just a cooling at the night side does not lead to MG looking solutions). There is however a change in the quantitative values, without affecting the qualitative aspects of the non linear momentum transfer, section 7.5. Therefore, relaxing the approximation of a wavenumber one heating function has no influence on the theory that accelerates the jet (except on the quantitative results): the projection onto different zonal wavenumbers changes the zonal amplitude of the MG circulation, but not its qualitative shape.

Globally, even for simulations with a proper treatment of the radiative transfer, as long as the planet is tidally locked we expect the linar steady circulation to be MG-like. In the paradigm proposed by SP11 and Tsai et al. [2014], the propagation of planetary waves impose this global MG circulation, exhibiting no superrotation, and

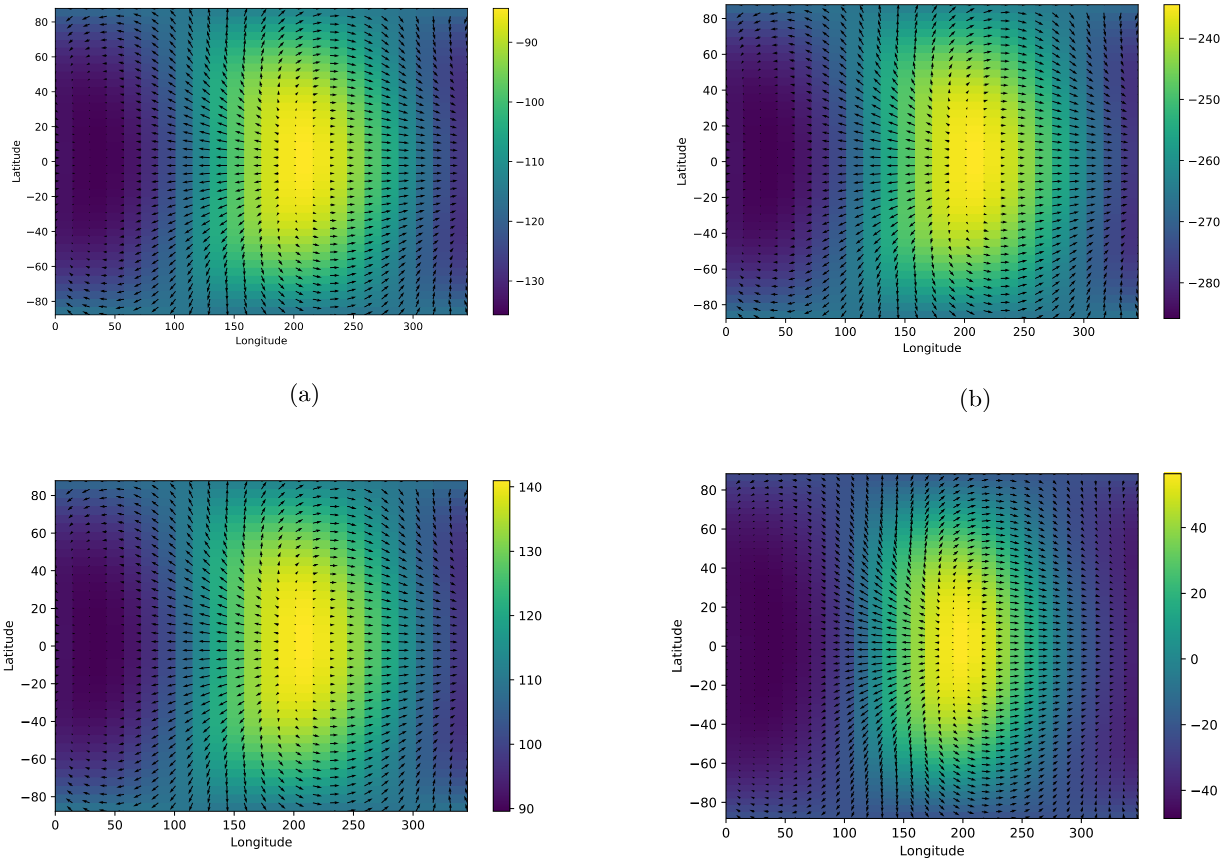

(a)

(b)

(c)

(d)

Figure 7.2: Perturbed pressure (colorscale in Pa) and winds (arrows) with different heating functions, with drag and radiative timescales defined as in Komacek and Showman [2016] with non-dimensional values of 1 (almost half an Earth day). Initial pressure at this height is 50mbar and the forcing is $\Delta T_{eq,top} = 50K$ in the top left figure. (a): Heating as in Komacek and Showman [2016] (b): Same as Komacek and Showman [2016] but with a cooling at the night side 4 times more efficient than the heating on the day side. (c): Same as Komacek and Showman [2016] with no cooling at the night side. (d): Heating rate extracted from the full radiative transfer calculations of the GCM (divided by a thousand to obtain comparable values).

the evolution to superrotation is due to eddy mean flow interactions around this primordial state. Therefore, the time to reach the linear steady state, which is by no means a non linear steady state, must be small relatively to other dynamical times in the system. In the case where the drag and radiative timescales are equal, this led Tsai et al. [2014] to conclude that their work could not apply to long diffusion timescales. We seek here to extent this reasoning to cases where the drag and radiative timescales differ, in order to determine how the atmosphere reacts at the first order. We will analytically restrict ourselves to the quasi geostrophic set of equations (2D cartesian, shallow water beta plane).

7.4 Wave propagation and dissipation

7.4.1 Decay time of damped waves

In this section, we study the decay timescale of the waves triggered by the heating function. These decay rates are essential as they can explain both the qualitative aspect of the linear steady states (equation (7.31) shows that if the decay rate is infinite the projection of the solution onto a given mode is zero) and the behaviour of the atmosphere over short timescales. This section focuses on the mathematical derivation, and a summary is provided in section 7.4.3. The physical interpretation is the goal of the section 7.5.

If $\tau_{\mathrm{drag}} = \tau_{\mathrm{rad}}$, writing $\mathrm{i}\gamma = \mathrm{i}\omega + \frac{1}{\tau_{\mathrm{drag}}}$ changes equations (7.17) to (7.19) into equations (7.7) to (7.9). The eigenvalues must be $\gamma_{n,l} = \omega_{n,l}$, obtained in the case with no dissipation, which means that the real part of the eigenvalue, the frequency, is not altered, but the imaginary part of ω is:

$$\Im(\omega) = \frac{1}{\tau_{\mathrm{drag}}} \ . \tag{7.32}$$

Therefore one can express e.g., $u_{n,l}$ as:

$$u_{n,l} = \tilde{u}_{n,l} \mathrm{e}^{\mathrm{i}\omega_{n,l} t} \mathrm{e}^{-t/\tau_{\mathrm{drag}}}, \tag{7.33}$$

where t is the time and $\tilde{u}_{n,l}$ is the eigenvector, not dependent on time. Therefore, all the modes decay with a characteristic time being the drag (or radiative) timescale: when $\tau_{rad} = \tau_{drag}$ the time to converge to the Matsuno-Gill circulation is the dissipation timescale, as one would naively expect, and all waves have the same exponential decay in time.

If $\tau_{\mathrm{drag}} \neq \tau_{\mathrm{rad}}$, Eq.(7.10) is slightly modified to obtain:

$$\frac{\partial^2 v}{\partial y^2} - \left((\mathrm{i}\omega + \tau_{\mathrm{drag}}^{-1})(\mathrm{i}\omega + \tau_{\mathrm{rad}}^{-1}) + k^2 + y^2 \frac{\mathrm{i}\omega + \tau_{\mathrm{rad}}^{-1}}{\mathrm{i}\omega + \tau_{\mathrm{drag}}^{-1}} - \frac{ik}{\mathrm{i}\omega + \tau_{\mathrm{drag}}^{-1}} \right) v = 0 \ . \tag{7.34}$$

It is easy to verify that setting $\tau_{\mathrm{drag}} = \tau_{\mathrm{rad}}$ or both their inverse equal to zero gives the results obtained above. We define the complex number c to be the fourth root of the muliplying term in front of y^2 defined as:

$$c^4 = \frac{\mathrm{i}\omega + \tau_{\mathrm{rad}}^{-1}}{\mathrm{i}\omega + \tau_{\mathrm{drag}}^{-1}} \tag{7.35}$$

with

$$\frac{\mathrm{i}\omega + \tau_{\mathrm{rad}}^{-1}}{\mathrm{i}\omega + \tau_{\mathrm{drag}}^{-1}} = r\mathrm{e}^{i\theta} \ , \ \ c = \sqrt[4]{r}\mathrm{e}^{i\theta/4}, \tag{7.36}$$

We then choose as a variable $z = cy$ (the cases $c = 0$ or $c = \infty$ are of no interest physically). With this variable, we have $\frac{\partial^2 v}{\partial y^2} = c^2 \frac{\partial^2 v}{\partial z^2}$. Eq.(7.34) simplifies to:

$$c^2 \frac{\partial^2 v}{\partial z^2} - \left((\mathrm{i}\omega + \tau_{\mathrm{drag}}^{-1})(\mathrm{i}\omega + \tau_{\mathrm{rad}}^{-1}) + k^2 + y^2 c^4 - \frac{ik}{\mathrm{i}\omega + \tau_{\mathrm{drag}}^{-1}} \right) v = 0 \ . \tag{7.37}$$

Dividing by c^2, we get:

$$\frac{\partial^2 v}{\partial z^2} - \frac{(\mathrm{i}\omega + \tau_{\mathrm{drag}}^{-1})(\mathrm{i}\omega + \tau_{\mathrm{rad}}^{-1}) + k^2 - ik/(\mathrm{i}\omega + \tau_{\mathrm{drag}}^{-1})}{c^2} v - z^2 v = 0, \tag{7.38}$$

and if we rename the big fraction m, which for now is a complex number, we simply have:

$$\frac{\partial^2 v}{\partial z^2} + (m - z^2)v = 0 \ . \tag{7.39}$$

The major difference with the Matsuno case is that now $z \in \mathrm{C}$, and so the boundary conditions are altered. As $|z| \to \infty$ when $y \to \pm\infty$, we have to solve this equation with the following boundary condition:

$$v \to 0 \quad \text{when} \quad |z| \to \infty \ . \tag{7.40}$$

As in the case where m is real, one could show that the only solutions are the parabolic cylinder functions (equation (7.12)), provided that:

$$\frac{-(\mathrm{i}\omega + \tau_{\mathrm{drag}}^{-1})(\mathrm{i}\omega + \tau_{\mathrm{rad}}^{-1}) - k^2 + ik/(\mathrm{i}\omega + \tau_{\mathrm{drag}}^{-1})}{c^2} = 2p + 1, \tag{7.41}$$

where $p \in \mathbb{N}$ and $\Re(c^2) > 0$ so that the solutions do decay when $y \to \infty$. This latter condition seems to be always verified when solved numerically for the conditions relevant to hot Jupiters. Naming $x = \mathrm{i}\omega + \tau_{\mathrm{drag}}^{-1}$ and $\gamma = \tau_{\mathrm{rad}}^{-1} - \tau_{\mathrm{drag}}^{-1}$, taking the square of equation (7.41) in order to obtain c^4 yields:

$$x^4(x+\gamma)^2 + 2k^2x^3(x+\gamma) - 2ikx^2(x+\gamma) - (2p+1)^2x(x+\gamma) + k^4x^2 - 2ik^3x - k^2 = 0 \ . \tag{7.42}$$

This is a polynomial of order six but we had to raise Eq.(7.41) to the power of two to get it, meaning that only three roots will also be roots of Eq.(7.41) (the three other ones would give $-(2p+1)$). This equation has already been obtained by Heng and Workman [2014] (their equation (121)), but they have used it only for deriving steady states solutions as in Wu et al. [2001] or Showman and Polvani [2011].

We have not come to an analytical expression for the roots, but have studied the exponentially growing or decaying part of the solution ($\Im(\omega)$) numerically with Mathematica for an extensive range of p,k, τ_{drag} and τ_{rad} values (we have verified that we perfectly recover the limits $\tau_{\mathrm{drag}}^{-1} = \tau_{\mathrm{rad}}^{-1} = 0$ and $\tau_{\mathrm{drag}}^{-1} = \tau_{\mathrm{rad}}^{-1}$). First, as expected no modes can exponentially grow around the rest background. Then, we have studied numerically the cases $k \sim 1$ and $p = 1, 3, 5$, the most important parameters for hot Jupiters, as the heating function is dominated by wavenumber 1 (nondimensional value around 0.7, see next section) and the p number represents the order of the Hermite polynomial, hence the number of zero in latitudes. If the heating function is a decaying exponential, which is the dominant shape of this function [Showman and Polvani, 2011, Tsai et al., 2014], then the projection of $\mathcal{Q}$ on the parabolic cylinder function stops at order 3 (this is not necessarily true when $\tau_{\mathrm{drag}} \neq \tau_{\mathrm{rad}}$ but we don't expect a significant alteration of this result).

From Mathematica, and further verifications with ECLIPS3D, we have obtained that when $\tau_{\mathrm{drag}} \sim \tau_{\mathrm{rad}}$, the characteristic time of decay is $\sim \tau_{\mathrm{drag}}$ as expected. If $\tau_{\mathrm{drag}} \ll \tau_{\mathrm{rad}}$ hence drag is much more efficient than radiation, then the time of decay is $\sim \tau_{\mathrm{drag}}$: drag controls the convergence timescale. However, if $\tau_{\mathrm{drag}} \gg \tau_{\mathrm{rad}}$, the situation is more complex. First, we recall that in the case $\tau_{\mathrm{drag}} = \tau_{\mathrm{rad}}$, the three solutions of equation (7.42) represent an eastward propagating gravity wave, a westward propagating gravity wave and a Rossby wave. Then, when $\tau_{\mathrm{drag}} \gg \tau_{\mathrm{rad}}$, we have numerically obtained that the decay rate σ_{lim} of two of the three solutions of equation (7.42) behaves as:

$$\sigma_{\mathrm{lim}} \approx \tau_{\mathrm{drag}}^{-1} + \tau_{\mathrm{rad}}^{1/(p+2)} . \tag{7.43}$$

Globally, if $\tau_{\mathrm{rad}} \to 0$, $\sigma_{\mathrm{lim}}^{-1}$ is the drag timescale, but if τ_{rad} is moderate, then the time of decay is more subtle. The really interesting thing is that, when we tend to the limit $\tau_{\mathrm{rad}} \to \tau_{\mathrm{drag}}$, these two modes exhibit the usual dispersion relation for gravity waves, and we will therefore call these two modes gravity modes even if we know that they are indeed gravity modes in the limit $\tau_{\mathrm{rad}} \to \tau_{\mathrm{drag}}$.

On the other hand, the third solution of equation (7.42) tends to the Rossby wave dispersion relation in the limit $\tau_{\mathrm{rad}} \to \tau_{\mathrm{drag}}$, and its time of decay is always of the order of the drag timescale when $\tau_{\mathrm{drag}} \gg \tau_{\mathrm{rad}}$. Therefore, this Rossby type mode is globally insensitive to the radiative timescale, and its decay rate is always the inverse of the drag timescale.

The conclusion is that all solutions are always exponentially decaying ($\Im(\omega) > 0$, as expected) but more interestingly that the parameter controlling the decay is only τ_{drag} for Rossby-like modes; τ_{rad} only leads to a correction to the frequency of decay. Qualitatively speaking, when $\tau_{\mathrm{drag}} \sim \tau_{\mathrm{rad}}$, $\tau_{\mathrm{drag}} \ll \tau_{\mathrm{rad}}$ or $\tau_{\mathrm{drag}} \gg \tau_{\mathrm{rad}}$, we always obtain $\Im(\omega) \sim \tau_{\mathrm{drag}}^{-1}$. For gravity-inertial modes, this stands when $\tau_{\mathrm{drag}} \ll$ or $\sim \tau_{\mathrm{rad}}$. However, there is a balance between τ_{rad} and τ_{drag} when $\tau_{\mathrm{rad}} \ll \tau_{\mathrm{drag}}$. We show the schematic behaviour of the decay rate as a function of the ratio $\tau_{\mathrm{rad}}/\tau_{\mathrm{drag}}$ in Figure 7.3. We now need to understand the decay rate of Kelvin waves to be able to draw physical conclusions.

7.4.2 The particular case of Kelvin waves

Kelvin waves are a particular solution of the homogeneous equations, as first pointed out by Matsuno [1966], where the meridional velocity is zero. Combining equations (7.17) and (7.19) with $v = 0$ yields:

$$\frac{\partial u}{\partial y} = \frac{\mathrm{i}k}{\mathrm{i}\omega + 1/\tau_{\mathrm{drag}}} y u, \tag{7.44}$$

hence

$$u = Aexp\left(\frac{\mathrm{i}k}{\mathrm{i}\omega + 1/\tau_{\mathrm{drag}}}\frac{y^2}{2}\right), \tag{7.45}$$

where A is a constant. If the boundary condition $u = 0$ for $y \to \pm\infty$ is to be verified, the term in front of $y^2/2$ must have a negative real part. Combining equations (7.17) and (7.19) with $v = 0$ yield a second order polynomial for ω in order for u and h not to be identically zero:

$$\omega^2 - \mathrm{i}\omega\left(\frac{1}{\tau_{\mathrm{rad}}} + \frac{1}{\tau_{\mathrm{drag}}}\right) - k^2 - \frac{1}{\tau_{\mathrm{rad}}\tau_{\mathrm{drag}}} = 0. \tag{7.46}$$

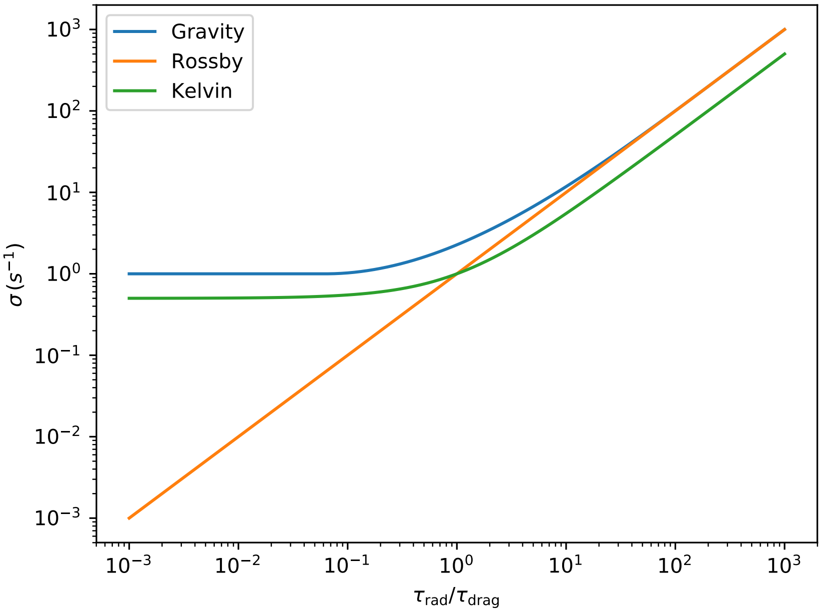

Figure 7.3: Decay rate σ as a function of $\tau_{\mathrm{rad}}/\tau_{\mathrm{drag}}$ for gravity, Rossby and Kelvin type modes as estimated in this chapter. For simplicity, we have assumed here $\tau_{\mathrm{rad}} = 1$.

This yields:

$$\omega = \frac{1}{2}\left(\mathrm{i}\left(\frac{1}{\tau_{\mathrm{rad}}} + \frac{1}{\tau_{\mathrm{drag}}}\right) \pm \sqrt{4k^2 - \left(\frac{1}{\tau_{\mathrm{rad}}} - \frac{1}{\tau_{\mathrm{drag}}}\right)^2}\right), \tag{7.47}$$

where the term in the square root can be negative and in that case the square root is equal to i times the square root of the absolute value. Then we obtain:

$$\frac{\mathrm{i}k}{\mathrm{i}\omega + \dfrac{1}{\tau_{\mathrm{drag}}}} = \frac{2\mathrm{i}k}{\left(\dfrac{1}{\tau_{\mathrm{drag}}} - \dfrac{1}{\tau_{\mathrm{rad}}}\right) \pm \mathrm{i}\sqrt{4k^2 - \left(\dfrac{1}{\tau_{\mathrm{rad}}} - \dfrac{1}{\tau_{\mathrm{drag}}}\right)^2}}\ . \tag{7.48}$$

Therefore, if we want to satisfy the boundary conditions, the term under the square root must be positive or this expression is a pure imaginary number. In other words, Kelvin waves propagate only when:

$$4k^2 > \left(\frac{1}{\tau_{\mathrm{rad}}} - \frac{1}{\tau_{\mathrm{drag}}}\right)^2\ . \tag{7.49}$$

In that regard, the chevron shaped pattern of the Matsuno-Gill solution obtained by Showman and Polvani [2011] is impossible to obtain, as it is a combination of mid latitudes Rossby and equatorial Kelvin, planetary waves. Additionally, when Kelvin waves propagate, as the term in the square root is positive we know the characteristic decaying frequency of Kelvin wave σ_K:

$$\sigma_K = \frac{1}{2}\left(\frac{1}{\tau_{\rm rad}} + \frac{1}{\tau_{\rm drag}}\right), \tag{7.50}$$

which is also displayed in Figure 7.3. We have verified with ECLIPS3D that the decay rate σ_K of the Kelvin wave follows the analytical calculations. For $\tau_{\rm rad}^{-1} = 0.03$ and $\tau_{\rm drag}^{-1} = 1$, we obtain $\sigma_K = 0.515$ where ECLIPSED gives 0.51501 and 0.51492 for two Kelvin wave modes (with different k values, which also give consistent frequency values). For $\tau_{\rm rad}^{-1} = 2$, the $k = 0.7$ (hence one oscillation on the planet) the Kelvin mode does not exist anymore with ECLIPS3D, as expected from the analytics.

7.4.3 Short summary

In this section, we have derived asymptotic values for the time decay of propagating waves, displayed in Figure 7.3. We call $\sigma_{\rm R}$, $\sigma_{\rm K}$, and $\sigma_{\rm g}$ the characteristic decay rate of Rossby, Kelvin and gravity type waves, respectively. For Kelvin waves, we obtained the analytical expression of this rate:

$$\sigma_{\rm K} = \frac{1}{2}\left(\tau_{\rm drag}^{-1} + \tau_{\rm rad}^{-1}\right) . \tag{7.51}$$

More generally, there are three limits:
- When $\tau_{\rm drag} \sim \tau_{\rm rad}$, we simply have $\sigma_{\rm R} \sim \sigma_{\rm K} \sim \sigma_{\rm g} \sim \tau_{\rm drag}^{-1}$
- When $\tau_{\rm drag} \ll \tau_{\rm rad}$, this conclusion is unchanged: $\sigma_{\rm R} \sim \sigma_{\rm K} \sim \sigma_{\rm g} \sim \tau_{\rm drag}^{-1}$, relatively to a factor of 2 notably for the Kelvin waves.
- When $\tau_{\rm drag} \gg \tau_{\rm rad}$, the three decays are different. The Rossby waves decay rate is unchanged: $\sigma_{\rm R} \sim \tau_{\rm drag}^{-1}$. The Kelvin wave decay rate, if these waves can propagate, is much bigger as $\sigma_{\rm K} \sim \tau_{\rm drag}^{-1}$ and the gravity wave decay rate is $\sigma_g \sim \tau_{\rm drag}^{-1} + \tau_{\rm rad}^{1/3}$ (we recall that these are non dimensional values, hence the necessary homogeneity of the equations).

In the next section, we use these decay rates to understand the shape of the linear steady circulation, and the transition to superrotation.

7.5 Transition to superrotation

7.5.1 Shape of the linear steady states

Before discussing the transition to superrotation in the non linear limit, we show in this section that our discussion on the decay timescale of waves explains the qualitative aspect of the linear steady states, obtained by Komacek and Showman [2016], see their Figure 5. First, the study of Wu et al. [2001] is particularly insightful: they have shown that the zonal damping rate is related to $\sqrt{\tau_{\rm drag}^{-1}\tau_{\rm rad}^{-1}}$. Hence, if the two timescales are small or one of them is vanishingly small, the zonal propagation of waves will be extremely limited in longitude. This is clearly seen in Komacek and Showman [2016], as when one or two of the timescales are short the temperature gradient is huge between day and night side and the winds are mostly limited to the day side: the waves, excited in the day side, have been damped before reaching the night side hence cannot redistribute heat nor lead to strong night side winds (in the linear limit).

With equations (7.49) and (7.50), we can provide further qualitative understanding of Komacek and Showman [2016]. Because of the strong asymmetric, steady forcing, the dominant wavenumber k ensures one oscillation around the planet. In other words, $2\pi r k = 2\pi$ so that once we have travelled through the whole circumference of the planet we are back to where we started. In non dimensional units, this leads to:

$$k \sim 0.7 \ . \tag{7.52}$$

Hence, supposing that one of the timescales τ is dominant over the other, ensuring that Kelvin waves propagate requires:

$$\tau > \frac{1}{2k} \sim 0.7 \tag{7.53}$$

Following SP11, the characteristic time used in the nondimensional equations is $T = \left(\sqrt{gH}\beta\right)^{-1/2}$ where g is the gravitational acceleration, H the initial, constant height of the shallow water flow and β the derivative of the Rossby parameter. The characteristic length is: $L = \left(\sqrt{gH}/\beta\right)^{1/2}$. Usual conditions for hot Jupiters, at the equator give $gH \sim 4 \times 10^6$m [Showman and Polvani, 2011] hence $L \sim 7 \times 10^7$m and $T \sim 3.5 \times 10^4$s. Therefore, in dimensional units on a shallow water beta plane, this corresponds to $\tau > 2.5 \times 10^4$s. Hence, if one of the timescales is inferior to 2.5×10^4s, Kelvin waves can propagate only if the other timescale is of the same order. But if both these timescales are $\lesssim 2 \times 10^4$s, the dissipation time for these Kelvin waves will be very short. Taking for simplicity the characteristic speed of waves to be $\sqrt{gH}$ which in our case is roughly 2×10^3m.s^{-1} then the time for a wave to travel around the whole planet is $\sim 2 \times 10^5$s. Therefore, for timescales $\lesssim 2 \times 10^4$s, even in the cases where Kelvin waves exist they can't propagate around the whole planet and lead to the stationary chevron shaped pattern of Showman and Polvani [2011], as predicted by Wu et al. [2001].

Writing equation (7.53) with dimensional units is quite insightful. Assuming that the most important wave number is $k = 1/r$, hence one oscillation around the planet as imposed by the forcing, Eq.(7.53), we can write:

$$\tau_d > \frac{r}{2\sqrt{gH}} \tag{7.54}$$

where the d subscript stands for dimensional. This equation shows that for a given τ_d, there is a minimal height under which the Kelvin waves do not propagate anymore. As shown first by Wu et al. [2000] then Tsai et al. [2014], the three dimensional structure of the propagating waves can be decomposed onto shallow water waves with different equivalent depth, solutions of the homogeneous equations but with the nondimensional height which varies with the modes. Tsai et al. [2014] then showed in their Figure 2 that the projection of the heating function of the vertical modes has a high amplitude for modes with equivalent height between $5H_{\mathrm{P}}$ and $0.2H_{\mathrm{P}}$, where H_{P} is the pressure scale height, roughly of the order of $4 \times 10^5 m$ in Hot Jupiter atmospheres. Therefore, for equivalent depth $H = 5H_{\mathrm{P}} \sim 2 \times 10^6 m$ and $H = 0.2H_{\mathrm{P}} \sim 8 \times 10^4 m$ we obtain:

$$10^4\mathrm{s} < \tau_d < 6 \times 10^4\mathrm{s} \ . \tag{7.55}$$

Equation (7.55) states that if $\tau_d < 10^4$s, no Kelvin waves can propagate with smaller height than $5H_{\mathrm{P}}$: the linear steady state will have an almost null projection onto Kelvin waves even if the heating function does project onto

Kelvin waves. On the other hand, if $\tau_d > 6 \times 10^4$s, the majority of the Kelvin waves excited by the forcing can propagate. We recall that if both timescales are comparable, then Kelvin waves can always propagate. This study is applicable when one of the timescales is dominant over the other.

This behaviour is visible in Figure 5 of Komacek and Showman [2016]. In the limit where the drag is too strong, the waves are damped efficiently, the thermal structure strongly resembles the thermal forcing, and there is no Kelvin wave structure at the equator. On the other hand, with low drag ($\tau_{\text{drag}} > 10^5$s) the Kelvin wave component is visible only when the radiative timescale is long as well (> a few 10^4s). As we have seen in section 7.4, in the limit of short radiative timescale the Kelvin waves do not propagate, whereas Rossby and gravity waves do propagate, but Rossby wave are much less damped: the dynamical shape of the atmosphere is dominated by the Rossby wave component, and the linear steady state strongly resembles Figure 7.1b. However, when τ_{rad} is further increased, the Kelvin wave component has more power, and eventually dominates at the equator.

Therefore, we can complete the picture with the case $\tau_{\text{drag}} = 10^5$s and $\tau_{\text{rad,top}} = 10^3$s. In Komacek and Showman [2016], according to their equation 9, at $P = 80$mbar the isobaric surface presented in Figure 5, the radiative timescale is 1.6×10^4s and the drag timescale 10^5s. According to our estimates, the Kelvin wave component should have non negligible power at the equator. Additionally, solving the polynomial (7.42) with these characteristic timescales yields a decaying frequency of ~ 0.8 nondimensional units for the most excited rossby and gravity waves, while the decaying time of the Kelvin waves in this case is ~ 1.2. This case therefore has a combination of (i) Kelvin waves propagating (ii) long enough dissipation for waves to travel around the whole planet and (iii) comparable dissipation times for Kelvin and Rossby waves. We expect the steady state of the atmosphere to look like a combination of planetary Rossby and Kelvin wave with roughly the same magnitude, hence the chevron shaped pattern predicted by SP11 in the Matsuno-Gill circulation. This is confirmed by Figure 5 of Komacek and Showman [2016]: in this limit, the linear steady states is similar to Figure 7.1a.

In this section, we have therefore assessed the validity of our decay rate estimations in the study of the linear steady states, under various drag and radiative timescale conditions. We now explore how this applies to the real evolution of hot Jupiters from numerical simulations, from the time when the heating is switched on to the final state of steady superrotation, as detailed in chapter 5. We begin with an order of magnitude analysis in section 7.5.2, showing the need to understand the low damping strong heating case, before turning to the study of non linear accelerations in section 7.5.3.

7.5.2 Order of magnitude analysis

In this section, we estimate the maximum forcing under which the consideration of a linear steady state is relevant. First, as we are performing a linear study, the value of the maximum velocity must be proportional to the amplitude of the forcing for constant τ_{rad} and τ_{drag}. The amplitude of the forcing can be well represented by the dayside-nightside equilibrium temperature difference we implement at the top of the atmosphere $\Delta T_{\text{eq,top}}$. Assuming that the radiative timescale is appropriately represented by the polynomial fit of Heng et al. [2011], adapted from Iro et al. [2005], the amplitude of the MG circulation will then only depend on $\Delta T_{\text{eq,top}}$ and the drag timescale.

Let us call u_{MG} the zonal velocity of the linear steady state. This steady state can only be reached if the non linear terms can accurately be neglected when $u = u_{\mathrm{MG}}$. The first neglected non linear term is the zonal advection, $u_{\mathrm{MG}}\partial u_{\mathrm{MG}}/\partial x \sim u_{\mathrm{MG}}^2/L$ where L is a characteristic length, whereas the linear terms are of the order of $u_{\mathrm{MG}}/\tau_{\mathrm{drag}}$. Hence we obtain a maximum speed u_{max} over which linear steady solutions will not be reached in a 3D GCM:

$$u_{\mathrm{max}} \sim \frac{L}{\tau_{\mathrm{drag}}} \ . \tag{7.56}$$

For the study of hot Jupiters, L ranges from half the planetary circumference in the MG case to the full circumference in the superrotating case. Roughly, $L \sim \pi r$. Calling $u_{\mathrm{MG},1}$ the maximum zonal wind at the equator for the Matsuno-Gill solution with $\Delta T_{\mathrm{eq,top}} = 1\mathrm{K}$, using the linearity of u_{MG} to the forcing we have for any $\Delta T_{\mathrm{eq,top}}$ at a constant τ_{drag}:

$$u_{\mathrm{MG},\Delta T_{\mathrm{eq,top}}} \approx u_{\mathrm{MG},1} * \left(\frac{\Delta T_{\mathrm{eq,top}}}{1\mathrm{K}}\right) \ . \tag{7.57}$$

Combining equations (7.56) and (7.57) yields a maximum forcing value for which the linear steady state can be reached:

$$\left(\frac{\Delta T_{\mathrm{max}}}{1K}\right) \approx \frac{1}{u_{\mathrm{MG},1}}\frac{L}{\tau_{\mathrm{drag}}} \ . \tag{7.58}$$

Above this value, the non linear considerations come into play before the linear steady state is reached, hence all the waves triggered by the forcing can be dissipated (see Eq.(7.31)). This has already been noted in Section 3.3.2 of Tsai et al. [2014], where they acknowledge that their analysis is strictly valid only in the strong or moderate damping scenario. As we see in Eq.(7.58), if τ_{drag} is too long, hence low damping scenario, the maximum forcing will be very small, and the linear approximation breaks for forcing amplitudes relevant for hot Jupiters.

There are therefore two limits: in the strong or moderate damping scenario, the atmosphere first reaches the linear steady solution and the subsequent evolution is due to the non linear acceleration. Hence if we suppose that roughly $\partial U/\partial t = U^2/L$, where the U^2/L term either comes from the advective or metric terms (which in essence are identical), then the characteristic time τ_{evol} for the atmosphere to significantly depart from the MG where $U = u_{\mathrm{MG}}$ is

$$\tau_{\mathrm{evol}} = \frac{L}{u_{\mathrm{MG}}} \ . \tag{7.59}$$

This is the Tsai et al. [2014] situation, where the waves change the mean flow in a quasi static way leading to the emergence and equilibration of superrotation.

In the low damping scenario, the atmosphere never reaches the Matsuno-Gill steady state. Let us suppose for example that the atmosphere is composed of a slowly oscillating, slowly decaying Rossby wave hence $\omega_R, \sigma_R \ll 1$ and a quickly oscillating, strongly damped Kelvin wave with $\omega_K, \sigma_K \gg 1$. This is the case when $\tau_{\mathrm{drag}} \gg 1$ and $\tau_{\mathrm{rad}} \ll 1$ (in nondimensional units). In this simplified case, equation (7.29) simplifies to:

$$X_{\mathrm{F}} = \frac{q_R}{\sigma_R - i\omega_R}\tilde{X}_R(x,y)\left(1 - e^{(i\omega_R - \sigma_R)(t)}\right) + \frac{q_K}{\sigma_K - i\omega_K}\tilde{X}_K(x,y)\left(1 - e^{(i\omega_K - \sigma_K)(t)}\right) , \tag{7.60}$$

where X_{F} is the vector of solution that depends on time. We know that in the linear steady state, assuming $q_R \sim q_K$, the Rossby wave component will have much more power than the Kelvin wave as $|i\omega_R - \sigma_R| \ll |i\omega_K - \sigma_K|$. We have studied this in the previous section: the linear steady state resembles that of Figure 7.1b. However, let us take a time t so that $|i\omega_K - \sigma_K| \ll 1$ and (necessarily) $|i\omega_R - \sigma_R| \ll 1$. Equation (7.60) can be linearised to first order:

$$X_{\mathrm{F}}(\sigma_R t, \sigma_K t \ll 1) \approx q_R \tilde{X}_R t + q_K \tilde{X}_K t \ . \tag{7.61}$$

In the limit of very short times, the Rossby and Kelvin wave component of the time dependent solution of the atmosphere are comparable (provided $q_R \sim q_K$). This even stands for $|i\omega_K - \sigma_K| \gtrsim 1$ but $|i\omega_R - \sigma_R| \ll 1$. In that case, the exponential term is almost zero for the Kelvin component, whereas the same linearisation stands for the Rossby component. Hence:

$$X_{\mathrm{F}}(\sigma_R t \ll 1, \sigma_K t \gtrsim 1) \approx q_R \tilde{X}_R t + \frac{q_K}{\sigma_K - i\omega_K}\tilde{X}_K \ . \tag{7.62}$$

Dividing the Rossby by the Kelvin components yields:

$$\left|\frac{f_R}{f_K}\right| = \left|\frac{q_R}{q_K}(\sigma_K - i\omega_K)t\right| \gtrsim \frac{q_R}{q_K} \ . \tag{7.63}$$

Provided that the projection of the heating function on the Rossby and Kelvin components is similar, the time dependent solution will therefore exhibit comparable Rossby and Kelvin components in the range of times where the first triggered Kelvin wave has not been completely damped, although the steady state will be dominated by the Rossby component.

This has important consequences for the triggering of superrotation. We have said in section 7.2.2 that the situations that exhibit superrotation in the non linear limit had a negative convergence of momentum at the equator in the linear limit, opposite to the proposed explanation of Showman and Polvani [2011] for the spin up of superrotation. This negative convergence arises from the domination of Rossby waves over other waves in the low drag limit, as we have shown in sections 7.4 and 7.5.2. However, this divergence of eastward momentum supposes that the linear steady state can be reached. In 3D GCMs with forcing relevant to the study of hot Jupiters, our estimations of equation (7.58) show that the linear steady state is not necessarily relevant.

Actually, in hot Jupiters with physically plausible heating and drag timescale, the linear steady state is never reached before non linear effects come into play. Figure 10 of SP11 shows the state of the atmosphere after 1 day of 3D GCM simulation, and because it resembles to the MG circulation (in this chapter, Figure 7.1a) they conclude that the study of the Matsuno-Gill steady state is relevant. Actually, if superrotation does occur, Komacek and Showman [2016] who use the same GCM show that the linear steady state should exhibit a 'reverse' Matsuno-Gill shape (our Figure 7.1b). Therefore, after 1 day, they haven't reached the linear steady state (our equation (7.30), Figure 7.1b) but they have reached the limit where the non linear effects come into play, which happens to be at $\sigma_K t \gtrsim 1$ and $\sigma_R t \ll 1$ and according to the work of this chapter (equation (7.62) and section 7.4.3) this resembles strongly to the chevron-shaped pattern cicrulation. Therefore, when non linear terms must be taken into account, the shape of the atmosphere (our Figure 7.1a) favours the meridional convergence of eastward momentum at the equator. We study this further in the next section using our own GCM (the UM presented in section 5.3).

7.5.3 3D GCM simulations with various forcings

Qualitative shape of the atmosphere

In order to assess the applicability of the linear shallow water result in 2D, we have run simulations in the UM were we only changed the strength of the forcing. We consider Newtonian heating within the framework on Heng et al. [2011]. When changing the forcing, we have chosen the pressure dependent radiative timescale of Iro et al. [2005] projected on height based coordinates, and our equilibrium temperature follows the values of Heng et al. [2011] for the mean temperature but the ΔT is varied from 0.1 to 100K. Obviously, this is only a toy model as we do not expect to find a tidally locked planet with an effective temperature of 1300K and a day night variation of 0.1K, but it allows to study the physical mechanisms. Atmospheric drag has not been explicitly implement in the UM, but is provided by a diffusion scheme as detailed in Mayne et al. [2014a] and in section 5.3 of this work.

First, as long as the linear effects are dominant, we should expect all simulations to have qualitatively similar features but with quantitative value that scales with the forcing. After 1 day of simulation, all of our simulations have the same shape, characteristic of Figure 7.1a, only the magnitude of the pressure differences and winds change. We recognize the chevron shaped pattern of SP11, but we state again that this is not the steady Matsuno-Gill solution.

The dissipation we have taken is equivalent to $\tau_{\mathrm{drag}} \sim$ a few 10^5s, and at $P \sim 80mbar$ the radiative timescale of Heng et al. [2011], adapted from Iro et al. [2005], is of the order of 2.5×10^4s. In this range of parameters, the MG state can only be considered as reached after $\sim$ 10 days, the time for the Rossby waves, the less dissipated ones (see section 7.4.3), to be dissipated. Therefore, we recover the results of equation (7.61) and the previous section: in the limit of short times, the atmosphere first tends to a situation with comparable powers in Rossby and Kelvin waves.

With ECLIPS3D, we have calculated the expected Matsuno-Gill steady state in this situation which is displayed in Figure 7.4a. We recover dominant mid latitude Rossby gyres are dominating, associated with equatorial winds mainly fueled by the rotating mid latitude winds. Clearly, the circulation is different to Figure 7.1a where the equatorial winds seem to break the global rotating motion. Additionally, we show in figure 7.4 the comparison between the atmosphere with $\delta T_{eq,top} = 1K$ and $\delta T_{eq,top} = 100K$ after 10 days. We see that the longitudinal extent of the westward winds is shrinked in the strongly forced case: the atmosphere has already diverged from the Matsuno-Gill linear steady state. Regarding the time of departure from the MG, in the $\delta T_{eq,top} = 1$K simulation the linear steady winds are of the order of 2m.s^{-1}. Therefore for $\delta T = 100$K we expect $u_{\mathrm{MG}} \sim 200$m.s^{-1}, hence with equation (7.59) a time to depart from MG of $\sim 10^6$s, which is about 10 days or the time to converge to the MG state. In Figure 7.4c, the maximum equatorial winds reach about 350m.s^{-1}: the order of magnitude is adequate.

These results bring two conclusions: (i) in the linear limit, as expected all simulations behave similarly and there is no threshold to superrotation triggered by the non linear acceleration once the MG state is reached. The only

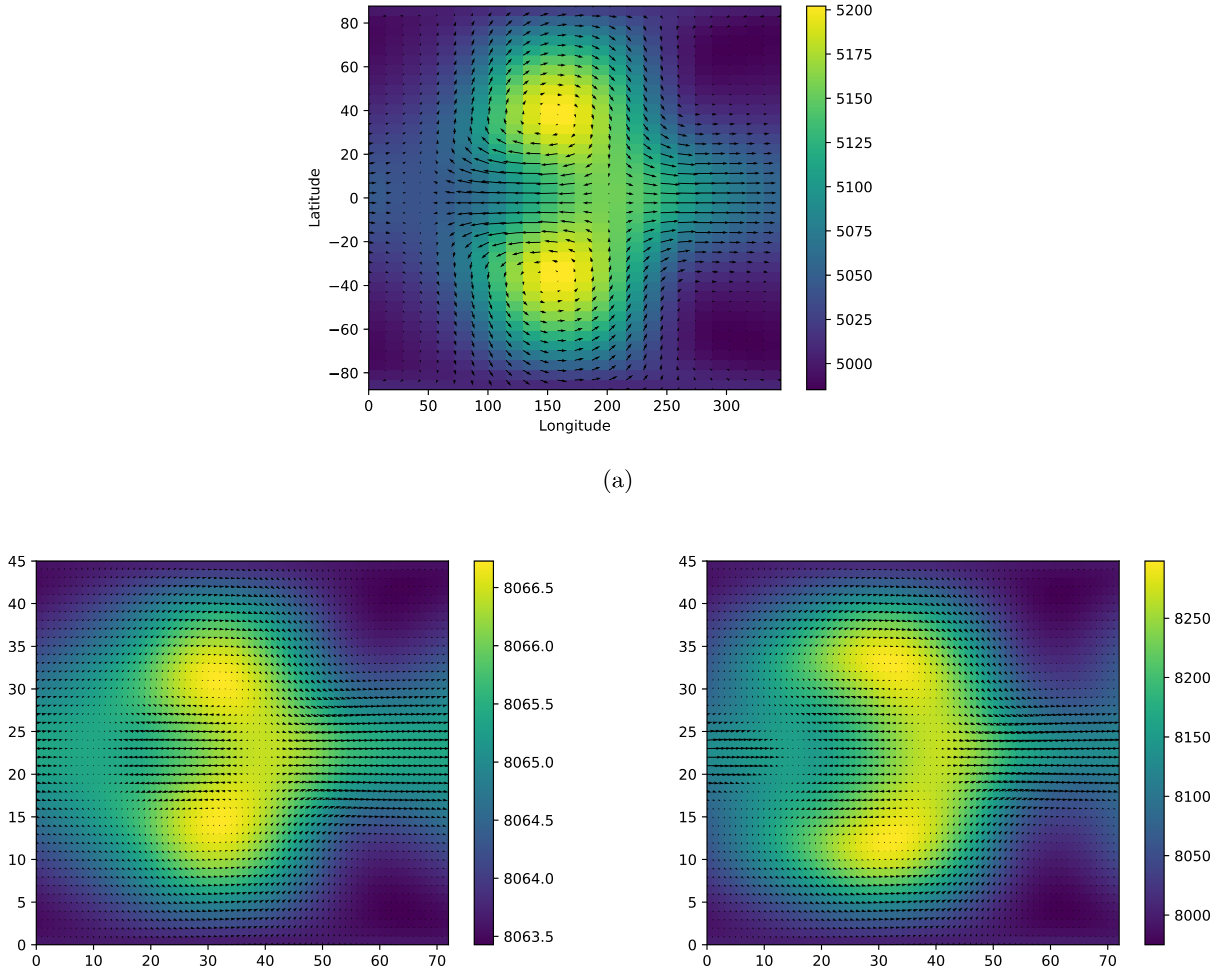

(a)

(b)

(c)

Figure 7.4: Pressure (color) and winds (arrows) for (a) linear steady state calculated with ECLIPS3D with $\delta T_{eq,top} = 100$K, $\tau_{\text{drag}} = 2 \times 10^5$s and τ_{rad} following Iro et al. [2005]. (b): 3D GCM result at the 80mbar level after 10 days of simulation, with $\delta T_{eq,top} = 1$K and the radiative timescale of Iro et al. [2005]. The characteristic speed is 1m.s^{-1}; (c): 3D GCM result at the 80mbar level after 10 days of simulation, with $\delta T_{eq,top} = 100$K and the radiative timescale of Iro et al. [2005]. The characteristic speed is 200m.s^{-1}

limiting problem is the time to reach a non linear steady state, which is inversely proportional to the strength of the forcing. (ii) If the time to depart from the MG steady state is much smaller than the time to reach the MG steady state, the global understanding of spin up of superrotation might be erroneous. This happens when the forcing is bigger than 100K in the conditions of Figure 7.4. If the drag timescale is further increased, this situation would require an even lower forcing. On the other hand, as shown by Komacek and Showman [2016], reducing the drag timescale below $\sim 10^5$s might lead to a suppresion of superrotation (in this situation, the drag timescale is lower than the advective timescale of a superrotating jet, explaining the breaking of superrotation).

Hence if superrotation does exist in hot Jupiter atmospheres, the steady linear considerations hardly apply for its acceleration where non linear effects quickly dominate. Notably, the study of both Tsai et al. [2014] and SP11 (and more recently Hammond and Pierrehumbert [2018], which have extended Tsai et al. [2014] in 2D but with a shear flow) would only apply in the limit of slow evolution, hence once the atmosphere is already close to a non linear steady state. This explains why the Figure 16 of Tsai et al. [2014] which represents their linear consideration compares so well with their Figure 15, taken from 3D numerical simulations: when the initial superrotation is already settled, the further evolution is slow and can be understood in the linear limit. However, they provide no comparison between the linear expectation and the 3D simulations during the original spin up phase of superrotation. As we have seen in this section, linear consideration apply as long as we consider time dependent solution. The assumption of a linear steady state is not justified in the spin up phase.

In this section, we have therefore shown the need to understand the linear evolution and not only the linear steady state for the spin up of superrotation. However, we have restricted ourselves to 2D shallow water situations for the analytical detail, and it therefore seems necessary to conclude this chapter by treating the vertical acceleration using GCM simulations.

Accelerations

In this section, we want to expolore the acceleration of the mean flow during the spin up of superrotation. Once the jet is settled and evolving slowly, the studies of Tsai et al. [2014] and Hammond and Pierrehumbert [2018] describe the evolution of superrotation, but the initial acceleration is less clear as we have explained through this chapter.

Following Mayne et al. [2017] or Hardiman et al. [2010]. the acceleration of the mean flow can be written as:

$$(\overline{\rho}\,\overline{u})_{,t} = -\frac{(\overline{\rho v}\,\overline{u}\cos^2\phi)_{,\phi}}{r\cos^2\phi} - \frac{(\overline{\rho w}\,\overline{u}r^3)_{,r}}{r^3} + 2\Omega\overline{\rho v}\sin\phi - 2\Omega\overline{\rho w}\cos\phi - (\overline{\rho' u'})_{,t} - \frac{\left[\overline{(\rho v)' u'}\cos^2\phi\right]_{,\phi}}{r\cos^2\phi} - \frac{\left[\overline{(\rho w)' u'} r^3\right]_{,r}}{r^3} + \overline{\rho G_\lambda}, \tag{7.64}$$

where G_λ denotes the body forces acting in the longitudinal direction (not considered here). The subscripts of this equation denotes partial derivatives, and every quantity X is defined as $X = \bar{X} + X'$ where a bar denotes an average on longitude. In this section, we don't mention mean flow-mean flow accelerations as we have verified that they are negligible during the spin up. Once the superrotation is settled, these accelerations should be taken into account as they balance the eddy accelerations and eventually lead to a non linear steady state (see notably the conclusions of Tsai et al. [2014] on this point).

Following SP11, the meridional eddy accelerations, involving v' and u', should bring momentum at the equator from the MG steady state whereas the vertical accelerations are preventing the spin up of superrotation. On Figure 7.5, we show the value of $(\overline{\rho}\,\overline{u})$ for $\delta T = 100$K after 50 days of simulations as well as the vertical and meridional accelerations. After 50 days, the jet extends from roughly 1mbar to 1bar with the maximum of $(\overline{\rho}\,\overline{u})$ around 0.2bar.

As in Figure 15 of Tsai et al. [2014], we observe that the vertical accelerations are slowing down the upper part of the jet, while extending the jet to deeper pressures. The meridional accelerations on the other hand compensate the vertical slowing down in the upper part of the jet. This is the usual picture, obtained once the jet is settled, in agreement with both Tsai et al. [2014] and SP11.

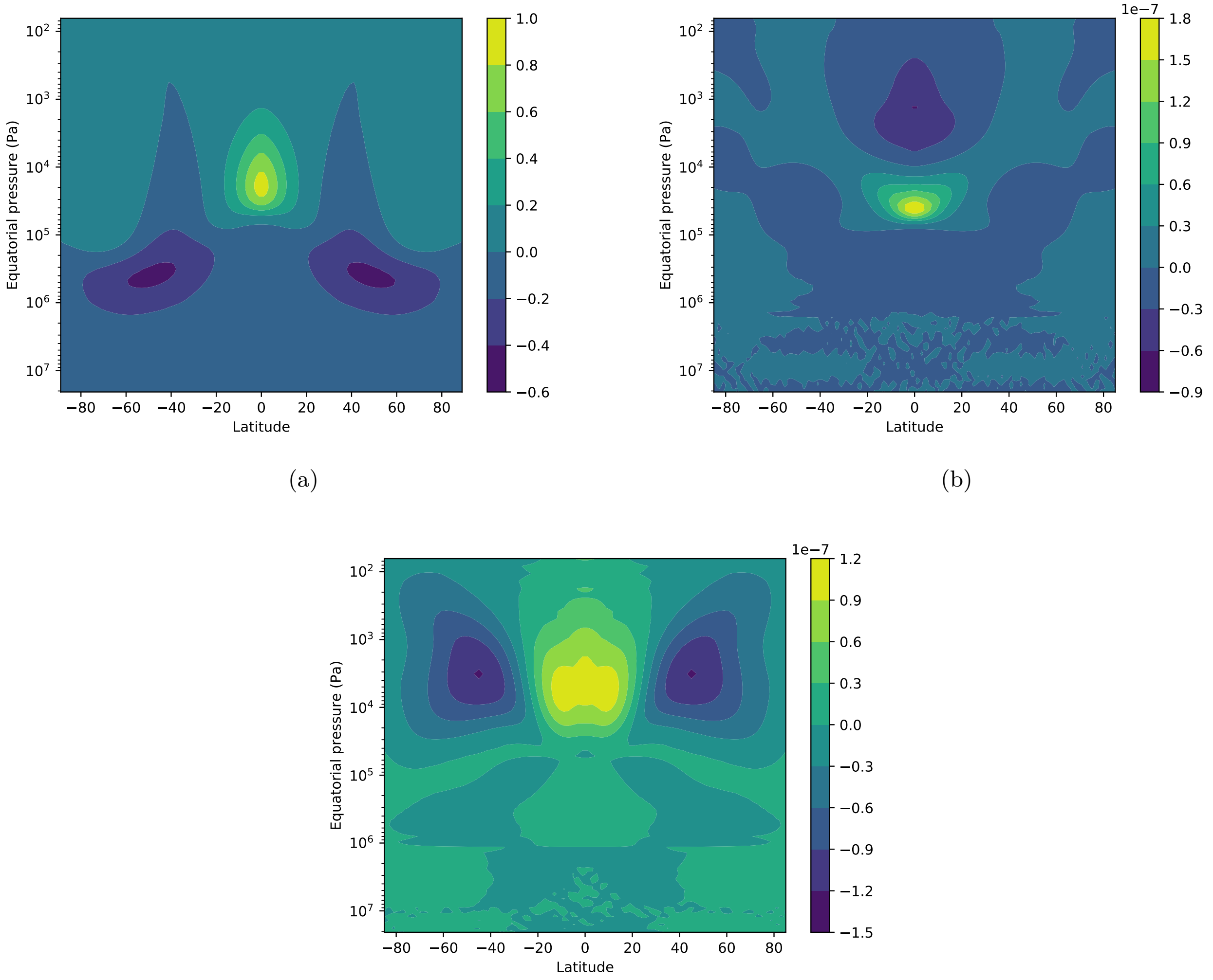

(a)

(b)

(c)

Figure 7.5: (a) $(\overline{\rho}\,\overline{u})$ (SI) as a function of pressure and latitude after 50 days of simulations with $\Delta T = 100$K. (b) Vertical acceleration (SI) for the same simulations. (c) Meriodonal accelerations (SI) for the same simulation.

However, as the forcing is smaller than the real forcing of hot Jupiters, we can study the initial creation of a jet more carefully. First, we observe that the jet sets up initially between 0.08 and 0.1 bar in about 15 days (not shown), and then extends upwards and downwards. We show on Figure 7.6 the meridional and vertical accelerations after 1, 5 and 20 days in the $\Delta T = 100$K case.

We see that in the region where superrotation is the strongest (see Figure 7.5), the vertical eddy acceleration always provides the maximum momentum convergence. Additionally, with time the location where the vertical motion accelerate the jet gets deeper. This can be understood in the following way: the superrotation is not affecting the mid latitude circulations, which keeps bringing eastward momentum to the equator. However, the global motion in the vertical direction is broken at the equator, as the zonal winds go only in one direction when superrotation sets up. This breaks the deposition of eastward wind at the equator, which was accompanied with a removal of westward wind on the night side of the planet. Globally, it appears that the vertical accelerations sets up the initial superrotation, which then tends to decrease and even change the sign of the vertical accelerations. Then, the global meridional motions act to sustain the jet once the vertical eddy acceleration are negative.

This phenomenon is even more stringent for longer drag timescales. In this case, Komacek and Showman [2016] have noticed that the meridional motion of the linear steady state is opposite to what is necessary to drive superrotation, although they do observe that the non linear steady state is indeed superrotating. We show on Figure 7.7 the accelerations for $\Delta T = 10$K after 20 days. The vertical accelerations clearly have a predominant role in the formation of the jet.

Globally, we can then resolve the discrepancy of Figure 4 and Figure 5 of Komacek and Showman [2016], discussed throughout chapter (notably section 7.2.2 and this section): nonlinearly superrotating atmospheres can have linear steady states that would oppose superrotation, in contradiction with Showman and Polvani [2011]. The study of Tsai et al. [2014], in the limit of strong dissipation, does not offer explanation for the apparent paradigm. First, as we have shown, the treatment of the time dependent linear solution shows that the linear steady state is not relevant in the high forcing case. After 1 day, the nonlinear terms become dominant whereas the MG steady state would require linear effects to dominate for at least 10 days. The shape of the atmosphere after 1 day is again given by our Figure 7.1a: it is the usual chevron shape pattern of SP11. Therefore, when non linear effects become dominant, they tend to accelerate the equator whereas if the linear steady state had been reached the deceleration by meridional motion could have been dominant: for adequate forcing in hot Jupiter conditions, the state of the atmosphere after 1 day always leads to meridional momentum convergence at the equator. Then, as seen on Figure 7.6, the vertical accelerations also need to be taken into account: at the 80mbar pressure range, vertical motion triggers the emergence of superrotation contrary to what is proposed by SP11. Only when superrotation is settled (Figure 7.5b) do the vertical accelerations tend to decelerate the jet, and extend it deeper.

Later on, once the superrotation is settled, the study of Tsai et al. [2014] applies to the slower evolution of the atmosphere, leading to the possible existence of a unique steady state. This steady state is permitted by both meridional and vertical accelerations, as we have seen through this work. This explains why superrotation is reached even when the dissipation is very low, although the initial acceleration is not included in the explanation of Tsai et al. [2014].

7.6 Conclusion

In this chapter, we have been driven by the will to understand the spin up of superrotation, and notably to explain the inherent discrepancy between the papers of Showman and Polvani [2011] and Komacek and Showman [2016]. In Showman and Polvani [2011], they propose that the superrotation is triggered by non linear accelerations around the linear steady state, that converge momentum to the equator. On the other hand, Komacek and Showman [2016] show that the configurations that exhibit superrotation is associated with momentum divergence at the equator in the linear steady state limit. These two situations needed to be reconciled.

In order to resolve this apparent contradiction, we have studied the general form of the time dependent linear response of the atmosphere to a constant, asymmetrical heating. This response depends on the shape of the forcing, the global shape and frequency of the waves and the decay rate of these waves. Our first conclusion, through the use of ECLIS3D, is that changing the longitudinal shape of the forcing is not of prime importance in the qualitative understanding of superrotation, although quantitatively it does affect the results. The use of a Newtonian cooling scheme with a wavenumber 1 in longitude is therefore a reasonable approximation.

We have also obtained an equation for the frequency and decay rates of the propagating waves, as in Heng and Workman [2014]. We could not solve this equation analytically for Rossby and gravity waves, and have therefore estimated the asymptotic behaviour of the waves through numerical solving with Mathematica. For Kelvin waves on the other hand, the analytical solution has been obtained. The estimated decay rates were reported in section 7.4.3 and Figure 7.3. Importantly, it shows that in the limit where the radiative timescale is dominant over drag, the Rossby waves are much less damped than other waves, whereas the damping rates are comparable when drag is of the order of radiative timescale or when drag is dominant.

From there, we have explained qualitatively the shape of the linear solution with different drag and radiative timescales, as presented in Figure 5 of Komacek and Showman [2016] and our Figure 7.1. The zonal dependency had also been estimated by Wu et al. [2001] by other means. Our major result is that in the limit of short times (compared to the damping rates), limits that were not studied by SP11 and Tsai et al. [2014], the waves present in the decomposition of the heating function contribute almost equally to the time dependent linear solution. This tends to create a Matsuno-Gill like circulation (Figure 7.1a) in the first day of the evolution of a hot Jupiter atmosphere in a GCM, although the actual linear steady state would be a "reverse" Matsuno-Gill, exhibiting eatward momentum divergence at the equator (Figure 7.1b). With order of magnitude analysis, we have concluded that in simulation representative of hot Jupiters, the linear steady state could not be reached but non linear terms were dominant after ~ 1 day, hence when the atmosphere resembles the Matsuno-Gill circulation. In that regard, the equator is accelerated although the steady state would tend to decelerate the equator, resolving part of the discrepancy between Komacek and Showman [2016] and SP11.

Finally, we have considered the non linear accelerations during the spin up of superrotation from 3D GCM simulations with different forcing, to assess the importance of the vertical accelerations. Once the jet is settled, the vertical acceleration tends to decelerate the upper part of the jet while extending it to deeper pressure. The meridional acceleration oppose this deceleration, and a steady state can be reached, as already shown by Tsai et al. [2014]. On the other hand, during the spin up, the vertical accelerations contribute equally with the meridional accelerations to settle an initial superrotation. This is in disagreement with Figure 11 of Showman and Polvani [2011], but their figure is averaged in the upper atmosphere (above 30 mbar) where superrotation does not develop or is weaker. Numerically, it seems that as a jet is initiated, the vertical circulation is altered preventing the deposition of eastward momentum at the equator, whereas the meridional circulation is roughly unchanged.

All in all, in this chapter, we have studied, on theoretical and semi analytical grounds the spin up of superrotation. We have shown that previous studies needed to be improved to provide a coherent understanding of the initial acceleration of the equator of hot Jupiters. Combined with the works of SP11, Tsai et al. [2014], Komacek and Showman [2016], Hammond and Pierrehumbert [2018], a global picture of the atmospheric dynamics of hot Jupiters can be drawn.

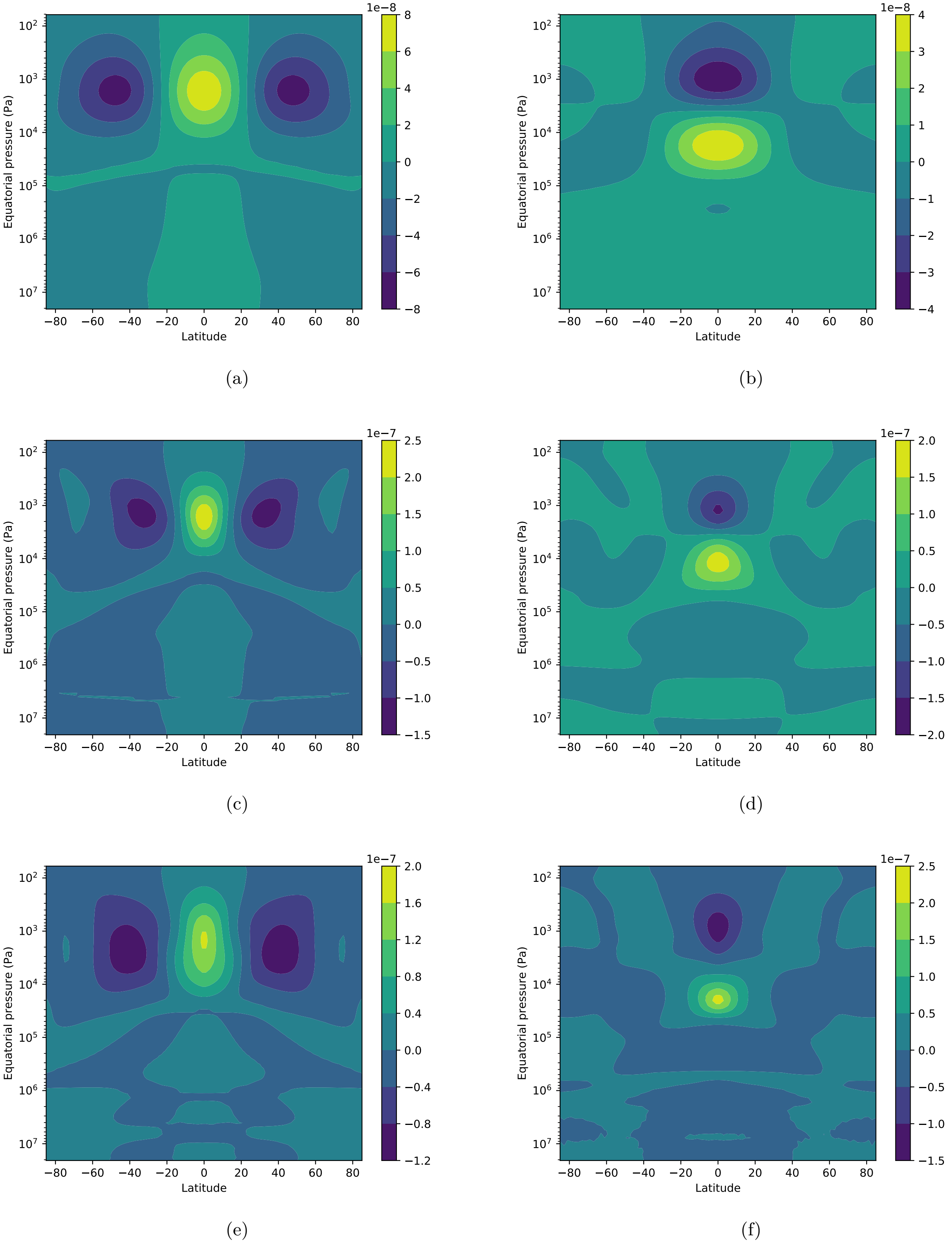

(a)

(b)

(c)

(d)

(e)

(f)

Figure 7.6: Left column: meridional acceleration in the $\Delta T = 100$K case after 1, 5 and 20 days. Right colum: same for vertical accelerations. Units in SI

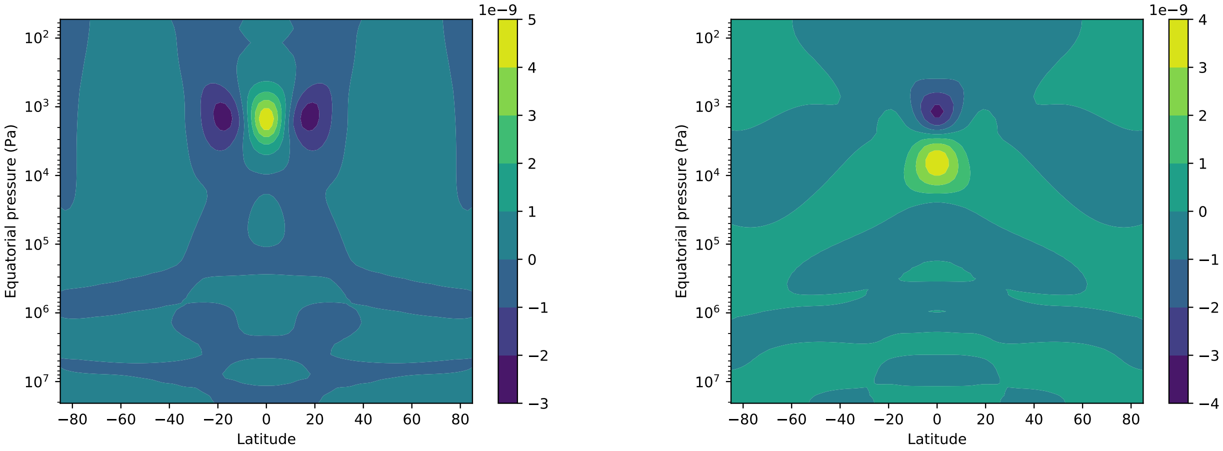

(a)

(b)

Figure 7.7: (a) Meridional acceleration in the $\Delta T = 10$K case after 20 days. (b): same for vertical accelerations. Units in SI

Chapter 8

Conclusion and perspectives

Le cosmos est mon campement
Caracole - La horde du contrevent - *Alain Damasio*

FROM the convective interior of Jupiter to the superrotating atmosphere of hot Jupiters, I have detailed throughout this thesis many physical mechanisms at stake in giant planets. As a start, I have focused on the structure of giant planets. Chapter 2 sets the theoretical and conceptual grounds, explaining how and why Jupiter and giant gaseous planets are in a globally convective state. With the latest data from Juno, this broad picture was improved but only in concert with a precise enough method to constrain the interior of Jupiter from the observation of its gravitational moments. I have detailed the concentric Maclaurin spheroid method [Hubbard, 2012, 2013, Wisdom and Hubbard, 2016], as well as the study of its maximum precision and limitation in chapter 3, as presented in Debras and Chabrier [2018]. The main idea is that the method decomposes the planet into concentric spheroid of constant density, but if an error is made in the upper layers then it is propagated and amplified through the whole structure of the planet. A thorough analysis of the errors has shown that the repartition of spheroids had to be chosen adequately (namely with a power law or exponential repartition) to ensure a small enough discretisation issue. Additionally, the treatment of the outer layers was not possible without altering significantly the precision of the method. We have shown that neglecting the high atmosphere, above 1 bar, as done by Wahl et al. [2017] led to an irreducible error of the order of 1×10^{-7} on J_2. This incertitude is lower than the first observations of Juno [Bolton et al., 2017] but higher the latest ones [Iess et al., 2018]. Therefore, the observations hare already more precise than the intrinsic precision of the method in its present form (although to date physical uncertainties dominate over the numerical uncertainties from the method itself).

The possibilites for improvement of this method are numerous. The main tracks are the inclusion of tidal effects and differential rotation in the CMS method itself, as well as a direct calculation of the moment of inertia and Love numbers to compare with forthcoming observations. One could also evaluate with physical arguments the influence of the high atmosphere layers (above 1 bar) to diminish the "irreducible" error of the CMS method as we have presented it. However, in its present state the method is precise enough to be used on other planets (the orientation of Uranus might require further developments). Notably, the observation of Saturn during the grand finale of Cassini are expected to drastically improve our knowledge of its gravitational moments, although the results are still not published.

From the values of the gravitational moments of Juno [Iess et al., 2018] and the knowledge of the equation of state of hydrogen and helium [Chabrier et al., 2018, Mazevet et al., 2018, Militzer and Hubbard, 2013, ,...], I have detailed the new interior models of Jupiter I have derived in chapter 4. We have first shown that traditional two or three layers models, with one or two homogeneous convective zone and a compact core, cannot reproduce both the observed gravitational moments of Juno and the elemental abundance observed by Galileo. Hence, Jupiter must be composed of at least four zones: an outer, homogenous and convective envelope, a zone of composition change, an inner homogeneous and convective envelope and a diluted core. A central compact core can also be present. Between the outer envelope and the inner envelope, the observational constraints require a significant increase in the entropy associated with an increase in the mean molecular weight, so that the density gets lower than the density of an adiabatic structure. This increase in entropy is degenerated with the size of the compact core. These models are constrained by the theoretical knowledge of phase transitions and separation [Stevenson and Salpeter, 1977a,b, Mazzola et al., 2018, ,...], layered convection [Leconte and Chabrier, 2012, Rosenblum et al., 2011, ,...], our understanding of the origin of Jupiter's magnetic field [Connerney et al., 2018, Gastine et al., 2014, Duarte et al., 2018, ,...] and constraints on the evolution of Jupiter [Hubbard, 1968, Guillot et al., 1994, ,...]. We have also provided an extensive discussion on the physical assumptions of our model, showing for example that it is safe to consider an adiabatic structure from the 1bar observation of Galileo or that our models do satisfy the condition for layered convection. Globally, our models are the first ones to satisfy the observational constrains of both Juno and Galileo, and show that the structure of Jupiter is more complex than previously thought, hampering the simple calculations from evolutionary codes.

Many questions however remain unanswered by our study. The current understanding of layered convection [e.g., Leconte and Chabrier, 2012, Rosenblum et al., 2011] does not allow certainty over whether layered convection is dominant or even present in the region of the planet where composition changes occur. The treatment of the diffusive core is very simple as well, and further work in the understanding of the erosion of a core by metallic hydrogen could clarify some of our issues [Moll et al., 2017]. Without improvement in theoretical physics, there are yet a few perspectives from our work. First, it seems necessary to study the effect of our interior structure on other observable signals, such as magnetic field and oscillations. If, combined with a dynamo evolution code [e.g., Gastine et al., 2014], our converged structures of Jupiter could yield a sufficiently strong magnetic field, further confidence could be given to our work. Notably, the latest studies of Connerney et al. [2018] and Moore et al. [2018] tend to show that stratified layers in the Mbar region could explain the multipolar shape of the outer Jovian magnetic field, in agreement with our work. Then, as stated above, adapting our understanding of Jupiter's structure to the case of Saturn could prove to be a robust test of our theories. More generally, the interior structure of Jupiter we derived could be a template for extrasolar Jupiter-like planets.

Subsequently, in chapter 5 we have presented our current knowledge of a particular, widely observed type of exoplanets: hot Jupiters. These planets have masses comparable to that of Jupiter but are orbiting their star so closely that they end up in a tidally locked state, with an extreme day side heating and night side cooling. Giant planet evolution theories, benchmarked with Jupiter and Saturn (e.g., Guillot et al. [1996], Goukenleuque et al.

[2000]) have shown that the radii of these hot Jupiters are too large compared to what we would expect: this is the inflated radius puzzle. Although layered convection, a physical mechanism relevant in Jupiter and Saturn, has been proposed as a mechanism to explain this inflation [Chabrier and Baraffe, 2007], the inflated radius issue required new theoretical and analytical methods to be resolved. From the works of Showman and Guillot [2002], Batygin and Stevenson [2010], Bodenheimer et al. [2001, ,...] the origin of the inflated radius has often been linked with dissipative processes at depth. However, Tremblin et al. [2017] has shown that a global vertical circulation advecting potential temperature, can yield a hotter adiabatic interior. For Jupiter, we have seen the importance of the external dynamical processes to improve our knowledge of its internal structure [Kaspi, 2013, Kaspi et al., 2017, 2018]. The issue of the inflated radius shows that understanding the interior structure of hot Jupiters requires to understand their atmospheric dynamics. We have therefore detailed in chapter 5 the numerical methods to study hot Jupiters atmospheric dynamics: global circulation models (GCMs), and particularly the university of Exeter's GCM, the Unified Model (UM). Applied to hot Jupiters, various GCMs exhibit a common feature: equatorial superrotation. We have questioned the numerical details and robustness of superrotation in Mayne et al. [2017], and have also shown in chapter 5 that the addition of clouds and disequilibrium chemistry might change the globally accepted paradigm of broad equatorial superrotation with an eastward shift of the hot spot (see notably the observations of Dang et al. [2018]).

The improvement of our understanding of hot Jupiter atmospheres with numerical methods will probably be associated with the improvement of the physical details of GCMs. The influence of the degree of idealisation of these codes on the numerical results has to be assessed, through exploration of parameter space [Mayne et al., 2017] or dedicated studies on the importance of neglected physical processes (shocks and turbulence for example, Fromang et al. [2016], Ryu et al. [2018], Watkins and Cho [2010], ...). Additionally, most GCMs use simplified equations for the dynamical evolution: the primitive equations. In hot Jupiters, Mayne et al. [2014a] have shown that the use of the primitive equations is a plausible approximation. In a submitted paper to the Astrophysical Journal, however, we show that this approximation breaks down in the regime of Super Earth or Warm Neptunes (Mayne, Drummond, Debras et al, submitted). My contribution was to estimate analytically the source of breaking of the primitive equations for these atmospheres, and the conclusion is that the traditional approximation, neglecting the vertical speed in front of the meridional speed, can break even when the aspect ratio of the atmosphere is small. Finally, extending on the works of Tremblin et al. [2017], Mayne et al. [2017], Lines et al. [2018b,a], we are very interested in understanding further the dynamical evolution of the atmosphere: we want to assess whether the 3D temperature structure does converge to an adiabat at depth, confirming the inflated radius explanation of Tremblin et al. [2017], and we want to study the changes in the atmospheric dynamics when radiatively active clouds are included, and not only a reflecting cloud distribution following the atmospheric circulation.

Globally, the study of the atmospheric dynamics of hot Jupiters requires understanding theoretically whether superrotation is a robust mechanism. To help us toward that goal, I have developed ECLIPS3D, a linear eigenvector code that solves for waves, instabilities and steady circulations around any 3D steady atmosphere. It has proven to be a reliable code that provides detailed insight into the linear development of processes at stake in planetary atmospheres, and I have used it extensively during my PhD to assess the validity of analytical calculations or explore numerically the shape of different type of waves or steady circulations. We plan to submit a public version of

ECLIPS3D, allowing for comparisons with other such codes and studies of wave processes in planetary atmospheres as well as in many different physical or astrophysical situations, the range of applicability of ECPLIS3D being virtually unlimited and its adaptibility very high. The main limiting issue is the resolution, and we therefore plan on changing the numerical library to a library more suited to the study of sparse matrices, or to provide a spectral decomposition of the eigenvectors in space as well as in time.

In the last chapter of this thesis, we have finally presented theoretical calculations for explaining the spin up of superrotation in hot Jupiters. Because of their particular physical conditions, the canonical understanding of superrotation from solar system planets is inappropriate in the context of hot Jupiters. Instead, we have extended on the works of Showman and Polvani [2011], Tsai et al. [2014], Komacek and Showman [2016], Hammond and Pierrehumbert [2018] that explain the importance of the linear steady state for hot Jupiter superrotation. I have calculated the decay rates of waves for different damping conditions, and shown which waves are mostly contributing to the linear steady state. However, in the short timescales limit, the linear time dependent solution of the forced atmosphere has an equal contribution from all the waves excited by the heating, although their contributions to the linear steady state is very different. Providing an order of magnitude analysis, I have shown that the linear steady state was never reached for typical conditions of hot Jupiters, and therefore that the linear time dependent solution was better suited to the understanding of superrotation. As non linear effects come into play when the mean circualtion of the atmosphere leads to a convergence of momentum at the equator, an initial superrotation is accelerated (although the linear *steady* state would have led to a divergence of eastward momentum at the equator). This allows to resolve a discrepancy inherent to the works or Showman and Polvani [2011] and Komacek and Showman [2016], detailed in chapter 7. Finally, the considerations of the non linear accelerations in weakly forced simulations allow to conclude on the importance of the vertical transport of eastward momentum during the spin up phase, which was assumed to be negative before our work. Globally, we explain the initial acceleration of superrotation in hot Jupiters, and the equilibration of this primordial jet is explained by Tsai et al. [2014]: a global, coherent understanding of superrotation can be drawn.

These semi analytical considerations on superrotation could be further improved in a few ways. First, it would prove valuable to provide a better treatment of the 3D structure of the atmosphere than our simple estimations of equation (7.55). The actual behaviour of GCM simulations is three dimensional, and even our qualitative conclusions are limited by the use of a 2D shallow water beta plane. Then, following Tsai et al. [2014] or Hammond and Pierrehumbert [2018], the addition of a background zonal flow in the equations could allow to assess the stability of superrotating flows. When the background flow is at rest, we know that no instability can grow, but instabilities can occur when the background flow is not zero. Simple order of magnitude calculations notably show that Kelvin Helmoltz or baroclinic instability could alter the transition to superrotation, although low resolution GCMs would not capture such phenomena. Finally, changing the latitudinal shape of the heating function, for example because clouds predominantly form in mid latitudes [Lines et al., 2018b] might lead to qualitative change on the shape of the linear solutions. This perspective of improvement has not been tested yet.

Therefore, in this thesis I have explored theoretically and numerically gaseous giant planets from the core of Jupiter to the outermost layers of hot Jupiters. Our new models of the interior of Jupiter show the need to constrain better the theoretical physics of phase transition and double diffusive convection, and our study on the superrotation of hot Jupiters highlights even further the crucial link between atmospheric dynamics and internal processess, particularly stringent in these far away worlds. There are many perspectives of improvement from these works, in order to reach one day a coherent understanding of giant planets structure, formation, atmospheric dynamics and evolution. However, as a conclusion I want to stress that our global picture of Jupiter still remains limited, with many degeneracies in the interior models, yielding substantial uncertainty on the evolution of the planet. Quite logically, our insight into the physical conditions of hot Jupiters is even more limited. Improving our understanding of giant planets is therefore a long, tedious task, where shortcuts can only lead to erroneous conclusions, but if performed with care, it will increase significantly our knowledge on the origin and evolution of planetary systems, including our own.

Bibliography

M. Agúndez, O. Venot, F. Selsis, and N. Iro. The Puzzling Chemical Composition of GJ 436b's Atmosphere: Influence of Tidal Heating on the Chemistry. *Astrophys. J.* , 781:68, February 2014. doi: 10.1088/0004-637X/781/2/68.

Roi Alonso. *Characterization of Exoplanets: Secondary Eclipses*, pages 1441–1467. Springer International Publishing, Cham, 2018. ISBN 978-3-319-55333-7. doi: 10.1007/978-3-319-55333-7_40. URL `https://doi.org/10.1007/978-3-319-55333-7_40`.

D. S. Amundsen, I. Baraffe, P. Tremblin, J. Manners, W. Hayek, N. J. Mayne, and D. M. Acreman. Accuracy tests of radiation schemes used in hot Jupiter global circulation models. *Astronomy and Astrophysics*, 564:A59, 2014.

D. S. Amundsen, N. J. Mayne, I. Baraffe, J. Manners, P. Tremblin, B. Drummond, C. Smith, D. M. Acreman, and D. Homeier. The UK Met Office global circulation model with a sophisticated radiation scheme applied to the hot Jupiter HD 209458b. *Astronomy and Astrophysics*, 595:A36, October 2016. doi: 10.1051/0004-6361/201629183.

D. S. Amundsen, P. Tremblin, J. Manners, I. Baraffe, and N. J. Mayne. Treatment of overlapping gaseous absorption with the correlated-k method in hot Jupiter and brown dwarf atmosphere models. *Astronomy and Astrophysics*, 598:A97, February 2017. doi: 10.1051/0004-6361/201629322.

E. Anders and N. Grevesse. Abundances of the elements - Meteoritic and solar. *Geochemica and Cosmochemica Acta*, 53:197–214, January 1989. doi: 10.1016/0016-7037(89)90286-X.

Akio Arakawa and Vivian R Lamb. Computational design of the basic dynamical processes of the ucla general circulation model. *General circulation models of the atmosphere*, 17:173–265, 1977.

B. A. Archinal, M. F. A'Hearn, E. Bowell, A. Conrad, G. J. Consolmagno, R. Courtin, T. Fukushima, D. Hestroffer, J. L. Hilton, G. A. Krasinsky, G. Neumann, J. Oberst, P. K. Seidelmann, P. Stooke, D. J. Tholen, P. C. Thomas, and I. P. Williams. *Celestial Mechanics And Dynamical Astronomy*, 109:101, 2011.

N. W. Ashcroft. Hydrogen Dominant Metallic Alloys: High Temperature Superconductors? *Physical Review Letters*, 92(18):187002, May 2004. doi: 10.1103/PhysRevLett.92.187002.

P. G. Baines. The stability of planetary waves on a sphere. *Journal of Fluid Mechanics*, 73:193–213, January 1976. doi: 10.1017/S0022112076001341.

I. Baraffe, G. Chabrier, and T. Barman. The physical properties of extra-solar planets. *Reports on Progress in Physics*, 73(1):016901, 2010.

K. Batygin and D. J. Stevenson. Inflating Hot Jupiters with Ohmic Dissipation. *The Astrophysical Journal Letters*, 714:L238–L243, May 2010. doi: 10.1088/2041-8205/714/2/L238.

B. Bézard, E. Lellouch, D. Strobel, J.-P. Maillard, and P. Drossart. Carbon Monoxide on Jupiter: Evidence for Both Internal and External Sources. *Icarus*, 159:95–111, September 2002. doi: 10.1006/icar.2002.6917.

G. L. Bjoraker, M. H. Wong, I. de Pater, T. Hewagama, M. Adamkovics, and G. S. Orton. The Gas Composition and Deep Cloud Structure of Jupiter's Great Red Spot. *ArXiv e-prints*, August 2018.

R. Blackburn. Inert Gases in Metals. *Mettalurgical Review*, 11:159–176, 1966.

L. S. Blackford, J. Choi, A. Cleary, E. D'Azevedo, J. Demmel, I. Dhillon, J. Dongarra, S. Hammarling, G. Henry, A. Petitet, K. Stanley, D. Walker, and R. C. Whaley. *ScaLAPACK Users' Guide.* Society for Industrial and Applied Mathematics, Philadelphia, PA, 1997. ISBN 0-89871-397-8 (paperback).

P. Bodenheimer, D. N. C. Lin, and R. A. Mardling. On the Tidal Inflation of Short-Period Extrasolar Planets. *The Astrophysical Journal*, 548:466–472, February 2001. doi: 10.1086/318667.

S. J. Bolton, A. Adriani, V. Adumitroaie, M. Allison, J. Anderson, S. Atreya, J. Bloxham, S. Brown, J. E. P. Connerney, E. DeJong, W. Folkner, D. Gautier, D. Grassi, S. Gulkis, T. Guillot, C. Hansen, W. B. Hubbard, L. Iess, A. Ingersoll, M. Janssen, J. Jorgensen, Y. Kaspi, S. M. Levin, C. Li, J. Lunine, Y. Miguel, A. Mura, G. Orton, T. Owen, M. Ravine, E. Smith, P. Steffes, E. Stone, D. Stevenson, R. Thorne, J. Waite, D. Durante, R. W. Ebert, T. K. Greathouse, V. Hue, M. Parisi, J. R. Szalay, and R. Wilson. Jupiter's interior and deep atmosphere: The initial pole-to-pole passes with the Juno spacecraft. *Science*, 356:821–825, 2017.

A. Burrows, M. S. Marley, and C. M. Sharp. The Near-Infrared and Optical Spectra of Methane Dwarfs and Brown Dwarfs. *Astrophys. J.* , 531:438–446, March 2000. doi: 10.1086/308462.

J. K. Campbell and S. P. Synnott. Gravity field of the Jovian system from Pioneer and Voyager tracking data. *The Astronomical journal*, 90:364–372, 1985.

J. K. Campbell and S. P. Synott. *Astronomical Journal*, 90:364, 1985.

H. Cao and D. J. Stevenson. Zonal flow magnetic field interaction in the semi-conducting region of giant planets. *Icarus*, 296:59–72, November 2017. doi: 10.1016/j.icarus.2017.05.015.

P. M. Celliers, M. Millot, S. Brygoo, R. S. McWilliams, D. E. Fratanduono, J. R. Rygg, A. F. Goncharov, P. Loubeyre, J. H. Eggert, J. L. Peterson, N. B. Meezan, S. Le Pape, G. W. Collins, R. Jeanloz, and R. J. Hemley. Insulator-metal transition in dense fluid deuterium. *Science*, 361:677–682, August 2018. doi: 10.1126/science.aat0970.

G. Chabrier and I. Baraffe. Heat Transport in Giant (Exo)planets: A New Perspective. *Astrophys. J., Lett.* , 661: L81–L84, May 2007. doi: 10.1086/518473.

G. Chabrier, D. Saumon, W. B. Hubbard, and J. I. Lunine. The molecular-metallic transition of hydrogen and the structure of Jupiter and Saturn. *The Astrophysical Journal*, 391:817–826, 1992.

G. Chabrier, T. Barman, I. Baraffe, F. Allard, and P. H. Hauschildt. The Evolution of Irradiated Planets: Application to Transits. *Astrophys. J., Lett.* , 603:L53–L56, March 2004. doi: 10.1086/383028.

G. Chabrier, J. Gallardo, and I. Baraffe. Evolution of low-mass star and brown dwarf eclipsing binaries. *Astronomy and Astrophysics*, 472:L17–L20, September 2007. doi: 10.1051/0004-6361:20077702.

G. Chabrier, S. Mazevet, and F. Soubiran. *To appear in ApJ*, 2018.

S. Chandrasekhar. *Hydrodynamic and hydromagnetic stability.* 1961.

D. Charbonneau, T. M. Brown, D. W. Latham, and M. Mayor. Detection of Planetary Transits Across a Sun-like Star. *The Astrophysical Journal*, 529:L45–L48, January 2000. doi: 10.1086/312457.

J. G. Charney. The Dynamics of Long Waves in a Baroclinic Westerly Current. *Journal of Atmospheric Sciences*, 4:136–162, October 1947. doi: 10.1175/1520-0469(1947)004<0136:TDOLWI>2.0.CO;2.

J. G. Charney and N. A. Phillips. Numerical Integration of the Quasi-Geostrophic Equations for Barotropic and Simple Baroclinic Flows. *Journal of Atmospheric Sciences*, 10:71–99, April 1953. doi: 10.1175/1520-0469(1953)010<0071:NIOTQG>2.0.CO;2.

U. R. Christensen and J. Aubert. Scaling properties of convection-driven dynamos in rotating spherical shells and application to planetary magnetic fields. *Geophysical Journal International*, 166:97–114, July 2006. doi: 10.1111/j.1365-246X.2006.03009.x.

U. R. Christensen and D. A. Yuen. Layered convection induced by phase transitions. *Journal of Geophysical Research*, 90:10, October 1985. doi: 10.1029/JB090iB12p10291.

E. R. Cohen and B. N. Taylor. *Rev. Mod. Phys.*, 59:1121, 1987.

J. E. P. Connerney, S. Kotsiaros, R. J. Oliversen, J. R. Espley, J. L. Joergensen, P. S. Joergensen, J. M. G. Merayo, M. Herceg, J. Bloxham, K. M. Moore, S. J. Bolton, and S. M. Levin. A New Model of Jupiter's Magnetic Field From Juno's First Nine Orbits. *Geophysical Research Letters*, 45:2590–2596, March 2018. doi: 10.1002/2018GL077312.

C. S. Cooper and A. P. Showman. Dynamic Meteorology at the Photosphere of HD 209458b. *The Qstrophysical Journal letters*, 629:L45–L48, August 2005. doi: 10.1086/444354.

R. Daley. The normal modes of the spherical non-hydrostatic equations with applications to the filtering of acoustic modes. *Tellus Series A*, 40:96–106, March 1988. doi: 10.1111/j.1600-0870.1988.tb00409.x.

L. Dang, N. B. Cowan, J. C. Schwartz, E. Rauscher, M. Zhang, H. A. Knutson, M. Line, I. Dobbs-Dixon, D. Deming, S. Sundararajan, J. J. Fortney, and M. Zhao. Detection of a westward hotspot offset in the atmosphere of hot gas giant CoRoT-2b. *Nature Astronomy*, 2:220–227, March 2018. doi: 10.1038/s41550-017-0351-6.

F. Debras and G. Chabrier. A complete study of the precision of the concentric MacLaurin spheroid method to calculate Jupiter's gravitational moments. *Astronomy and Astrophysics*, 609:A97, January 2018. doi: 10.1051/0004-6361/201731682.

Hans J. Deeg and Roi Alonso. *Transit Photometry as an Exoplanet Discovery Method*, pages 633–657. Springer International Publishing, Cham, 2018. ISBN 978-3-319-55333-7. doi: 10.1007/978-3-319-55333-7_117. URL https://doi.org/10.1007/978-3-319-55333-7_117.

W. C. Demarcus. The constitution of Jupiter and Saturn. *The Astronomical Journal*, 63:2, January 1958. doi: 10.1086/107672.

I. Dobbs-Dixon and E. Agol. Three-dimensional radiative-hydrodynamical simulations of the highly irradiated short-period exoplanet HD 189733b. *Monthly Notices of the Royal Astronomical Society*, 435:3159–3168, 2013.

B. Drummond, P. Tremblin, I. Baraffe, et al. The effects of consistent chemical kinetics calculations on the pressure-temperature profiles and emission spectra of hot Jupiters. *A & A*, 594:A69, October 2016. doi: 10.1051/0004-6361/201628799.

B. Drummond, N. J. Mayne, I. Baraffe, P. Tremblin, J. Manners, D. S. Amundsen, J. Goyal, and D. Acreman. The effect of metallicity on the atmospheres of exoplanets with fully coupled 3D hydrodynamics, equilibrium chemistry, and radiative transfer. *Astronomy and Astrophysics*, 612:A105, May 2018a. doi: 10.1051/0004-6361/201732010.

B. Drummond, N. J. Mayne, J. Manners, I. Baraffe, J. Goyal, P. Tremblin, D. K. Sing, and K. Kohary. The 3D thermal, dynamical and chemical structure of the atmosphere of HD 189733b: implications of wind-driven chemistry for the emission phase curve. *ArXiv e-prints*, October 2018b.

B. Drummond, N. J. Mayne, J. Manners, A. L. Carter, I. A. Boutle, I. Baraffe, É. Hébrard, P. Tremblin, D. K. Sing, D. S. Amundsen, and D. Acreman. Observable Signatures of Wind-driven Chemistry with a Fully Consistent Three-dimensional Radiative Hydrodynamics Model of HD 209458b. *The Astrophysical Journal*, 855:L31, March 2018c. doi: 10.3847/2041-8213/aab209.

L. D. V. Duarte, J. Wicht, and T. Gastine. Physical conditions for Jupiter-like dynamo models. *Icarus*, 299:206–221, January 2018. doi: 10.1016/j.icarus.2017.07.016.

T. M. Evans, D. K. Sing, H. R. Wakeford, N. Nikolov, G. E. Ballester, B. Drummond, T. Kataria, N. P. Gibson, D. S. Amundsen, and J. Spake. Detection of H_2O and Evidence for TiO/VO in an Ultra-hot Exoplanet Atmosphere. *Astrophys. J., Lett.* , 822:L4, May 2016. doi: 10.3847/2041-8205/822/1/L4.

T. M. Evans, D. K. Sing, T. Kataria, J. Goyal, N. Nikolov, H. R. Wakeford, D. Deming, M. S. Marley, D. S. Amundsen, G. E. Ballester, J. K. Barstow, L. Ben-Jaffel, V. Bourrier, L. A. Buchhave, O. Cohen, D. Ehrenreich, A. García Muñoz, G. W. Henry, H. Knutson, P. Lavvas, A. Lecavelier Des Etangs, N. K. Lewis, M. López-Morales, A. M. Mandell, J. Sanz-Forcada, P. Tremblin, and R. Lupu. An ultrahot gas-giant exoplanet with a stratosphere. *Nature* , 548:58–61, August 2017. doi: 10.1038/nature23266.

B. M. Fisher, G. S. Orton, J. Liu, T. Schneider, M. E. Ressler, and W. F. Hoffman. The organization of Jupiter's upper tropospheric temperature structure and its evolution, 1996-1997. *Icarus*, 280:268–277, December 2016. doi: 10.1016/j.icarus.2016.07.016.

W. M. Folkner, L. Iess, J. D. Anderson, S. W. Asmar, D. R. Buccino, D. Durante, M. Feldman, L. Gomez Casajus, M. Gregnanin, A. Milani, M. Parisi, R. S. Park, D. Serra, G. Tommei, P. Tortora, M. Zannoni, S. J. Bolton, J. E. P. Connerney, and S. M. Levin. Jupiter gravity field estimated from the first two juno orbits. *Geophysical Research Letters*, 44(10):4694–4700, 2017. ISSN 1944-8007. doi: 10.1002/2017GL073140. URL `http://dx.doi.org/10.1002/2017GL073140`. 2017GL073140.

J. J. Fortney and W. B. Hubbard. Phase separation in giant planets: inhomogeneous evolution of Saturn. *Icarus*, 164:228–243, July 2003. doi: 10.1016/S0019-1035(03)00130-1.

T. Fouchet, S. Guerlet, D. F. Strobel, A. A. Simon-Miller, B. Bézard, and F. M. Flasar. An equatorial oscillation in Saturn's middle atmosphere. *Nature* , 453:200–202, May 2008. doi: 10.1038/nature06912.

S. Fromang, J. Leconte, and K. Heng. Shear-driven instabilities and shocks in the atmospheres of hot Jupiters. *Astronomy and Astrophysics*, 591:A144, July 2016. doi: 10.1051/0004-6361/201527600.

T. Gastine, J. Wicht, L. D. V. Duarte, M. Heimpel, and A. Becker. Explaining Jupiter's magnetic field and equatorial jet dynamics. *Geophysical Review Letters*, 41:5410–5419, August 2014. doi: 10.1002/2014GL060814.

P. Gaulme, F.-X. Schmider, J. Gay, T. Guillot, and C. Jacob. Detection of Jovian seismic waves: a new probe of its interior structure. *Astronomy and Astrophysics*, 531:A104, 2011.

P. J. Gierasch. Meridional circulation and the maintenance of the Venus atmospheric rotation. *Journal of Atmospheric Sciences*, 32:1038–1044, June 1975. doi: 10.1175/1520-0469(1975)032<1038:MCATMO>2.0.CO;2.

A. E. Gill. Some simple solutions for heat-induced tropical circulation. *Quarterly Journal of the Royal Meteorological Society*, 106(449):447–462, 1980.

P. Goldreich and S. Tremaine. Disk-satellite interactions. *Astrophys. J.* , 241:425–441, October 1980. doi: 10.1086/158356.

F. González-Cataldo, H. F. Wilson, and B. Militzer. Ab Initio Free Energy Calculations of the Solubility of Silica in Metallic Hydrogen and Application to Giant Planet Cores. *Astrophys. J.* , 787:79, May 2014. doi: 10.1088/0004-637X/787/1/79.

C. Goukenleuque, B. Bézard, B. Joguet, E. Lellouch, and R. Freedman. A Radiative Equilibrium Model of 51 Peg b. *Icarus*, 143:308–323, February 2000. doi: 10.1006/icar.1999.6256.

T. Guillot and D. Gautier. Giant Planets. *ArXiv e-prints*, 2014.

T. Guillot and A. P. Showman. Evolution of "51 Pegasus b-like" planets. *Astronomy and Astrophysics*, 385:156–165, April 2002. doi: 10.1051/0004-6361:20011624.

T. Guillot, D. Gautier, G. Chabrier, and B. Mosser. Are the giant planets fully convective? *Icarus*, 112:337–353, December 1994. doi: 10.1006/icar.1994.1188.

T. Guillot, A. Burrows, W. B. Hubbard, J. I. Lunine, and D. Saumon. Giant Planets at Small Orbital Distances. *Astrophysical Journal Letters*, 459:L35, March 1996. doi: 10.1086/309935.

T. Guillot, D. J. Stevenson, W. B. Hubbard, and D. Saumon. *The interior of Jupiter*, pages 35–57. 2004.

T. Guillot, Y. Miguel, B. Militzer, W. B. Hubbard, Y. Kaspi, E. Galanti, H. Cao, R. Helled, S. M. Wahl, L. Iess, W. M. Folkner, D. J. Stevenson, J. I. Lunine, D. R. Reese, A. Biekman, M. Parisi, D. Durante, J. E. P. Connerney, S. M. Levin, and S. J. Bolton. A suppression of differential rotation in Jupiter's deep interior. *Nature*, 555:227–230, March 2018. doi: 10.1038/nature25775.

M. Hammond and R. T. Pierrehumbert. Wave-Mean Flow Interactions in the Atmospheric Circulation of Tidally Locked Planets. *ArXiv e-prints*, October 2018.

C. J. Hansen and S. D. Kawaler. *Stellar Interiors. Physical Principles, Structure, and Evolution.* 1994. doi: 10.1007/978-1-4419-9110-2.

S. C. Hardiman, D. G. Andrews, A. A. White, N. Butchart, and I. Edmond. Using Different Formulations of the Transformed Eulerian Mean Equations and Eliassen-Palm Diagnostics in General Circulation Models. *Journal of Atmospheric Sciences*, 67:1983–1995, June 2010. doi: 10.1175/2010JAS3355.1.

B. Haurwitz. The Motion of Atmospheric Disturbances on the Spherical Earth. *Journal of Marine Research*, 3: 254–267, 1940.

Isaac M Held and Max J Suarez. A proposal for the intercomparison of the dynamical cores of atmospheric general circulation models. *Bulletin of the American Meteorological Society*, 75(10):1825–1830, 1994.

R. Helled and D. Stevenson. The Fuzziness of Giant Planets Cores. *Astrophys. J., Lett.* , 840:L4, May 2017. doi: 10.3847/2041-8213/aa6d08.

C. Helling and P. Woitke. Dust in brown dwarfs. V. Growth and evaporation of dirty dust grains. *Astronomy and Astrophysics*, 455:325–338, August 2006. doi: 10.1051/0004-6361:20054598.

C. Helling, G. Lee, I. Dobbs-Dixon, et al. The mineral clouds on HD 209458b and HD 189733b. *MNRAS*, 460: 855–883, July 2016. doi: 10.1093/mnras/stw662.

K. Heng and A. P. Showman. Atmospheric Dynamics of Hot Exoplanets. *Annual Review of Earth and Planetary Sciences*, 43:509–540, May 2015. doi: 10.1146/annurev-earth-060614-105146.

K. Heng and J. Workman. Analytical Models of Exoplanetary Atmospheres. I. Atmospheric Dynamics via the Shallow Water System. *Astrophys. J., Suppl. Ser.* , 213:27, August 2014. doi: 10.1088/0067-0049/213/2/27.

K. Heng, K. Menou, and P. J. Phillipps. Atmospheric circulation of tidally locked exoplanets: a suite of benchmark tests for dynamical solvers. *MNRAS*, 413:2380–2402, 2011.

Kevin Heng and Mark S. Marley. *Radiative Transfer for Exoplanet Atmospheres*, pages 2137–2152. Springer International Publishing, Cham, 2018. ISBN 978-3-319-55333-7. doi: 10.1007/978-3-319-55333-7_102. URL https://doi.org/10.1007/978-3-319-55333-7_102.

G. W. Henry, G. W. Marcy, R. P. Butler, and S. S. Vogt. A Transiting “51 Peg-like” Planet. *The Astrophysical Journal*, 529:L41–L44, January 2000. doi: 10.1086/312458.

J. R. Holton. *An introduction to dynamic meteorology.* Academic Press, 1992.

J. R. Holton and R. S. Lindzen. An Updated Theory for the Quasi-Biennial Cycle of the Tropical Stratosphere. *Journal of Atmospheric Sciences*, 29:1076–1080, September 1972. doi: 10.1175/1520-0469(1972)029<1076:AUTFTQ>2.0.CO;2.

B. j. Hoskins. Stability of the Rossby-Haurwitz wave. *Quarterly Journal of the Royal Meteorological Society*, 99: 723–745, October 1973. doi: 10.1002/qj.49709942213.

W. B. Hubbard. Thermal structure of Jupiter. *The Astrophysical Journal*, 152:745–754, June 1968. doi: 10.1086/149591.

W. B. Hubbard. Gravitational field of a rotating planet with a polytropic index of unity. *Soviet Astronomy*, 18: 621–624, 1975.

W. B. Hubbard. NOTE: Gravitational Signature of Jupiter’s Deep Zonal Flows. *Icarus*, 137:357–359, February 1999. doi: 10.1006/icar.1998.6064.

W. B. Hubbard. High-precision maclaurin-based models of rotating liquid planets. *The Astrophysical Journal Letters*, 756(1):L15, 2012.

W. B. Hubbard. Concentric Maclaurin spheroid models of rotating liquid planets. *The Astrophysical Journal*, 768: 43, 2013.

W. B. Hubbard and M. S. Marley. Optimized Jupiter, Saturn, and Uranus interior models. *Icarus*, 78:102–118, 1989.

W. B. Hubbard and B. Militzer. A preliminary jupiter model. *The Astrophysical Journal*, 820(1):80, 2016.

W. B. Hubbard, G. Schubert, D. Kong, and K. Zhang. On the convergence of the theory of figures. *Icarus*, 242, 2014.

H. H. Hyman. The chemistry of the noble gases. *Journal of Chemical Education*, 41:174, April 1964. doi: 10.1021/ed041p174.

E. Iaroslavitz and M. Podolak. Atmospheric mass deposition by captured planetesimals. *Icarus*, 187:600–610, April 2007. doi: 10.1016/j.icarus.2006.10.008.

L. Iess, W. M. Folkner, D. Durante, M. Parisi, Y. Kaspi, E. Galanti, T. Guillot, W. B. Hubbard, D. J. Stevenson, J. D. Anderson, D. R. Buccino, L. G. Casajus, A. Milani, R. Park, P. Racioppa, D. Serra, P. Tortora, M. Zannoni, H. Cao, R. Helled, J. I. Lunine, Y. Miguel, B. Militzer, S. Wahl, J. E. P. Connerney, S. M. Levin, and S. J. Bolton. Measurement of Jupiter’s asymmetric gravity field. *Nature*, 555:220–222, March 2018. doi: 10.1038/nature25776.

L. G. Ireland and M. K. Browning. The Radius and Entropy of a Magnetized, Rotating, Fully Convective Star: Analysis with Depth-dependent Mixing Length Theories. *Astrophys. J.* , 856:132, April 2018. doi: 10.3847/1538-4357/aab3da.

N. Iro, B. Bézard, and T. Guillot. A time-dependent radiative model of HD 209458b. *Astrnonomy and Astrophysics*, 436:719–727, June 2005. doi: 10.1051/0004-6361:20048344.

C. Jablonowski and D. L. Williamson. A baroclinic instability test case for atmospheric model dynamical cores. *Quarterly Journal of the Royal Meteorological Society*, 132:2943–2975, October 2006. doi: 10.1256/qj.06.12.

E. Kalnay de Rivas. Further numerical calculations of the circulation of the atmosphere of Venus. *Journal of Atmospheric Sciences*, 32:1017–1024, 1975.

A. Kasahara and J.-H. Qian. Normal Modes of a Global Nonhydrostatic Atmospheric Model. *Monthly Weather Review*, 128:3357, May 2000. doi: 10.1175/1520-0493(2000)128<3357:NMOAGN>2.0.CO;2.

Y. Kaspi. Inferring the depth of the zonal jets on Jupiter and Saturn from odd gravity harmonics. *Geophysical Review Letters*, 40:676–680, February 2013. doi: 10.1029/2012GL053873.

Y. Kaspi, T. Guillot, E. Galanti, Y. Miguel, R. Helled, W. B. Hubbard, B. Militzer, S. M. Wahl, S. Levin, J. E. P. Connerney, and S. J. Bolton. The effect of differential rotation on Jupiter's low-degree even gravity moments. *Geophysical Research Letter*, 44:5960–5968, June 2017. doi: 10.1002/2017GL073629.

Y. Kaspi, E. Galanti, W. B. Hubbard, D. J. Stevenson, S. J. Bolton, L. Iess, T. Guillot, J. Bloxham, J. E. P. Connerney, H. Cao, D. Durante, W. M. Folkner, R. Helled, A. P. Ingersoll, S. M. Levin, J. I. Lunine, Y. Miguel, B. Militzer, M. Parisi, and S. M. Wahl. Jupiter's atmospheric jet streams extend thousands of kilometres deep. *Nature*, 555:223–226, March 2018. doi: 10.1038/nature25793.

R. Kippenhahn and A. Weigert. *Stellar Structure and Evolution.* 1990.

M. D. Knudson, M. P. Desjarlais, R. W. Lemke, T. R. Mattsson, M. French, N. Nettelmann, and R. Redmer. Probing the Interiors of the Ice Giants: Shock Compression of Water to 700 GPa and 3.8g/cm^3. *Physical Review Letters*, 108(9):091102, March 2012. doi: 10.1103/PhysRevLett.108.091102.

M. D. Knudson, M. P. Desjarlais, A. Becker, R. W. Lemke, K. R. Cochrane, M. E. Savage, D. E. Bliss, T. R. Mattsson, and R. Redmer. Direct observation of an abrupt insulator-to-metal transition in dense liquid deuterium. *Science*, 348:1455–1460, June 2015. doi: 10.1126/science.aaa7471.

H. A. Knutson, D. Charbonneau, L. E. Allen, et al. A map of the day-night contrast of the extrasolar planet HD 189733b. *Nature*, 447:183–186, May 2007. doi: 10.1038/nature05782.

T. D. Komacek and A. P. Showman. Atmospheric Circulation of Hot Jupiters: Dayside-Nightside Temperature Differences. *The Astrophyiscal Journal*, 821:16, 2016.

D. S. Kothari. The Theory of Pressure-Ionization and Its Applications. *Proceedings of the Royal Society of London Series A*, 165:486–500, April 1938. doi: 10.1098/rspa.1938.0073.

Laura Kreidberg. *Exoplanet Atmosphere Measurements from Transmission Spectroscopy and Other Planet Star Combined Light Observations*, pages 2083–2105. Springer International Publishing, Cham, 2018. ISBN 978-3-319-55333-7. doi: 10.1007/978-3-319-55333-7_100. URL https://doi.org/10.1007/978-3-319-55333-7_100.

H. Kurokawa and S.-i. Inutsuka. On the Radius Anomaly of Hot Jupiters: Reexamination of the Possibility and Impact of Layered Convection. *Astrophys. J.* , 815:78, December 2015. doi: 10.1088/0004-637X/815/1/78.

J. Leconte and G. Chabrier. A new vision of giant planet interiors: Impact of double diffusive convection. *Astronomy and Astrophysics*, 540:A20, 2012.

J. Leconte and G. Chabrier. Layered convection as the origin of Saturn's luminosity anomaly. *Nature Geoscience*, 6:347–350, May 2013. doi: 10.1038/ngeo1791.

G. Lee, I. Dobbs-Dixon, C. Helling, K. Bognar, and P. Woitke. Dynamic mineral clouds on HD 189733b. I. 3D RHD with kinetic, non-equilibrium cloud formation. *A & A*, 594:A48, October 2016. doi: 10.1051/0004-6361/201628606.

R. B. Leighton, R. W. Noyes, and G. W. Simon. Velocity Fields in the Solar Atmosphere. I. Preliminary Report. *The Astrophysical Journal*, 135:474, 1962.

N. K. Lewis, A. P. Showman, J. J. Fortney, M. S. Marley, R. S. Freedman, and K. Lodders. Atmospheric Circulation of Eccentric Hot Neptune GJ436b. *Astrophys. J.* , 720:344–356, September 2010. doi: 10.1088/0004-637X/720/1/344.

C. Li, A. Ingersoll, M. Janssen, S. Levin, S. Bolton, V. Adumitroaie, M. Allison, J. Arballo, A. Bellotti, S. Brown, S. Ewald, L. Jewell, S. Misra, G. Orton, F. Oyafuso, P. Steffes, and R. Williamson. The distribution of ammonia on Jupiter from a preliminary inversion of Juno microwave radiometer data. *Geophysical Research Letters*, 44:5317–5325, June 2017. doi: 10.1002/2017GL073159.

J. Li and J. Goodman. Circulation and Dissipation on Hot Jupiters. *Astrophys. J.* , 725:1146–1158, December 2010. doi: 10.1088/0004-637X/725/1/1146.

A. Licari. *Microscopic modelling of compact stars and planets*. PhD thesis, ENS de Lyon, 2016.

R. D. Lindzen. Planetary Waves on Beta-Planes. *Monthly Weather Review*, 95:441, 1967. doi: 10.1175/1520-0493(1967)095<0441:PWOBP>2.3.CO;2.

S. Lines, J. Manners, N. J. Mayne, J. Goyal, A. L. Carter, I. A. Boutle, G. K. H. Lee, C. Helling, B. Drummond, D. M. Acreman, and D. K. Sing. Exonephology: transmission spectra from a 3D simulated cloudy atmosphere of HD 209458b. *Monthly Notices of the Royal Astronomical Society*, 481:194–205, November 2018a. doi: 10.1093/mnras/sty2275.

S. Lines, N. J. Mayne, I. A. Boutle, J. Manners, G. K. H. Lee, C. Helling, B. Drummond, D. S. Amundsen, J. Goyal, D. M. Acreman, P. Tremblin, and M. Kerslake. Simulating the cloudy atmospheres of HD 209458 b and HD 189733 b with the 3D Met Office Unified Model. *ArXiv e-prints*, March 2018b.

W. Lorenzen, B. Holst, and R. Redmer. Demixing of Hydrogen and Helium at Megabar Pressures. *Physical Review Letters*, 102(11):115701, March 2009. doi: 10.1103/PhysRevLett.102.115701.

W. Lorenzen, B. Holst, and R. Redmer. Metallization in hydrogen-helium mixtures. *Physical Review B*, 84(23): 235109, December 2011. doi: 10.1103/PhysRevB.84.235109.

P. Loubeyre, R. Le Toullec, and J.-P. Pinceaux. Helium compressional effect on H_2 molecules surrounded by dense H_2-He mixtures. *Physical Review B*, 32:7611–7613, December 1985. doi: 10.1103/PhysRevB.32.7611.

F. J. Low. Planetary radiation at infrared and millimeter wavelengths. *Lowell Observatory Bulletin*, 6:184–187, 1965.

S. H. Lubow, C. A. Tout, and M. Livio. Resonant Tides in Close Orbiting Planets. *The Astrophysical Journal*, 484: 866–870, July 1997. doi: 10.1086/304369.

P. Lynch. On resonant Rossby-Haurwitz triads. *Tellus Series A*, 61:438–445, May 2009. doi: 10.1111/j.1600-0870.2009.00395.x.

S. P. Lyon and J. D. Johnson. *ANL Rep. LA-UR-92-3407 (Los Alamos:LANL)*, 1992.

Nikku Madhusudhan. *Atmospheric Retrieval of Exoplanets*, pages 2153–2182. Springer International Publishing, Cham, 2018. ISBN 978-3-319-55333-7. doi: 10.1007/978-3-319-55333-7_104. URL `https://doi.org/10.1007/978-3-319-55333-7_104`.

Taroh Matsuno. Quasi-Geostrophic Motions in the Equatorial Area. *Journal of the Meteorological Society of Japan*, 44:25–43, 1966.

N. J. Mayne, I. Baraffe, D. M. Acreman, C. Smith, M. K. Browning, D. Skålid Amundsen, N. Wood, J. Thuburn, and D. R. Jackson. The unified model, a fully-compressible, non-hydrostatic, deep atmosphere global circulation model, applied to hot Jupiters. ENDGame for a HD 209458b test case. *Astronomy and Astrophysics*, 561:A1, January 2014a. doi: 10.1051/0004-6361/201322174.

N. J. Mayne, I. Baraffe, D. M. Acreman, C. Smith, N. Wood, D. S. Amundsen, J. Thuburn, and D. R. Jackson. Using the UM dynamical cores to reproduce idealised 3-D flows. *Geoscientific Model Development*, 7:3059–3087, 2014b.

N. J. Mayne, F. Debras, I. Baraffe, J. Thuburn, D. S. Amundsen, D. M. Acreman, C. Smith, M. K. Browning, J. Manners, and N. Wood. Results from a set of three-dimensional numerical experiments of a hot Jupiter atmosphere. *A & A*, 604:A79, August 2017. doi: 10.1051/0004-6361/201730465.

M. Mayor and D. Queloz. A Jupiter-mass companion to a solar-type star. *Nature*, 378:355–359, 1995.

S. Mazevet et al. *To appear in A&A*, 2018.

G. Mazzola, R. Helled, and S. Sorella. Phase Diagram of Hydrogen and a Hydrogen-Helium Mixture at Planetary Conditions by Quantum Monte Carlo Simulations. *Physical Review Letters*, 120(2):025701, January 2018. doi: 10.1103/PhysRevLett.120.025701.

K. Menou and E. Rauscher. Atmospheric Circulation of Hot Jupiters: A Shallow Three-Dimensional Model. *Astrophys. J.* , 700:887–897, July 2009. doi: 10.1088/0004-637X/700/1/887.

D. H. Menzel, W. W. Coblentz, and C. O. Lampland. Planetary Temperatures Derived from Water-Cell Transmissions. *The Astrophysical Journal*, 63:177–187, April 1926. doi: 10.1086/142965.

T. M. Merlis and T. Schneider. Atmospheric dynamics of Earth-like tidally locked aquaplanets. *Journal of Advances in Modeling Earth Systems*, 2:13, December 2010. doi: 10.3894/JAMES.2010.2.13.

Y. Miguel, T. Guillot, and L. Fayon. Jupiter internal structure: the effect of different equations of state. *Astronomy and Astrophysics*, 596:A114, December 2016. doi: 10.1051/0004-6361/201629732.

B. Militzer and W. B. Hubbard. Ab Initio Equation of State for Hydrogen-Helium Mixtures with Recalibration of the Giant-planet Mass-Radius Relation. *The Astrophysical Journal*, 774:148, September 2013. doi: 10.1088/0004-637X/774/2/148.

G. M. Mirouh, P. Garaud, S. Stellmach, A. L. Traxler, and T. S. Wood. A New Model for Mixing by Double-diffusive Convection (Semi-convection). I. The Conditions for Layer Formation. *Astrophys. J.* , 750:61, May 2012. doi: 10.1088/0004-637X/750/1/61.

R. Moll, P. Garaud, C. Mankovich, and J. J. Fortney. Double-diffusive Erosion of the Core of Jupiter. *The Astrophysical Journal*, 849:24, November 2017. doi: 10.3847/1538-4357/aa8d74.

B. Monserrat, M. Martinez-Canales, R. J. Needs, and C. J. Pickard. Helium-iron compounds at terapascal pressures. *ArXiv e-prints*, June 2018.

Kimberly M. Moore, Rakesh K. Yadav, Laura Kulowski, Hao Cao, Jeremy Bloxham, John E. P. Connerney, Stavros Kotsiaros, John L. Jørgensen, JoséM. G. Merayo, David J. Stevenson, Scott J. Bolton, and Steven M. Levin. A complex dynamo inferred from the hemispheric dichotomy of jupiter's magnetic field. *Nature*, 561(7721):76–78, 2018. doi: 10.1038/s41586-018-0468-5. URL `https://doi.org/10.1038/s41586-018-0468-5`.

M. A. Morales, E. Schwegler, D. Ceperley, C. Pierleoni, S. Hamel, and K. Caspersen. Phase separation in hydrogen-helium mixtures at Mbar pressures. *Proceedings of the National Academy of Science*, 106:1324, February 2009. doi: 10.1073/pnas.0812581106.

M. A. Morales, C. Pierleoni, and D. M. Ceperley. Equation of state of metallic hydrogen from coupled electron-ion Monte Carlo simulations. *Physical Review E*, 81(2):021202, February 2010. doi: 10.1103/PhysRevE.81.021202.

M. A. Morales, S. Hamel, K. Caspersen, and E. Schwegler. Hydrogen-helium demixing from first principles: From diamond anvil cells to planetary interiors. *Physical Review B*, 87(17):174105, May 2013a. doi: 10.1103/PhysRevB.87.174105.

M. A. Morales, J. M. McMahon, C. Pierleoni, and D. M. Ceperley. Nuclear Quantum Effects and Nonlocal Exchange-Correlation Functionals Applied to Liquid Hydrogen at High Pressure. *Physical Review Letters*, 110(6):065702, February 2013b. doi: 10.1103/PhysRevLett.110.065702.

Christoph Mordasini. *Planetary Population Synthesis*, pages 2425–2474. Springer International Publishing, Cham, 2018. ISBN 978-3-319-55333-7. doi: 10.1007/978-3-319-55333-7_143. URL `https://doi.org/10.1007/978-3-319-55333-7_143`.

R. Moreno, A. Marten, H. E. Matthews, and Y. Biraud. Long-term evolution of CO, CS and HCN in Jupiter after the impacts of comet Shoemaker-Levy 9. *Planetary and Space science*, 51:591–611, August 2003. doi: 10.1016/S0032-0633(03)00072-2.

T. D. Morton, S. T. Bryson, J. L. Coughlin, J. F. Rowe, G. Ravichandran, E. A. Petigura, M. R. Haas, and N. M. Batalha. False Positive Probabilities for all Kepler Objects of Interest: 1284 Newly Validated Planets and 428 Likely False Positives. *The Astrophysical Journal*, 822:86, May 2016. doi: 10.3847/0004-637X/822/2/86.

J. I. Moses. Chemical kinetics on extrasolar planets. *Philosophical Transactions of the Royal Society of London Series A*, 372:20130073–20130073, March 2014. doi: 10.1098/rsta.2013.0073.

R. Musella, S. Mazevet, and F. Guyot. Physical properties of MgO at deep planetary conditions. *ArXiv e-prints*, May 2018.

W. J. Nellis, M. Ross, and N. C. Holmes. Temperature Measurements of Shock-Compressed Liquid Hydrogen: Implications for the Interior of Jupiter. *Science*, 269:1249–1252, September 1995. doi: 10.1126/science.7652570.

N. Nettelmann. Low- and high-order gravitational harmonics of rigidly rotating Jupiter. *ArXiv e-prints 1708.06177*, August 2017.

N. Nettelmann, A. Becker, B. Holst, and R. Redmer. Jupiter Models with Improved Ab Initio Hydrogen Equation of State (H-REOS.2). *Astrophys. J.* , 750:52, May 2012. doi: 10.1088/0004-637X/750/1/52.

Richard Dixon Oldham. The constitution of the interior of the earth, as revealed by earthquakes. *Quarterly Journal of the Geological Society*, 62(1-4):456–475, 1906.

E. J. Öpik. Jupiter: Chemical composition, structure, and origin of a giant planet. *Icarus*, 1:200–257, 1962. doi: 10.1016/0019-1035(62)90022-2.

G. S. Orton, A. J. Friedson, J. Caldwell, H. B. Hammel, K. H. Baines, J. T. Bergstralh, T. Z. Martin, M. E. Malcom, R. A. West, W. F. Golisch, D. M. Griep, C. D. Kaminski, A. T. Tokunaga, R. Baron, and M. Shure. Thermal maps of Jupiter - Spatial organization and time dependence of stratospheric temperatures, 1980 to 1990. *Science*, 252:537–542, April 1991. doi: 10.1126/science.252.5005.537.

Vivien Parmentier and Ian J. M. Crossfield. *Exoplanet Phase Curves: Observations and Theory*, pages 1419–1440. Springer International Publishing, Cham, 2018. ISBN 978-3-319-55333-7. doi: 10.1007/978-3-319-55333-7_116. URL `https://doi.org/10.1007/978-3-319-55333-7_116`.

P. J. E. Peebles. The Structure and Composition of Jupiter and Saturn. *The Astrophysical Journal*, 140:328, July 1964. doi: 10.1086/147922.

J. P. Peixoto and A. H. Oort. *Physics of climate*. 1992.

C. M. Pépin, G. Geneste, A. Dewaele, M. Mezouar, and P. Loubeyre. Synthesis of FeH_5: A layered structure with atomic hydrogen slabs. *Science*, 357:382–385, July 2017. doi: 10.1126/science.aan0961.

D. Perez-Becker and A. P. Showman. Atmospheric Heat Redistribution on Hot Jupiters. *The Astrophysical Journal*, 776:134, October 2013. doi: 10.1088/0004-637X/776/2/134.

R. Perna, K. Heng, and F. Pont. The Effects of Irradiation on Hot Jovian Atmospheres: Heat Redistribution and Energy Dissipation. *The Astrophysical Journal*, 751, 2012.

Norman A. Phillips. The general circulation of the atmosphere: A numerical experiment. *Quarterly Journal of the Royal Meteorological Society*, 82(352):123–164, 1956.

J. B. Pollack, O. Hubickyj, P. Bodenheimer, J. J. Lissauer, M. Podolak, and Y. Greenzweig. Formation of the Giant Planets by Concurrent Accretion of Solids and Gas. *Icarus*, 124:62–85, November 1996. doi: 10.1006/icar.1996.0190.

J. Pratt, I. Baraffe, T. Goffrey, T. Constantino, M. Viallet, M. V. Popov, R. Walder, and D. Folini. Extreme value statistics for two-dimensional convective penetration in a pre-main sequence star. *Astronomy and Astrophysics*, 604:A125, August 2017. doi: 10.1051/0004-6361/201630362.

W. Ramsay and R. W. Travers. An attempt to cause Helium or Argon to pass through Red-hot Palladium, Platinum or Iron. *Proceedings of the Royal Society of London*, 61:267, 1897.

E. Rauscher and K. Menou. A General Circulation Model for Gaseous Exoplanets with Double-gray Radiative Transfer. *The Astrophysical Journal*, 750:96, 2012.

A. C. Riddle and J. W. Warwick. *Icarus*, 27:457, 1976.

E. Roche. La Constitution Interieure de Notre Planete. *L'Astronomie*, 2:200–206, 1883.

E. Rosenblum, P. Garaud, A. Traxler, and S. Stellmach. Turbulent Mixing and Layer Formation in Double-diffusive Convection: Three-dimensional Numerical Simulations and Theory. *Astrophys. J.* , 731:66, April 2011. doi: 10.1088/0004-637X/731/1/66.

C. G. Rossby. Dynamics of steady ocean currents in the light of experimental fluid dynamics. *Papers in Phys. Oceanog. and Meteor.*, 5:1–43, 1936.

T. Ryu, M. Zingale, and R. Perna. Turbulence-driven thermal and kinetic energy fluxes in the atmospheres of hot Jupiters. *Monthly Notices of the Royal Astronomical Society*, 481:5517–5531, December 2018. doi: 10.1093/mnras/sty2638.

E. E. Salpeter. On Convection and Gravitational Layering in Jupiter and in Stars of Low Mass. *Astrophys. J., Lett.* , 181:L83, April 1973. doi: 10.1086/181190.

A. Santerne. Populations of Extrasolar Giant Planets from Transit and Radial Velocity Surveys. *ArXiv e-prints*, May 2018.

D. Saumon and G. Chabrier. Fluid hydrogen at high density - Pressure ionization. *Physical Review A*, 46:2084–2100, August 1992. doi: 10.1103/PhysRevA.46.2084.

D. Saumon and T. Guillot. Shock Compression of Deuterium and the Interiors of Jupiter and Saturn. *Astrophys. J.* , 609:1170–1180, July 2004. doi: 10.1086/421257.

D. Saumon, G. Chabrier, and H. M. van Horn. An Equation of State for Low-Mass Stars and Giant Planets. *Astrophysical Journal Supplements*, 99:713, 1995.

T. Schneider and J. Liu. Formation of Jets and Equatorial Superrotation on Jupiter. *Journal of Atmospheric Sciences*, 66:579, 2009. doi: 10.1175/2008JAS2798.1.

M. Schöttler and R. Redmer. Ab Initio Calculation of the Miscibility Diagram for Hydrogen-Helium Mixtures. *Physical Review Letters*, 120(11):115703, March 2018. doi: 10.1103/PhysRevLett.120.115703.

A. Seiff, D. B. Kirk, T. C. D. Knight, R. E. Young, J. D. Mihalov, L. A. Young, F. S. Milos, G. Schubert, R. C. Blanchard, and D. Atkinson. Thermal structure of Jupiter's atmosphere near the edge of a 5-μm hot spot in the north equatorial belt. *Journal of Geophysical Research*, 103:22857–22890, 1998.

A. P. Showman and T. Guillot. Atmospheric circulation and tides of "51 Pegasus b-like" planets. *Astronomy and Astrophysics*, 385:166–180, April 2002. doi: 10.1051/0004-6361:20020101.

A. P. Showman and L. M. Polvani. Equatorial Superrotation on Tidally Locked Exoplanets. *The Astrophysical Journal*, 738:71, September 2011. doi: 10.1088/0004-637X/738/1/71.

A. P. Showman, C. S. Cooper, J. J. Fortney, and M. S. Marley. Atmospheric Circulation of Hot Jupiters: Three-dimensional Circulation Models of HD 209458b and HD 189733b with Simplified Forcing. *The Astrophyisical Journal*, 682:559–576, 2008.

A. P. Showman, J. J. Fortney, Y. Lian, et al. Atmospheric Circulation of Hot Jupiters: Coupled Radiative-Dynamical General Circulation Model Simulations of HD 189733b and HD 209458b. *The Astrophysical Journal*, 699:564–584, July 2009. doi: 10.1088/0004-637X/699/1/564.

A. P. Showman, X. Tan, and X. Zhang. Atmospheric Circulation of Brown Dwarfs and Jupiter and Saturn-like Planets: Zonal Jets, Long-term Variability, and QBO-type Oscillations. *ArXiv e-prints*, July 2018.

D. K. Sing, J. J. Fortney, N. Nikolov, H. R. Wakeford, T. Kataria, T. M. Evans, S. Aigrain, G. E. Ballester, A. S. Burrows, D. Deming, J.-M. Désert, N. P. Gibson, G. W. Henry, C. M. Huitson, H. A. Knutson, A. L. D. Etangs, F. Pont, A. P. Showman, A. Vidal-Madjar, M. H. Williamson, and P. A. Wilson. A continuum from clear to cloudy hot-Jupiter exoplanets without primordial water depletion. *Nature*, 529:59–62, 2016.

F. Soubiran and B. Militzer. Miscibility Calculations for Water and Hydrogen in Giant Planets. *Astrophys. J.* , 806:228, June 2015. doi: 10.1088/0004-637X/806/2/228.

F. Soubiran and B. Militzer. The Properties of Heavy Elements in Giant Planet Envelopes. *Astrophys. J.* , 829:14, September 2016. doi: 10.3847/0004-637X/829/1/14.

F. Soubiran, S. Mazevet, C. Winisdoerffer, and G. Chabrier. Optical signature of hydrogen-helium demixing at extreme density-temperature conditions. *Physical Review B*, 87(16):165114, April 2013. doi: 10.1103/PhysRevB.87.165114.

A. Staniforth and N. Wood. The Deep-Atmosphere Euler Equations in a Generalized Vertical Coordinate. *Monthly Weather Review*, 131:1931, 2003. doi: 10.1175//2564.1.

A. Staniforth and N. Wood. Aspects of the dynamical core of a nonhydrostatic, deep-atmosphere, unified weather and climate-prediction model. *Journal of Computational Physics*, 227:3445–3464, March 2008. doi: 10.1016/j.jcp.2006.11.009.

M. E. Stern. The “Salt-Fountain” and Thermohaline Convection. *Tellus Series A*, 12:172–175, May 1960. doi: 10.1111/j.2153-3490.1960.tb01295.x.

D. J. Stevenson. *The interior of Jupiter.* PhD thesis, Cornell Univ., Ithaca, NY., 1976.

D. J. Stevenson. Solubility of helium in metallic hydrogen. *Journal of Physics F Metal Physics*, 9:791–801, May 1979. doi: 10.1088/0305-4608/9/5/007.

D. J. Stevenson. Cosmochemistry and structure of the giant planets and their satellites. *Icarus*, 62:4–15, April 1985. doi: 10.1016/0019-1035(85)90168-X.

D. J. Stevenson and E. E. Salpeter. The phase diagram and transport properties for hydrogen-helium fluid planets. *Astrophysical Journal Supplement Series*, 35:221–237, October 1977a. doi: 10.1086/190478.

D. J. Stevenson and E. E. Salpeter. The dynamics and helium distribution in hydrogen-helium fluid planets. *Astrophysical Journal Supplement Series*, 35:239–261, October 1977b. doi: 10.1086/190479.

D. P. Thorngren, J. J. Fortney, R. A. Murray-Clay, and E. D. Lopez. The Mass-Metallicity Relation for Giant Planets. *Astrophys. J.* , 831:64, November 2016. doi: 10.3847/0004-637X/831/1/64.

J. Thuburn and Y. Li. Numerical simulations of Rossby Haurwitz waves. *Tellus Series A*, 52:181, March 2000. doi: 10.1034/j.1600-0870.2000.00107.x.

J. Thuburn, N. Wood, and A. Staniforth. Normal modes of deep atmospheres. I: Spherical geometry. *Quarterly Journal of the Royal Meteorological Society*, 128:1771–1792, 2002a.

J. Thuburn, N. Wood, and A. Staniforth. Normal modes of deep atmospheres. I: Spherical geometry. *Quarterly Journal of the Royal Meteorological Society*, 128:1771–1792, 2002b. doi: 10.1256/003590002320603403.

P. Tremblin, G. Chabrier, N. J. Mayne, D. S. Amundsen, I. Baraffe, F. Debras, B. Drummond, J. Manners, and S. Fromang. Advection of Potential Temperature in the Atmosphere of Irradiated Exoplanets: A Robust Mechanism to Explain Radius Inflation. *Astrophys. J.* , 841:30, May 2017. doi: 10.3847/1538-4357/aa6e57.

S.-M. Tsai, I. Dobbs-Dixon, and P.-G. Gu. Three-dimensional Structures of Equatorial Waves and the Resulting Super-rotation in the Atmosphere of a Tidally Locked Hot Jupiter. *The Astrophysical Journal*, 793:141, October 2014. doi: 10.1088/0004-637X/793/2/141.

S.-M. Tsai, D. Kitzmann, J. R. Lyons, J. Mendonça, S. L. Grimm, and K. Heng. Towards Consistent Modeling of Atmospheric Chemistry and Dynamics in Exoplanets: Validation and Generalization of Chemical Relaxation Method. *ArXiv e-prints*, November 2017.

P. A. Ullrich, T. Melvin, C. Jablonowski, and A. Staniforth. A proposed baroclinic wave test case for deep- and shallow-atmosphere dynamical cores. *Quarterly Journal of the Royal Meteorological Society*, 140:1590–1602, July 2014. doi: 10.1002/qj.2241.

G. K. Vallis. *Atmospheric and Oceanic Fluid Dynamics.* Cambridge University Press, Cambridge, U.K., 2006.

A. Vazan, R. Helled, and T. Guillot. Jupiter's evolution with primordial composition gradients. *Astronomy and Astrophysics*, 610:L14, February 2018. doi: 10.1051/0004-6361/201732522.

U. von Zahn, D. M. Hunten, and G. Lehmacher. Helium in Jupiter's atmosphere: Results from the Galileo probe helium interferometer experiment. *Journal of Geophysical Research*, 103:22815–22830, 1998.

S. M. Wahl, H. F. Wilson, and B. Militzer. Solubility of Iron in Metallic Hydrogen and Stability of Dense Cores in Giant Planets. *Astrophys. J.* , 773:95, August 2013. doi: 10.1088/0004-637X/773/2/95.

S. M. Wahl, W. B. Hubbard, B. Militzer, T. Guillot, Y. Miguel, N. Movshovitz, Y. Kaspi, R. Helled, D. Reese, E. Galanti, S. Levin, J. E. Connerney, and S. J. Bolton. Comparing Jupiter interior structure models to Juno gravity measurements and the role of a dilute core. *ArXiv e-prints*, 2017.

H. R. Wakeford, D. K. Sing, T. Kataria, D. Deming, N. Nikolov, E. D. Lopez, P. Tremblin, D. S. Amundsen, N. K. Lewis, A. M. Mandell, J. J. Fortney, H. Knutson, B. Benneke, and T. M. Evans. HAT-P-26b: A Neptune-mass exoplanet with a well-constrained heavy element abundance. *Science*, 356:628–631, May 2017. doi: 10.1126/science.aah4668.

P. Wang and J. L. Mitchell. Planetary ageostrophic instability leads to superrotation. *Geophysical Research Letters*, 41(12):4118–4126, 2014.

C. Watkins and J. Y.-K. Cho. Gravity Waves on Hot Extrasolar Planets. I. Propagation and Interaction with the Background. *Astrophys. J.* , 714:904–914, May 2010. doi: 10.1088/0004-637X/714/1/904.

M. Wheeler and G. N. Kiladis. Convectively Coupled Equatorial Waves: Analysis of Clouds and Temperature in the Wavenumber-Frequency Domain. *Journal of Atmospheric Sciences*, 56:374–399, February 1999. doi: 10.1175/1520-0469(1999)056<0374:CCEWAO>2.0.CO;2.

A. A. White, B. J. Hoskins, I. Roulstone, and A. Staniforth. Consistent approximate models of the global atmosphere: shallow, deep, hydrostatic, quasi-hydrostatic and non-hydrostatic. *Quarterly Journal of the Royal Meteorological Society*, 131:2081–2107, July 2005. doi: 10.1256/qj.04.49.

E. Wigner and H. B. Huntington. On the Possibility of a Metallic Modification of Hydrogen. *The Journal of Chemical Physics*, 3:764–770, December 1935. doi: 10.1063/1.1749590.

R. Wildt. On the State of Matter in the Interior of the Planets. *The Astrophysical Journal*, 87:508, June 1938. doi: 10.1086/143941.

G. P. Williams. Barotropic Instability and Equatorial Superrotation. *Journal of Atmospheric Sciences*, 60:2136–2152, September 2003. doi: 10.1175/1520-0469(2003)060<2136:BIAES>2.0.CO;2.

D. L. Williamson, J. B. Drake, J. J. Hack, R. Jakob, and P. N. Swarztrauber. A standard test set for numerical approximations to the shallow water equations in spherical geometry. *Journal of Computational Physics*, 102: 211–224, September 1992. doi: 10.1016/S0021-9991(05)80016-6.

H. F. Wilson and B. Militzer. Sequestration of Noble Gases in Giant Planet Interiors. *Physical Review Letters*, 104 (12):121101, March 2010. doi: 10.1103/PhysRevLett.104.121101.

H. F. Wilson and B. Militzer. Solubility of Water Ice in Metallic Hydrogen: Consequences for Core Erosion in Gas Giant Planets. *Astrophys. J.* , 745:54, January 2012a. doi: 10.1088/0004-637X/745/1/54.

H. F. Wilson and B. Militzer. Rocky Core Solubility in Jupiter and Giant Exoplanets. *Physical Review Letters*, 108 (11):111101, March 2012b. doi: 10.1103/PhysRevLett.108.111101.

Joshua N. Winn. *Planet Occurrence: Doppler and Transit Surveys*, pages 1949–1966. Springer International Publishing, Cham, 2018. doi: 10.1007/978-3-319-55333-7_195. URL https://doi.org/10.1007/978-3-319-55333-7_195.

J. Wisdom. Non-perturbative hydrostatic equilibrium. 1996. URL http://web.mit.edu/wisdom/www/interior.pdf.

J. Wisdom and W. B. Hubbard. Differential rotation in Jupiter: A comparison of methods. *Icarus*, 267:315–322, 2016.

P. Woitke and C. Helling. Dust in brown dwarfs. II. The coupled problem of dust formation and sedimentation. *Astronomy and Astrophysics*, 399:297–313, February 2003. doi: 10.1051/0004-6361:20021734.

P. Woitke and C. Helling. Dust in brown dwarfs. III. Formation and structure of quasi-static cloud layers. *Astronomy and Astrophysics*, 414:335–350, January 2004. doi: 10.1051/0004-6361:20031605.

M. H. Wong, P. R. Mahaffy, S. K. Atreya, H. B. Niemann, and T. C. Owen. Updated Galileo probe mass spectrometer measurements of carbon, oxygen, nitrogen, and sulfur on Jupiter. *Icarus*, 171:153–170, September 2004. doi: 10.1016/j.icarus.2004.04.010.

T. S. Wood, P. Garaud, and S. Stellmach. A New Model for Mixing by Double-diffusive Convection (Semi-convection). II. The Transport of Heat and Composition through Layers. *Astrophys. J.* , 768:157, May 2013. doi: 10.1088/0004-637X/768/2/157.

John Woodward. *An essay toward a natural history of the earth: and terrestrial bodies, especially minerals: as also of the sea, rivers, and springs. With an account of the universal deluge: and of the effects that it had upon the earth.* London,Printed for R. Wilkin, 1695.

Jason T. Wright. *Radial Velocities as an Exoplanet Discovery Method*, pages 619–631. Springer International Publishing, Cham, 2018. ISBN 978-3-319-55333-7. doi: 10.1007/978-3-319-55333-7_4. URL https://doi.org/10.1007/978-3-319-55333-7_4.

Z. Wu, E. S. Sarachik, and D. S. Battisti. Vertical Structure of Convective Heating and the Three-Dimensional Structure of the Forced Circulation on an Equatorial Beta Plane*. *Journal of Atmospheric Sciences*, 57:2169–2187, July 2000. doi: 10.1175/1520-0469(2000)057<2169:VSOCHA>2.0.CO;2.

Z. Wu, E. S. Sarachik, and D. S. Battisti. Thermally Driven Tropical Circulations under Rayleigh Friction and Newtonian Cooling: Analytic Solutions*. *Journal of Atmospheric Sciences*, 58:724–741, April 2001. doi: 10.1175/1520-0469(2001)058<0724:TDTCUR>2.0.CO;2.

R. T. Zellem, N. K. Lewis, H. A. Knutson, et al. The 4.5 μm Full-orbit Phase Curve of the Hot Jupiter HD 209458b. *The Astrophysical Journal*, 790:53, July 2014. doi: 10.1088/0004-637X/790/1/53.

V. N. Zharkov and T. V. Gudkova. Models of giant planets with a variable ratio of ice to rock. *Annales Geophysicae*, 9:357–366, 1991.

V. N. Zharkov and V. P. Trubitsyn. *The physics of planetary interiors*. 1978.

Appendix A

Supplementary calculations in the CMS method

A.1 Simplifications for the angular part

Here, we show in details how we got rid of the angular part in eqn.(3.6). The integral we want to simplify is:

$$II = \int_0^1 \int_0^{a_J} \rho(r') r'^{2k+2} P_{2k}(\mu) dr' d\mu. \tag{A.1}$$

This integral can be approached differently: instead of just considering an integral over r' and μ, we can rather follow the surfaces of constant density. Then, $r'(\mu)$ is defined in order to have $\rho(r'(\mu)) = cst$ when μ varies from 0 to 1. Another way to say it is that we take the value of ρ for a given equatorial radius r_{eq}, and calculate the integral over constant ρ from equator to pole.

In order to go further, we will consider that the surfaces of constant potential are ellipsoids with the same ratio of polar to equatorial radius e. That gives, for every equipotential surface:

$$r'(\mu) = \frac{r_{eq}}{\sqrt{1+e^2\mu^2}}, \tag{A.2}$$

where r_{eq} is the equatorial radius of the spheroid. In reality, this is not exactly the case, the isobaric shperoids are not ellipsoids and the innermost ones are less flattened than the outermost ones, but it gives an idea of the integral over μ.

We just have to change variables: $\mu \to \mu$ and $r' \to \frac{r_{eq}}{\sqrt{1+e^2\mu^2}}$. With μ varying from 0 to 1 and r_{eq} from 0 to a_J, we have not changed the domain of integration because outside of the outermost ellipsoid - in our ellipsoidal approximation - we had $\rho(a_J, \mu > 0) = 0$. The Jacobian is $\frac{1}{\sqrt{1+e^2\mu^2}}$ and we obtain:

$$II = \int_0^{a_J} \rho(r_{eq}) r_{eq}^{2k+2} \int_0^1 \frac{P_{2k}(\mu)}{\left(\sqrt{1+e^2\mu^2}\right)^{2k+3}} d\mu \, dr_{eq}. \tag{A.3}$$

From eqn.(3.7), we see that the density only depends on l/l_0, the mean radius of one isobaric layer above the external mean radius. With eqn.(A.2), we can then write $l = \beta \times r_{eq}$ with the same β for all r_{eq}. The β will cancel in the fraction, and we can simply change l/l_0 by r_{eq}/a_J.

We just have to calculate the other part of the integral, with the analytical expression of eqn.(A.2):

$$< P_{2k} >= \int_0^1 \left(\frac{1}{1+e^2\mu^2} \right)^{\frac{2k+3}{2}} P_{2k}(\mu) d\mu. \tag{A.4}$$

Since there is no simple way to do it, we keep it in our equations, but the interesting aspect is that it no longer depends on r': we have reduced our equation to a simple integral.
We can check whether this is correct or not. So far, we have supposed that the equipotential surfaces are ellipsoids and that they have the same e value. Considering that we integrate along these surfaces by varying the equatorial radius from the center to a_J, we showed that we can write:

$$\begin{aligned} J_{2k} \sim -\frac{4\pi}{M a_J^{2k}} & \left(\int_0^1 \left(\frac{1}{1+e^2\mu^2} \right)^{\frac{2k+3}{2}} P_{2k}(\mu) d\mu \right) \\ & \times \int_0^{a_J} \rho(r_{eq}) r_{eq}^{2k+2} dr_{eq}. \end{aligned} \tag{A.5}$$

It is easy to calculate these integrals as we know their analytical expression. We just need to choose the correct e and m values. From the observed equatorial and polar radii of Jupiter (see table 3.1), we get:

$$e = \sqrt{71492^2/66854^2 - 1} \approx 0.378897 \tag{A.6}$$

These radii also give us the value for the mean density: $\bar{\rho} = \dfrac{M_J}{\frac{4}{3}\pi a_J^2 (a_J)_{polaire}} \approx 1326.5$ kg m^{-3}, which allows us to calculate

$$m = \frac{3\omega^2}{4\pi G\bar{\rho}} \approx 0.083408 \tag{A.7}$$

Implemented in eqn.(A.5) with the expression of density from eqn.(3.7), a numerical integration gives:

$$\begin{aligned} J_2 &= -1.6348804 \cdot 10^{-2} \text{ with } J_2^{theory} = -1.3988511 \cdot 10^{-2} \\ J_4 &= 6.4398288 \cdot 10^{-4} \text{ with } J_4^{theory} = 5.3182810 \cdot 10^{-4} \\ J_6 &= -3.5163544 \cdot 10^{-5} \text{ with } J_6^{theory} = -3.0118323 \cdot 10^{-5} \end{aligned} \tag{A.8}$$

There is about 20% difference with the theoretical results, which is expected as we have chosen the outermost e value, which is the largest.
With $e = 0.36$, we obtain less than 10% difference on these moments. Considering further approximations that will be made in the next appendices, a 0.9 factor is acceptable to compare the theory with the numerical results and we will retain this $e = 0.36$ value in our calculations.

A.2 Supplementary calculations for the general case

Going back to eqn.(3.6), eqn.(3.7) and eqn.(A.4) we have:

$$|\Delta J_{2k}| \sim \left| \frac{4\pi}{M a_J^{2k}} \sum_{i=0}^{N-1} < P_{2k} > \int_{r_{i+1}}^{r_i} \bar{A} \left[\frac{sin(\alpha \frac{r'}{a_J})}{\frac{r'}{a_J}} - \frac{sin(\alpha \frac{R_i}{a_J})}{\frac{R_i}{a_J}} \right] r'^{2k+2} dr' \right|, \tag{A.9}$$

$$\text{with } R_i = \frac{r_{i+1} + r_i}{2}, \tag{A.10}$$

$$\text{and } \bar{A} = \bar{\rho} A. \tag{A.11}$$

If the number of layers is large, which is the case, we can approximate $|R_i - r'| \ll R_i$ everywhere. This approximation is less valid in the ~ 10 deepest layers, but their impact on the gravitational moments is negligible (Figure 3.2). With:

$$\gamma = \frac{\alpha}{a_J}, \tag{A.12}$$

Let us develop the sinus to order 2:

$$\frac{\sin\left(\gamma r'\right)}{r'} = \frac{\sin\left(\gamma R_i \left(1 + \dfrac{r' - R_i}{R_i}\right)\right)}{R_i \left(1 + \dfrac{r' - R_i}{R_i}\right)}$$

$$\frac{\sin\left(\gamma r'\right)}{r'} \simeq \frac{1}{R_i}\left(1 - \frac{\xi}{R_i} + \left(\frac{\xi}{R_i}\right)^2\right)\left(\sin(\gamma R_i)\cos(\gamma\xi) + \cos(\gamma R_i)\sin(\gamma\xi)\right),$$

$$\text{where } \xi = r' - R_i \ll R_i.$$

We know that $\alpha \sim \pi$. In the internal layers, $a_J \gg R_i$, so $\gamma\xi = \dfrac{\alpha}{a_J}\xi \ll \dfrac{\xi}{R_i}$. On the outside, $a_J \sim R_i$ so $\gamma\xi \sim \dfrac{\xi}{R_i}$. As mentioned above, $\dfrac{\xi}{R_i} \ll 1$, which means that everywhere $\gamma\xi \ll 1$. Therefore:

$$\frac{\sin\left(\gamma r'\right)}{r'} \simeq \frac{1}{R_i}\left(1 - \frac{\xi}{R_i} + \left(\frac{\xi}{R_i}\right)^2\right)\left(\sin(\gamma R_i)\left(1 - \frac{(\gamma\xi)^2}{2}\right) + \cos(\gamma R_i)\left(\gamma\xi\right)\right),$$

$$\frac{\sin\left(\gamma r'\right)}{r'} \simeq \frac{\sin(\gamma R_i)}{R_i} + \xi\left(\frac{\gamma}{R_i}\cos(\gamma R_i) - \frac{1}{R_i^2}\sin(\gamma R_i)\right) + \xi^2\left(-\frac{\gamma^2}{2R_i}\sin(\gamma R_i) - \frac{\gamma}{R_i^2}\cos(\gamma R_i) + \frac{1}{R_i^3}\sin(\gamma R_i)\right) \tag{A.13}$$

The zeroth order term is obviously going to be cancelled in eqn.(A.9) so:

$$|\Delta J_{2k}| \sim \left| \frac{4\pi}{M a_J^{2k}} \sum_{i=0}^{N-1} < P_{2k} > \frac{\bar{A} a_J}{R_i} \times \int_{r_{i+1}}^{r_i} \left[(r' - R_i)\left(\gamma\cos(\gamma R_i) - \frac{1}{R_i}\sin(\gamma R_i)\right) + \right.\right.$$
$$\left.\left. (r' - R_i)^2 \left(-\frac{\gamma^2}{2}\sin(\gamma R_i) - \frac{\gamma}{R_i}\cos(\gamma R_i) + \frac{1}{R_i^2}\sin(\gamma R_i)\right)\right] r'^{2k+2} dr' \right|. \tag{A.14}$$

Let us write

$$C_1 = \left(\gamma\cos(\gamma R_i) - \frac{1}{R_i}\sin(\gamma R_i)\right)$$
$$C_2 = \left(-\frac{\gamma^2}{2}\sin(\gamma R_i) - \frac{\gamma}{R_i}\cos(\gamma R_i) + \frac{1}{R_i^2}\sin(\gamma R_i)\right). \tag{A.15}$$

This gives a simplified expression for the potential:

$$|\Delta J_{2k}| \sim \left| \frac{4\pi}{Ma_J^{2k}} \sum_{i=0}^{N-1} < P_{2k} > \frac{\bar{A}a_J}{R_i} \int_{r_{i+1}}^{r_i} \left(C_1(r'-R_i) + C_2(r'-R_i)^2 \right) r'^{2k+2} dr' \right| \tag{A.16}$$

Developping the power of r' yields:

$$\begin{aligned} r'^{2k+2} &= R_i^{2k+2} \left(1 + \frac{r'-R_i}{R_i} \right)^{2k+2}, \\ r'^{2k+2} &\simeq R_i^{2k+2} \left(1 + (2k+2)\frac{r'-R_i}{R_i} \right). \end{aligned} \tag{A.17}$$

Then, the integral I is given by:

$$I \simeq R_i^{2k+2} \int_{r_{i+1}}^{r_i} \left[C_1(r'-R_i) + \left(C_2 + (2k+2)\frac{C_1}{R_i} \right) (r'-R_i)^2 \right] dr'. \tag{A.18}$$

If we change the variable of integration $r' \rightarrow (r'-R_i)$, and using eqn.(A.10):

$$I \simeq R_i^{2k+2} \int_{\frac{r_{i+1}-r_i}{2}}^{\frac{r_i-r_{i+1}}{2}} \left[C_1 r' + \left(C_2 + (2k+2)\frac{C_1}{R_i} \right) r'^2 \right] dr'. \tag{A.19}$$

As a first calculation, we can choose a constant Δr with depth, as suggested in H13, $\Delta r = \frac{a_J}{N}$. If we want another repartition of spheroids, we will just have to change a Δr by Δr_i depending on depth:

$$I \simeq R_i^{2k+2} \int_{-\frac{\Delta r}{2}}^{\frac{\Delta r}{2}} \left[C_1 r' + \left(C_2 + (2k+2)\frac{C_1}{R_i} \right) r'^2 \right] dr'. \tag{A.20}$$

This is easily calculated and we get:

$$I \simeq R_i^{2k+2} \left(C_2 + (2k+2)\frac{C_1}{R_i} \right) \frac{\Delta r^3}{12}. \tag{A.21}$$

Puting this expression into eqn.(A.14), we obtain an intermediate formula:

$$|\Delta J_{2k}| \sim \left| \frac{4\pi}{Ma_J^{2k}} \sum_{i=0}^{N-1} < P_{2k} > \bar{A}a_J R_i^{2k+1} \left(C_2 + (2k+2)\frac{C_1}{R_i} \right) \frac{\Delta r^3}{12} \right|. \tag{A.22}$$

Let us consider two cases: in the internal layers, where $a_J \gg R_i$:

$$C_1 \sim \gamma - \frac{\gamma^3 R_i^2}{2} - \gamma + \frac{\gamma^3 R_i^2}{6} = -\frac{\alpha^3}{3}\frac{R_i^2}{a_j^3}, \tag{A.23}$$

$$C_2 \sim -\frac{\gamma^3 R_i}{2} - \frac{\gamma}{R_i} + \frac{\gamma^3 R_i}{2} + \frac{\gamma}{R_i} - \frac{\gamma^3 R_i}{6} = -\frac{\alpha^3}{6}\frac{R_i}{a_j^3}. \tag{A.24}$$

In the external layers, $a_J \approx R_i$, there is no obvious approximation. We assume that C_1 and C_2 are of the same order of magnitude as the coefficient in front of the sinusoidal functions and, remembering that $\frac{R_i}{a_J} \sim 1$:

$$C_1 \sim \gamma \sim \frac{1}{R_i} = \left(\frac{R_i}{a_j} \right)^2 \frac{1}{a_J} = \frac{R_i^2}{a_j^3}, \tag{A.25}$$

$$C_2 \sim \gamma^2 \sim \frac{1}{R_i^2} = \frac{R_i}{a_J}\frac{1}{a_J^2} = \frac{R_i}{a_j^3}. \tag{A.26}$$

If we neglect the factor $\frac{\alpha^3}{3}$ (which varies with height):

$$\begin{aligned} C_1 &\sim \frac{R_i^2}{a_j^3} \\ C_2 &\sim \frac{R_i}{a_j^3}, \end{aligned} \tag{A.27}$$

which yields the aproximated relation:

$$C_2 + (2k+2)\frac{C_1}{R_i} \sim (2k+3)\frac{R_i}{a_J^3}. \tag{A.28}$$

In Figure A.1, we plot the exact and approximated values of $C2 + (2k+2)C1$ for $k = 1$. As expected, in the interior we recover the factor 10 shift $(\alpha^3/3)$ between the real and estimated value, whereas in the externalmost layers this term is smaller so we underestimate the error by a factor $\sim 2-5$. Everything is thus consistent with our assumptions.

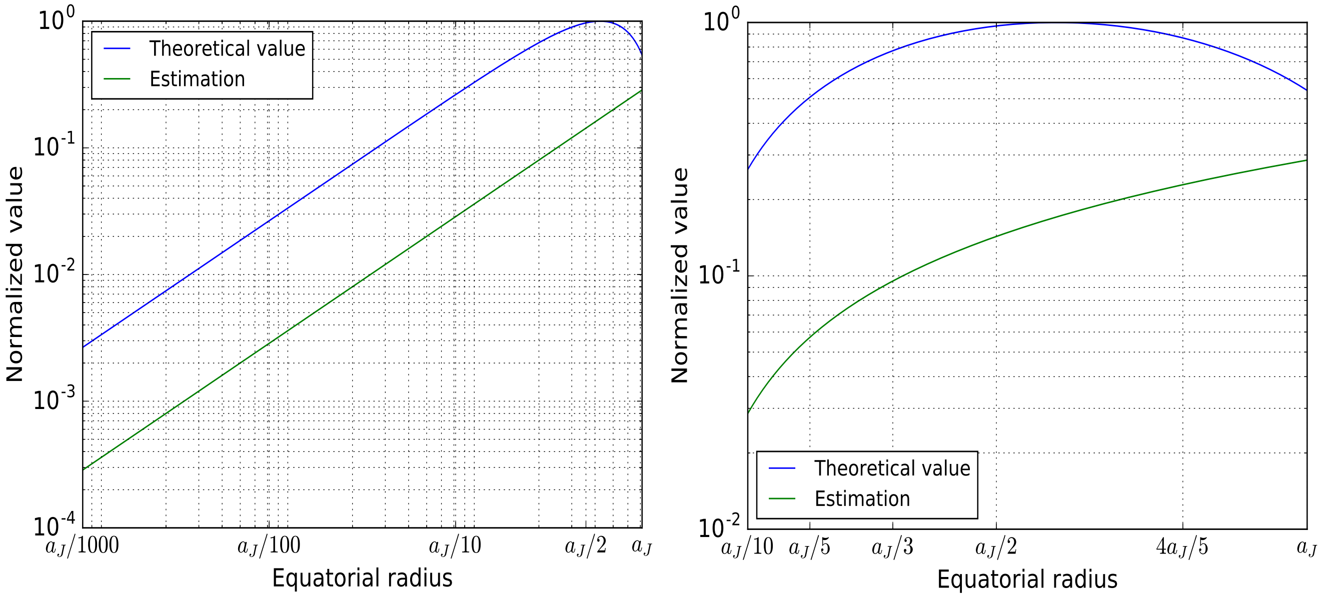

Figure A.1: Normalized value of $C2 + 4C1/R_i$ and of its approximation $5R_i/a_J^3$ (eqn.(A.28)) as a function of altitude R_i. (a) From center to exterior; (b) zoom on the external layers

With these assumptions, we can now write (redefining $< P_{2k} >$ as its absolute value):

$$|\Delta J_{2k}| \sim 4\pi(2k+3)\frac{\Delta r^3}{12}\frac{\bar{A} < P_{2k} >}{M}\sum_{i=0}^{N-1}\left(\frac{R_i}{a_J}\right)^{2k+2} \tag{A.29}$$

It is important to note that up to now, if Δr was not constant we would still have the same result by using Δr_i instead of Δr in the sum. This is done in appendix A.3.3

In the case of a linear spacing of the spheroids, $\Delta r = \frac{a_J}{N}$, we can go further:

$$\frac{\Delta r^3 \bar{A}}{M} = \frac{a_J^3}{N^3}\frac{A\bar{\rho}}{M} = \left(\frac{a_J^3\bar{\rho}}{M}\right)\frac{A}{N^3} = \frac{3}{4\pi}\frac{A}{N^3} \sim \frac{1}{4N^3}, \tag{A.30}$$

because, from eqn.(A.10), $A \sim \frac{\pi}{3}$ if $m \ll 1$, which is valid for Jupiter (and for the vast majority of celestial bodies). As $r_{i+1} = r_i - \Delta r$ and $r_0 = a_J$, $r_i = a_J - i \times \Delta_r$, we get:

$$R_i = \frac{r_i + r_{i+1}}{2} = a_J - \left(i + \frac{1}{2}\right)\Delta r = a_J\left(1 - \frac{\left(i + \frac{1}{2}\right)}{N}\right). \tag{A.31}$$

Combining eqn.(A.29), eqn.(A.30) and eqn.(A.31) gives the final result, as written in eqn.(3.9):

$$|\Delta J_{2k}| \sim (2k+3)\frac{\pi}{12}\frac{< P_{2k} >}{N^3}\sum_{i=0}^{N-1}\left(1 - \frac{\left(i + \frac{1}{2}\right)}{N}\right)^{2k+2} \tag{A.32}$$

A.3 Supplementary calculations for J2

The formula for J_2 is directly derived from eqn.(3.9):

$$|\Delta J_2| \sim \frac{5\pi}{12}\frac{< P_2 >}{N^3}\sum_{i=0}^{N-1}\left(1 - \frac{\left(i + \frac{1}{2}\right)}{N}\right)^4. \tag{A.33}$$

A.3.1 Linear spacing

First, we want to calculate $\langle P_2 \rangle$ from eqn.(A.4). A simple numerical integration yields (in absolute value):

$$< P_2 > \approx 0.035982 \tag{A.34}$$

We could expand the sum in eqn.(A.33) with the binomial theorem, but it is easy to show that the first order will be equivalent to neglecting the factor 1/2 in the term $(i + 1/2)$. So we have directly:

$$P = \left(1 - \frac{\left(i + \frac{1}{2}\right)}{N}\right)^4 \sim 1 - \frac{4}{N}i + \frac{6}{N^2}i^2 - \frac{4}{N^3}i^3 + \frac{i^4}{N^4}. \tag{A.35}$$

As eqn.(A.35) corresponds to the 1st order expansion in i in eqn.(A.33), we need to make sure that these terms do not cancel in the sum for this approximation to be correct. This sum is

$$\sum_{i=0}^{N-1} P \approx N - \frac{N(N-1)}{2}\frac{4}{N} + \frac{(N-1)N(2N-1)}{6}\frac{6}{N^2} - \frac{(N-1)^2N^2}{4}\frac{4}{N^3} + \frac{(N-1)(N)(2N-1)(3(N-1)^2 + 3(N-1) - 1)}{30N^4}$$

$$\sum_{i=0}^{N-1} P \approx N - 2N + 2N - N + \frac{N}{5},$$

$$\text{so} \quad \sum_{i=0}^{N-1} \left(1 - \frac{\left(i + \frac{1}{2}\right)}{N} \right)^4 \sim \frac{N}{5}. \tag{A.36}$$

If we wanted to keep every term up to this stage, we would find that the second order term is $1/2 \ll N/5$. Our approximations were thus justified. Finally, eqn.(A.33), eqn.(A.34) and eqn.(A.36) yield:

$$|\Delta J_2| \sim \frac{\pi}{12} \frac{< P_2 >}{N^2} \approx \frac{9.42 \times 10^{-3}}{N^2}. \tag{A.37}$$

A.3.2 Hubbard and Militzer spacing

In HM16, the spacing is not exactly linear. The planet is separated in two domains: first, from the outside boundary to $r_i = 0.5\, a_J$, they use 341 spheroids, and 171 inside this limit. Then, outside $\Delta r^{ext} = 3\Delta r/4$ and inside $\Delta r^{in} = 3\Delta r/2$. Moreover, the first spheroid is a bit particular as it has a a zero density over half its size. We will not consider it here: since it is just one spheroid, the impact on the analytical derivation of the error is small.

Using eqn.(A.29), we can write it with a general number N as:

$$|\Delta J_{2k}| \sim \frac{4\pi(2k+3)}{12} \frac{\bar{A} < P_{2k} >}{M} \left[\sum_{i=0}^{\frac{2N}{3}} \left(\frac{3\Delta r}{4}\right)^3 \left(\frac{R_i^{ext}}{a_J}\right)^{2k+2} + \sum_{i=\frac{2N}{3}+1}^{N-1} \left(\frac{3\Delta r}{2}\right)^3 \left(\frac{R_i^{int}}{a_J}\right)^{2k+2} \right] \tag{A.38}$$

$$R_i^{ext} = a_J \left(1 - \frac{3}{4N} \left(i + \frac{1}{2} \right) \right), \tag{A.39}$$

$$R_i^{int} = a_J \left(0.5 - \frac{3}{2N} \left((i - \frac{2N}{3}) + \frac{1}{2} \right) \right) \tag{A.40}$$

Which can be rewritten:

$$|\Delta J_{2k}| \sim \frac{4\pi(2k+3)}{12} \frac{\bar{A} < P_{2k} >}{M} \frac{27\Delta r^3}{8} \left[\frac{1}{8} \sum_{i=0}^{\frac{2N}{3}} \left(\frac{R_i^{ext}}{a_J}\right)^{2k+2} + \sum_{i=0}^{\frac{N}{3}} \left(\frac{R_{i-\frac{2N}{3}}^{int}}{a_J}\right)^{2k+2} \right]. \tag{A.41}$$

For $k = 1$, using eqn.(A.30) and eqn.(A.36), we have:

$$|\Delta J_2| \sim \frac{5 \times 27 \times \pi < P_2 >}{12 \times 8 \times N^3} \left[\frac{1}{8} \left(\frac{4}{3} \frac{2 \times N}{3} \right) \frac{1}{5} + \frac{1}{2^4} \left(\frac{1}{3} \frac{N}{3} \right) \frac{1}{5} \right]$$

$$|\Delta J_2| \sim \frac{9}{256} \frac{\pi < P_2 >}{N^2}. \tag{A.42}$$

Compared to eqn.(3.11), this is approximately twice better in terms of errors.

A.3.3 Cubic spacing

In this appendix, we calculate the error for a cubic repartition of the spheroids, i.e. Δr depends on i as $r_i = a_J - \frac{i^3}{N^3} a_J$.

Using eqn.(A.29), we get:

$$\Delta r_i = ((i+1)^3 - i^3)\frac{a_J}{N^3} = \frac{\Delta(i^3)}{N^2}\Delta r, \tag{A.43}$$

$$R_i = a_J\left(1 - \frac{i^3 + (i+1)^3}{2N^3}\right). \tag{A.44}$$

Straightforwardly, we get the new eqn.(3.9):

$$|\Delta J^c_{2k}| \simeq (2k+3)\frac{\pi}{12}\frac{<|P_{2k}|>}{N^5} \times \sum_{i=0}^{N-1}\Delta(i^3)\left(1 - \frac{i^3+(i+1)^3}{2N^3}\right)^{2k+2}, \tag{A.45}$$

which gives for J_2:

$$|\Delta J^c_2| \simeq \frac{5\pi <P_2>}{12N^5}\sum_{i=0}^{N-1}\Delta(i^3)\left(1 - \frac{i^3+(i+1)^3}{2N^3}\right)^4. \tag{A.46}$$

We develop again the various terms:

$$\Delta(i^3) = 3i^2 + 3i + 1 \sim 3i^2, \tag{A.47}$$

$$P^c = \left(1 - \frac{i^3+(i+1)^3}{2N^3}\right)^4,$$

$$P^c = \left(1 - \frac{1}{N^3}i^3 - \frac{3}{2N^3}i^2 - \frac{3}{2N^3}i - \frac{1}{2N^3}\right)^4 \simeq \left(1 - \frac{i^3}{N^3}\right)^4,$$

$$P^c \simeq 1 - 4\frac{i^3}{N^3} + 6\frac{i^6}{N^6} - 4\frac{i^9}{N^9} + \frac{i^{12}}{N^{12}}, \tag{A.48}$$

$$\Delta(i^3)P^c \simeq 3\left(i^2 - 4\frac{i^5}{N^3} + 6\frac{i^8}{N^6} - 4\frac{i^{11}}{N^9} + \frac{i^{14}}{N^{12}}\right). \tag{A.49}$$

In order to calculate the sum, we need the leading term of $\sum_{i=0}^{N-1} i^k$. With:

$$(a+1)^k - a^k = \sum_{i=0}^{k-1}\binom{k}{i}a^i, \tag{A.50}$$

$$\sum_{a=1}^{N-1}\left((a+1)^k - a^k\right) = \sum_{i=0}^{k-1}\binom{k}{i}\sum_{a=1}^{N-1}a^i, \tag{A.51}$$

but the terms in the sum will cancel two by two:

$$\sum_{a=1}^{N-1}\left((a+1)^k - a^k\right) = N^k - 1, \tag{A.52}$$

$$\text{so:}\quad N^k - 1 = \sum_{i=0}^{k-1}\binom{k}{i}\sum_{a=1}^{N-1}a^i. \tag{A.53}$$

With this formula, it is easy to show by recurrence that $\sum_{a=1}^{N-1} a^i = O(N^{i+1})$. Therefore, in the equation above only the $k-1$ term can lead to N^k. Then the result:

$$\sum_{a=1}^{N-1}a^{k-1} \sim \frac{N^k}{\binom{k}{k-1}} = \frac{N^k}{k}. \tag{A.54}$$

Now, we can get the leading order terms of the sum of eqn.(A.49):

$$\sum_{i=0}^{N-1} \Delta(i^3)P^c \sim 3\left(\frac{N^3}{3} - \frac{4N^3}{6} + \frac{6N^3}{9} - \frac{4N^3}{12} + \frac{N^3}{15}\right) = \frac{N^3}{5} \tag{A.55}$$

The result is thus the same as in the linear case:

$$|\Delta J_2^c| \sim \frac{\pi}{12}\frac{< P_2 >}{N^2}. \tag{A.56}$$

A.3.4 Exponential spacing

For an exponential repartition of the spheroids, we have:

$$\lambda_{i+1} = \lambda_i - \beta e^{i\alpha}. \tag{A.57}$$

Then, considering the difference $\lambda_{i+1} - \lambda_i$ as a geometric sequence, we have:

$$\lambda_i = 1 - \beta\frac{e^{i\alpha} - 1}{e^{\alpha} - 1}. \tag{A.58}$$

Now, with the condition that the first layer (normalized to the radius of Jupiter) is 1 and the last one is 0:

$$\lambda_i = 1 - \frac{e^{i\alpha} - 1}{e^{N\alpha} - 1}. \tag{A.59}$$

To determine the error we need:

$$R_i = 1 + \frac{1}{e^{N\alpha} - 1} - \frac{e^{i\alpha}}{2(e^{N\alpha} - 1)} - \frac{e^{(i+1)\alpha}}{2(e^{N\alpha} - 1)} = \frac{e^{N\alpha}}{e^{N\alpha} - 1} - e^{i\alpha}\frac{1 + e^{\alpha}}{2(e^{N\alpha} - 1)}, \tag{A.60}$$

$$\Delta r = \frac{e^{(i+1)\alpha} - e^{i\alpha}}{e^{N\alpha} - 1} = e^{i\alpha}\frac{e^{\alpha} - 1}{e^{N\alpha} - 1} = \beta e^{i\alpha}. \tag{A.61}$$

If we want the increment to be reasonable, we do not want $e^{N\alpha} - 1$ to be too large. We choose

$$\alpha = \frac{\gamma}{N}, \tag{A.62}$$

where we vary γ between 5 and 10, depending on how sharp we want the exponential function to be (see Figure 3.3).

Then, using eqn.(A.29), we have to calculate, for J_2:

$$\sum_{i=0}^{N-1} (\Delta r_i)^3 R_i^4 = \beta^3 \sum_{i=0}^{N-1} e^{3i\alpha}\left(\frac{e^{N\alpha}}{e^{N\alpha} - 1} - e^{i\alpha}\frac{1 + e^{\alpha}}{2(e^{N\alpha} - 1)}\right)^4,$$

$$\sum_{i=0}^{N-1} (\Delta r_i)^3 R_i^4 = \beta^3 \sum_{i=0}^{N-1} e^{3i\alpha}(\delta - \epsilon e^{i\alpha})^4, \tag{A.63}$$

$$\beta = \frac{e^{\alpha} - 1}{e^{N\alpha} - 1}\ ,\ \delta = \frac{e^{N\alpha}}{e^{N\alpha} - 1}\ ,\ \epsilon = \frac{1 + e^{\alpha}}{2(e^{N\alpha} - 1)}. \tag{A.64}$$

Then, developing the power of 4 brackets and using the well known result for the sum of the terms of a geometric sequence:

$$\sum_{i=0}^{N-1}(\Delta r_i)^3 R_i^4 = \beta^3\delta^4\left(\frac{e^{3N\alpha}-1}{e^{3\alpha}-1} - 4\frac{\epsilon}{\delta}\frac{e^{4N\alpha}-1}{e^{4\alpha}-1} + 6\left(\frac{\epsilon}{\delta}\right)^2\frac{e^{5N\alpha}-1}{e^{5\alpha}-1} - 4\left(\frac{\epsilon}{\delta}\right)^3\frac{e^{6N\alpha}-1}{e^{6\alpha}-1} + \left(\frac{\epsilon}{\delta}\right)^4\frac{e^{7N\alpha}-1}{e^{7\alpha}-1}\right) \tag{A.65}$$

Now, we will consider that $7\alpha \ll 1$, $e^{N\alpha} \gg 1$, which is a reasonable approximation in the range $\gamma = 5 - 10$ and $N > 512$. Then:

$$\beta \sim \frac{\alpha}{e^{N\alpha}}\ ,\ \delta \sim 1\ ,\ \epsilon \sim \frac{1}{e^{N\alpha}}\ ,\ \frac{e^{3N\alpha}-1}{e^{3\alpha}-1} \sim \frac{e^{3N\alpha}}{3\alpha}, \tag{A.66}$$

$$\sum_{i=0}^{N-1}(\Delta r_i)^3 R_i^4 \sim \left(\frac{\alpha}{e^{N\alpha}}\right)^3\left(\frac{e^{3N\alpha}}{3\alpha} - 4\frac{e^{3N\alpha}}{4\alpha} + 6\frac{e^{3N\alpha}}{5\alpha} - 4\frac{e^{3N\alpha}}{6\alpha} + \frac{e^{3N\alpha}}{7\alpha}\right),$$

$$\sum_{i=0}^{N-1}(\Delta r_i)^3 R_i^4 \sim -\frac{\alpha^2}{105} = -\frac{\gamma^2}{105\, N^2}. \tag{A.67}$$

We checked numerically that our approximations yield an error allways smaller than ≈ 10%.

Implementing these results into eqn.(A.29) yields:

$$|\Delta J_2^{exp}| \sim \frac{\pi < P_2 >}{252} * \frac{\gamma^2}{N^2} \approx 0.000449\left(\frac{\gamma}{N}\right)^2, \tag{A.68}$$

with $\gamma \in [5 - 10]$.

A.4 Neglecting the high atmsophere

The neglected potential on a point (μ, r_j) of the jth spheroid reads:

$$\phi_{neg} = 4\pi G\sum_{k=0}^{\infty}(r_j)^{2k}P_{2k}(\mu)\int_{a_{1bar}}^{a_{ext}}\int_0^1 \frac{\rho(\vec{r'})}{r'^{2k-1}}P_{2k}(\mu')d\mu' dr'. \tag{A.69}$$

With $\rho = \rho_{ext} = cst$ and Appendix A.1:

$$I = \int_{a_{1bar}}^{a_{ext}}\int_0^1 \rho(\vec{r'})\frac{1}{r'^{2k-1}}P_{2k}(\mu')d\mu' dr' \simeq \rho_{ext}\int_{a_{1bar}}^{a_{ext}}\frac{1}{r'^{2k-1}}dr'\int_0^1 P_{2k}(\mu')(1+e^2\mu'^2)^{k-1}d\mu'. \tag{A.70}$$

For any $k > 0$ we integrate a Legendre polynomial of degree $2k$ with a polynomial of order $2(k-1)$. By orthgononality of the Legendre base, only the $k = 0$ term is non zero. Thus

$$\phi_{neg} \simeq 4\pi G\rho_{ext}\left[\frac{1}{2}(a_{ext}^2 - a_{1bar}^2)\frac{\arctan(e)}{e}\right]. \tag{A.71}$$

With $a_{ext} = a_{1bar} + \Delta a$:

$$(a_{ext}^2 - a_{1bar}^2) \simeq 2a_{1bar}\Delta a, \text{ and so} \tag{A.72}$$

$$\phi_{neg} \simeq 4\pi G \rho_{ext} a_{1bar} \Delta a \frac{\arctan(e)}{e}. \tag{A.73}$$

Using the exterior $e \simeq 0.38$ and defining $\bar{\rho_S}$ as the density of Jupiter if it was a sphere of radius a_{1bar}, the neglected potential simply reads:

$$\phi_{neg} \simeq 2.87 \frac{GM}{a_{1bar}} \left(\frac{\rho_{ext}}{\bar{\rho_S}}\right) \left(\frac{\Delta a}{a_{1bar}}\right) \tag{A.74}$$

This expression does not depend on r_j nor on μ: the first order error is a constant neglected potential on each spheroid.This means that the hydrostatic condition will not be perturbed by the neglected high atmosphere, because it is only sensitive to the gradient of the potential. As the 1 bar pressure is set at the observed radius, we do not expect a change in the pressure-density profile of the planet from the direct effect of this neglected potential.

On the other hand, this neglected potential will affect the calculation of the shapes of the spheroids. If we call $\Delta U = \phi_{neg} \times \dfrac{a_{1bar}}{GM}$ and U_j the dimensionless potential of the jth spheroid, we can derive the first order perturbation of equation (51) of H13:

$$\begin{aligned}
-\frac{1}{\zeta_j(\mu)} \left(\sum_{i=j}^{N-1} \sum_{k=0}^{\infty} \tilde{J}_{i,2k} \left(\frac{\lambda_i}{\lambda_j}\right)^{2k} \zeta_j(\mu)^{-2k} P_{2k}(\mu) + \sum_{i=0}^{j-1} \sum_{k=0}^{\infty} \tilde{J}'_{i,2k} \left(\frac{\lambda_j}{\lambda_i}\right)^{2k+1} \zeta_j(\mu)^{2k+1} P_{2k}(\mu) + \sum_{i=0}^{j-1} \tilde{J}''_{i,0} \lambda_j^3 \zeta_j(\mu)^3 \right) \\
+ \frac{1}{2} \lambda_j^3 \zeta_j(\mu)^2 (1-\mu^2) = U_j + \Delta U.
\end{aligned} \tag{A.75}$$

For simplicity, we set $x = \bar{\zeta}_j(\mu)$ the solution without the neglected potential and Δx the variation to this solution. Both x and Δx depend on μ. It is then straightforward to write eqn.(A.75) at the first order:

$$\begin{aligned}
-\frac{1}{x} \Bigg(- \sum_{i=j}^{N-1} \sum_{k=0}^{\infty} \tilde{J}_{i,2k} \left(\frac{\lambda_i}{\lambda_j}\right)^{2k} x^{-2k} \left(2k \frac{\Delta x}{x}\right) P_{2k}(\mu) + \sum_{i=0}^{j-1} \sum_{k=0}^{\infty} \tilde{J}'_{i,2k} \left(\frac{\lambda_j}{\lambda_i}\right)^{2k+1} x^{2k+1} \left((2k+1) \frac{\Delta x}{x}\right) P_{2k}(\mu) \\
+ \sum_{i=0}^{j-1} \tilde{J}''_{i,0} \lambda_j^3 x^3 \left(3 \frac{\Delta x}{x}\right) \Bigg) \\
+ \frac{1}{x} \frac{\Delta x}{x} \left(\sum_{i=j}^{N-1} \sum_{k=0}^{\infty} \tilde{J}_{i,2k} \left(\frac{\lambda_i}{\lambda_j}\right)^{2k} x^{-2k} P_{2k}(\mu) + \sum_{i=0}^{j-1} \sum_{k=0}^{\infty} \tilde{J}'_{i,2k} \left(\frac{\lambda_j}{\lambda_i}\right)^{2k+1} x^{2k+1} P_{2k}(\mu) + \sum_{i=0}^{j-1} \tilde{J}''_{i,0} \lambda_j^3 x^3 \right) \\
+ \lambda_j^3 x^2 \left(\frac{\Delta x}{x}\right) (1-\mu^2) = \Delta U.
\end{aligned} \tag{A.76}$$

The second bracket can be simplified by the fact that x satisifies equation (51) of H13:

$$\begin{aligned}
-\frac{\Delta x}{x} \left(- \sum_{i=j}^{N-1} \sum_{k=0}^{\infty} 2k \tilde{J}_{i,2k} \left(\frac{\lambda_i}{\lambda_j}\right)^{2k} x^{-2k-1} P_{2k}(\mu) + \sum_{i=0}^{j-1} \sum_{k=0}^{\infty} (2k+1) \tilde{J}'_{i,2k} \left(\frac{\lambda_j}{\lambda_i}\right)^{2k+1} x^{2k} P_{2k}(\mu) + \sum_{i=0}^{j-1} 3 \tilde{J}''_{i,0} \lambda_j^3 x^2 \right) \\
- \frac{\Delta x}{x} \left(U_j - \frac{1}{2} \lambda_j^3 x^2 (1-\mu^2) \right) + \left(\frac{\Delta x}{x}\right) \lambda_j^3 x^2 (1-\mu^2) = \Delta U.
\end{aligned} \tag{A.77}$$

Now, let us restrict ourselves to the outermost spheroid $j = 0$, $\lambda_j = 1$. Only the first sum will remain, and we recognise eqn.(3.2):

$$\frac{\Delta x}{x} \left(\sum_{k=0}^{\infty} 2k J_{2k}^{ext} x^{-2k-1} P_{2k}(\mu) - U_j + \frac{3}{2} x^2 (1-\mu^2) \right) = \Delta U. \tag{A.78}$$

With Juno data, we know the first few J_{2k}^{ext} and the contribution of each J_{2k} to the sum is strongly decreasing with k so we can use only the first 4 even gravitational moments. From here, we approximate x given by the CMS program as a polynomial of order 15 (which gives errors of a few 10^{-14}), but allows us to obtain as many evaluations of Δx as we want.

We noticed that around $\mu \sim 0.5$ the bracketed term tends to 0 so Δx should not be defined. That means that at this point some neglected effect should be taken into account. However, with the polynomial approximation for x, we can use Riemann sum to evaluate the change on equation (40) of H13:

$$\tilde{J}_{i,2k} = -\frac{3}{2k+3} \frac{\delta\rho_i \lambda_i^3 \int_0^1 P_{2k}(\mu)\zeta_i(\mu)^{2k+3} d\mu}{\sum_{j=0}^{N-1} \delta\rho_j \lambda_j^3 \int_0^1 \zeta_j(\mu)^3 d\mu}. \tag{A.79}$$

We find that the undefined region for Δx has a negligible influence on the integral because it is almost ponctual. We also find that the change in the denominator which is, as expected, of the order of the neglected mass, is 10× smaller than the change in the numerator. Therefore, the change in the numerator dominates the uncertainties on J_2. By comparing for different number of points in the Riemann sum, we obtain:

$$\frac{\Delta J_{2,0}}{J_{2,0}} \simeq 100 \times \Delta U \simeq 287 \times \left(\frac{\rho_{ext}}{\bar{\rho_S}}\right)\left(\frac{\Delta a}{a_{1bar}}\right). \tag{A.80}$$

This result has a variation of about a factor 2 (due to the bad handling of the divergence zone) and this evaluation is rather a lower bound for $\Delta J_{2,0}$.

Appendix B

ECLIPS3D

B.1 Equations in ECLIPS3D

B.1.1 3D, general case

In this appendix we detail the derivation of the full linearised equations for the longitudinal component of the momentum equation, and in the interests of brevity provide only the final expressions for the remaining components. These equations assume a dependence of g on r as $g \propto 1/r^2$, and every other quantity is dependent on the three spatial variables, longitude, latitude and radial distance from the centre of the planet. Here, we consider that Q is 0 for simplicity, and relax this assumption in §B.1.4.

The longitudinal equation of momentum is:

$$\frac{\partial u}{\partial t} + \frac{u}{r\cos\phi}\frac{\partial u}{\partial \lambda} + \frac{v}{r}\frac{\partial u}{\partial \phi} + w\frac{\partial u}{\partial r} + 2\Omega w\cos\phi - 2\Omega v\sin\phi + \frac{1}{\rho r\cos\phi}\frac{\partial p}{\partial \lambda} + \frac{uw}{r} - \frac{uv\tan\phi}{r} = 0. \tag{B.1}$$

Term by term we obtain (refer to Eq.(6.2) for definition of perturbed variables):

$$\left(\frac{\partial u}{\partial t}\right)' = \frac{1}{\rho_i}\frac{\partial u'}{\partial t}$$

$$\left(\frac{u}{r\cos\phi}\frac{\partial u}{\partial \lambda}\right)' = \frac{u'}{\rho_i r\cos\phi}\frac{\partial u_i}{\partial \lambda}$$

$$+ \frac{u_i}{r\cos\phi}\left(\frac{1}{\rho_i}\frac{\partial u'}{\partial \lambda} - \frac{u'}{\rho_i^2}\frac{\partial \rho_i}{\partial \lambda}\right)$$

$$\left(\frac{v}{r}\frac{\partial u}{\partial \phi}\right)' = \frac{v'}{\rho_i r}\frac{\partial u_i}{\partial \phi} + \frac{v_i}{r}\left(\frac{1}{\rho_i}\frac{\partial u'}{\partial \phi} - \frac{u'}{\rho_i^2}\frac{\partial \rho_i}{\partial \phi}\right)$$

$$\left(w\frac{\partial u}{\partial r}\right)' = \frac{w'}{\rho_i}\frac{\partial u_i}{\partial r} + w_i\left(\frac{1}{\rho_i}\frac{\partial u'}{\partial r} - \frac{u'}{\rho_i^2}\frac{\partial \rho_i}{\partial r}\right)$$

$$(2\Omega w\cos\phi)' = 2\Omega\frac{w'}{\rho_i}\cos\phi$$

$$(2\Omega v\sin\phi)' = 2\Omega\frac{v'}{\rho_i}\sin\phi$$

$$\begin{aligned}
&\left(\frac{1}{\rho r\cos\phi}\frac{\partial p}{\partial\lambda}\right)' = \frac{1}{\rho_i r\cos\phi}\left(\frac{\partial p'}{\partial\lambda}+\frac{1}{\rho_i}\frac{\partial p_i}{\partial\lambda}\left(\frac{\theta'}{g}-\frac{p'}{c_i^2}\right)\right)\\
&\left(\frac{uw}{r}\right)' = \frac{1}{\rho_i r}\left(u'w_i+u_iw'\right)\\
&\left(\frac{uv\tan\phi}{r}\right)' = \frac{\tan\phi}{\rho_i r}\left(u'v_i+u_iv'\right).
\end{aligned}$$

Therefore, the final five perturbed equations are:

$$\begin{aligned}
&\frac{\partial u'}{\partial t}+u'\left(\frac{1}{r\cos\phi}\frac{\partial u_i}{\partial\lambda}-\frac{u_i}{\rho_i r\cos\phi}\frac{\partial\rho_i}{\partial\lambda}-\frac{v_i}{\rho_i r}\frac{\partial\rho_i}{\partial\phi}-\frac{w_i}{\rho_i}\frac{\partial\rho_i}{\partial r}+\frac{w_i}{r}-\frac{v_i\tan\phi}{r}\right)+\frac{\partial u'}{\partial\lambda}\left(\frac{u_i}{r\cos\phi}\right)+\frac{\partial u'}{\partial\phi}\left(\frac{v_i}{r}\right)+\frac{\partial u'}{\partial r}\left(w_i\right)\\
&+v'\left(\frac{1}{r}\frac{\partial u_i}{\partial\phi}-2\Omega\sin\phi-\frac{u_i\tan\phi}{r}\right)+w'\left(\frac{\partial u_i}{\partial r}+2\Omega\cos\phi+\frac{u_i}{r}\right)+p'\left(\frac{-1}{c_i^2\rho_i r\cos\phi}\frac{\partial p_i}{\partial\lambda}\right)+\frac{\partial p'}{\partial\lambda}\left(\frac{1}{r\cos\phi}\right)\\
&+\theta'\left(\frac{1}{g\rho_i r\cos\phi}\frac{\partial p_i}{\partial\lambda}\right)=0
\end{aligned}\tag{B.2}$$

$$\begin{aligned}
&\frac{\partial v'}{\partial t}+u'\left(\frac{1}{r\cos\phi}\frac{\partial v_i}{\partial\lambda}+2\Omega\sin\phi+\frac{2u_i\tan\phi}{r}\right)+v'\left(-\frac{u_i}{\rho_i r\cos\phi}\frac{\partial\rho_i}{\partial\lambda}+\frac{1}{r}\frac{\partial v_i}{\partial\phi}-\frac{v_i}{\rho_i r}\frac{\partial\rho_i}{\partial\phi}-\frac{w_i}{\rho_i}\frac{\partial\rho_i}{\partial r}+\frac{w_i}{r}\right)+\frac{\partial v'}{\partial\lambda}\left(\frac{u_i}{r\cos\phi}\right)\\
&+\frac{\partial v'}{\partial\phi}\left(\frac{v_i}{r}\right)+\frac{\partial v'}{\partial r}\left(w_i\right)+w'\left(\frac{\partial v_i}{\partial r}+\frac{v_i}{r}\right)+p'\left(\frac{-1}{c_i^2\rho_i r}\frac{\partial p_i}{\partial\phi}\right)+\frac{\partial p'}{\partial\phi}\left(\frac{1}{r}\right)+\theta'\left(\frac{1}{g\rho_i r}\frac{\partial p_i}{\partial\phi}\right)=0
\end{aligned}\tag{B.3}$$

$$\begin{aligned}
&\frac{\partial w'}{\partial t}+u'\left(\frac{1}{r\cos\phi}\frac{\partial w_i}{\partial\lambda}-2\Omega\cos\phi-\frac{2u_i}{r}\right)+v'\left(\frac{1}{r}\frac{\partial w_i}{\partial\phi}-\frac{2v_i}{r}\right)+w'\left(-\frac{u_i}{\rho_i r\cos\phi}\frac{\partial\rho_i}{\partial\lambda}-\frac{v_i}{\rho_i r}\frac{\partial\rho_i}{\partial\phi}-\frac{w_i}{\rho_i}\frac{\partial\rho_i}{\partial r}+\frac{\partial w_i}{\partial r}\right)\\
&+\frac{\partial w'}{\partial\lambda}\left(\frac{u_i}{r\cos\phi}\right)+\frac{\partial w'}{\partial\phi}\left(\frac{v_i}{r}\right)+\frac{\partial w'}{\partial r}\left(w_i\right)+p'\left(\frac{-1}{c_i^2\rho_i}\frac{\partial p_i}{\partial r}\right)+\frac{\partial p'}{\partial r}+\theta'\left(\frac{1}{g\rho_i r}\frac{\partial p_i}{\partial r}\right)=0
\end{aligned}\tag{B.4}$$

$$\begin{aligned}
&\frac{\partial p'}{\partial t}+u'\left(\frac{1}{\rho_i r\cos\phi}\frac{\partial p_i}{\partial\lambda}-\frac{c_i^2}{\rho_i r\cos\phi}\frac{\partial\rho_i}{\partial\lambda}\right)+\frac{\partial u'}{\partial\lambda}\left(\frac{c_i^2}{r\cos\phi}\right)+v'\left(\frac{1}{\rho_i r}\frac{\partial p_i}{\partial\phi}-\frac{c_i^2}{r}\left(\frac{1}{\rho_i}\frac{\partial\rho_i}{\partial\phi}+\tan\phi\right)\right)+\frac{\partial v'}{\partial\phi}\left(\frac{c_i^2}{r}\right)\\
&+w'\left(c_i^2\left(\frac{2}{r}+\frac{N_i^2}{g}\right)\right)+\frac{\partial w'}{\partial r}\left(c_i^2\right)+p'\left(\gamma\left(\frac{1}{r\cos\phi}\frac{\partial u_i}{\partial\lambda}+\frac{1}{r}\frac{\partial v_i}{\partial\phi}-\frac{v_i}{r}\tan\phi+\frac{\partial w_i}{\partial r}+\frac{2}{r}w_i\right)\right)\\
&+\frac{\partial p'}{\partial\lambda}\left(\frac{u_i}{r\cos\phi}\right)+\frac{\partial p'}{\partial\phi}\left(\frac{v_i}{r}\right)+\frac{\partial p'}{\partial r}\left(w_i\right)=0
\end{aligned}\tag{B.5}$$

$$\begin{aligned}
&\frac{\partial\theta'}{\partial t}+u'\left(\frac{g}{r\cos\phi}\frac{1}{\theta_i}\frac{\partial\theta_i}{\partial\lambda}\right)+v'\left(\frac{g}{r}\frac{1}{\theta_i}\frac{\partial\theta_i}{\partial\phi}\right)+w'\left(N_i^2\right)+\theta'\left(\frac{u_i}{r\cos\phi}\left(\frac{1}{\theta_i}\frac{\partial\theta_i}{\partial\lambda}-\frac{1}{\rho_i}\frac{\partial\rho_i}{\partial\lambda}\right)+\frac{v_i}{r}\left(\frac{1}{\theta_i}\frac{\partial\theta_i}{\partial\phi}-\frac{1}{\rho_i}\frac{\partial\rho_i}{\partial\phi}\right)\right.\\
&\left.+w_i\left(\frac{N_i^2}{g}-\frac{1}{g}\frac{\partial g}{\partial r}-\frac{1}{\rho_i}\frac{\partial\rho_i}{\partial r}\right)\right)+\frac{\partial\theta'}{\partial\lambda}\left(\frac{u_i}{r\cos\phi}\right)+\frac{\partial\theta'}{\partial\phi}\left(\frac{v_i}{r}\right)+\frac{\partial\theta'}{\partial r}\left(w_i\right)=0
\end{aligned}\tag{B.6}$$

with $\partial X'/\partial t = i\sigma X'$.

B.1.2 2D, axisymmetric

For the axisymmetric case, the equations are directly obtained from the 3D case by choosing a longitudinal wavenumber m such that $X'(t,r,\phi,\lambda) = X'(r,\phi)\mathrm{e}^{\mathrm{i}\sigma t}\mathrm{e}^{\mathrm{i}(\mathrm{m}/2\pi)\lambda}$.

B.1.3 Two layer equivalent depth

The reference for this particular case can be found in Showman and Polvani [2011] or Vallis [2006]. We consider a dynamic layer above a quiescent layer, reservoir of mass or energy, and study the horizontal winds u and v as well as the height of the layer h, depending on both x and y the cartesian horizontal coordinates. We follow the definitions of Showman and Polvani [2011] for the variables, hence consider adimensional equations. There is consequently only three equations to be implemented:

$$\frac{\partial u'}{\partial t} + u'\left(\frac{\partial u_i}{\partial x}\right) + \frac{\partial u'}{\partial x}(u_i) + \frac{\partial u'}{\partial y}(v_i) + v'\left(\frac{\partial u_i}{\partial y} - y\right) + \frac{\partial h'}{\partial x} = 0 \tag{B.7}$$

$$\frac{\partial v'}{\partial t} + u'\left(\frac{\partial v_i}{\partial x} + y\right) + v'\left(\frac{\partial v_i}{\partial y}\right) + \frac{\partial v'}{\partial x}(u_i) + \frac{\partial v'}{\partial y}(v_i) + \frac{\partial h'}{\partial y} = 0 \tag{B.8}$$

$$\frac{\partial h'}{\partial t} + u'\left(\frac{\partial H}{\partial x}\right) + \frac{\partial u'}{\partial x}(H) + v'\left(\frac{\partial H}{\partial y}\right) + \frac{\partial v'}{\partial y}(H) + h'\left(\frac{\partial u_i}{\partial x} + \frac{\partial v_i}{\partial y}\right) + \frac{\partial h'}{\partial x}(u_i) + \frac{\partial h'}{\partial y}(v_i) = 0 \tag{B.9}$$

where $H = H(x, y)$ is the initial steady height.

B.1.4 Heating rate

Particular care must be taken when dealing with the heating rate. If we call the heating rate Q_i, as the initial state is steady the zeroth order term will cancel the terms involving Q_i in Eq.(6.1e). However, two situations must be considered: the θ/T factor in Eq.(6.1e) has to be linearised, and will be a source of additional terms. Additionally, if Q_i depends on the atmospheric state (for example with Newtonian heating, see next appendix), a perturbation in the atmosphere will be associated with a change Q' in Q_i. Therefore, if we write equation Eq.(B.6) as

$$\frac{g\rho_i}{\theta_i}\left(\frac{D\theta}{Dt}\right)' = 0 \quad , \tag{B.10}$$

where the $g\rho_i/\theta_i$ factor arises from the definition of θ', the final equation involving the heating rate is:

$$\frac{g\rho_i}{\theta_i}\left(\frac{D\theta}{Dt}\right)' + p'\left(\frac{g\kappa}{RT_i^2}\frac{Q_i}{c_p}\right) - \frac{Q'}{c_p}\left(\frac{g\rho_i}{T_i}\right) = 0, \tag{B.11}$$

where Q', if it exists, depends linearly on the linearised atmospheric variables.

Moreover, obtaining Eq.(B.5) implies to use Eq.(6.1e), and therefore additional terms also have to be included. More precisely, one could show that Eq.(B.5) can be written as

$$\left(\frac{Dp}{Dt} + \gamma p \vec{\nabla}\cdot\vec{v}\right)' = 0 \quad . \tag{B.12}$$

With the Q terms we obtain:

$$\left(\frac{Dp}{Dt} + \gamma p \vec{\nabla}\cdot\vec{v}\right)' + \gamma R\frac{Q_i}{c_p}\left(\frac{\theta'}{g} - \frac{p'}{c_i^2}\right) + \frac{Q'}{c_p}(-\gamma R\rho_i) = 0 \quad . \tag{B.13}$$

These new terms in Eqs.(B.6) and (B.5) have to be implemented in the matrix from which we solve for eigenvectors, but do not lead to a change in the way of finding the eigenvectors.

B.1.5 Steady linear circulation

Following Showman and Polvani [2011] and subsequently Komacek and Showman [2016], we have implemented the possibility to solve for linear steady states instead of waves and instabilities. We therefore have to impose a heating of the atmosphere, associated to dissipative processes in order to reach a steady state.

This heating function is extremely different from the heating of Appendix B.1.4: in Appendix B.1.4, we linearized the heating term coming from the initial steady solution of Navier Stokes equations. Here, we prescribe a small forcing of the atmosphere that will make it depart from its initial steady state, and seek for the new steady state that the atmosphere will reach at the linear order (because the heating has a small amplitude). For simplicity reasons, we will consider that the initial steady state was obtained without forcing of the atmosphere (hence Q in Eqs.(6.1e), (B.11) and (B.13) is identically null), and call Q_l the small amplitude, linear forcing we impose.

In that case, the perturbed variables are assumed to be constant with time (σ is taken to be zero). The dissipative effects will just be linear drags in Eqs.(6.1a), (6.1b) and (6.1c) expressed as $-\vec{v}/\tau_{\text{drag}}$ where τ_{drag} is a characteristic time for the drag, eventually dependent on the space coordinates [see Showman and Polvani, 2011].

If Q_l is constant, then we just have to modify Eqs.(B.5) and (B.6) in a similar way than in Appendix B.1.4:

$$\frac{g\rho_i}{\theta_i}\left(\frac{D\theta}{Dt}\right)' = \frac{g\rho_i}{T_i}\frac{Q_l}{c_p}$$

$$\left(\frac{Dp}{Dt} + \gamma p\vec{\nabla}\cdot\vec{v}\right)' = \gamma R\rho_i\frac{Q_l}{c_p}$$

which, as Q_l is order 1, just consisted in neglecting the second order terms in Eqs.(B.13) and (B.11) and moving the constant heating terms to the right hand side. A dissipative or diffusive process could also be added in the energy equation.

Additionally, a special case must be discussed: Newtonian Heating [see e.g., Mayne et al., 2014b]. In that case, Q_l is not constant but depends on the thermodynamic state of the atmosphere. More precisely, calling Q_{N} the Newtonian heating rate:

$$\frac{Q_{\text{N}}}{c_p} = \frac{T_{\text{eq}} - T}{\tau_{\text{rad}}}, \tag{B.14}$$

where T_{eq} is a prescribed equilibrium temperature and τ_{rad} a characteristic radiative time, both depending on space variables.

For the linear forcing approximation to remain correct, T_{eq} must be sufficiently close to the initial temperature T_i, but then a small change in T_i will have an impact on Q_{N} of the same order of Q_{N} itself. With our choice of perturbed variables, it is easy to show that:

$$T' = T_i\left(p'\frac{\kappa}{p_i} + \theta'\frac{1}{g\rho_i}\right), \tag{B.15}$$

and subsequently

$$\frac{Q_N}{c_p} = \frac{T_{\text{eq}} - T_i}{\tau_{\text{rad}}} - \frac{T'}{\tau_{\text{rad}}} \equiv \frac{Q_{\text{N},i}}{c_p} - \frac{T_i}{\tau_{\text{rad}}}\left(p'\frac{\kappa}{p_i} + \theta'\frac{1}{g\rho_i}.\right) \tag{B.16}$$

Finally Eqs.(B.5) and (B.6) can be rewritten as (using $\gamma R T_i = c_i^2$):

$$\left(\frac{Dp}{Dt} + \gamma p\vec{\nabla}\cdot\vec{v}\right)' + \frac{c_i^2\rho_i}{\tau_{\text{rad}}}\left(p'\frac{\kappa}{p_i} + \theta'\frac{1}{g\rho_i}\right) = \frac{Q_{\text{N},i}}{c_p}\left(\gamma R\rho_i\right) \tag{B.17}$$

$$\frac{g\rho_i}{\theta_i}\left(\frac{D\theta}{Dt}\right)' + \frac{g\rho_i}{\tau_{\mathrm{rad}}}\left(p'\frac{\kappa}{p_i} + \theta'\frac{1}{g\rho_i}\right) = \frac{Q_{\mathrm{N},i}}{c_p}\left(\frac{g\rho_i}{T_i}\right). \tag{B.18}$$

To summarise, when looking for a steady linear circulation with Newtonian heating, we need to invert the matrix C as advertised in Section 6.2.4, where C arises from Eqs.(B.2) to (B.6) and includes the heating rates and dissipations expressed in the text of this Appendix, and in Eqs.(B.17) and (B.18).

B.2 A posteriori energy equation

In order to obtain a semi analytical verification for the frequency, we integrate the energy of the modes over the whole volume, and express it as an a posteriori condition on the frequency σ. In this part, we will assume that the bottom boundary condition is a no escape condition ($w' = 0$) and that the initial state is in the hydrostatic balance: $\frac{\partial p_i}{\partial r} = -\rho_i g$, with no initial heating (see B.1.4). These assumptions could be relaxed, but would be sources of numerous additional terms whereas they are always verified in our setups.

In the 2D axisymmetric case at rest with no angular dependency in the initial variables, Thuburn et al. [2002b] used as variables u' , $-\mathrm{i}v'$, $-\mathrm{i}w'$, p' and θ' because this simplifies greatly the calculation. In order to allow for easier verification of our equations, we adopt the same definition for the perturbed variables. However, for simplicity reason, we drop the primes in the next equation and use v and w, not $\mathrm{i}v'$ and $\mathrm{i}w'$. Therefore, one has to remember that the v and w expressed in the following equations are actually $-\mathrm{i}v'$ and $-\mathrm{i}w'$ where v' and w' are the solutions of Eq.(6.8). The other variables are not affected.

Denoting a complex conjugate by a star, we express the integral of energy as:

$$\iiint_\Omega \frac{1}{\rho_i}\Big(\mathrm{i}u^*(B.2) + v^*(B.3) + w^*(B.4) + \mathrm{i}\frac{p^*}{c_i^2}(B.5) + \mathrm{i}\frac{\theta^*}{N_i^2}(B.6)\Big)\mathrm{d}V = 0 \tag{B.19}$$

where Ω is the whole volume, $\mathrm{d}V = r^2\cos\phi\,\mathrm{d}r\mathrm{d}\phi\mathrm{d}\lambda$ the infinitesimal volume and (B.2) is the left hand side of the complete equation Eq.(B.2) etc.

The calculation are really cumbersome, but present no particular difficulty. In order to have a physical insight in the leading mechanism from this a posteriori energy equation, we have decided to separate this integral into 5 parts:

- The first part involves only the thermodynamic initial state (no velocities) with a dependency on the radial variable r solely. An initial atmosphere at rest with no angular dependency would have contributions to the energy only from this part.
- The second part involves the terms coming from the angular dependency in the thermodynamic steady variables only.
- The third part comes from the steady zonal velocity u_i.
- The fourth part is generated by the steady meridional velocity v_i.
- And finally the last part is due to the initial steady vertical velocity w_i.

Denoting this decomposition of the energy integral as [1] to [5], and remembering $\partial/\partial t = -i\sigma$ we obtain an a posteriori equation on σ:

$$\sigma = -\frac{\iiint_\Omega \frac{1}{\rho_i}\left([1]+[2]+[3]+[4]+[5]\right)\mathrm{d}V}{\iiint_\Omega E\mathrm{d}V} \tag{B.20}$$

This is similar to Eq.(6.4). The $1/\rho_i$ factor might seem useless as it is already in Eq.(B.19) but is a necessary density weighting to obtain the appropriate equations. E is unchanged:

$$E = \frac{1}{2\rho_i}\left((|u|^2+|v|^2+|w|^2+\frac{|\theta|^2}{N_i^2}+\frac{|p|^2}{c_i^2}\right) \tag{B.21}$$

After sorting (real component, then imaginary then complex), the calculation gives:

$$[1] = \Re\left(f(u^*v) - F(u^*w) + \frac{\mathrm{i}}{r\cos\phi}u^*\frac{\partial p}{\partial\lambda} + \frac{1}{r}v^*\frac{\partial p}{\partial\phi} + \frac{g}{c_i^2}w^*p + w^*\frac{\partial p}{\partial r} - w^*\theta\right) \tag{B.22}$$

$$\begin{aligned}[2] = {} & \Re\left[\frac{1}{r\cos\phi}\left(\frac{1}{\rho_i c_i^2}\frac{\partial p_i}{\partial\lambda}\mathrm{i}up^* + \frac{\partial p_i/\partial\lambda}{\partial p_i/\partial r}\mathrm{i}u\theta^*\right) - \frac{1}{r}\left(\frac{1}{\rho_i c_i^2}\frac{\partial p_i}{\partial\phi}vp^* + \frac{\partial p_i/\partial\phi}{\partial p_i/\partial r}v\theta^*\right)\right] + \frac{\mathrm{i}}{2r\cos\phi}\left(\frac{\partial\theta_i/\partial\lambda}{\partial\theta_i/\partial r} - \frac{\partial p_i/\partial\lambda}{\partial p_i/\partial r}\right)u\theta^* \\ & - \frac{1}{2r}\left(\frac{\partial\theta_i/\partial\phi}{\partial\theta_i/\partial r} - \frac{\partial p_i/\partial\phi}{\partial p_i/\partial r}\right)v\theta^*\end{aligned} \tag{B.23}$$

$$\begin{aligned}[3] = {} & \Re\left(\frac{u_i\tan\phi}{r}u^*v - \frac{u_i}{r}u^*w\right) + \frac{\mathrm{i}}{2}\left[\frac{u_i}{r\cos\phi}\frac{\partial\rho_i}{\partial\lambda}\left(-2E + \frac{1}{\rho_i c_i^2}|p|^2\right) + \frac{1}{r\cos\phi}\frac{\partial u_i}{\partial\lambda}|u|^2 + \frac{u_i}{N_i^2\theta_i r\cos\phi}\frac{\partial\theta_i}{\partial\lambda}|\theta|^2 + \frac{\gamma}{c_i^2 r\cos\phi}\frac{\partial u_i}{\partial\lambda}|p|^2\right] \\ & + \frac{\mathrm{i}}{2r\cos\phi}u_i\left(u^*\frac{\partial u}{\partial\lambda} + v^*\frac{\partial v}{\partial\lambda} + w^*\frac{\partial w}{\partial\lambda} + \frac{\theta^*}{N_i^2}\frac{\partial\theta}{\partial\lambda} + \frac{p^*}{c_i^2}\frac{\partial p}{\partial\lambda}\right) + \frac{u_i\tan\phi}{2r}uv^* - \frac{1}{2r}\frac{\partial u_i}{\partial\phi}vu^* - \frac{u_i}{2r}uw^* - \frac{1}{2}\frac{\partial u_i}{\partial r}wu^*\end{aligned} \tag{B.24}$$

$$\begin{aligned}[4] = {} & -\Im\left(\frac{v_i}{r}v^*w\right) + \frac{\mathrm{i}}{2r}\left[v_i\left(\frac{\partial\rho_i}{\partial\phi}\left(-2E + \frac{|p|^2}{\rho_i c_i^2}\right) - \tan\phi|u|^2 - \frac{\gamma\tan\phi}{c_i^2}|p|^2 + \frac{1}{\theta_i}\frac{\partial\theta_i}{\partial\phi}\frac{|\theta^2|}{N_i^2}\right) + \frac{\partial v_i}{\partial\phi}\left(|v|^2 + \frac{\gamma}{c_i^2}|p|^2\right)\right] \\ & + \mathrm{i}\frac{v_i}{2r}\left(u^*\frac{\partial u}{\partial\phi} + v^*\frac{\partial v}{\partial\phi} + w^*\frac{\partial w}{\partial\phi} + \frac{\theta^*}{N_i^2}\frac{\partial\theta}{\partial\phi} + \frac{p^*}{c_i^2}\frac{\partial p}{\partial\phi} - w^*v\right) + \frac{1}{2r\cos\phi}\frac{\partial v_i}{\partial\lambda}uv^* + \frac{\mathrm{i}}{2}\frac{\partial v_i}{\partial r}wv^*\end{aligned} \tag{B.25}$$

$$\begin{aligned}[5] = {} & \mathrm{i}\frac{w_i}{2}\left[\frac{\partial\rho_i}{\partial r}\left(-2E + \frac{|p|^2}{\rho_i c_i^2}\right) + \frac{|u|^2}{r} + \frac{|v|^2}{r} + \frac{|w|^2}{r} + \frac{|\theta|^2}{N_i^2}\left(\frac{N_i^2}{g} - \frac{1}{g}\frac{\partial g}{\partial r}\right) + \frac{2\gamma}{c_i^2 r}|p|^2\right] + \frac{\mathrm{i}}{2}\frac{\partial w_i}{\partial r}\left(|w|^2 + \frac{\gamma}{c_i^2}|p|^2\right) \\ & + \mathrm{i}\frac{w_i}{2}\left(u^*\frac{\partial u}{\partial r} + v^*\frac{\partial v}{\partial r} + w^*\frac{\partial w}{\partial r} + \frac{\theta^*}{N_i^2}\frac{\partial\theta}{\partial r} + \frac{p^*}{c_i^2}\frac{\partial p}{\partial r}\right) + \frac{1}{2r\cos\phi}\frac{\partial w_i}{\partial\lambda}uw^* + \frac{\mathrm{i}}{2r}\frac{\partial w_i}{\partial\phi}vw^*\end{aligned} \tag{B.26}$$

Appendix C

Non orthogonality in the case $\tau_{\mathrm{rad}} \neq \tau_{\mathrm{drag}}$

In the case $\tau_{\mathrm{rad}} = \tau_{\mathrm{drag}}$, Matsuno [1966] has obtained a simple equation linking $u_{n,l}$ and $v_{n,l}$, the horizontals speed of the eigenvector (n,l), from equations (7.7) and (7.9):

$$u_{n,l} = \frac{\omega_{n,l} y v_{n,l} + k\partial v_{n,l}/\partial y}{i(\omega_{n,l} - k)(\omega_{n,l} + k)} \ . \tag{C.1}$$

A similar equation is obtained for $h_{n,l}$. As $v_{n,l} \propto \psi_n(y) = H_n(y)e^{-y^2/2}$, with H_n the nth Hermite polynomial, the use of the recurrence relations of the Hermite polynomials:

$$\frac{\mathrm{d}H_n(y)}{\mathrm{d}y} = 2nH_{n-1}(y), \tag{C.2}$$

$$H_{n+1}(y) = 2yH_n(y) - 2nH_{n-1}(y), \tag{C.3}$$

the eigenvector (n,l) is simply written as:

$$\begin{pmatrix} v_{n,l} \\ u_{n,l} \\ h_{n,l} \end{pmatrix} = \begin{pmatrix} \mathrm{i}(\omega_{n,l}^2 - k^2)\psi_n(y) \\ \frac{1}{2}(\omega_{n,l} - k)\psi_{n+1}(y) + n(\omega_{n,l} + k)\psi_{n-1}(y) \\ \frac{1}{2}(\omega_{n,l} - k)\psi_{n+1}(y) - n(\omega_{n,l} + k)\psi_{n-1}(y) \end{pmatrix} \ . \tag{C.4}$$

The orthogonality of the solution is easily proven, and the completeness is proved by use of the completeness of the Hermite functions.

In the case $\tau_{\mathrm{rad}} \neq \tau_{\mathrm{drag}}$, equation (C.1) is slightly changed to get:

$$u_{n,l} = \frac{(\mathrm{i}\omega_{n,l} + \tau_{\mathrm{rad}}^{-1}) y v_{n,l} + \mathrm{i}k\partial v_{n,l}/\partial y}{k^2 + (\mathrm{i}\omega_{n,l} + \tau_{\mathrm{rad}}^{-1})(\mathrm{i}\omega_{n,l} + \tau_{\mathrm{drag}}^{-1})}, \tag{C.5}$$

and we recall that $v_{n,l} \propto H_n(c_{n,l}y)e^{-c_{n,l}^2 y^2/2}$ where

$$c_{n,l}^4 = \frac{\mathrm{i}\omega_{n,l} + \tau_{\mathrm{rad}}^{-1}}{\mathrm{i}\omega_{n,l} + \tau_{\mathrm{drag}}^{-1}} \ . \tag{C.6}$$

Therefore, the expression of the eigenvector (n,l) is:

$$\begin{pmatrix} v_{n,l} \\ u_{n,l} \\ h_{n,l} \end{pmatrix} = \begin{pmatrix} (k^2 + (\mathrm{i}\omega_{n,l} + \tau_{\mathrm{rad}}^{-1})(\mathrm{i}\omega_{n,l} + \tau_{\mathrm{drag}}^{-1}))\psi_n(c_{n,l}y) \\ \frac{1}{2}\left(\frac{\mathrm{i}\omega_{n,l} + \tau_{\mathrm{rad}}^{-1}}{c_{n,l}} - \mathrm{i}kc_{n,l}\right)\psi_{n+1}(c_{n,l}y) + n\left(\frac{\mathrm{i}\omega_{n,l} + \tau_{\mathrm{rad}}^{-1}}{c_{n,l}} + \mathrm{i}kc_{n,l}\right)\psi_{n-1}(c_{n,l}y) \\ \frac{1}{2}\left(c_{n,l}(\mathrm{i}\omega_{n,l} + \tau_{\mathrm{drag}}^{-1}) - \frac{\mathrm{i}k}{c_{n,l}}\right)\psi_{n+1}(c_{n,l}y) - n\left(c_{n,l}(\mathrm{i}\omega_{n,l} + \tau_{\mathrm{drag}}^{-1}) + \frac{\mathrm{i}k}{c_{n,l}}\right)\psi_{n-1}(c_{n,l}y) \end{pmatrix} . \tag{C.7}$$

The dependency with $c_{n,l}$ in the parabolic cylinder function makes it much harder to calculate the scalar products between two eigenvectors, and in the general case there is no reason for these eigenvectors to be perpendicular to one another.

On the other hand, it is easily shown that the set of eigenvectors (n,l) are linearly independent (thanks to the Hermite polynomials). We are working on a rigorous proof to assess that they form a complete ensemble of solutions, allowing for a projection of the heating function onto these eigenvectors.